Synthesis and characterization of rare-earth doped borates phosphors for application in solid state lighting

By

Lephoto Mantwa Annah

(MSc)

A thesis submitted in fulfilment of the requirements for the degree

PHILOSOPHIAE DOCTOR

in the

Faculty of Natural and Agricultural Sciences

Department of Physics

at the

University of the Free State (QwaQwa campus)

Promoter: Prof. O.M. Ntwaeaborwa

Co-promoter: Dr. K.G. Tshabalala

October 2017

Acknowledgements

Let me extend my heartfelt gratitude to some individual of which without it would not have been possible. ***But first let me THANK GOD****.*

- **Prof O. M. Ntwaeborwa –** as my supervisor, I would like to express my deep gratitude to you. Thak you for your patience, guidance and encouragements. It was not an easy journey but you never gave up on me as you always told me to do my best and you will always help were possible. May the God-Almighty bless you and prosper in everything you do.
- **Dr K. G. Tshabalala –** as my co-supervisor, I would like to thank you for always been there for me. Listening to my frustrations, your everyday support and advices. I really appreciate it.
- **Mr S. J. Motloung –** thank you for the discussions we had. Thank you for your support and advices. *I am sorry for breaking most of the crucibles* and thank you for buying me new ones so I can continue with the lab work.
- **Prof H. C. Swart –** Thank you for always opening the doors of UFS Physics department (Bloemfontein campus) for me to use the research techniques throughout this research.
- **Ms. S. Kiprotich –** thank you for your help and advices.
- **Staff members (Prof F. B. Dejene, Dr L. F. Koao, Mr R. O. Ocaya and Ms M. K. Lebeko) and fellow students of Physics department (QwaQwa campus) –** I am grateful to all of you with your invaluable contributions.
- **Dr I. Ahemen, Dr F. G. Hone and Dr O. Echendu –** Thank you all for your invaluable contributions.
- **Dr J. P. Mofokeng (**Chemistry department QwaQwa campus) – thank you for your assistance with FTIR measurements.
- **Dr P. P. Mokoena –** thank you for assisting with FE-SEM measurements.
- **Dr M. M. Duvenhage –** thank you for assisting with ToF-SIMS measurements.
- **Dr A. K. Bedyal –** thank you for assisting with Thermoluminescence (TL) analysis.

- **Prof R. E. Kroon –** thank you for assisting with 325 nm He-Cd laser measurements and always been there to assist with research techniques (PL and UV) when they were giving me problems.
- **Dr T. K. Pathak –** thank you for assisting with 325 nm He-Cd laser measurements.
- **Dr G. H. Mhlongo –** thank you for assisting with HRTEM measurements.
- **University of the Free State (UFS) and National Research Foundation (NRF) –** thank you for financial support throughout this research.
- **My family and friends –** Thank you all for your support and encourangemets for me to persue my dreams. Thank you mom (Lephoto Mosela) for not giving up on me and listening to my stories about my research. Thank you for helping me raise my son (Ndabezitha Lephoto) and taking care of him when I had to travel to Bloefomtein to characterize my samples and when I had to attend conferences. I know it was not an easy job but you did it for me anyway. May the God-Almighty bless you abundantly and keep you. My granny (Lephoto Maria), Sister (Ncana Mampho), Siblings (Lephoto Tsietsi "*Gift*", karabo "*Tata*" and Keneuwe "*Toto*"), thank you for being in my life and taking part in the upbringing of my son while I was away. Be Blessed Family!

"Every successful individual knows that his or her archievement depends on a community of persons working together" – ***Paul Ryan***

Declaration

I, the undersigned, hereby declare that the work contained in this thesis is my own original work except as indicated in the references. It has not been submitted before for any degree or examination in this or any other university.

-Lephoto Mantwa Annah

Signature ……..

Date ……..……..

Dedication

This thesis is dedicated to me and my family.

And above all

To the Almighty God.

Colossians 3:17 – "*And whatever you do, in word or deed, do everything in the name of the Lord Jesus, giving thanks to God the Father through him."*

Abstract

Inorganic borates have long been a focus of research for their variety of structure types, transparency to a wide range of wavelengths, high laser damage tolerance, and high optical quality. In the current study, borates such as BaB_8O_{13} and $LiBaBO_3$ were synthesized by using solution combustion method and solid state method respectively. These hosts were doped and co-doped with rare-earth ions such as europium (Eu^{3+}), samarium (Sm^{3+}), dysprosium (Dy^{3+}), cerium (Ce^{3+}) and non-rare-earth ion bismuth (Bi^{3+}). The structure, particle morphology, stretching vibrations, photoluminescence and chemical composition of the materials were studied using different analytical techniques. The structure of the materials was studied using X-ray diffraction (XRD). Particle morphology was examined by scanning electron microscope (SEM) and transmission electron microscopy (TEM). The chemical composition analysis was carried out using energy dispersive spectrometer (EDS). The stretching frequency modes were examined using Fourier transform infrared spectroscopy (FTIR). The thermal analysis was carried out by thermogravimetric analysis (TGA). The optical properties of the materials were characterized using photoluminescence (PL) spectroscopy and ultraviolet-visible (UV-Vis) spectroscopy at room temperature. Thermoluminescence analysis was also carried out in this study.

The XRD patterns of BaB_8O_{13} doped with different rare-earths ions confirmed the formation of orthorhombic structure with cell parameters a = 8.550 Å, b = 17.350 Å and c = 13.211 Å. The patterns showed some extra peaks which were attributed to unreacted precursors. SEM images showed agglomeration of particles with irregular shapes. The infrared stretching frequencies detected in the spectral wavenumber range of 650 – 1600 cm^{-1} also confirmed the formation of the BaB_8O_{13} host matrix. The chemical compositions from the EDS analysis confirmed the formation of the desired powder phosphors. From BaB_8O_{13}: Bi^{3+} powder phosphors, the broad PL emission due to $^1S_0 - {}^3P_1$ transitions of Bi^{3+} ions was observed at 548 nm in the green region of the visible spectrum under 271 nm excitation. The Commission International de I'Eclairage (CIE) coordinates of x = 0.3267 and y = 0.6004 suggest that the phosphor can be used as a source of green light in light emitting devices of different types. The decay spectra were also recorded and their characteristics showed that the phosphors consist of a single exponential

decay process. The BaB_8O_{13}: Ce^{3+} powder phosphors showed PL emission at around 515 nm ascribed to $5d^1 - 4f^1$ transition of Ce^{3+} after excitation at 270 nm. A standard CIE diagram derived from relative emissions from the powder phosphors suggested a unique emission concentrated in the green region, thus the phosphor serve as a potential source of green light in light emitting devices. BaB_8O_{13}: Eu^{3+} emits red light, and the strongest peak was located at 614 nm, which was attributed to the $^5D_0 \rightarrow {}^7F_2$ transition of Eu^{3+}. BaB_8O_{13}: Sm^{3+} produced red-orange light, and the major emission peak was located at 596 nm which was assigned to the $^4G_{5/2} \rightarrow {}^6H_{7/2}$ transition of Sm^{3+}. When excited at 402 nm, the PL emission intensity from BaB_8O_{13}: *0.05*Eu^{3+}; *0.005*Sm^{3+} at 614 nm was enhanced considerably compared to that of the sample without Sm^{3+}, suggesting that energy was transferred from Sm^{3+} to Eu^{3+}. The CIE coordinates of BaB_8O_{13}: *0.05*Eu^{3+}; *0.005*Sm^{3+} powder phosphor (0.637, 0.362) were located in the red region indicating that the phosphor can be used as a source of red light in LEDs. The luminescence spectra of BaB_8O_{13}: Dy^{3+} excited by 350 nm showed two intense peaks at 480 nm and 574, corresponding to the $^4F_{9/2} \rightarrow {}^6H_{15/2}$ and $^4F_{9/2} \rightarrow {}^6H_{13/2}$ transitions of Dy^{3+}, respectively. According to the CIE coordinates, this phosphor has great potential as a single-component white-light-emitting phosphor for near-UV LEDs.

The XRD patterns of the $LiBaBO_3$ phosphors showed that they crystallized in a pure monoclinic phase. The scanning electron microscopy images showed that the powders were made up of fluffy needle-like particles that were randomly aligned. The band-gap of the $LiBaBO_3$ host was estimated to be 3.33 eV from the UV-Vis absorption data. Blue emission was observed from the $LiBaBO_3$ host which was ascribed to the self-activation of the host matrix. In addition, greenish-blue (493 nm) and red (613 nm) emissions were observed from europium-doped samples and were attributed to the emissions of Eu^{2+} and Eu^{3+}, respectively. Furthermore, after co-doping with Bi^{3+}, the emission intensity of Eu^{3+} located at 613 nm was significantly enhanced. From the CIE coordinates, the tunable color properties of $LiBaBO_3$: Eu^{3+} indicated that the phosphors provide a potential to be a single component white light phosphor. $LiBaBO_3$: Dy^{3+} showed three emission peaks at 482 nm (blue), 575 nm (yellow) and 664 nm (red) which were attributed to $^4F_{9/2} - {}^6H_{15/2}$, $^4F_{9/2} - {}^6H_{13/2}$ and $^4F_{9/2} - {}^6H_{11/2}$ transitions of Dy^{3+} respectively. The CIE chromatic coordinates and color-correlated temperature were also determined for this phosphor.

Keywords

Borates, Phosphors, Combustion method, Solid state method, Rare earths, Light emitting diodes

Acronyms

- **XRD** X-ray diffraction
- **SEM** Scanning electron microscopy
- **TEM** Transmission electron microscopy
- **FTIR** Fourier transmission infrared
- **TOF-SIMS** Time-of-flight secondary ion mass spectroscopy
- **TGA** Thermo gravimetric analysis
- **UV-Vis** Ultraviolet visible spectroscopy
- **PL** Pholuminescence
- **TL** Thermoluminescence
- **JCPDS** Joint Committee on Powder Diffraction Standards
- **CIE** Commission Internationale de l'Eclairage
- **SSL** Solid-state lighting
- **LED** Light-emitting-diode
- **RE** Rare-earth
- **Ce^{3+}** Cerium
- **Eu^{3+}** Europium
- **Dy^{3+}** Dysprosium
- **Sm^{3+}** Samarium
- **Bi^{3+}** Bismuth

Table of contents

List of figures

List of tables

Chapter 1

General Introduction

1.1 Overview

Because fossil fuels are becoming scarce and the expected climate change, our standard of living can only be maintained by a significant increase in energy efficiency. Large amounts of energy are consumed for lighting and during operation of displays. Thus, the targets are the development of economical light sources like white light-emitting diodes and display panels with enhanced efficiency. A possible contribution might be delivered by phosphors which allow the conversion of thermal radiation into electrical energy [1].

Approximately 17% of the total energy consumed in South Africa is transformed into lighting [2]. The incandescent light bulbs had lit up our lives since the beginning of the twentieth century, when they superseded the first electric lamps, which were the carbon-arc lamps. In the incandescent bulbs, a large part of the power consumed is converted into heat rather than visible light. Since other electrical light sources are more effective, the incandescent bulbs raise some financial and ecological concerns [3]. The common incandescent light bulb (**figure 1.1** (**a**)), which works by heating a filament to over 3000 °C, has a power conversion efficiency (PCE) of 5 % (that is 95 % of the electricity used is lost as heat). A 60 W bulb will consume 525.6 KWh/yr [2]. The first alternative to the incandescent light bulb was the high-efficiency compact fluorescent lamp, or CFL. However, CFLs have problems about the inclusion of mercury in the design and have, sometimes, a color quite different from that of incandescent lamps [3]. A compact fluorescence lamp (CFL) (**figure 1.1** (**b**)), which excites a coated phosphor by discharging gas, has a better PCE of up to 20 % and a 13-15 W bulb will only consume 131.4 KWh/yr. However, it is very sensitive to low and high temperatures and will stop working at

temperatures below -20 °C and above 50 °C. It also contains 1 - 5 mg of mercury per bulb, which is an environmentally hazardous material [2].

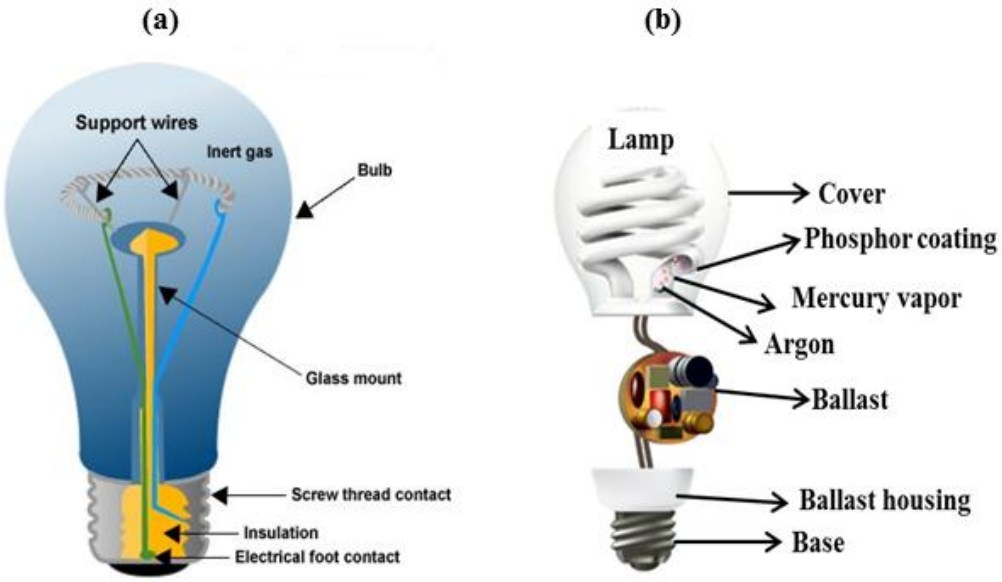

Figure 1.1: Schematic diagram of (**a**) an incandescent light bulb [4] and (**b**) a compact fluorescent lamp [5].

Since the conventional incandescent and fluorescent lamps rely on either heat or discharge of gases, both phenomena are associated with large energy losses that occur because of the high temperatures and large Stokes shifts involved [6]. In 1996, a totally new lighting device was invented by Nichia Chemical Co. by means of a GaN based blue LED chip coated with yttrium aluminum garnet yellow phosphor ($Y_3Al_5O_{12}$: Ce, YAG: Ce) [7]. A schematic of these phosphor-converted white light-emitting diodes (pc-WLEDs) is shown in **figure 1.2**. When the chip is driven under certain current, blue light is emitted by the InGaN chip through electron-hole recombination in the p-n junctions. Some of the blue light from the LED excites the YAG: Ce phosphor to emit yellow light, and then the rest of the blue light is mixed with the yellow light to generate white light. This lighting style based on LED is called solid-state lighting (SSL) [6].

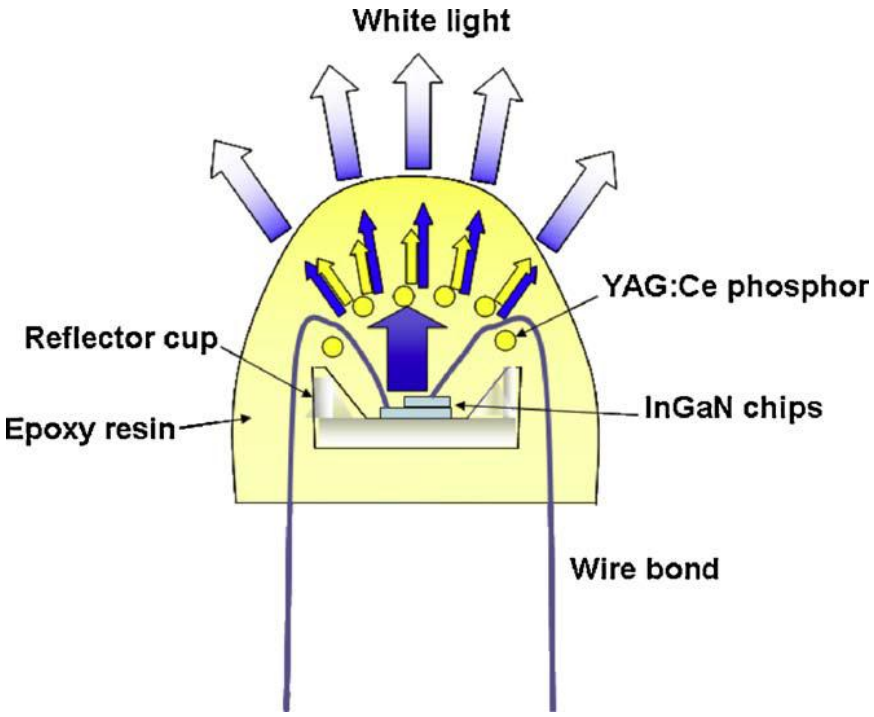

Figure 1.2: Schematic structure of dichromatic pc-WLEDs [6].

Traditional light-emitting diodes (LEDs) emit mono-chromatic light. However, white LEDs, by definition, emit poly-chromatic light. Therefore, white LEDs are a significant departure from traditional LEDs. In the spirit of this significant departure, the phrase "solid-state lighting" is frequently employed for the field of white LEDs. While traditional LEDs, i.e. monochromatic LEDs, created mostly their own new markets, the implication of the phrase "solid- state lighting" is that LEDs are used to replace conventional lighting sources: Incandescent lamps (Thomas Edison's light bulb) and fluorescent lamps. Therefore, the phrase "solid-state lighting" is meant for white LEDs that are used in applications traditionally served by conventional white-light sources (incandescent and fluorescent lamps) [8].

In an LED, electricity is converted into light. It is well recognized that LEDs offer the following advantages. (1) Energy savings: LED requires less energy to emit equivalent light compared to other light sources. (2) Long lifetime: Due to their compact physical characteristics, LEDs are also more long-lasting than other lamps. Incandescent bulbs tend to last 1000 hours as heat destroys the filament, and fluorescent lamps tend to last 10,000 hours. While LEDs can last over 50,000 hours or more in theory. (3) Environment-friendly characteristics: Unlike fluorescent lamps, there is no mercury in LEDs, indicating that LEDs are environment-friendly whenever

they are are discarded. (4) Wide color temperatures: LEDs provide a wider range of color temperature (4500 K–12,000 K) and a wider operation temperature (−20 °C to 85 °C). (5) Quick startup: LEDs do not have low-temperature startup problems, which is different from many other lighting sources, such as metal halogen lamps [9, 10]. Based on the above advantages, so far, LEDs have been considered as the fourth generation of light sources in a variety of fields, such as general lighting in homes and offices, street lighting, automotive lighting, and backlighting in liquid-crystal displays (LCDs) and so on [8, 11].

1.2 Problem statement and aim

In order to generate white light in LEDs, three methods have been employed: (1) utilizing three individual monochromatic LED chips with red, green and blue colors (triclour-LEDs); (2) combining blue LED with yellow-emitting phosphors; (3) coupling ultraviolet (UV) LEDs with red, green and blue phosphor blends [12]. For the first approach, it has high cost and complicated driver circuit. Besides, it suffers from an intolerable shortcoming which is drifts of color rendering index (CRI) and color temperature (CT) due to susceptibility to the temperature of the devices. To solve these problems, phosphor-converted WLEDs (pc-WLEDs) technology has emerged. The popular method is to combine an InGaN blue LED and the yellow conversion phosphor YAG: Ce^{3+}, but the innate deficiency of the red component results in low CRI and high CT values. Thus, the strategy of depositing tricolor (red, green, and blue) phosphors on a UV LED chip has been developed. The advantage of this method is that it is much easier to create white light with improved CRI and CT [13].

The other approach in current academic interests in white light are displaced by pursuing single-component white- light phosphors to get small color aberration, great color rendering index and lower production cost. The ultraviolet LED chips coated with white light emitting single phased phosphor becomes a strong and bold step towards the fabrication of stable WLEDs. Because of these problems, developing a single-phase WLED phosphor is one of the effective solutions, and has attracted much attention in WLED applications [14].

Due to an ongoing search for phosphors to be used in the next generation of lighting, materials of different compositions with desired properties are required. These shortcomings of LEDs serve as motivation to develop new phosphors that emit blue, green and red light simultaneously,

which can be efficiently excited by the n-UV/UV or n-UV excited white light emission resulting from a single-phase phosphor [15-17]. Phosphors based on borate host matrices have been attracting intense attention due to advantages such as relative low synthesis temperature and excellent chemical and thermal stability [18, 19]. Doping borate hosts with rare-earth (RE) ions should lead to production of phosphors that could be used in solid state lighting (SSL) and displays. This project set out to produce phosphor based on borates doped with a variety of rare-earth elements such as cerium, europium and dysprosium, among others, and they were evaluated for a possible application in SSL.

1.3 Objectives of the study

- To prepare Inorganic Borate hosts (BaB_8O_{13} and $LiBaBO_3$) luminescent materials doped with rare earth ions using solution combustion and solid state method.
- To analyze the structure and particle morphology of BaB_8O_{13} and $LiBaBO_3$ host matrices doped different rare earth ions (RE^{3+} = Ce^{3+}, Eu^{3+}, Sm^{3+} and Dy^{3+}).
- To investigate the photoluminescent properties of rare-earths doped BaB_8O_{13} and $LiBaBO_3$.
- To study energy transfer between Bi^{3+} and Eu^{3+} in $LiBaBO_3$.
- To study energy transfer between Eu^{3+} and Sm^{3+} in BaB_8O_{13}.

1.4 Thesis layout

Chapter (2) provides a theoretical background on luminescence processes such as; photoluminescence and thermoluminescence. A brief background on the rare earth ions, namely Ce^{3+}, Eu^{3+}, Sm^{3+} and Dy^{3+} is given. Energy transfer, concentration quenching and defects in solids are also discussed. In addition a detailed discussion of borate host matrices and their crystal structures is also presented. **Chapter (3)** gives a description of the synthesis methods and characterization techniques. **Chapter (4)** presents photoluminescence studies of green emitting BaB_8O_{13}: Bi^{3+} phosphors. **Chapter (5)** reports on the study of photoluminescence and energy transfer of Eu^{3+}-Sm^{3+} co-doped BaB_8O_{13} phosphors. **Chapter (6)** focuses on the analysis of the structure, particle morphology and photoluminescent properties of green emitting BaB_8O_{13}: Ce^{3+} phosphor. **Chapter (7)** discusses the synthesis and photominescent properties of dysprosium

doped BaB_8O_{13} phosphor**.** Tunable emission from $LiBaBO_3:Eu^{3+}$; Bi^{3+} is presented in **Chapter (8)**. In **Chapter (9)**, photoluminescent properties, structure and particle morphology of $LiBaBO_3$: Dy^{3+} is presented. **Chapter (10)** presents the summary and conclusion of the thesis and suggestions for future work. The list of publications and the conference presentations are also included.

References

[1] H. A. Höppe, *Angewandte Chemie International Edition*, **48** (2009) 3572 - 3582.

[2] M. M. Duvenhage, H. C. Swart and O. M. Ntwaeaborwa, Investigation of the luminescent properties of metal quinolates (Mqx) for use in OLED devices, PhD *thesis*, University of the Free State, (2014).

[3] https://arxiv.org/ftp/arxiv/papers/1411/1411.6620.pdf (accessed 26/07/2017).

[4] https://za.pinterest.com/pin/497718196288696091/ (accessed 26/07/2017).

[5] https://www.energystar.gov/products/lighting_fans/light_bulbs/learn_about_cfls (Accessed 26/07/2017).

[6] S. Ye, F. Xiao, Y. X. Pan, Y. Y. Ma, Q.Y. Zhang, *Materials Science and Engineering R*, **71** (2010) 1 - 34.

[7] Y. Li, L. Chang, H. Chen, C. Yen, K. Pan, B. Huang, W. Kuo, L. Chow, D. Zhou and E. Popko, *Materials*, **10** (2017) 432, doi:10.3390/ma10040432.

[8] J. Cho, J. H. Park, J. K. Kim and E. F. Schubert, *Laser Photonics Reviews*, **11** (2017) 1600147, doi:10.1002/lpor.201600147.

[9] X. Luo, R. Hu, S. Liu and K. Wang, *Progress in Energy and Combustion Science*, **56** (2016) 1 - 32.

[10] Y. Fang, F. Liu, J. Hou, Y. Zhang, X. Zheng, N. Zhang, G. Zhao, M. Liao, G. Dai, M. Long and Y. Liu, *Journal of Luminescence*, **177** (2016) 280 - 285.

[11] Y. Narukawa, *Optics & Photonics News*, **15** (2004) 24 - 29.

[12] S. Kaur, M. Jayasimhadri and A. S. Rao, *Journal of Alloys and Compounds*, **697** (2017) 367 - 373.

[13] G. Wang, X. Wang, L. Dong and Q Yang, *Royal Society of Chemistry Advances*, **6** (2016) 42770 - 42777.

[14] Y. P. Manwar, R. S. Palaspagar, R. P. Sonekar and S. K. Omanwar, *Journal of Materials Science: Materials Electronics*, **28** (2017) 994 - 998.

[15] R. Shrivastava, J. Kaur, V. Dubey, T. Wang, Y. Hu, L. Chen, X. Wang and M. He, *Journal of Materials Science: Materials Electronics*, **27** (2016) 13235 - 13241.

[16] C. Liang, H. You, Y. Fu, X. Teng, K. Liu, J. He, *Optik*, **131** (2017) 335 - 342.

[17] W. Luo, D. Tu, R. Li, X. Mao, Y. Xu, J. Ren, B. Li and H. Wu, *Journal of Materials Sciences*, **52** (2017) 9764 - 9772.

[18] J. Li, H. Yan and F. Yan, *Optik*, **127** (2016) 5984 - 5989.

[19] Z.S. Khana, N. B. Ingaleb and S. K. Omanwar, *Optik*, **127** (2016) 6062 - 6065.

Chapter 2

Theoretical Background

2.1 Introduction

This chapter presents a brief introduction to Luminescence. Photoluminescence and thermoluminescence are discussed in detail. Theoretical aspects of rare earth elements, energy transfer, concentration quenching and defects in solids are discussed. The crystal structures of $LiBaBO_3$ and BaB_8O_{13} hosts are also discussed briefly.

2.2 Luminescence

When a solid absorbs photons or charged particles, a number of energy conversion processes are possible, as illustrated in **figure 2.1**. These include luminescence (photon emission), electron emission, thermal emission, and chemical/structural change. Luminescence is defined as the absorption of photons or charged particles by a substance which is then followed by a photon emission in excess of that due to thermal agitation (incandescence) and which is strongly dependent upon-the nature of the emitting substance (unlike incandescence) [1]. Luminescence is reffered as an old technique. First observed in an extract of Lignum nephriticum by Monardes in 1565, it took until 1852 to be fully described by Sir G. G. Stokes who reported the theoretical basis for the mechanism of absorption (excitation) and emission. Today luminescence, in its varied forms, is one of the fastest growing and most useful analytical techniques in science. Applications can be found in areas as diverse as materials science, environmental science, microelectronics, physics, chemistry, biology, biochemistry, medicine, pharmaceutical science,

toxicology and clinical chemistry. This rapid growth has occurred only in the past couple of decades and has been principally driven by the unique needs of the life sciences [2].

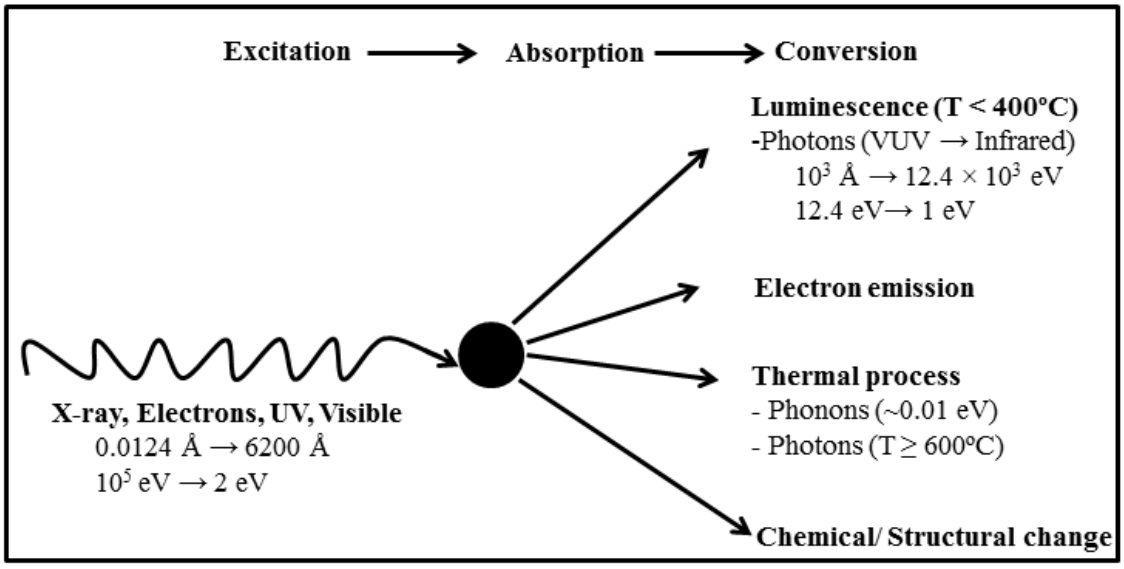

Figure 2.1: Conversion of primary excitation energy in solids [1].

Luminescent materials also known as phosphors consist of a host lattice which constitutes the bulk of the phosphor. The characteristic luminescence properties are usually obtained by adding ("doping") to the host material relatively small amounts of foreign ions called activators. An activator is a foreign ion which when incorporated into a host lattice give rise to centers which can be excited to luminescence called activator centers. Typical activators are rare earth ions or transition-metal ions, ions undergoing s-p transitions (like Bi^{3+}). A sensitizer is a foreign ion incorporated into a host lattice and is capable of transferring harvesting and transferring primary excitation energy to a neighboring activator (absorber), thus inducing luminescence. **Figure 2.2** (**a**) shows a schematic representation of a phosphor made up of a host (H) and an activator (A). The activator can create a center which absorbs excitation energy and converts it into visible radiation. The role of a sensitizer (S) is illustrated in **figure 2.2** (**b**). It may occur that an activator with the desired emission does not have a significant absorption for the available excitation energy. In such a case it may be possible to use a sensitizer which absorbs the excitation energy

and then transfers this energy to the activator, which can then emit its characteristic luminescence [1, 3].

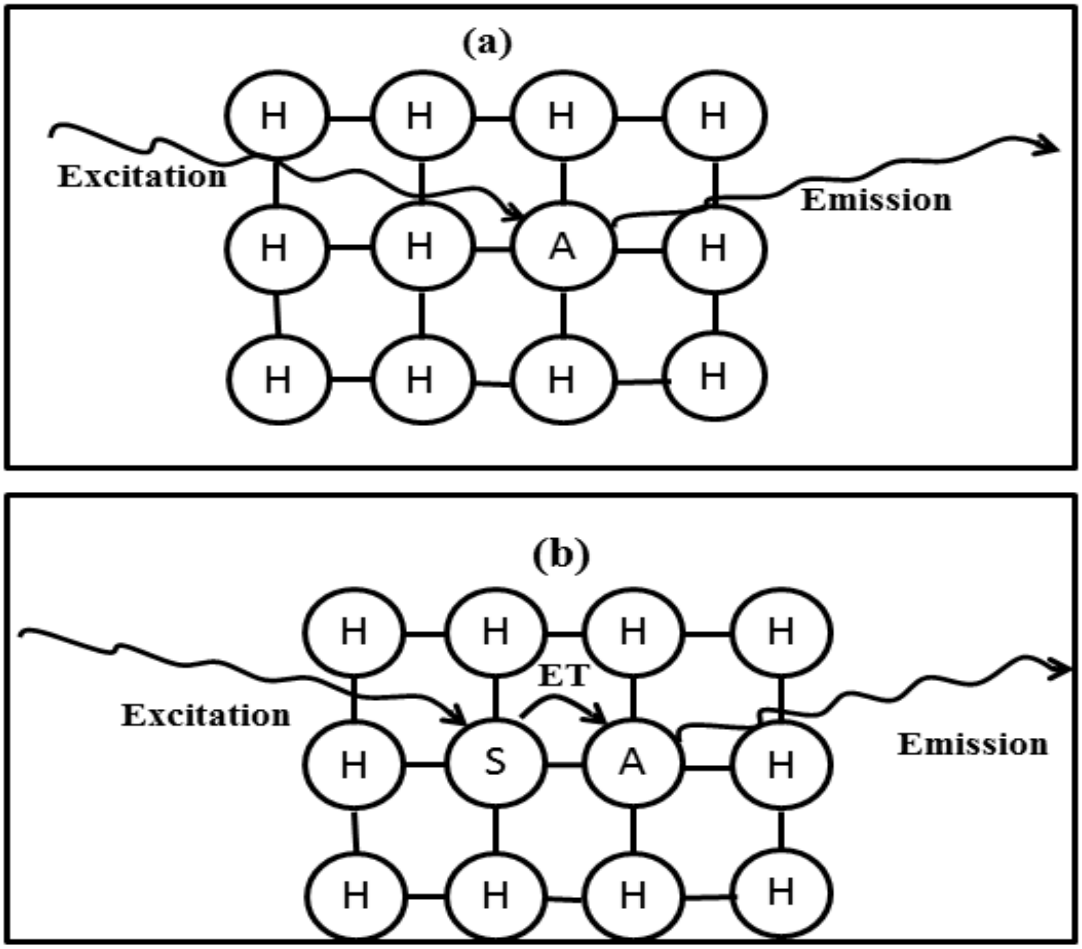

Figure 2.2: a) schematic representation of the role of an activator (A) doped in a host (H) lattice in the luminescence process, **b**) schematic representation of the role of a sensitizer (S) and its relationship to an activator (A) and the host lattice (H), were ET represent the energy transfer [3].

2.2.1 Luminescence mechanisms

In order to create an emission, an electron needs to be excited from the ground state (E_1). A photon is released during a transition of an electron from the excited (E_2) to the ground state. In order to start this transition, an electron is stimulated in the excited state. This process is shown in **figure 2.3** [4].

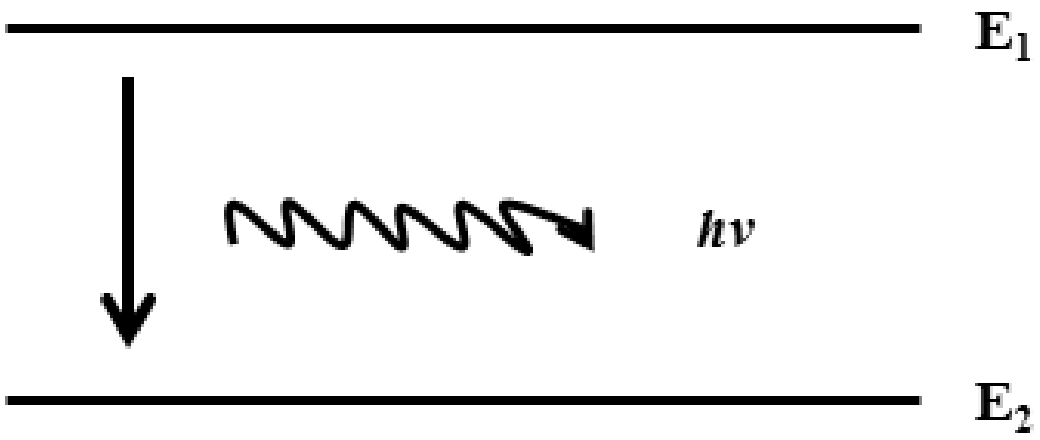

Figure 2.3: Transition of an electron from the excited (E_1) to ground (E_2) state in a double-state system that results in the release of a photon [4].

In semiconductors, the ground state is usually referred to as electrons in the valance band while excited state electrons are known as the conduction band. Unlike the metals in semiconductors, these two states are separated by an energy gap called the bandgap (Eg). Therefore, the minimum energy of the bandgap is necessary to excite an electron from the ground to the excited state. Luminescence from semiconductors can be observed by exciting the electrons to higher states like the conduction band and subsequent decay to the ground state. There are different methods of providing the excitation that cause luminescence from a material. Depending on the origin of excitation, there are several types of luminescence such as photoluminescence, electroluminescence, cathodoluminescence, chemiluminescence, thermoluminescence, etc. When an electron is promoted from the valance band to the conduction band, a hole will remain in the valance band [4]. In this study, only two types of luminescence will be discussed: photoluminescence and thermoluminescence.

2.2.2 Photoluminescence

Photoluminescence in the ultraviolet-visible comprises of two similar phenomena: fluorescence and phosphorescence. In the process of luminescence, when radiation is incident on a material some of its energy is absorbed and re-emitted as a light of a longer wavelength (Stokes law). The wavelength of light emitted is characteristic of a luminescent substance and not of the incident

radiation. The light emitted could either be visible light, ultra-violet, or an infrared light. This cold emission, i.e. luminescence, that does not include the emission of blackbody radiation, involves two steps: (1) The excitation of electronic system of a solid material to higher energy state, and (2) subsequent emission of photons or simply light. The emission of light takes place at characteristics time 'τ_c' after absorption of the radiation. Luminescence can be classified on the basis of duration of emission, τ_c, in to two parts:

1. Fluorescence where $\tau_c < 10^{-8}$ s (temperature independent process), and

2. Phosphorescence where $\tau_c > 10^{-8}$ s (temperature dependent process).

The Phosphorescence phenomenon can further be divided into two parts: (a) short period $\tau_c < 10^{-4}$ s (b) and the long period where $\tau_c > 10^{-4}$ s is called thermoluminescence (TL). In the field of science and technology, each luminescence process mentioned above has its own significance and advantages [5].

The Fluorescence emission is seen to be spontaneous due to short lifetimes, 'τ_c' $< 10^{-8}$ s. In other words, the fluorescence emission occurs simultaneously with absorption of radiation and stops immediately as radiation comes to an end. Phosphorescence on the other hand is characterized by delay between radiation absorption and time 't_{max}' to reach full intensity. Also phosphorescence is seen to continue for some time after the excitation has been removed. If the delay time is much shorter it is more difficult to distinguish between fluorescence and phosphorescence. Hence phosphorescence is subdivided into two main types, namely, short-period ($\tau_c < 10^{-4}$ s) and long-period ($\tau_c > 10^{-4}$ s) phosphorescence. Fluorescence is essentially independent of temperature, whereas decay of phosphorescence exhibits strong temperature dependence. The family tree of luminescence phenomena is shown in **figure 2.4** [5].

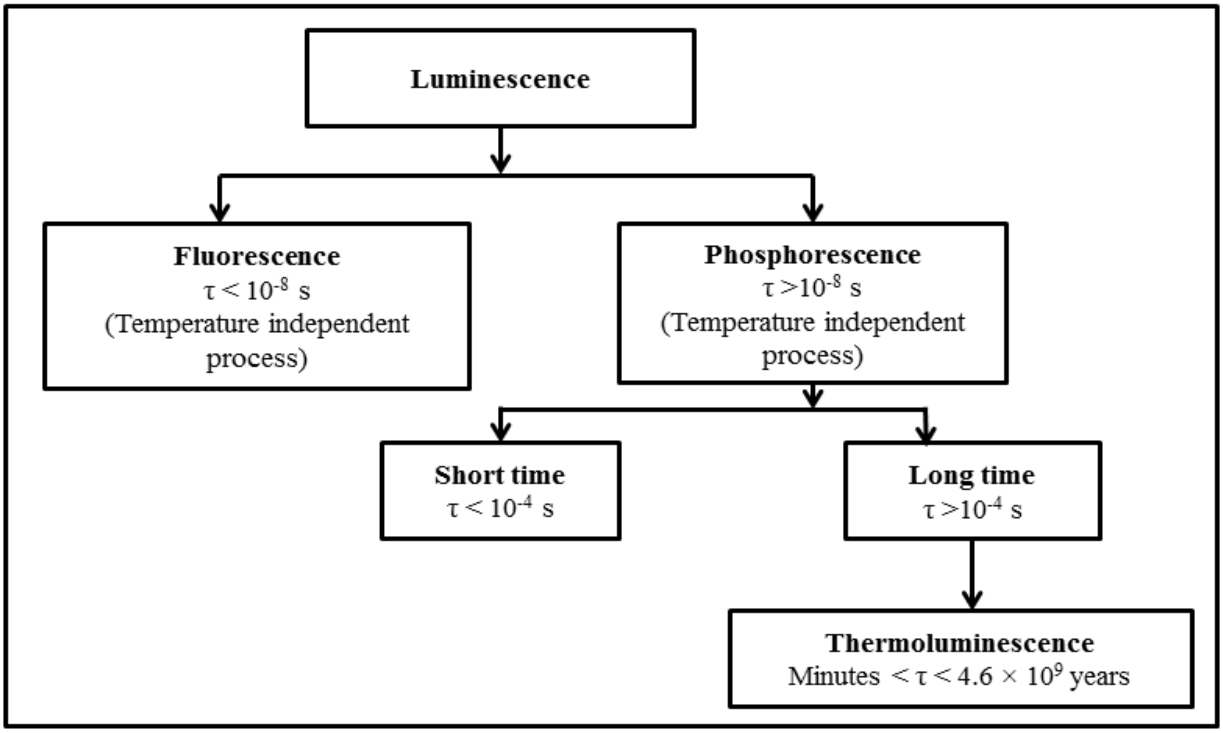

Figure 2.4: Classification of luminescence on the basis of duration of emission [**5**].

2.2.3 Thermoluminesce

Thermoluminescence (TL) is one of the well-known luminescence processes. The term thermoluminescence applies to the emission of light from irradiated solids based on the effect that a small portion of absorbed radiation energy stored at low temperature is emitted in the form of light when heated. Upon irradiation of solids with ionizing radiation, electron hole pairs are generated which can move freely between the conduction and valance band and some electrons or holes may become trapped at certain active sites in the host material. These traps are provided by lattice defects or impurities, the fixation between the conduction and valance band is energetically metastable. These charge carriers can be captured again by traps or recombine in the luminescence center. They remain in this state until they acquire sufficient thermal energy to escape. As the material is heated, electrons are released from the traps and light is emitted as they recombine with holes. The intensity of the emitted light can be measured as a function of temperature, which is detected as a glow-curve [**6**].

2.2.3.1 Simple TL model

There are two delocalized bands, conduction band (CB) and valence band (VB). Between these two energy bands, two localized levels (metastable states) are considered, one behaves as a recombination center (R) and the other as a trap (T). The activation energy or trap depth (*E*) is defined as the distance between the trap and the bottom of the CB. This energy is the required to release a charge, i.e an electron that is trapped in T. In the valence band, if an electron absorption of radiation energy ($h\nu > E_g$) producing free electrons and holes (**see. figure 2.5**), the free carriers may either recombine with each other, become trapped or remain free in their respective delocalized bands. In **figure 2.5**, symbols **a, b, c, d, R, E, g, E_f and E_g** represents the generation of holes and electrons, electron trapping, hole trapping, electron release by heating, recombination center with light emission, activation energy or trap depth, hole trap depth, Fermi level and the forbidden energy, respectively. Arrhenius's equation is described as the probability per unit of release of an electron from a trap and considered that the electrons in the trap have a Maxwellian distribution of thermal energies:

$$p = s \exp\left\{-\frac{E}{KT}\right\} \qquad (2.1)$$

Where:

K is Boltzmann's constant = 8.617×10^{-5} eV/k, the T is absolute temperature (*K*), the E is the trap depth or activation energy (eV), the *s* is frequency factor (not temperature dependent), depending on the frequency of the number of hits of an electron in the trap [**7**].

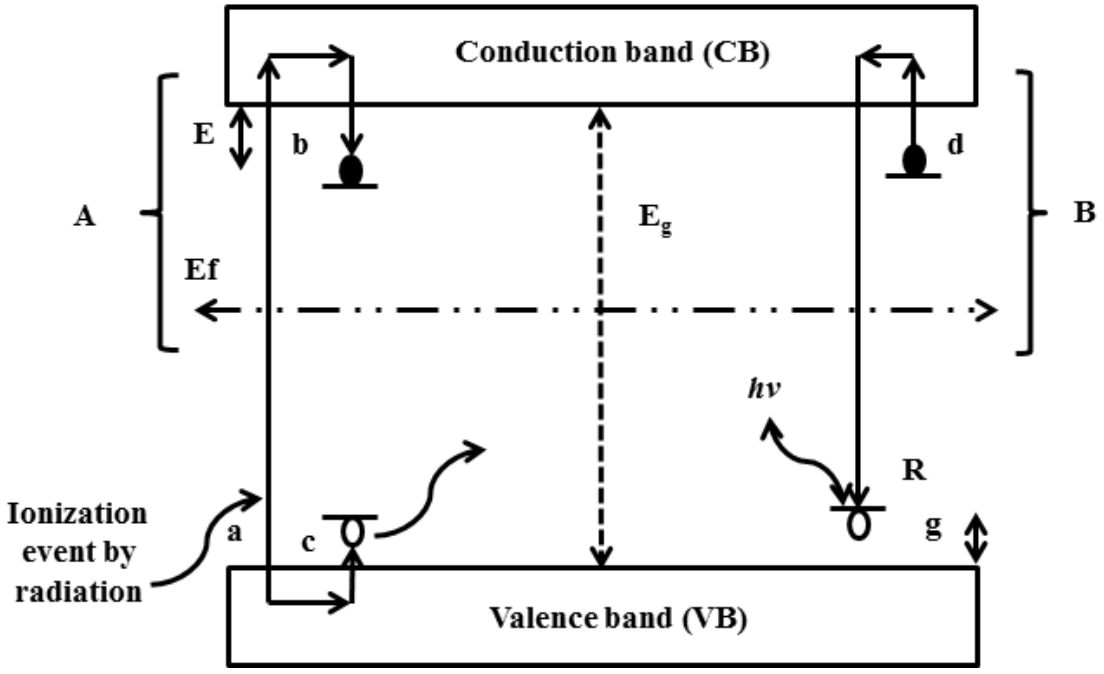

Figure 2.5: Simple two-level model for thermoluminescence, open and closed circles are hole and electron, respectively [**7**].

2.3 Rare earth ions

The history of the rare earth elements (also called lanthanides) started almost 220 years ago in 1788 when Geijer reported on a black stone found close to the Swedish town of Ytterby. The stone was called Yttria [8].The lanthanides are a fascinating group of elements and their optical properties arise from the inner f-electrons which are starting with one in cerium and ending with thirteen in ytterbium. The transition probabilities within the four f-orbital are forbidden by Laporte rule and become partially allowed either by mixing of the four f with 5 d-orbital or with a charge transfer states of the neighboring ligands. Since the beginning of the twentieth century, the radiative transitions of lanthanide ions have received academic and industrial attention [9]. The characteristic absorption and emission spectra of lanthanide compounds in the visible, near-ultraviolet, and infrared are attributed to transitions between 4f levels due to the fact that they present sharp line with oscillator strengths typically of the order of 10^{-6}. These transitions are forbidden to first order by electric dipoles, but are allowed by the electric quadrupole, vibronic, magnetic dipole and forced electric dipole mechanisms. It has been noticed, since more than fifty years ago, that among these only the magnetic dipole and forced electric dipole mechanisms

could account for the observed intensities. The magnetic dipole character of the $^5D_0 \rightarrow {}^7F_1$ transition of the Eu^{3+} ion was demonstrated in 1939 by Deutschbein [9, 10].

Rare-earth doped luminescent materials are extensively used in the lighting industry [11-16] as well as plasma display panel (PDP) technologies [16]. **Table 2.1** presents the number of 4f electrons and the radius of the R^{3+} ion for the rare-earth elements [17, 18]. Four rare earths such as Cerium (Ce^{3+}), Europium (Eu^{3+}), Samarium (Sm^{3+}) and Dysprosium (Dy^{3+}) are used as dopants in this current study. Depending on the rare earth ions, the luminescence spectra can be divided into two types: broad band and sharp lines. The luminescence of Ce^{3+} is characteristic of broad absorption and emission bands, which are due to the 4f-5d electronic transitions, whereas the luminescence spectra of other trivalent lanthanide ions consist of a group of sharp lines, which are attributable to the 4f-4f electronic transitions. Each group of sharp lines corresponds to an electronic transition between an excited state and a ground state designated by the total angular momentum, J, and it can be properly assigned by employing the Dieke diagram [19].

Table 2.1: The number of 4*f* electrons and the radius of the R^{3+} ion for the rare-earth elements [17, 18].

Rare earth Element	**symbol**	**Atomic number**	**Number of 4f electrons**	**Number of unpaired 4f electrons**	**ionic radius (Å)**
Lanthanum	La	57	0	0	1.045
Cerium	Ce	58	1	1	1.010
Praseodymium	Pr	59	2	2	0.997
Neodymium	Nd	60	3	3	0.983
Promethium	Pm	61	4	4	0.970
Samarium	Sm	62	5	5	0.958
Europium	Eu	63	6	6	0.947
Gadolinium	Gd	64	7	7	0.938

Terbium	Tb	65	8	6	0.923
Dysprosium	Dy	66	9	5	0.912
Holmium	Ho	67	10	4	0.901
Erbium	Er	68	11	3	0.890
Thulium	Tm	69	12	2	0.880
Ytterbium	Yb	70	13	1	0.868
Lutetium	Lu	71	14	0	0.861
Scandium	Sc	21	0	0	0.745
Yttrium	Y	39	0	0	0.900

2.3.1 Cerium

The cerium Ce^{3+} ion has the simplest electron configuration among the rare earth ions. The $4f^1$ ground-state configuration is divided into two sublevels, $^2F_{5/2}$ and $^2F_{7/2}$, and these two sublevels are separated by about 2,000 cm^{-1} as a result of spin-orbit coupling. This is the reason for the double structure usually observed in the Ce^{3+} emission band. The $5d^1$ excited state configuration is split into two to five components by the crystal field, with the splitting number depending on the crystal field symmetry. The Ce^{3+} emission is strongly affected by the host lattice through the crystal field splitting of the 5d orbital and the nephelauxetic effect, and usually varies from the ultraviolet to the blue spectral region. But in covalent and strong crystal field surroundings, the 5d orbital significantly shifts to lower energies, resulting in yellow and even red emission colors of Ce^{3+} [19]. The excited state derived from the 5d state is sensitive to the crystal field and is coupled to the lattice vibrations which results in broader band emission rather than line emission [20]. The Ce^{3+} free ion has a $4f^1$ ground configuration with the lowest 5d state at 47 937 cm^{-1}. When this ion is placed in a crystal, the lowest 4f to 5d electric dipole allowed transition has been reported to be in the range of 20 000 to 40 000 cm^{-1} depending on the particular compound or matrix investigated [21].

2.3.2 Europium

The emission of Eu^{3+} ion consists usually of lines in the red spectral area, which are ascribed to the $^5D_0$–^7F_J (J = 0, 1, 2, 3, 4, 5 and 6) transitions. The red light emitting phosphor of Eu^{3+}-doped material has found an important application in the lighting and displays. More significantly, it has effective and intrinsic absorption due to the 4f–4f transition of Eu^{3+} [22]. The red emission at ~600 nm originating from the magnetic dipole transition of $^5D_0 \rightarrow {}^7F_1$ dominates when the Eu^{3+} site has inversion symmetry (in this case, the electric-dipole transition is strictly forbidden due to the parity selection rule). On the other hand, the red emission at 610–630 nm from the electric-dipole transition of $^5D_0 \rightarrow {}^7F_2$ dominates if it is a noninversion symmetry site [19].

2.3.3 Samarium

Sm^{3+} has a complex energy level structure with important ground ^6H_J and ^6F_J multiplets as well as excited level $^4G_{5/2}$, $^4F_{3/2}$ and $^4G_{7/2}$ located at 17860, 18857 and 20009 cm^{-1}. Its fluorescence can be observed in the visible and near-infrared regions. The emission of Sm^{3+} ions associated with the intra-4f shell transition is very efficient. Therefore, Sm^{3+} ions often play a very important role in the luminescent process of materials [23, 24].

2.3.4 Dysprosium

Usually, dysprosium ions (Dy^{3+}) exhibit solid-state luminescence in a variety of lattices because they are mainly consist of two fine bands in the blue and yellow regions corresponding to the $^4F_{9/2} \rightarrow {}^6H_{15/2}$ and $^4F_{9/2} \rightarrow {}^6H_{13/2}$ transitions, respectively. However, in different hosts, the ratio of the two dominant Dy^{3+} emission bands arising from the transitions $^4F_{9/2} \rightarrow {}^6H_{15/2}$ (blue) and $^4F_{9/2} \rightarrow {}^6H_{13/2}$ (yellow) is different. The chemical environment surrounding Dy^{3+} strongly influences the yellow emission because of $\Delta J = 2$, while the blue emission is relatively invariable. By adjusting the yellow-to-blue intensity ratio (Y/B) values appropriately, there is an opportunity to obtain near-white light emissions [25].

2.4 Bismuth

Bismuth is a non-rare earth element and it was first recognized during the middle ages, but, with no ability to isolate the metal it was often confused with tin, lead, antimony and zinc. Research

by Johan Heinrich Pott and Claude Geoffroy led to a better understanding of bismuth and its unique properties in the mid-18th century [26]. Bismuth is reported as the only nontoxic heavy metal and is most commonly obtained as a byproduct during Pb, Cu, W, and Sn ore refining. Despite being the last radioactively stable element on the periodic table, the cost of bismuth is relatively low. In research industry, bismuth-based materials have gained attention for potential use in photoluminescence (PL) related fields [27].

Several researchers studied the luminescence properties of Bi^{3+} doped phosphors. Bismuth can exist in materials in different valence states, such as 0, +1, +2, +3, and +5, or even mixed valence states of +1 and +5. In all of these valence states only Bi^{3+} is normally most stable in most host materials [28]. Since last century Bi^{3+} doped crystals have been noticed as one of series works on fluorescence properties of ions with ns^2 configuration. To date, Bi^{3+} doped borate, silicate, phosphate and germanate glasses have been reported. However, these reports mainly emerged between 1970s and 1990s and concentrated on absorption and emission spectra [29]. Due to its various unique physical and chemical properties, the non-RE bismuth is an excellent candidate for making up the disadvantages of RE ions. It is reported that bismuth can possess various luminescent species ranging from UV light to visible/near-infrared/even far-infrared light. As for the visible luminescence, the bismuth valences are mainly focusing on trivalent bismuth (Bi^{3+}) and bivalent bismuth (Bi^{2+}), in which the former is always selected as the sensitizer of RE ions for improving the RE luminescence, while the latter can emit either orange or red under UV/blue excitations [30, 31].

Electronic configuration of Bi^{3+} is $[Xe]4f^{14}5d^{10}6s^2$. The ground state is $^1S_0$ with $6s^2$ configuration, and the excited states from $6s6p$ configuration are $^3P_0$, $^3P_1$, $^3P_2$ and $^1P_1$ in a sequence of energy increasing. The transitions $^1S_0 \rightarrow {}^3P_0$ or $^3P_2$ are spin forbidden and $^1S_0 \rightarrow {}^3P_1$ or $^1P_1$ are lifted by spin-orbit coupling. So, the latter two have relatively higher absorption strength than the former two. Backward radiative transition $^3P_1 \rightarrow {}^1S_0$ is Laporte allowed and the decay time usually is counted between 10^{-6} and 10^{-8} s [29, 31, 32]. The s^2-sp transition of Bi^{3+} is an allowed one: Luminescence spectrum of ions with s^2- sp transition such as Bi^{3+}, Pb^{2+}, Sn^{2+}, and Sb^{3+} shows a very broad gaussian band. For example, the band halfwidth of Sn^{2+} is ~0.65 eV. The characteristics of a broad band can be explained with their configurational coordinate energy

diagram. The potential energy curve of the luminescent center in the lattice can be plotted as a function of the distance r between the central cation and surrounding anions. In the potential energy diagram, the coordinate of the excited state minimum is shifted from that of the ground state minimum. This shift is very large for s^2-sp transition, and the excited p state is much wider than the ground s state. Therefore, luminescence from s^2-sp transition is observed to be a very broad emission band [33].

2.5 Energy transfer

When a material is exposed to a source of radiation, some of the energy may be absorbed through the creation of electronic excited states. This energy is later dissipated through the emission of light or heat. Between the time that the electronic excited states are created and the time the energy is dissipated, the energy may move around from one atom or molecule to another within the material. This process is called the energy transfer. It is a phenomenon which occurs in many different types of material under a wide variety of physical conditions. This generality has made energy transfer an important topic for study by physicists, chemists, and biologists with many different special research interests [34]. The luminescent materials have several types of energy transfer [35].

i. **Resonant energy transfer between ions of same energy level**—where the excitation energy of an ion migrates to another one of the same species that is in the ground state. This type of transfer is divided into three categories:

(a) Multipolar interaction – A situation where both transitions are of electric dipole character.

(b) Exchange interaction – Occurs when the donor and the acceptor are both located so close that their electronic wave functions overlap and the transfer is due to a quantum mechanical interaction.

c) Phonon-assisted energy transfer – Occurs when there is a difference E between the transition energies of the donor and the acceptor, and is compensated by either a phonon emission or absorption.

ii. **Spectral diffusion**—In this case, an ion that is excited can give its energy to other ions that are at different sites and/or lattice environment, due to the fact that the doping ions stay at a slightly different lattice environment. In this case, the emission spectrum will shift to longer wavelengths and show an increment on the width of the emission peak.

iii. **Energy donation**—In this case, the energy transfer can occur between different ions, i.e a donor and an acceptor. When an ion is at an excited higher energy level, it can transfer most of its energy to other ions. The other ions stay at a lower energy levels and release the differential energy in the form of phonons.

iv. **Sensitizer's transfer**—A donor that usually has a strong absorption of external radiation and transfers it very efficiently to an acceptor is called a sensitizer; the caused emission is greatly enhanced. This process is also known as sensitization of the luminescence.

v. **Quenching centers transfer**—In this case, the acceptor kills the emission of the donating ions, and these ions neither emit at the required wavelength nor emit at all. Mostly, the phosphors that exhibit this type of luminescence are activated by sensitizers or co-activators (e.g. Mn^{2+}).

Resonance energy transfer occurs between a sensitizer (S) and an activator (A) with the same radiative frequency, and the mechanism could be of exchange interaction or electric multipolar interaction. The phenomenon of energy transfer could be demonstrated by the overlap of emission spectrum of S and excitation spectrum of A. Dexter's energy transfer formula is described as [36]:

$$P_{SA} = 2\pi/\hbar \left| \langle S, A^* | H_{SA} | S^*, A \rangle \right|^2 \int F_S(E) F_A(E) dE \qquad (2.2)$$

where the integral describes the spectral overlap; $F_S(E)$ and $F_A(E)$ represent the normalized shapes of the sensitizer and activator, respectively; the matrix element represents the interaction between initial state $|S*, A\rangle$ and final state $\langle S, A*|; H_{SA}$ is the Hamiltonian of the interaction; P_{SA} is the probability of energy transfer and, when the spectral overlap is absent, the phenomenon of resonance energy-transfer vanishes, as shown in **figure 2.6 and figure 2.7**, respectively. Furthermore, the energy-transfer probability is related to the type of interaction. For

electric multipolar interaction, the distance dependence is given by $R^{-\alpha}$ where α is 6 and 8 corresponding to electric dipole-dipole and dipole-quadrupole interactions, respectively. For exchange interaction, the distance dependence is exponential, and the wavefunction overlap between S and A is required [36].

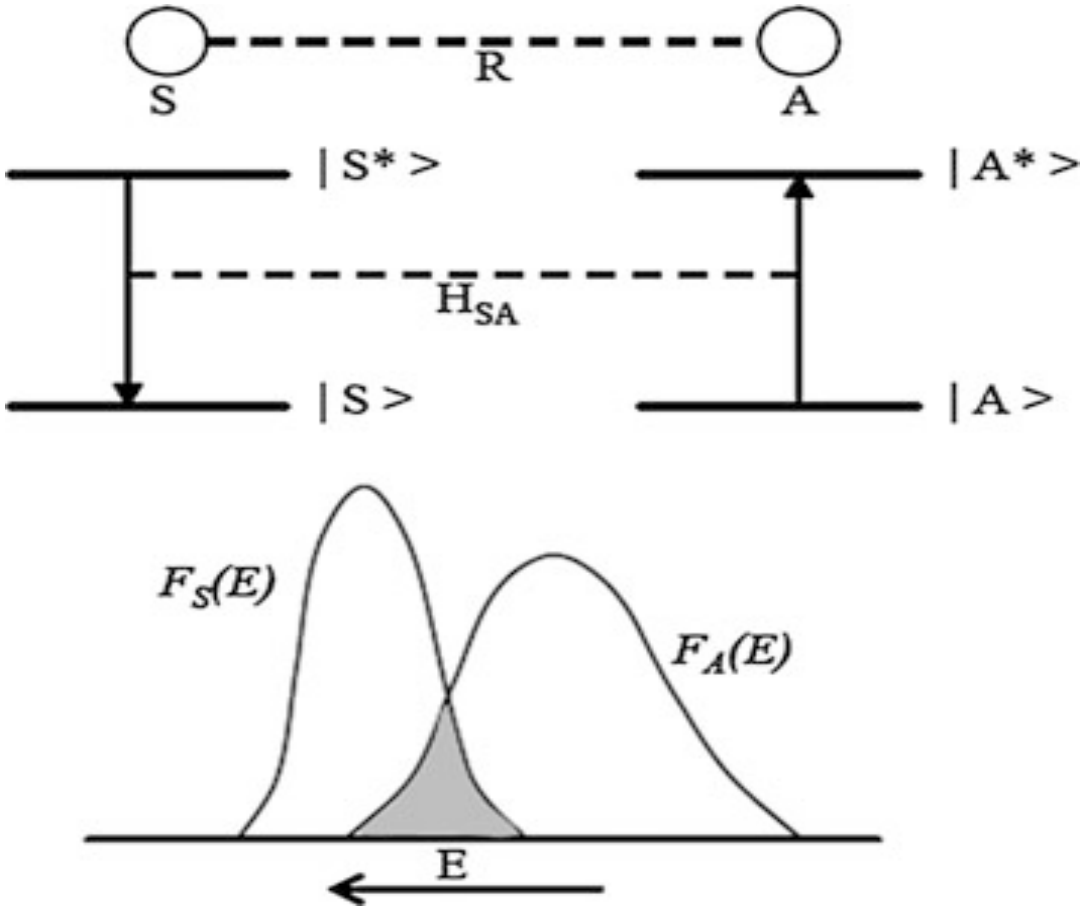

Figure 2.6: Diagram of the energy transfer between a sensitizer and an activator [36].

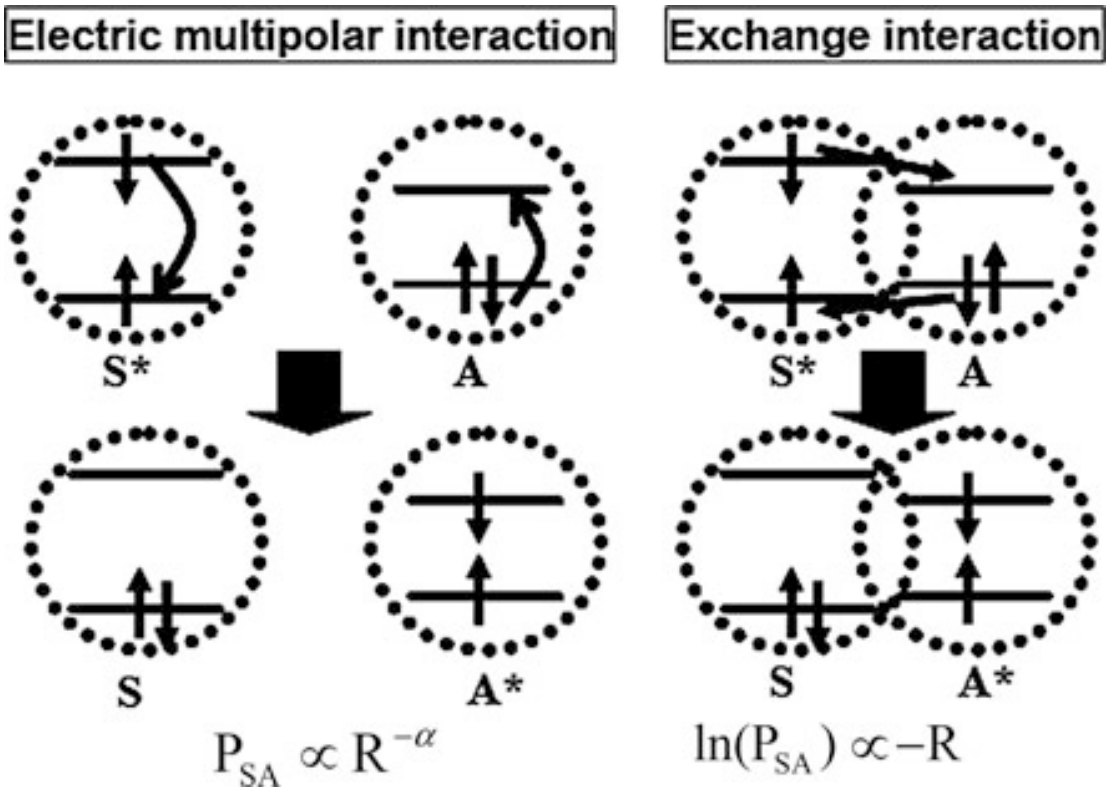

Figure 2.7: Diagrams of the energy-transfer mechanisms of electric multipolar and exchange interactions [36].

2.6: Concentration quenching

Concentration quenching is one of the factors that can severely constrain the luminescence intensity of rare-earth ions in different matrices. The magnitude of the concentration quenching depends not only on the concentration of rare-earth ions but also on their distribution over the matrix bulk. In this respect, the results of investigations into the concentration quenching can provide valuable information not only on the functional properties of the material but also on its chemical structure. However, in order to obtain this information, it is necessary to develop a model relating the concentration dependence of the luminescence intensity and the distribution of rare-earth ions over the matrix bulk [37].

The concentration quenching is determined primarily by the dipole–dipole interaction between rare-earth ions, which weakens as R^{-6} with an increase in the distance between the ions. Such a

rapid decrease in the probability of the dipole–dipole interaction allow one to use an approximation according to which the luminescence is completely quenched for all the ions separated by a distance shorter than R, whereas the luminescence of ions separated by a distance longer than R is not subjected to complete concentration quenching. In particular, Alekseev et al. noted that, for concentration quenching, the effective radius of the dipole–dipole interaction between rare-earth ions is approximately equal to 0.5 nm [37].

Another quenching process is related to energy transfer. If the concentration of luminescent ions chosen is too high, energy transfer occurs over the luminescent ions until the energy reaches a center where a nonradiative transition occurs. Two remarks have to be made here: Energy transfer underlies sensitization schemes, in which case energy transfer is a useful process. Though the sensitizer emission is quenched, the activator emission appears. This allows practical application of sensitization schemes. In general the centers for nonradiative recombination are not known. In many cases, therefore, the possibility to increase the concentration of luminescent ions is limited. The mechanism leading to quantum yield loss is called concentration quenching. Whether or not this mechanism takes place can be easily deduced by investigating the quantum efficiency or the decay time of the emission as a function of the activator concentration [38].

The large difference between absorption and emission wavelength (Stokes shift) reduces energy transfer and therefore concentration quenching. On the other hand, a very large Stokes shift increases the probability for thermal quenching, as the ground state parabola will cross the excited state parabola at a lower energy, allowing the ground state parabola to be reached without emission of a photon. This is a direct consequence of the quadratic dependence of the potential energy of the electronic states on the metal-ligand distance. For the same reason, thermal quenching becomes less probable when the emission energy increases. Degradation of luminescent materials can be due to additional centers to which energy can be transferred, without efficient photon generation by these centers (killing centers, killers, centers for nonradiative recombination). Such centers can be, e.g., vacancies generated as a consequence of the operation of the device or sensitizer or activator ions that have changed their valence during operation of the device [38].

The time-averaged photoluminescence intensity of many phosphors as a function of activator concentration initially increases proportionately with the activator concentration and then decreases, going through a maximum at some concentration. The decrease at high activator concentration is referred to as self-concentration quenching (SCQ). Self-concentration quenching in inorganic phosphors is due either to an electrostatic multipolar interaction or to a magnetic dipole interaction (exchange coupling). The self-concentration quenching is considered an important parameter when discussing the practical aspects of luminescence. A difficulty in determining the self-concentration quenching may be that the same phosphor exhibits different concentration dependence (CD) curves according to the type of excitation to which it is subjected [39].

Optically excited rare earth doped materials suffer from the concentration quenching effect, i.e. the intensity of the rare earth luminescence decreases with increasing dopant concentration. This effect dominates if the excitation energy is transferred between many ions in the time necessary for the radiative decay (called energy transfer here, frequently also called energy migration). In such a situation the probability to reach a path of non-radiative decay is strongly enhanced. Since the energy transfer probability is increased with decreasing dopant distance (i.e. increasing concentration), e.g. concentration quenching is a typical effect at high concentrations [40].

2.7: Defects in solids: Point defects and line defects

Imperfections or defects: Any deviation from the perfect atomic arrangement in a crystal is said to contain imperfections or defects. **Figure 2.8** shows different types of crystal defects. Using the term "defect" is sort of a misnomer since these features are commonly intentionally used to manipulate the mechanical properties of a material. Adding alloying elements to a metal is one way of introducing a crystal defect. Crystal imperfections have strong influence upon many properties of crystals, such as strength, electrical conductivity and hysteresis loss of ferromagnets. Thus some important properties of crystals are controlled by imperfections and the nature of the host crystals [41].

- The conductivity of some semiconductors is due entirely to trace amount of chemical impurities.

- Color, luminescence of many crystals arise from impurities and imperfections
- Atomic diffusion may be accelerated enormously by impurities or imperfections
- Mechanical and plastic properties are usually controlled by imperfections

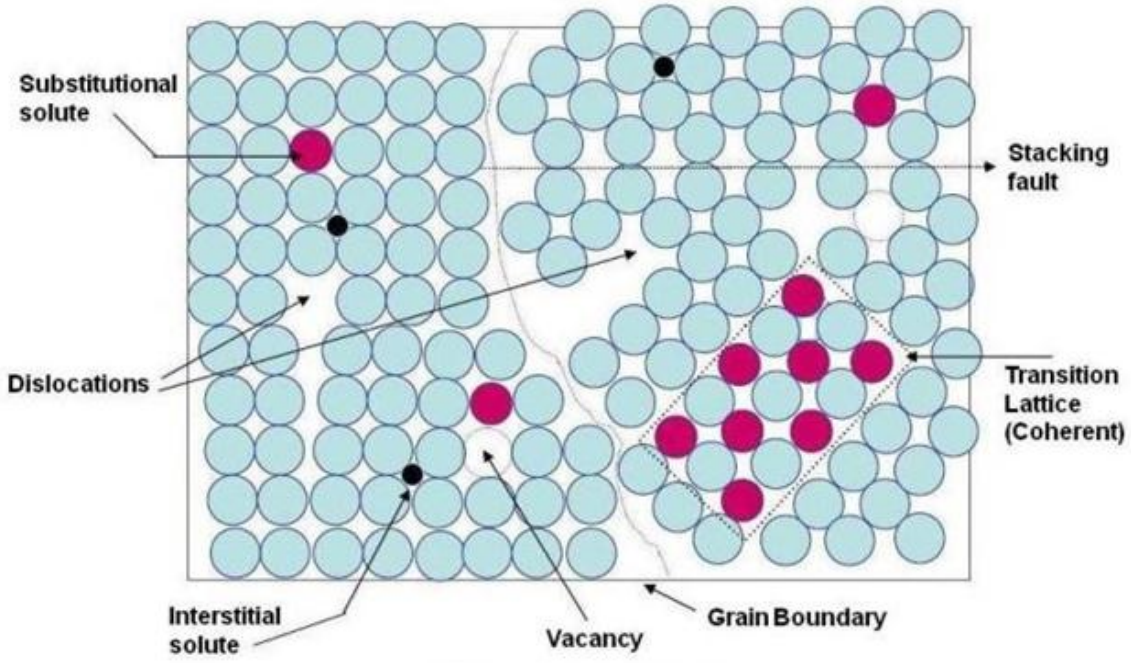

Figure 2.8: Various crystal defects [41].

Imperfections in crystalline solids are normally classified according to their dimension as follows:

1. Point imperfections (Zero dimensional defects)
2. Line imperfections (one dimensional defects)
3. Plane or surface imperfections (Two dimensional defects)
4. Volume imperfections (three dimensional defects)

2.7.1 Point defects

A point defect disturbs the crystal pattern at an isolated site. It is useful to distinguish intrinsic defects, which can appear in a pure material, from extrinsic defects, which are caused by solute or impurity atoms [41].

2.7.1.1: Intrinsic defects

An intrinsic defect is formed when an atom is missing from a position that ought to be filled in the crystal, creating a vacancy, or when an atom occupies an interstitial site where no atom would ordinarily appear, causing an interstitialcy. Because the interstitial sites in most crystalline solids are small (or have an unfavorable bonding configuration, as, for example, in the diamond lattice) interstitialcies are high-energy defects that are relatively uncommon. Vacancies, on the other hand, are present in a significant concentration in all crystalline materials. Their most pronounced effect is to govern the migration of atoms on the crystal lattice (solid state diffusion). In order for an atom to move easily from one crystal lattice site to another the target site must be vacant [42].

Ordered compounds can have more complex intrinsic defects. In most compounds the different species are charged to at least some degree. An intrinsic defect destroys the local charge balance, which must be restored in some way. The compound defects that preserve charge balance are easiest to visualize in binary ionic solids like NaCl. An isolated vacancy in an ionic solid creates an excess charge. The excess charge can be compensated by a paired vacancy on the sublattice of the other specie; for example, the excess charge associated with a Na vacancy is balanced if there is a Cl vacancy nearby. A neutral defect that involves paired vacancies on the cation and anion sublattices is called a Schottky defect. Alternatively, the charge imbalance caused by the vacancy can be corrected by adding an interstitial of the same specie; a Na vacancy is compensated by a Na interstitial. A neutral defect that is made up of a paired vacancy and interstitial is called a Frenkel defect. In compounds whose atoms are less strongly ionized it is energetically possible for species to exchange sites, so that an A-atom appears on the B-sublattice or vice versa. This type of point defect is called an anti-site defect, and is fairly common in semiconducting compounds such as GaAs [42].

2.7.1.2: Extrinsic defects

The extrinsic point defects are foreign atoms, which are called solutes if they are intentionally added to the material and are called impurities if they are not. The foreign atom may occupy

lattice sites, in which case it is called a substitutional solute (or impurity) or it may fill an interstitial site, in which case it is called an interstitial solute. Since the interstitial sites are relatively small, the type of the solute is largely determined by its size. Small atoms, such as hydrogen, carbon and nitrogen are often found in interstitial sites. Larger atoms are usually substitutional.

More complex extrinsic defects appear in compounds. If the valence of a substitutional defect in an ionic solid differs from that of the lattice ion then the excess charge is often compensated by a paired vacancy or interstitial. For example, when Mg^{++} ions are substituted for Na^{+} in NaCl they tend to be paired with vacancies on the Na sublattice to maintain local charge neutrality. In semiconductors substitutional atoms with the wrong valence act as electron donors or acceptors [42].

2.7.2 Line defects

Linear crystal defects are edge and screw dislocations.

- **Edge dislocation** is an extra half plane of atoms "inserted" into the crystal lattice. Due to the edge dislocations metals possess high plasticity characteristics: ductility and malleability.
- **Screw dislocation** forms when one part of crystal lattice is shifted (through shear) relative to the other crystal part. It is called screw as atomic planes form a spiral surface around the dislocation line.

For quantitative characterization of a difference between a crystal distorted by a dislocation and the perfect crystal the Burgers vector is used. The dislocation density is a total length of dislocations in a unit crystal volume. The dislocation density of annealed metals is about 1010 - 1012 m^{-2}. After work hardening the dislocation density increases up to 1015 - 1016 m^{-2}. Further increase of dislocation density causes cracks formation and fracture [43].

2.8 Borates

Since the 1930s, when the first borate crystal structures were determined at ambient conditions by Zachariasen, Goldschmidt, Hauptmann and others, more than 2500 (re-)determined crystal

structures of hydrous and anhydrous borates have been listed in the ICSD Database (ICSD-2016) up to now. Modern descriptors of borate rigid groups, fundamental building blocks (FBBs) and finite clusters were introduced. The nomenclature of crystal structures and several classifications of borates have been described in a large number of review papers. As a result, the basic crystal chemistry principles of borates were established [44]:

(1) Boron atoms do occur equiprobably in both triangular and tetrahedral coordination to oxygen atoms and hydroxyl groups in the structures of crystals and glasses.

(2) The BO_3 triangles or/and the BO_4 tetrahedra are connected via common corners (oxygen atoms) to form rigid cyclic 3B-groups composed from three of such polyhedra; several such groups can also be linked via shared BO_4 tetrahedra, thus forming multiple cyclic rigid groups. BO_4 tetrahedra scarcely share edges. These ways of condensation lead to the formation of boron–oxygen entities that do not change significantly in various crystals and glasses.

(3) The rigid groups or their combinations linked by shared oxygen atoms constitute the fundamental building blocks (FBB) of the structure [44].

Due to interesting chemical and physical properties exhibited by inorganic solid state borate materials, these materials become centre of attention for the material scientists. Borates form a great number of compounds having diverse structures due to three-fold or four-fold coordination of borate atoms. Borates intrinsically possess characteristics that are advantageous for optical materials, which include wide transparency range, large electronic band gap, good thermal and chemical stability, low preparative temperature, optical stability with good nonlinear characteristics and exceptionally high optical damage threshold. The unique crystal structure of borates determines their enhanced UV transparency, good nonlinearity and relatively high resistance against laser induced damage. Borate compounds are very good hosts for development of luminescent materials. Variety of borate host materials doped with rare earth and other ions have been reported as phosphor materials for variety of applications [45]. In this study BaB_8O_{13} and $LiBaBO_3$ borate phosphor powders were studied.

2.8.1 BaB_8O_{13}

The first systematic study of the system $BaO\text{-}B_2O_3$ was performed by Guertler in 1904. Carli and Levin et.al studied the phase equilibrium diagram of the binary system $BaO\text{-}B_2O_3$. The $BaO\text{-}B_2O_3$ structure consists of two separated interlocking three-dimensional infinite network, each of which is built up from alternating triborate and pentaborate groups and triborate groups are linked on to pentaborate groups [46]. In 1949, Levin and McMurdie were the first to characterize barium tetraborate ($BaO\text{-}4B_2O_4$) and tabulated the X-ray powder pattern and some optical data for the compound. Levin and McMurdie stated that the observed phase of $BaO\text{-}4B_2O_4$ compound appears as irregular grains, many of which are striated as a polysynthetic twinning and uniaxial negative or biaxial negative with a small optic axial angle. In 1960, Krogh Moe determined the following unit-cell dimensions from single-crystal from Weissenburg photographs: a = 8.56, b = 2 × 8.69 (very week doubling of b axis) and c = 13.20 Å. The photographs showed the phase to be probably orthorhombic with a pronounced pseudotetragonal symmetry (in agreement with the optical properties). The investigated crystal showed some twinning (Where directions of a and b axes were interchanged) [47]. BaB_8O_{13} crystallizes in the orthorhombic system with space group $P4_122$. In BaB_8O_{13}, Ba^{2+} can decompose 3D B–O networks into low-dimensional B–O frameworks and BaB_8O_{13} has a layered B–O framework. The BaB_8O_{13} compound, as exhibited in **figure 2.9**, features a 2D zig-zag layered B–O framework with a fundamental building block (FBB) of (B_8O_{16}) groups [48**]**.

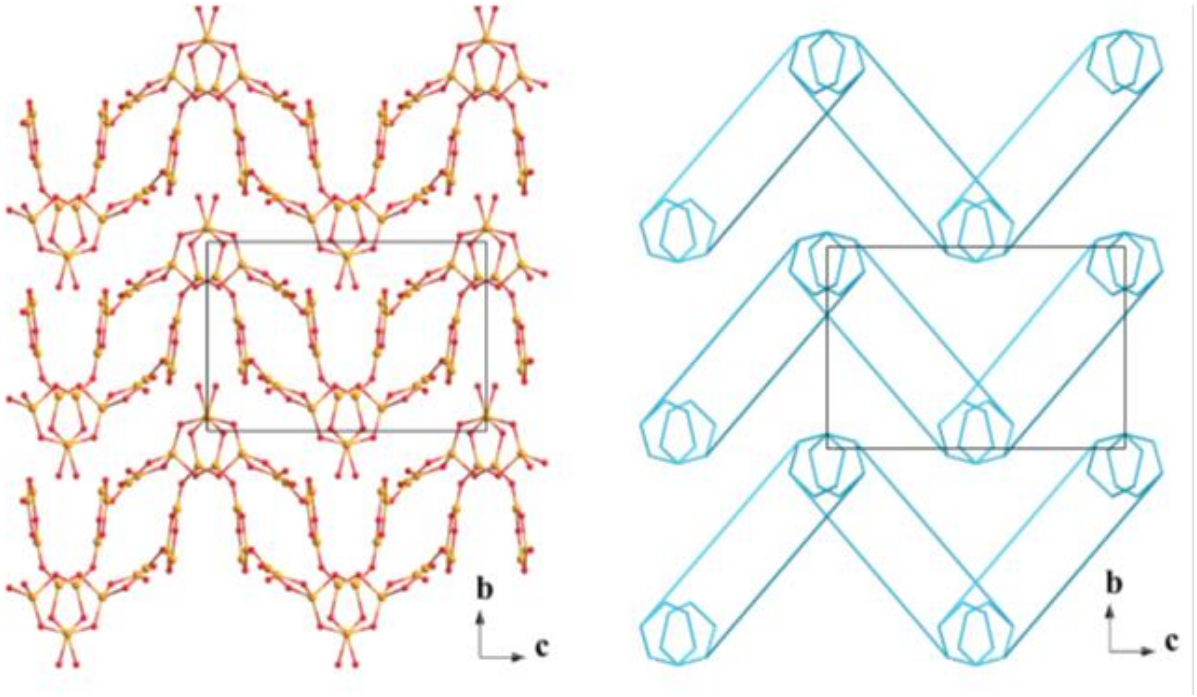

Figure 2.9: Layered structures of BaB_8O_{13} [48].

2.8.2 $LiBaBO_3$

$LiBaBO_3$ crystallizes in the monoclinic cell with space group P21/n (or P21/c). Drawings of the contents of the unit cell of compound $LiBaBO_3$ are shown in **figure 2.10**. It is found that $LiBaBO_3$ structure can be constructed from a stack of [Ba-O] and [Li-O] layers along the $[10\bar{1}]$ direction and B atoms localized in adjacent layers as a bridging role. In the [Li-O] layers, the adjacent polyhedrons constructed from the LiO_5 form dimers by sharing edges, and each dimer connects with the four adjacent dimers by the four O atoms to form two-dimensional sheets along the *ac* diagonal plane, as shown in **Fig. 2.11**. The Li atoms are coordinated by five O atoms and the LiO_5 polyhedron is a distorted trigonal bipyramid. An average bond length of the Li-O in the $LiBaBO_3$ crystal is close to that of the LiSrBO3 crystal, where the one for $LiSrBO_3$ varies from 1.955(7) to 2.169(8) Å with an average value of 2.056 Å. The B-O distances vary from 1.369(4) to 1.385(6) Å with an average value of 1.377 Å and the O-B-O angles are between 118.3(7) ° and 122.6(7) °. These values are normal in a $[BO_3]$ plane of $LiBaBO_3$ [49].

.

In $LiBaBO_3$ crystal, the Ba atoms are coordinated by nine O atoms and the BaO_9 polyhedron is described as a mono-capped distorted square antiprism. The Ba-O distances vary from 2.622(6) to 3.185(5) Å with an average value of 2.813 Å, which compared well to the expected value 2.850 Å calculated from the crystal radii for the nine coordinate Ba^{2+} ions. In the [Ba-O] layers, the Ba atoms through sharing the planes of three oxygen atoms extend along the *ac* diagonal direction to form chains, and the adjacent chains link together by the two oxygen atoms to form puckering sheets in the *b* direction, as shown in **figure 2.12**. These sheets are connected along the $[10\bar{1}]$ direction to form the three-dimensional framework by the bridging O atoms of the [Li-O] layers [49].

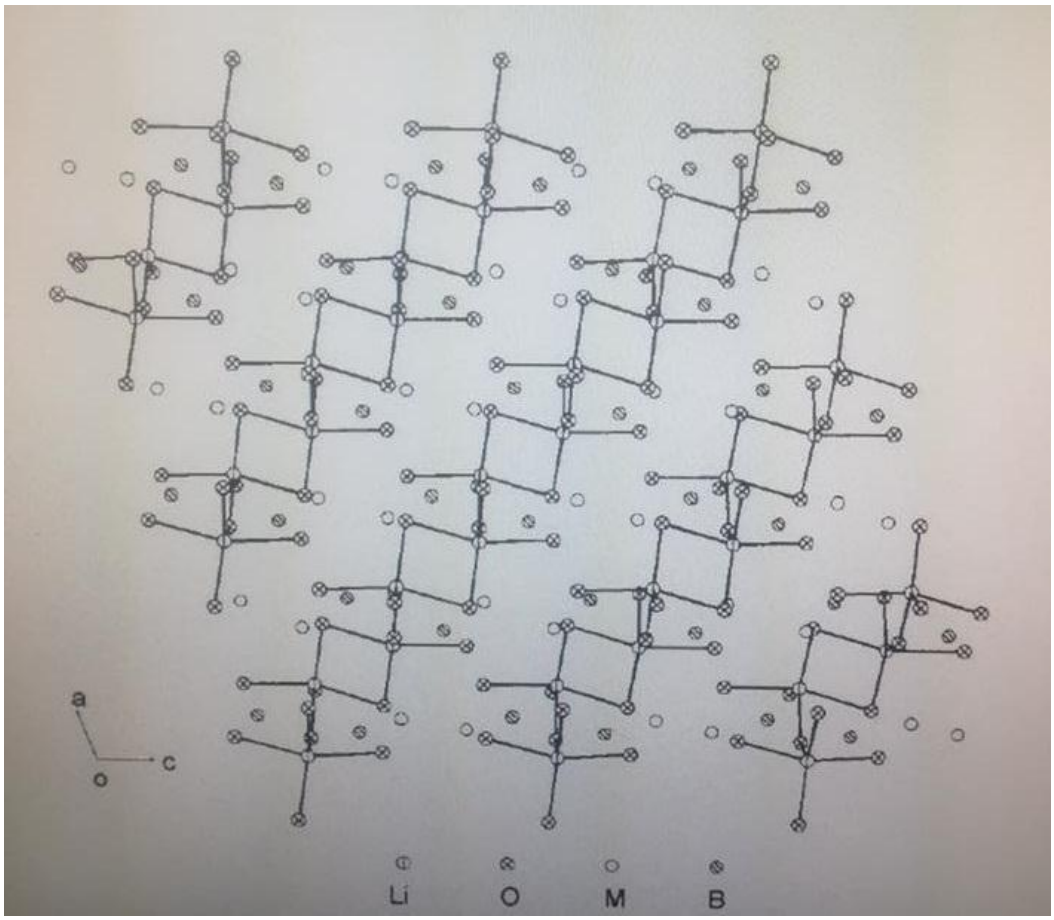

Figure 2.10: Crystal structure stacked from the [Ba-O] and $[10\bar{1}]$ direction in $LiBaBO_3$. The Ba-O bonds are omitted for clarity [49].

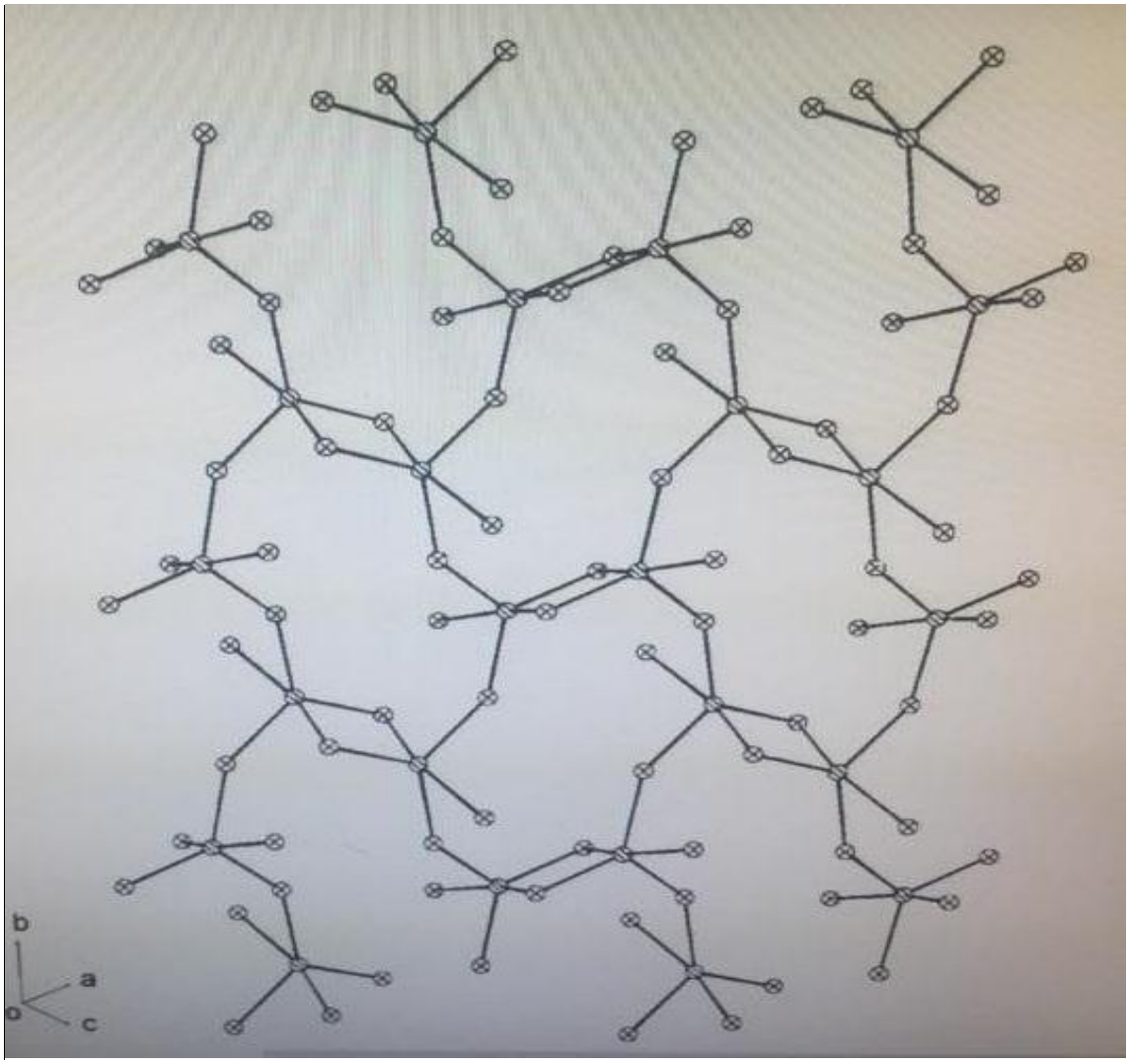

Figure 2.11: Structure of the [Li-O] layer along the *ac* diagonal plane in $LiBaBO_3$ [49].

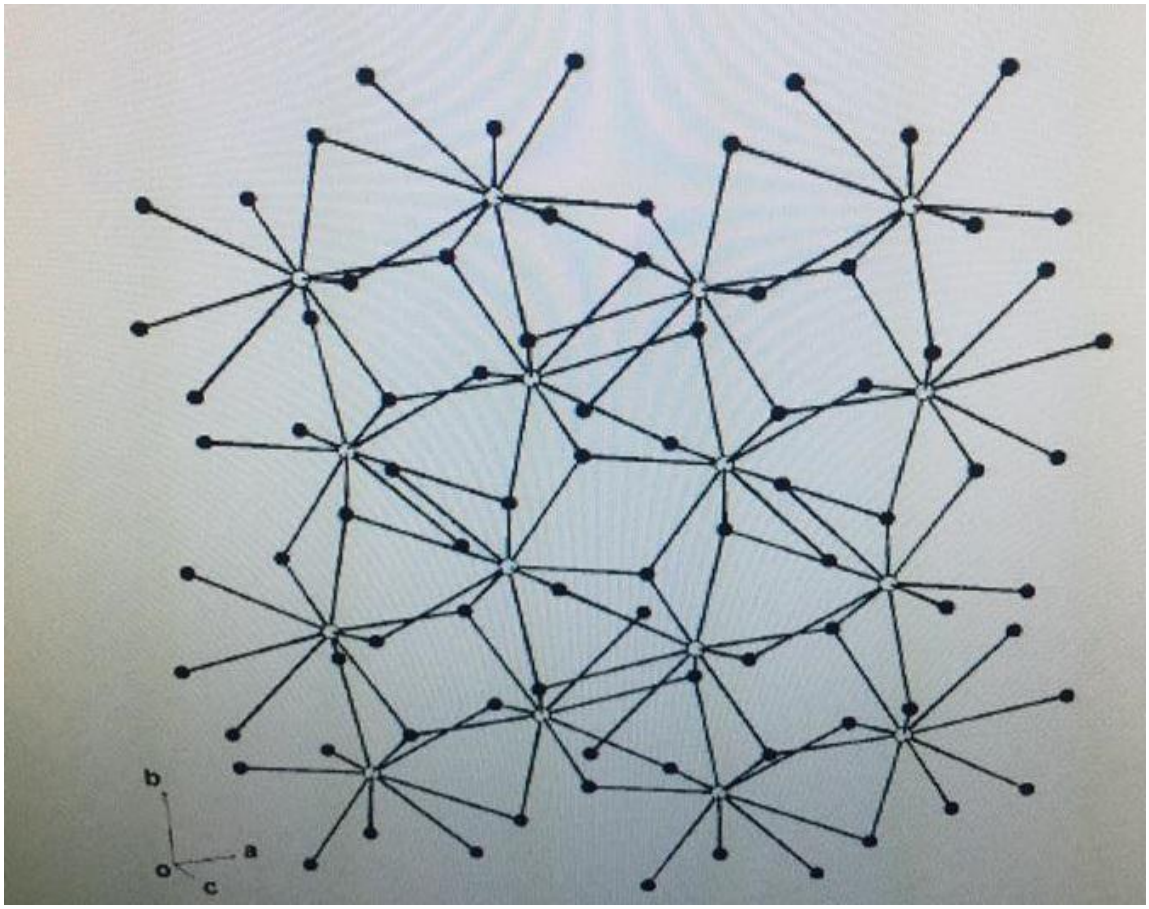

Figure 2.12: Structure of the [Ba-O] layer along the *ac* diagonal plane in $LiBaBO_3$ [49].

References

[1] J. A. DeLuca, *Journal of Chemical Education*, **57** (1980) 541 - 545.

[2] Luminescence: An Introduction http://www.perkinelmer.co.kr/files/Introduction%20to%20Luminescence.PDF **(**accessed on 07/06/2017).

[3] C. da and A. Srivastava, *The Electrochemical Society Interface*, **15** (2006) 55 - 58.

[4] S. H. Mousavi, S. A. Jafari Mohammdi, H. Haratizadeh and P. W. de Oliveira, *Advances in Optical Communication*, (2014), http://dx.doi.org/10.5772/59103.

[5] K. V. R. Murthy and H. S. Virk, *Defect and Diffusion Forum*, **347** (2014) 1 - 34.

[6] S. K. Chauhan, R. Kumar, S. Nadanasabapathy, and A. S. Bawa, Comprehensive Reviews in Food Science and Food Safety, **8** (2009) 4 - 6.

[7] H. Aboud, H. Wagiran and R. Hussin, *International Journal of Scientific & Engineering Research*, **3** (2012) 1 - 15.

[8] V. M Bachmann, Studies on Luminescence and Quenching Mechanisms in Phosphors for Light Emitting Diodes, ISBN: 978-90-3934600-6 (2007).

[9] R. Resfeld, *AIMS Materials Science*, **2** (2015) 37 - 60.

[10] O. L. Malta and Luís D. Carlos, *Quimica Nova*, **26** (2003) 889 - 895.

[11] J. G. Bunzli, S. Comby, A. Chauvin and C. D. B. Vandevyver, *Journal of Rare Earths*, **25** (2007) 257 - 274.

[12] R. Naik, S. C. Prashantha, H. Nagabhushana, S. C. Sharma, H. P. Nagaswarupa, K. S. Anantharaju, B. M. Nagabhushana, H. B. Premkumar and K. M. Girish, Spectrochimica Acta Part A: Molecular and Biomolecular Spectroscopy, **140** (2015) 516 - 523.

[13] L. Li, W. Jiang, H. Pan, X. Xu, Y. Tang, J. Ming, Z. Xu, and R. Tang, *Journal of Physical Chemistry C*, **111** (2007) 4111 - 4115.

[14] X. Ji, F. Zhu, H. Zhai and R. Tang, *Frontiers of Materials Science in China*, **4** (2010) 382 -386.

[15] Y. Q Li, Structure and luminescence properties of novel rare-earth doped silicon nitride based materials Eindhoven: *Technische Universiteit Eindhoven*, doi: 10.6100/IR594350 (2005).

[16] K. G. Tshabalala, H. C. Swart and O. M. Ntwaeaborwa, Synthesis and Characterization of down-conversion, *PhD thesis*, University of the Free State, (2014).

[17] V. K. Pecharsky and K. A. Gschneidner, Jr, Rare Earth Elements, https://www.britannica.com/science/rare-earth-element (accessed on 07/06/2017).

[18] S. B. Castor, and J. B. Hendrick, Rare Earth Elements, http://www.fieldexexploration.com/images/property/1_RareEarths_FLX_02.pdf (accessed on 07/06/2017).

[19] J. Xie, Y. Q. Li, N. Hirosaki and H. Yamamoto, Nitride phosphors and solid state lighting, CRC Press, Taylor and Francis Group, London, 2011, ISBN: 978-1-4398-3011-6.

[20] V. V Shinde and S. J Dhoble, *IOP Conference Series: Materials Science and Engineering*, **73** (2015) 012038.

[21] P. A. Tanner, C. S. K. Mak, N. M. Edelstein, K. M. Murdoch, G. Liu, J. Huang, L. Seijo and Z. Barandiara, Journal of the American Chemical Society, **125** (2003) 13225 - 13233.

[22] X. J. Geng, Y. W. Tian, Y. J. Chen · L. J. Xiao and Y. Xie, *Applied Physics B*, **107** (2012) 177 - 181.

[23] G. Liu, Y. Zhang, J. Yin, and W. F. Zhang, *Journal of Luminescence*, **128** (2008) 2008 - 2012.

[24] S. Hachani, B .Moine, A. El-akrmi and M. Ferid, Journal of Luminescence, **130** (2010) 1774 - 1783.

[25] X. Wua, Y.Lianga, S.Liua, Y. Zhua, R.Xua, M. Tonga and K. Lia, *Spectroscopy Letters*, **50** (2017) 48 - 54.

[26] T. Bell, Metal profile: Bismuth, https://www.thebalance.com/metal-profile-bismuth-2340128 (accessed on 07/06/2017).

[27] B. J. Deibert, E. Velascom, W. Liu, S. J. Teat, W. P. Lustig and J. Li, *Crystal Growth and Design*, **16** (2016) 4178 - 4182.

[28] A. B. Gawande, R. P. Sonekar and S. K. Omanwar, *International Journal of Optics*, (2014) Article ID 418459, doi: org/10.1155/2014/418459.

[29] W. Xu, M. Peng, Z. Ma, G. Dong, and J. Qiu, *Optics Express*, **20** (2012) 15692.

[30] H. Zhang, F. Kang, Y. Zhao, M. Peng, D. Y. Lei and X. Yang, *Journal of Materials Chemistry C*, **5** (2017) 314 - 321.

[31] R. Cao, T. Fu, Y. Cao, S. Jiang, Q. Gou, Z. Chen and P. Li, Journal of Materials Science: Material Electronics, **27** (2016) 3514 -3519.

[32] L. Wang, B. K. Moon, S. H. Park, J. H. Kim, J. Shi, K. H. Kim and J. H. Jeong, New Journal of Chemistry, **40** (2016) 3552.

[33] C. Kim, C. Pyun, H. Choi and S. Kim, Bulletin of the Korean Chemistry Society, **20** (1999) 337 - 340.

[34] R. C. Powell and G. Blasse, Structure and bonding, Luminescence and energy transfer, Spinger-Verlag, Heidelberg, New York, 1980.

[35] K. N. Shinde, S. J. Dhoble and H. C. Swart, Phosphate Phosphors for Solid-State Lighting, Spinger-Verlag, Heidelberg, New York, 2012.

[36] Teng-Ming Chen and Yoan-Jen Yang, Phosphors. Up Conversion Nano Particles, Quantum Dots and Their Applications, Spinger-Verlag, Heidelberg, New York, 2017.

[37] Y. S. Tver'yanovich, *Glass Physics and Chemistry*, **29** (2003) 166 - 168.

[38] C. R. Ronda, Luminescence from Theory to Applications, WILEY-VCH Verlag GmbH & Co. KGaA, Weinheim, 2008.

[39] L. Ozawa, *Journal of Electrochemical Society: Solid-state Science and Technology*, **126** (1979) 106 - 109.

[40] F. Benza and H. P. Strunk, *American Institute of Physics Advances*, **2** (2012) 042115.

[41] M. J. Rahman, Structure of Matter, http://teacher.buet.ac.bd/mjrahman/Class%20Note3_Jellur.pdf (accessed on 19/06/2017).

[42] J. W. Morris, Jr, Defects in Crystals http://www.mse.berkeley.edu/groups/morris/MSE205/Extras/defects.pdf (accessed on 19/06/2017).

[43] D. Kopeliovich, Imperfections of crystal structure, http://www.substech.com/dokuwiki/doku.php?id=imperfections_of_crystal_structure (accessed on 19/06/2017).

[44] R. Bubnova, S. Volkov, B. Albert and S. Filatov, *Crystals*, **7** (2017) 93 doi:10.3390/cryst7030093.

[45] P. A. Nagpure, N. S. Bajaj, R. P. Sonekar and S. K. omanwar, *Indian journal of Pure an Applied Physics*, **49** (2011) 799 - 802.

[46] Y. Xie, S. Zhang, Q. Zheng, Z. Pei and Q. Su, Journal of Material Science and Technology, **20** (2004) 517 - 522.

[47] J. Krogh-Moe, Acta Crystallographica, **B25** (1969) 2153 - 2154.

[48] L. Liu, Y. Yang, X. Dong, C. Lei, S. Han and S. Pan, *European Journal of Inorganic Chemistry*, (2015) 3328 - 3335, doi: 10.1002/ejic.201500399.

[49] W. D. Cheng, H. Zhang, Q. S. Lin, F. K. Zheng and J. T. Chen, *Chemistry of Materials*, **13** (2001) 1841 - 1847.

Chapter 3

Synthesis and Characterization Techniques

3.1 Introduction

This Chapter gives a brief description of the methods used to prepare the powder phosphors and the techniques used for their characterizations. Two methods were used to synthesize the powder phosphors, namely combustion method and solid state method. The powder phosphors of BaB_8O_{13}*:* R^{3+} *(*R^{3+} *=* Ce^{3+}*,* Sm^{3+}*,* Eu^{3+} *and* Bi^{3+}*) where synthesized by combustion method while those of* $LiBaBO_3$*:* R^{3+} *(*R^{3+} *=* Dy^{3+}*,* Eu^{3+} *and* Bi^{3+}*) where synthesized by solid state method. The characterization techniques that were used to analyze the powder phosphors are X-ray diffraction, scanning electron microscopy, photoluminescence spectroscopy, thermoluminescence spectroscopy and ultraviolet visible absorption spectroscopy.*

3.2 Synthesis methods

3.2.1 Combustion method

Many exothermic non-catalytic solid-solid or solid-gas reactions, after being ignited locally can release enough heat to sustain the self-propagating combustion front throughout the specimen without additional energy. Since 1970's, this kind of exothermic reactions has been used in the process of synthesizing refractory compounds in the former Soviet Union. This novel technique, so called combustion/ micropyretic synthesis of self-propagating high temperature synthesis (SHS), has been intensively studied for process implication. This technique employs exothermic reaction processing, which circumvents difficulties associated with conventional methods of time and energy intensive sintering process [1].

Two basic combustion synthesis modes are commonly employed, namely, the wave propagation mode and the thermal explosion mode. In the wave propagation mode, the compacted powders are ignited at a point by heat source. After ignition, the heat to propagate the combustion wave is obtained from the heat released by the formation of the synthesized product. The unreacted portion in front of the combustion wave is heated by this combustion heat, undergoes synthesis, the wave propagates, thus causing further reaction and synthesis. In the thermal explosion mode, the specimen is heated in a furnace. The furnace may be kept at the ignition temperature or the specimen may be heated in the furnace at a pre-determined heating rate to the ignition temperature. The combustion reaction in this mode may occur more or less simultaneously at all points in the specimen. Although the synthesized product phases obtained by both techniques are similar, there may be differences in the amount of residual porosity, final dimensions and the thermal gradient during the processing [1].

3.2.1.1 Solution combustion synthesis

Solution combustion synthesis (SCS) is a promising method to prepare high-purity, small-sized and spherical particle phosphors because the starting raw materials are homogeneously mixed in liquid phases, and the high temperature generated instantly by exothermic reaction can volatilize low boiling point impurities leading to purer products. In addition, SCS results in products with narrow particle distribution because of the decrease in reaction time (a few seconds during the combustion reaction). When heated rapidly at 500 ºC/ 550 ºC/ 600 ºC, the solution containing stoichiometric amount of redox mixture boils, dehydrate, followed by decomposition generating combustible gases. The volatile combustible gases ignite and burn with a flame. The large amount of escaping gases dissipates heat and thereby prevents the material from sintering and thus provides conditions for formation of nanocrystalline phase. Also, as the gases escape they leave voluminous, foaming and crystalline fine powder occupying the entire volume of the container and have no chance of forming agglomerations unlike in the other conventional processes. Therefore, in combustion synthesis, instantaneous and in situ very high temperature, combined with release of large volume of volatiles from liquid [2-5]. **Figure 3.1** shows the schematic diagram of solution combustion method.

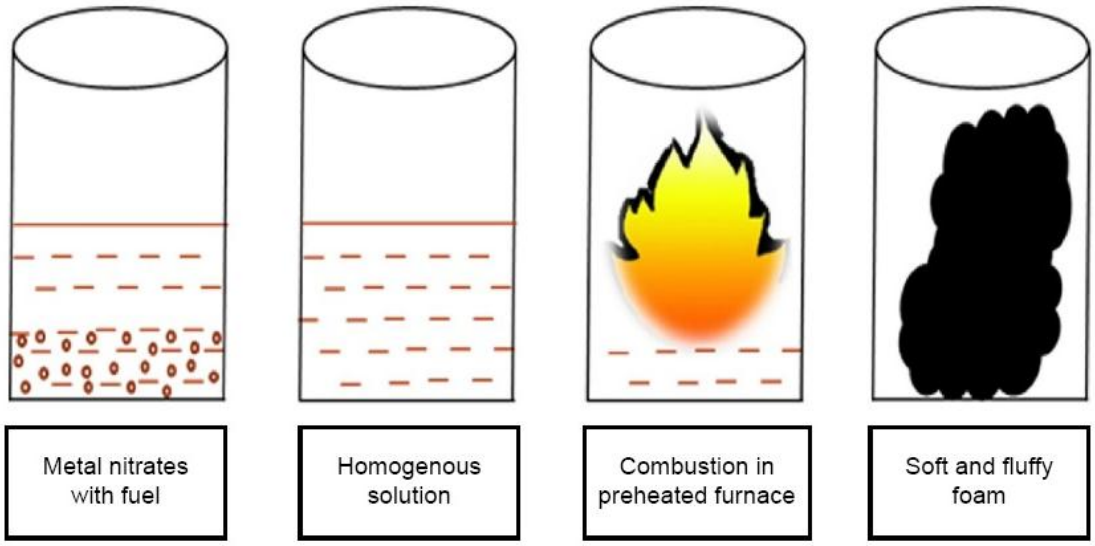

Figure 3.1: Schematic diagram of combustion method [6].

3.2.2 Solid state method

The solid state method (SSR) is commonly used to produce many kinds of phosphors powders including borates phosphors [7-10]. It is generally accepted way for the mass production of phosphors. This method usually involves four sequential steps: (1) matter diffusion at interfaces between solid particles, (2) chemical reactions at the atomic level, (3) nuclei formation, and (4) solid phase transport and growth of new phase. For the solid state reaction to proceed smoothly and effectively, the starting powders are thus required to have high chemical reactivity, large surface area, good dispersion or low agglomeration [11].

A solid state reaction route, also called a dry media reaction or a solvent less reaction, is a chemical reaction in which solvents are not used. In a normal reaction, the reacting agents, also called the reactants, are placed in a solvent before the reaction can take place. These reactants react to form a new substance. After the reaction is completed, scientists are able to remove the new product from the solvent. A solid-state reaction, however, allows the reactants to chemically react without the presence of a solvent. The solid state reaction route is the most widely used method for the preparation of polycrystalline solids from a mixture of solid starting materials.

Solids do not react with each other at room temperature and it is necessary to heat them at elevated temperatures, as high as 1000 ºC to 1500 ºC in order for the proper reaction to occur at an appreciable rate. Thus, both, thermodynamic and kinetic factors are important in solid state reaction [12].

The factors on which the feasibility and rate of a solid state reaction include, reaction conditions, structural properties of the reactants, surface area of the solids, their reactivity and the thermodynamic free energy change associated with the reaction. After the reactants have been weighed out in the required amounts, they are mixed. For manual mixing of small quantities, usually an agate mortar and pestle are employed. For the subsequent reaction at high temperatures, it is necessary to choose a suitable material of container which is chemically inert to the reactants under the heating conditions. Containers may be crucibles or boats made from foil. For low temperature reactions, other metals like Nickel (below 600 – 700 ºC) can be used [12].

The heating programme depends very much on the form and reactivity of the reactants. In the control of either temperature or atmosphere, nature of the reactant chemicals is considered in detail. A good furnace is used for heat treatment. There are several conditions under which a solid state reaction can take place. This synthesis route is very easy and does not require expensive as well as sophisticated equipments. The major advantage of SSR method is the final product in solid form is structurally pure with the desired properties depending on the final sintering temperatures. This method is environment friendly and no toxic or unwanted waste is produced after the SSR is complete. In this process the powders produced from SSR method is very fine as well as the cross contamination is very less. This method is also very convenient for large scale production on industrial scale [12].

3.3 Characterization techniques

3.3.1 X-ray Diffraction

X-ray powder diffraction (XRD) is a rapid analytical technique primarily used for phase identification of a crystalline material and can provide information on unit cell dimensions. The

analyzed material is finely ground, homogenized, and average bulk composition is determined. Max von Laue, in 1912, discovered that crystalline substances act as three-dimensional diffraction gratings for X-ray wavelengths similar to the spacing of planes in a crystal lattice. X-ray diffraction is now a common technique for the study of crystal structures and atomic spacing. X-ray diffraction is based on constructive interference of monochromatic X-rays and a crystalline sample. These X-rays are generated by a cathode ray tube, filtered to produce monochromatic radiation, collimated to concentrate, and directed toward the sample. The interaction of the incident rays with the sample produces constructive interference (and a diffracted ray) when conditions satisfy Bragg's Law ($n\lambda = 2d \sin\theta$). This law relates the wavelength of electromagnetic radiation to the diffraction angle and the lattice spacing in a crystalline sample. These diffracted X-rays are then detected, processed and counted. By scanning the sample through a range of 2θ angles, all possible diffraction directions of the lattice should be attained due to the random orientation of the powdered material. Conversion of the diffraction peaks to d-spacings allows identification of the mineral because each mineral has a set of unique d-spacings. Typically, this is achieved by comparison of d-spacings with standard reference patterns [13].

Experimentally, the Bragg law can be utilized in two ways. By using X-rays of known wavelength λ and measuring θ, we can determine the spacing d of various planes in a crystal: this is structure analysis. Alternatively, we can use a crystal with planes of known spacing d, measure θ, and thus determine the wavelength λ of the radiation used: this is X-ray spectroscopy. The essential features of an X-ray spectrometer are shown in **figure 3.2**. X-rays from the tube T are incident on a crystal C which may be set at any desired angle to the incident beam by rotation about an axis through O, the center of the spectrometer circle. D is an ionization chamber or some form of counter which measures the intensity of the diffracted X-rays; it can also be rotated about and set at any desired angular position [14].

The crystal is usually cut or cleaved so that a particular set of reflecting planes of known spacing is parallel to its surface, as suggested by the drawing. In use, the crystal is positioned so that its reflecting planes make some particular angle θ with the incident beam, and D is set at the corresponding angle 2θ. The intensity of the diffracted beam is then measured and its wavelength calculated from the Bragg law, this procedure being repeated for various angles θ. W. H. Bragg designed and used the first x-ray spectrometer, and the Swedish physicist Siegbahn developed it

into an instrument of very high precision [14]. In this study a Bruker D8 Advanced X−ray diffractometer (XRD) equipped with monochromatic *CuKα* radiation and Siemens diffractometer D5000 with CuKα = 1.54 Å.

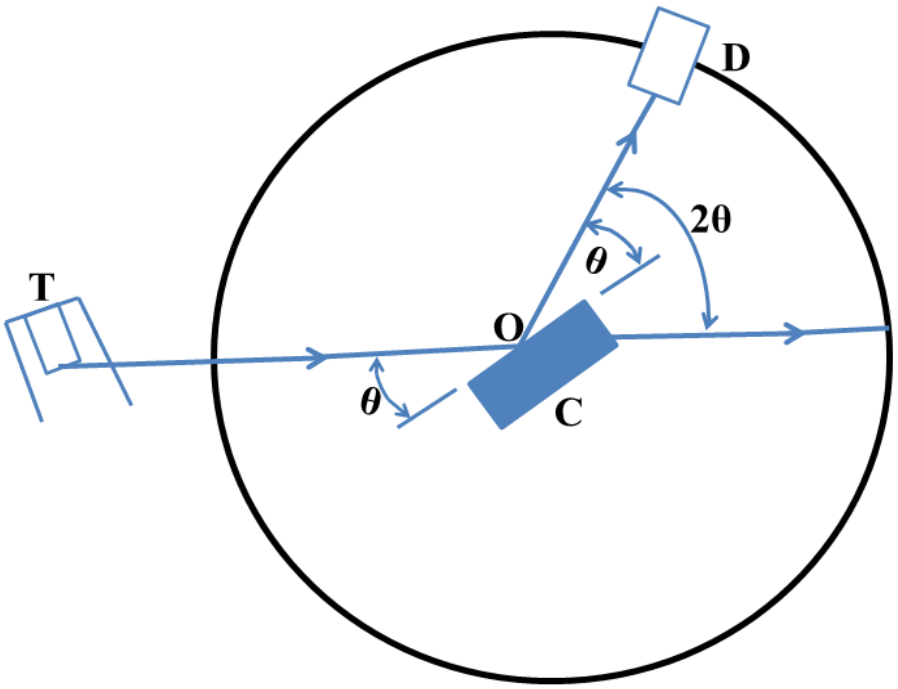

Figure 3.2: The X-ray diffraction system [14].

3.3.2 Scanning Electron Microscopy and energy dispersive x-ray spectroscopy

In microscopy the question arises- Why employ electron beams instead of light beams to produce magnified images and the answer has to do with resolution. When doing microscopy to produce magnified image of objects, diffraction (bending of waves around narrow openings and obstacles) limits the resolution and hence the quality of image in terms of fine details one can see. The optical wavelengths from deep UV to IR are in range of hundreds of nanometers while electron beam of energy in keV have wavelengths in fractions of nanometers. The dependence of diffraction on the wavelength of the beam makes electron beam more suitable than beams of wavelengths in the optical region. The diffraction also depends on the size of the objects. A Scanning Electron Microscope (SEM) with electron beams in the keV range allows one to produce image of objects in the micro to nanometer range with relatively lower diffraction

effects. Using a SEM to produce proper image requires a judicious choice of beam energy, intensity, width and proper preparation of the sample being studied. The electron beam in a SEM is nowadays generated using a field emission filament that uses ideas of quantum tunneling. Other methods are also available. The deflection of electron beam of certain energy E is accomplished by means of electromagnetic lenses. Typical E values for conventional SEM can range from as low as 2-5 keV to 20-40 keV [15].

A basic SEM consists of an electron gun (field emission type or others) that produces the electron beams, electromagnetic optics guide the beam and focus it. The detectors collect the electrons that come from the sample (either direct scattering or emitted from the sample) and the energy of the detected electron together with their intensity (number density) and location of emission is used to put together image. The latest SEM also offer energy dispersive photon detectors that provide analysis of x-rays that are emitted from the specimen due to the interactions of incident electrons with the atoms of the sample [15]. **Figure 3.3** shows the schematic diagram of an SEM. In this study, the surface morphology and elemental composition of the phosphor powders were investigated using a Jeol JSM 7800F thermal field emission scanning electron microscope (FE-SEM).

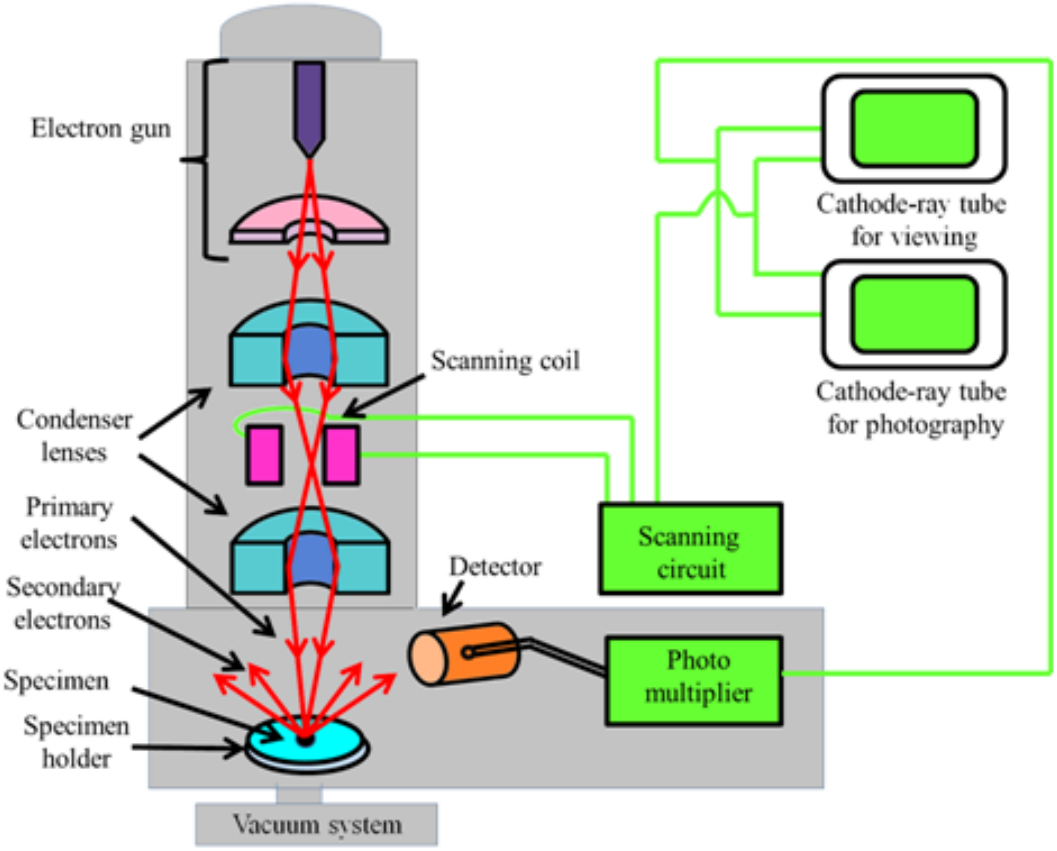

Figure 3.3: Schematic diagram of Scanning Electron Microscopy [16].

3.3.3 Transmission Electron Microscopy (TEM)

Transmission electron microscopy (TEM) is an imaging technique where a beam of electrons is focused onto a specimen causing an enlarged version to appear on a fluorescent screen or layer of photographic film. The first practical TEM was built by Albert Prebus and James Hillier at the University of Toronto in 1938 using concepts developed earlier by Max Knoll and Ernst Ruska.

Many physical techniques rely on the interaction between high energy electrons and the atoms in a solid. There are many possible interactions and some of the more useful (in that they give rise to measurable effects) are simulated. In the simulations, high energy electrons, typically 20 keV or higher, are allowed to interact, one by one, with a single atom of aluminium. This atom is assumed to be part of a solid metallic specimen and it contributes 3 electrons to a valence band

or conduction band. In TEM a thin specimen is illuminated with electrons, the primary electrons [17].

The wealth of information TEM can provide is due to the different electron-specimen interactions and versatility of TEM operation methods. **Figure 3.4** shows a cross-sectional view of a simplified TEM model. Changing the convergence of the illuminating beam and using different apertures or detectors can lead to different operating modes for specific applications. **Figure 3.5** shows different types of signals generated by a high energy electron beam (usually 80–300 KeV) passing through a thin specimen. Images are formed by the detection of transmitted beams. The objective lens aperture can be used to selectively choose the direct beam to form images, which are known as bright field (BF) images. If the scattered electrons are chosen, the corresponding images are dark field (DF) images. The BF and DF images sometimes are very useful to deliberately enhance or suppress signals of a particular material, crystal plane, or defects [18].

Analyzing the energy loss of the in-elastically scattered beam can help to determine the elemental composition and bonding configurations of materials, which is the principle of Electron energy loss spectroscopy (EELS). Above the specimen, the characteristic X-ray signals can be utilized for Energy-dispersive X-ray spectroscopy (EDS) analysis. Collecting the signals of the secondary electrons and backscattered electrons can form surface-sensitive SEM-like images. In imaging techniques, an important issue is the image contrast. The contrast can be understood as the differentiation of the object of interest from the background due to differences in intensity (brightness or darkness). Whether the object is brighter or darker than the background depends on the TEM operation and the materials themselves. A common feature of BF images is that the vacuum is whiter than the specimen. In contrast, the vacuum is black in DF images as the direct beam is blocked by the apertures [18]. In this study, High-resolution transmission electron microscopy (HR-TEM) analyses were carried with a JEOL-TEM 2100 instrument.

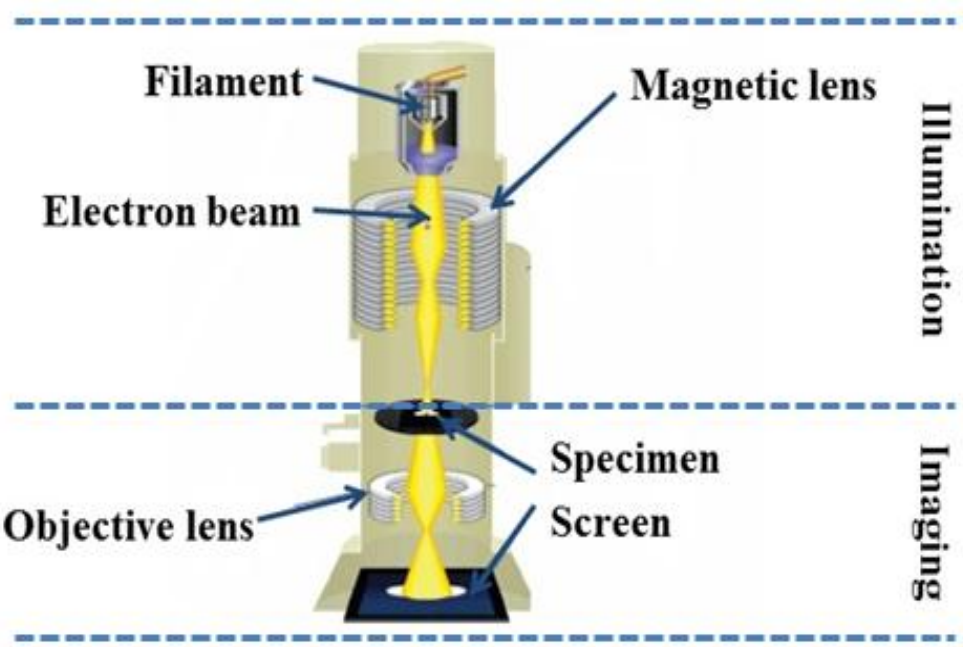

Figure 3.4: Schematic setup of transmission electron microscopy (TEM) [17].

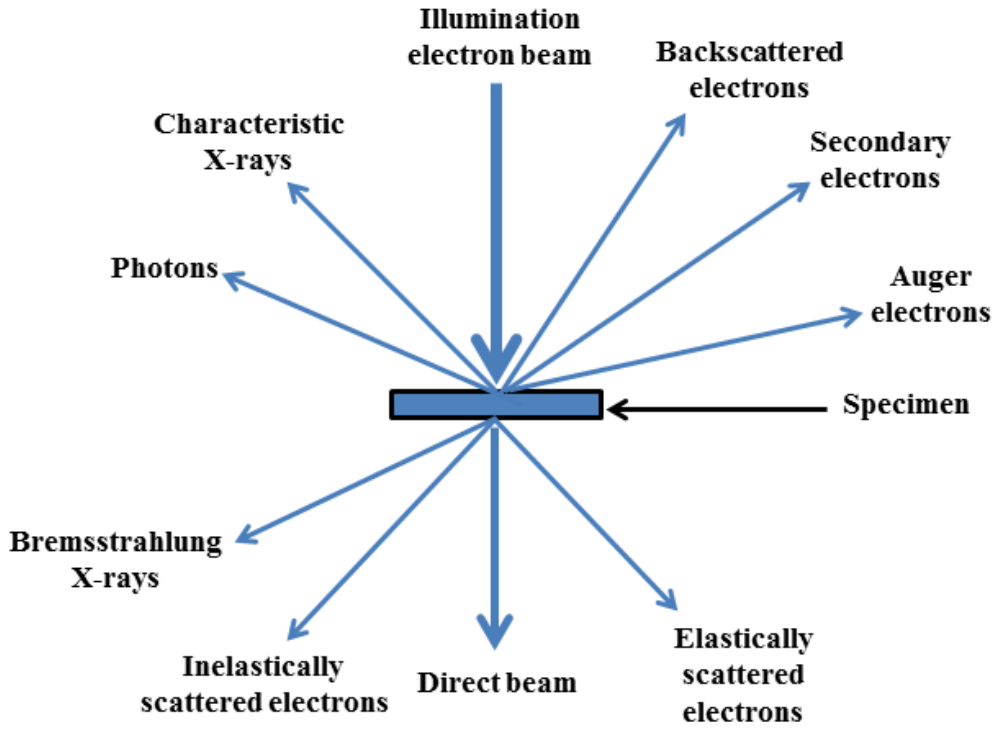

Figure 3.5: signals generated when high-energy electrons interact with a specimen [18].

3.3.4 Fourier-transform infrared spectroscopy (FTIR)

Fourier-transform infrared (FTIR) spectroscopy is based on the idea of the interference of radiation between two beams to yield an interferogram. The latter is a signal produced as a function of the change of path length between the two beams. The two domains of distance and frequency are interconvertible by the mathematical method of Fourier-transformation. The basic components of an FTIR spectrometer are shown schematically in **figure 3.6**. The radiation emerging from the source is passed through an interferometer to the sample before reaching a detector. Upon amplification of the signal, in which high-frequency contributions have been eliminated by a filter, the data are converted to digital form by an analog-to-digital converter and transferred to the computer for Fourier-transformation [19].

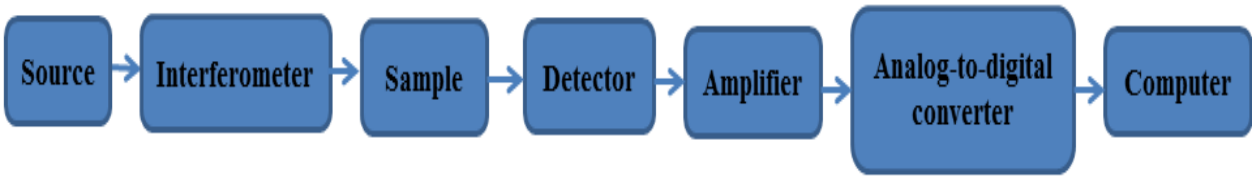

Figure 3.6: Basic components of an FTIR spectrometer [19].

There are a number of interferometer designs used by FTIR manufacturers. The oldest and perhaps the most common type of interferometer in use today is the Michelson interferometer. It is named after Albert Abraham Michelson (1852–1931) who first built his interferometer in the 1880s and went on to win a Nobel Prize in Physics for the discoveries he made with it. The optical design of a Michelson interferometer is shown in **figure 3.7**. The Michelson interferometer consists of four arms. The top arm in **figure 3.7** contains the infrared source and a collimating mirror to collect the light from the source and make its rays parallel. The bottom arm of the Michelson interferometer contains a fixed mirror, i.e., a mirror that is in a fixed position and does not move. This is in contrast to the right arm of the interferometer, which contains a moving mirror which is capable of moving left and right. The left arm of the interferometer contains the sample and detector. At the heart of the interferometer is an optical device called a

beamsplitter. A beamsplitter is designed to transmit some of the light incident upon it and reflect some of the light incident upon it. In **figure 3.7** the light transmitted by the beamsplitter travels toward the fixed mirror, and the light reflected by the beamsplitter travels toward the moving mirror. Once the light beams reflect from these mirrors they travel back to the beamsplitter, where they are recombined into a single light beam that leaves the interferometer, interacts with the sample, and strikes the detector [20]. Perkin Elmer Spectrum 100 FTIR spectrometer was used in this study.

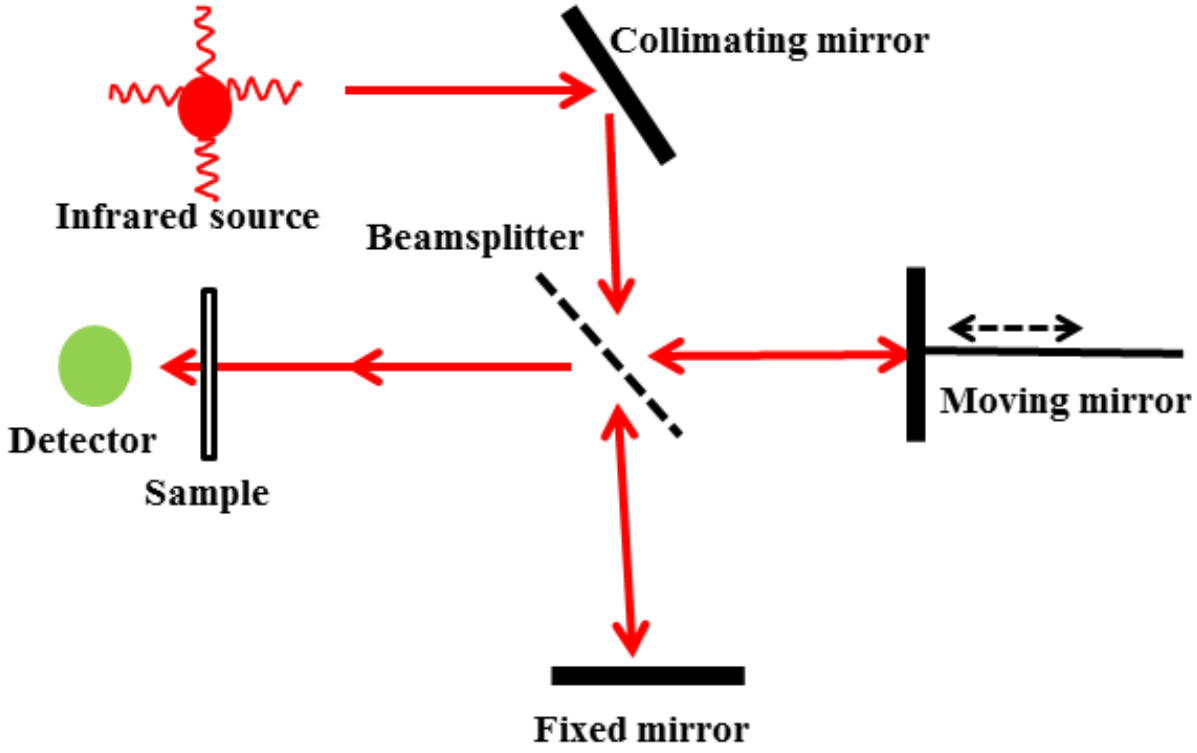

Figure 3.7: The optical diagram of a Michelson interferometer [20].

3.3.5 Thermo gravimetric analysis (TGA)

Thermal analysis is the analysis of a change in a property of a sample, which is related to an imposed change in the temperature. The sample is usually in the solid state and the changes that occur on heating include melting, phase transition, sublimation, and decomposition. The analysis of the change in the mass of a sample on heating is known as Thermogravimetric analysis

(TGA). TGA measures mass changes in a material as a function of temperature (or time) under a controlled atmosphere. Its principal uses include measurement of a material's thermal stability and composition. TGA is most useful for dehydration, decomposition, desorption, and oxidation processes [21]. A TGA analysis is performed by gradually raising the temperature of a sample in a furnace as its weight is measured on an analytical balance that remains outside of the furnace. In TGA, mass loss is observed if a thermal event involves loss of a volatile component. Chemical reactions, such as combustion, involve mass losses, whereas physical changes, such as melting, do not. The weight of the sample is plotted against temperature or time to illustrate thermal transitions in the material – such as loss of solvent and plasticizers in polymers, water of hydration in inorganic materials, and, finally, decomposition of the material [22]. TG curves are recorded using a thermobalance. It consists of an electric microbalance, a furnace, a temperature programmer and a recorder (instrument connected to thermobalance to record the output/curves [23]. The block diagram of a thermobalance is shown in **figure 3.8.** In this study**,** Perkin Elmer STA 6000 Simultaneous Thermal Analyzer was used.

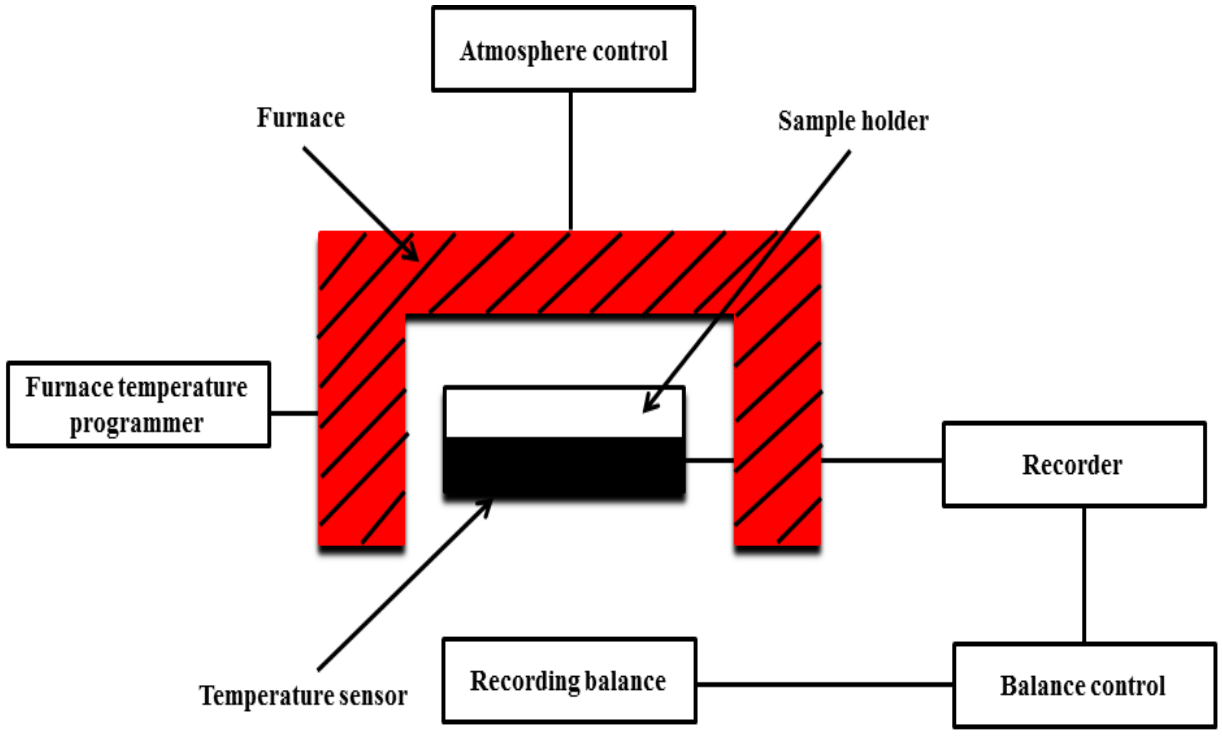

Figure 3.8: Schematic diagram of a thermobalance [23].

3.3.6 Time-of-Flight Secondary Ion Mass Spectroscopy (ToF-SIMS)

During the last years' time of light secondary ion mass spectrometry (TOF-SIMS) has left its academic origin and is meanwhile used in many industrial laboratories for surface characterization [24]. Time of flight secondary ion mass spectrometry (ToF-SIMS) is a highly sensitive surface analytical technique which enables determination of surface chemistry and surface chemical mapping. Furthermore, the extremely short analysis depth (~1 nm) of ToF-SIMS enables molecular orientation to be elucidated. Initially, ToF-SIMS application was dominated by inorganic materials, especially within the semiconductor and coatings industries and later, in minerals processing with regards to surface chemistry, organic contaminants and adsorbates. In many instances the surface of a sample in terms of texture and composition is most critical in controlling chemical, physical and biological interactions [25].

ToF-SIMS is a variant of so-called static SIMS, in which sub-monolayer surface sensitivity is attained without significant damage to the sample surface, providing both elemental and molecular information from highly complex surfaces. ToF-SIMS utilises a primary ion pulse that is accelerated and focused onto the surface of a sample held under ultra-high vacuum. The schematic diagram of ToF-SIMS system is shown in **figure 3.9**. The bombarding particle subsequently impacts the surface resulting in a sputter plume containing secondary particles from the sample surface. These sputtered particles consist of atoms, whole molecules and fragments of molecules. A certain portion of these will possess a charge described by their species' ionisation efficiency. The charge on the secondary ion allows it to be accelerated, along with all other ions of the same polarity, to an equal kinetic energy. At this point, the ions enter a time-of-flight (drift) region where they become separated according to their mass-to-charge ratio (typically, the ions are only singly charged). Since each ion has equal kinetic energy, their drift velocity will be governed by the relation of kinetic energy to mass. Thus by measuring the time it takes for the secondary ions to reach the spatially resolved detector, the mass-to-charge ratio can be deduced and a mass spectrum ensues for every detector pixel. Thus a spectrum can be extracted for any region of an image and similarly, an image can be generated from any mass fragment. As one can expect, the positive and negative ions require separate acquisition and in addition, their expulsion from the sample surface can lead to a charge build up. Thus the sample needs to be held at an optimised potential and is ideally conducting, or easily neutralised with an electron

flood gun. Most ToF-SIMS instruments available today are capable of sub-micron ion image resolution with simultaneous high mass resolution [26].

The experimental conditions have to be carefully chosen to obtain the required information from ToF-SIMS. Typically, an instrument will consist of multiple ion sources, have depth profiling capabilities, allow effective charge compensation by use of an electron flood gun, enable positive ion yield enhancement with use of an O_2 gas bleed, and have full computer control for operation, data work-up and full retrospective analysis [26].

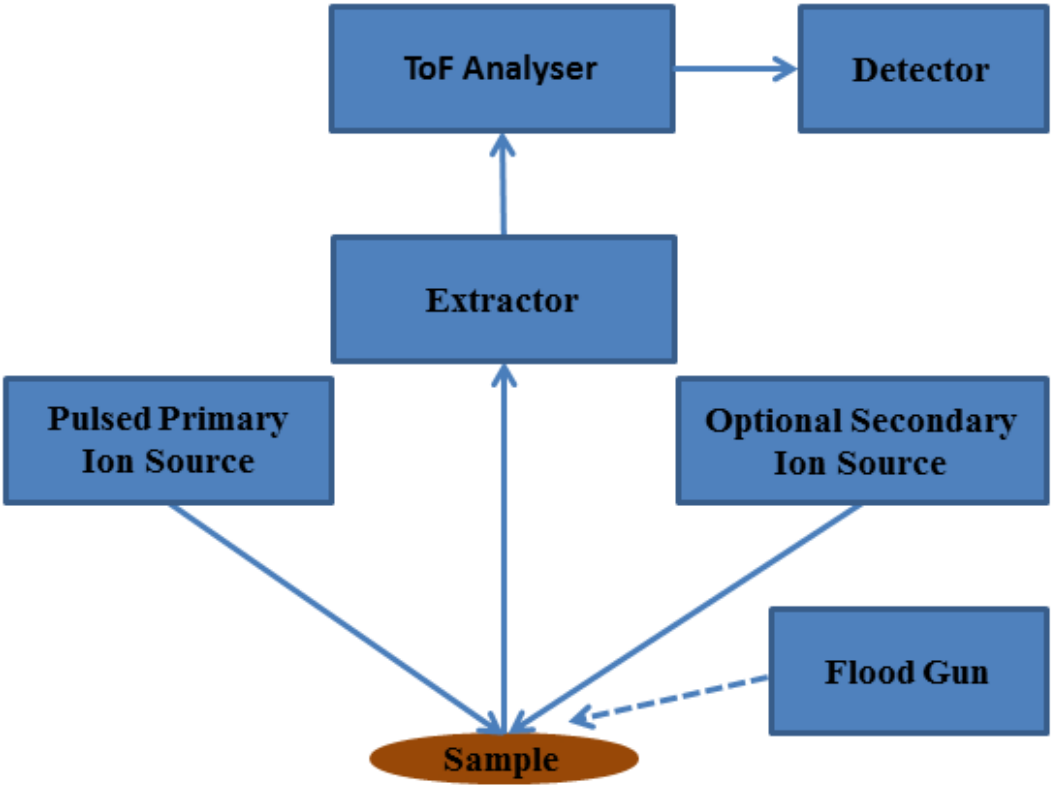

Figure 3.9: Schematic diagram of ToF-SIMS system [26].

3.3.7 Ultraviolet-visible spectroscopy (UV-Vis)

Ultraviolet (UV) spectroscopy is a physical technique of the optical spectroscopy that uses light in the visible, ultraviolet, and near infrared ranges. The Beer-Lambert law states that the absorbance of a solution is directly proportional to the concentration of the absorbing species in

the solution and the path length. Thus, for a fixed path length, UV/VIS spectroscopy can be used to determine the concentration of the absorber in a solution. It is necessary to know how rapidly the absorbance changes with concentration. Ultraviolet and visible spectrometers have been in general use for the last 35 years and over this period have become the most important analytical instrument in the modern day laboratory [27].

The interaction of light of the UV-Vis-NIR region with catalytic solids is considered to be a complex process due to absorption and scattering phenomena. These phenomena are largely overcome by the application of techniques such as diffuse reflectance spectroscopy (DRS). DRS is based on the reflection of light by a powdered sample, and the dimensions of the individual particles in such powdered sample are comparable to the wavelength; i.e., 0.2-3 μm. This makes it impossible to distinguish the phenomena of reflection, refraction and diffraction; the light is scattered [28].

Diffuse reflectance spectroscopy technique is based on the reflection of light in the ultraviolet (10 – 420 nm), visible (420 – 700 nm) and near-infrared (700 – 2500 nm) regions by a powder sample. In a diffuse reflectance spectrum (DRS), the ratio of the lights scattered from a (> 2 – 3 mm) thick layer of sample and an ideal non-absorbing reference sample is measured as a function of the wavelength λ (i.e. $F_{SKM}(R_\infty)$ vs λ in nm). The relation between the diffuse reflectance of the sample (R_∞), absorption (K) and scattering (S) coefficients are related by the Schuster–Kubelka–Munk (SKM) remission function:

$$F_{SKM} = \frac{(1-R_\infty)^2}{2R_\infty} = \frac{K}{S} \qquad (3.1)$$

The SKM remission function relates the experimentally determined diffuse reflectance of a thick sample to K and S. At constant S, $F_{SKM}(R_\infty)$ is directly proportional to K and a plot of $F_{SKM}(R_\infty)$ vs concentration of absorbing species should be a straight line passing through the origin. This linear relationship can be used for quantitative studies on powder samples of infinite layer thickness containing uniformly distributed metal ions in low concentration. The remission function also depends strongly on particle size for weak absorbers but not for strong absorbers which absorb almost all the incident photons [29].

There are different types of spectrometers. In this study, the single-beam spectrometer will be discussed. The single-beam spectrometers have single optical channel that is configured to measure either sample or reference channel but not both simultaneously. The resultant spectrum is in the ratio of the transmission spectra from sample and reference measurements. In practice, the response of the detector measured with zero photon energy flux is measured as the dark current (Dark). The final transmission (in T units) spectrum from this device is given as [30]:

$$Spectrum = \left(\frac{Sample_T - Dark}{\text{Re } ference_T - Dark} \right) \tag{3.2}$$

If the spectrometer has any instabilities (optical, mechanical or electronic), the time constant between sample and reference measurements become critical. Single beam instruments must either be more inherently stable or alternate between sample and reference measurements at a frequency so as to make negligible the rate of change of the spectrometer. The spectrometer is consists of the Light source, detectors, filters, gratings, beam splitters [30]. **Figure 3.10** shows the schematic diagram of a single beam UV-vis spectrophotometer. In this study the diffuse reflectance spectra were recorded using a Lambda 950 UV–Vis spectrophotometer.

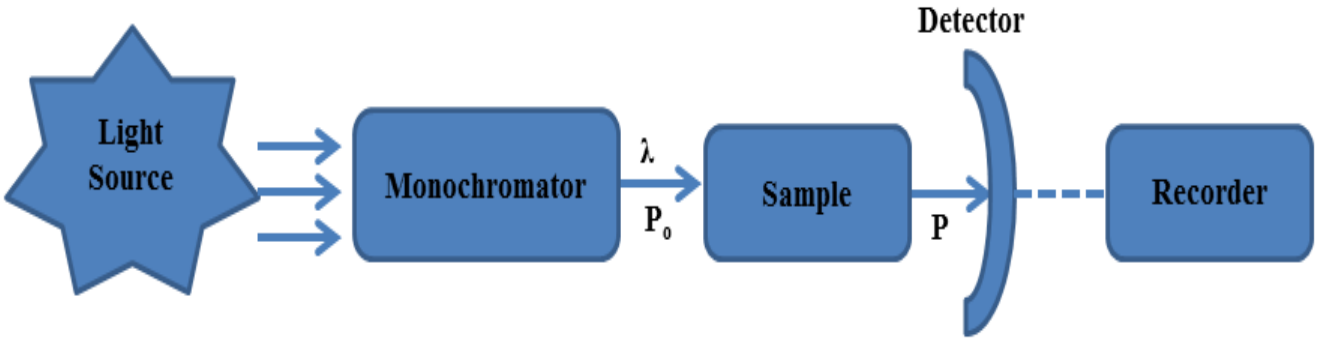

Figure 3.10: Schematic diagram of UV-visible spectrophotometer [31].

3.3.8 Photoluminescence spectroscopy (PL)

Photoluminescence (PL) is a standard technique for characterization of semiconducting and lasing materials complementary to optical absorption. An examination of the difference between the lowest absorption peak and the photoluminescence peak gives information about the nature

of the emitting state. Temperature and intensity dependent steady-state PL and time resolved PL measurements yield the energies and life times of the trap sites involved in the radiative recombination. Particle size selection is accomplished by tuning the laser to the red edge of the absorption band. It excites only the largest particles in the different size distribution [32].

Photoluminescence excitation (PLE) spectroscopy is similar to PL except that in PLE a single luminescence band is monitored while the excitation wavelength is varied. The excitation source is either a tunable dye laser or high intensity arc lamp-monochromator combination. PLE can be used to effectively reduce the inhomogeneous width of the transitions by extracting information from a subset of the nanoparticle distribution. Only the smallest crystallites in the sample are probed in PLE when monitoring a narrow spectral region on the blue edge of the luminescence band**.** PLE is also used to probe quantum dot size distribution as well as to study higher excited states [32].

All fluorescence spectroscopic experiments contain three basic items: a source of light, a sample holder and a detector. In addition, to be of analytical use, the wavelength of incident radiation needs to be selectable and the detector signal capable of precise manipulation and presentation (**figure 3.11**). In simple filter fluorimeters, the wavelengths of excited and emitted light are selected by filters which allow measurements to be made at any pair of fixed wavelengths. Simple fluorescence spectrometers have a means of analysing the spectral distribution of the light emitted from the sample, the fluorescence emission spectrum, which may be by means of either a continuously variable interference filter or a monochromator. In more sophisticated instruments, monochromators are provided for both the selection of exciting light and the analysis of sample emission [33].

In principle, the greatest sensitivity can be achieved by the use of filters, which allow the total range of wavelengths emitted by the sample to be collected, together with the highest intensity source possible. In practice, to realize the full potential of the technique, only a small band of emitted wavelengths is examined and the incident light intensity is not made excessive, to minimize the possible photodecomposition of the sample [33]. From **figure 3.11**, an excitation wavelength is selected by one monochromator, and luminescence is observed through a second

monochromator, usually positioned at 90° to the incident light to minimize the intensity of scattered light reaching the detector. If the excitation wavelength is fixed and the emitted radiation is scanned, an emission spectrum is produced [34]. In this study, photoluminescence studies were performed using different PL spectrometers. The PL spectra were recorded at room temperature using a Hitachi F-7000 fluorescence spectrophotometer, Varian-Carry Eclipse system which uses a xenon lamp as a source of excitation and a 325 nm He-Cd gas laser as an excitation source.

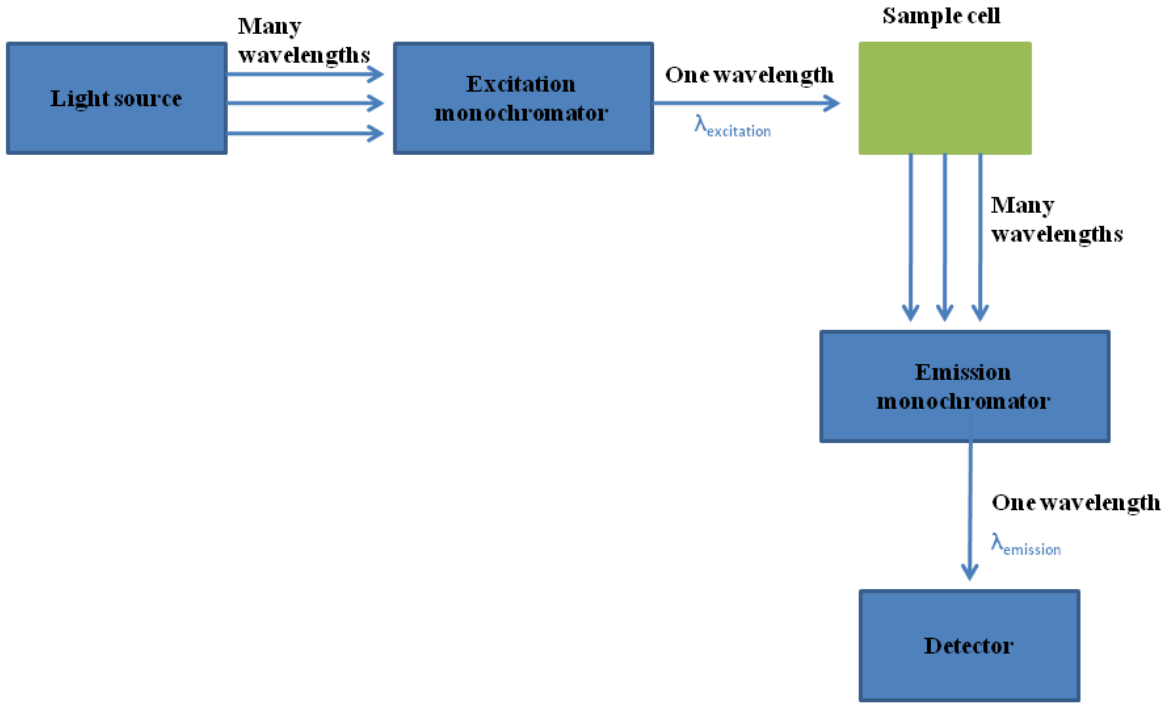

Figure 3.11: Schematic diagram of PL spectrometer [34].

3.3.9 Thermoluminescence (TL)

TL or more specifically Thermally Stimulated Luminescence (TSL) is stimulated thermally after initial irradiation given to a phosphor by some other means (α- rays, β-rays, γ- rays, UV rays and X-rays). Thermally stimulated luminescence (TSL) is the phenomenon of emission of light from a solid which has been previously exposed to ionizing radiation under conditions of increasing temperature.

Unlike other luminescence process such as Electroluminescence, Chemiluminescence, etc, here heat is not an exciting agent, but it acts only as a stimulant. Hence it is better known as thermally stimulated luminescence (TSL). Excitation is achieved by any conventional sources like ionizing radiation, α- rays, β-rays, γ- rays, and UV rays and X-rays. TSL is exhibited by a host of materials, glasses, ceramics, plastics and some organic solids. By far insulating solids doped with suitable chemical impurities, termed as activator, are the most sensitive TL materials. The band theory of solids is normally used to explain this phenomenon [35].

When a solid is irradiated, electrons and holes are produced. Defects in solids result in the presence of the localized energy levels within the forbidden gap. On irradiation, electrons and holes can be trapped at these defect sites. When the solid is heated, these trapped electrons/holes get enough thermal energy to escape from the trap to the conduction band (or valence band). From here they may get re-trapped again or may recombine with trapped holes/electrons. The site of recombination is called recombination center. If this recombination is radiative, the center is called luminescence center. Alternatively a trapped hole can be released by heating which can recombine with a trapped electron resulting in luminescence. It is not required that all charge recombination should result in luminescence, they may be non- radiative too [35].

The plot of intensity of emitted light versus the temperature is known as a TL glow curve. A glow curve may exhibit one or many peaks depending upon the number of electron/hole traps with different trap depths, present in the lattice. These peaks may or not be well separated. The position, shape and intensity of the glow peaks therefore are characteristic of the specific material and the impurities and defects presents. Therefore each TSL peak corresponds to the release for an electron (or hole) from a particular trap level within the band gap of the material. The nature of the TL glow peaks gives information about the luminescent centers present in the material. It may be mentioned that TSL is highly sensitive to structural imperfections in crystals [35]. A Schematic representation of the TL system components is shown in **figure 3.12** [36]. The TL system that was used in this study is a TL 10091, NUCLEONIX spectroscopy, which used a 254 nm UV lamp.

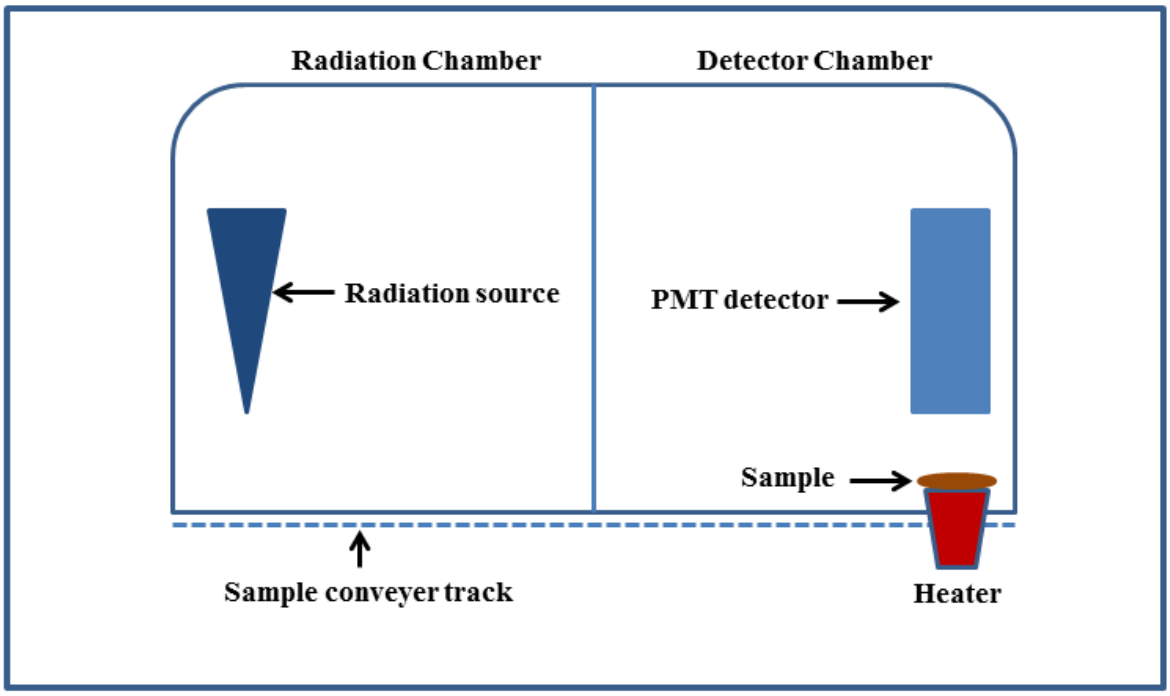

Figure 3.12: Schematic representation of the TL system components [36].

3.4 References

[1] H. Li, Materials Science Research Trends, Nova Science Publishers, Inc, New York, 2008.

[2] A. Lakshmanan, The Role of Sintering in the Synthesis of Luminescence Phosphors, file:///C:/Users/ufs/Documents/Research%20data%202016/Books/Combustion%20synthesis.pdf (accessed 20/6/2017).

[3] N. S. Sawala, C. B. Palan, A. O. Chauhan and S. K. Omanwar, *Optik - International Journal for Light and Electron Optics* , (2016) 1 - 12, doi.org/10.1016/j.ijleo.2016.02.064.

[4] J. T. Ingle, R. P. Sonekar, S. K. Omanwar, Y. Wang, and L. Zhao, *Combustion Science Technology*, **186** (2014) 83 - 89.

[5] M. A. Lephoto, O. M. Ntwaeaborwa, S. S. Pitale, H. C. Swart, J. R.Botha, B. M. Mothudi, *Physica B*, **407** (2012) 1603 - 1606.

[6] K. Venkatesan, D. R. Babu, M. P. K. Bai, R. Supriya, R. Vidya, S. Madeswaran, P. Anandan, M. Arivanandhan and Y. Hayakawa, *International Journal of Nanomedicine*, **10** (2015) 189 - 198.

[7] J. Huang, L. Zhou, Q. Pang, F. Gong, J. Suna and W. Wanga, Luminescence, **24** (2009) 363 - 366.

[8] P. Li, Z. Wang, Z. Yang, Q. Guo and X. Li, *Materials Letters*, **63** (2009) 751 - 753.

[9] X. Zhang and M. Gong, *Dalton Transactions*, **43** (2014) 2465 - 2472.

[10] W. Liu, C. Huang, C. Wu, Y. Chiu, Y. Yeh and T. Chen, *Journal of Material Chemistry*, **21** (2011) 6869 - 6874.

[11] L. Wang and R. Xie, Materials for Solid State Lighting and Displays, John Wiley and Sons Ltd, UK, (2017).

[12] http://shodhganga.inflibnet.ac.in/bitstream/10603/40974/10/10_chapter%202.pdf (accessed on 20/06/2017).

[13] B. L. Dutrow and C. M. Clark, Geochemical Instrumentation and Analysis http://serc.carleton.edu/research_education/geochemsheets/techniques/XRD.html (accessed on 20/06/2017).

[14] B. D. Cullity, Elements of X-Ray Diffraction Second Edition, Addison-Wesley Publishing Company, Inc. Philippines, (1978).

[15] R. Mehta, Scanning Electron Microscopy, InTech publishing, Croatia, (2012).

[16] I. Guwahati, Microscopic Techniques, http://nptel.ac.in/courses/102103044/18 (accessed on 20/06/2017).

[17] H. Ma, K. Shieh and T. X. Qiao, *Nature and Sci*ence, **4** (2006) 14 - 22.

[18] Y. Lin, J. A. McCarthy, K. R. Poeppelmeier and L. D. Marks, *Catalysis by Well-Defined Structures*, (2016) 193 - 238, doi: 10.1016/B978-0-12-801217-8.00007-4.

[19] B. Stuart, Infrared Spectroscopy: Fundamentals and Applications, John Wiley & Sons, Ltd, 2004

[20] B. C. Smith, Fundamentals of Fourier Transform Infrared Spectroscopy, Taylor & Francis Group, LLC, New York, (2011).

[21] Differential thermal analysis (DTA) / Thermogravimetric analysis (TG) http://www.ishuchita.com/Ist%20Year/Material%20Science/Differential%20Thermal%20Analysis%20%28DTA%29.pdf (accessed on 20/06/2017).

[22] Thermogravimetric Analysis (TGA),

http://photometrics.net/PhotoMetrics/thermogravimetric-analysis-tga/(accessed on 20/06/2017).

[23] Thermogravimetric Analysis (TGA),

https://www.slideshare.net/KalsoomMohammed/thermogravimetry-analysis ttga?next_slideshow=1 (accessed on 20/06/2017).

[24] B. Hagenhoff, *Mikrochimica Acta*, **132** (2000) 259 - 271.

[25] T. J. Barnes, I. M. Kempson and C. A. Prestidge, *International Journal of Pharmaceutics*, **417** (2011) 61 - 69.

[26] R. N. S. Sodhi, *Royal Society of Chemistry*, **129** (2004) 483 - 487.

[27] R. S. Shah, R. R. Shah, R. B. Pawar and P. P. Gayakar, *International Journal of Institutional Pharmacy and Life Sciences*, **5** (2015) 490 - 505.

[28] B. M. Weckhuysen, Spectroscopy of Catalysts, American Scientific Publishers, 2004

[29] G. Rao and H. R. Sahu, *Indian Academy of Sciences*, **113** (2001) 651 - 658.

[30] J. Workman. Jr and A. W. Springsteen, Applied Spectroscopy, A Compact Reference for Practitioners, Academic Press, UK, (1998).

[31] https://chem.libretexts.org/Core/Physical_and_Theoretical_Chemistry/Spectroscopy/Electronic_Spectroscopy/Electronic_Spectroscopy%3A_Application (accessed on 21/06/2017).

[32] http://shodhganga.inflibnet.ac.in/bitstream/10603/1292/11/11_chapter%205.pdf (accessed on 21/06/2017).

[33] An Introduction to Fluorescence Spectroscopy, PerkinElmer, Inc, (2000)

https://www.chem.uci.edu/~dmitryf/manuals/Fundamentals/Fluorescence%20Spectroscopy.pdf (accessed on 21/06/2017).

[34] R. Ye and A. R. Barron, Photoluminescence Spectroscopy and its Application,

http://cnx.org/contents/gbsDEZju@2/Photoluminescence-Spectroscopy (accessed on 21/06/2017).

[35] J. N. Reddy, K. V. R. Murthy, Thermoluminescence Basic Theory Applications and Experiments, http://www.nucleonix.com/Manuals/TL1009I_Man.pdf (accessed on 21/06/2017).

[36] L. L. Noto, H. C. Swart and O. M. Ntwaeaborwa, Persistent luminescence mechanism of tantalite phosphors**,** *PhD thesis*, University of the Free State, (2014).

Chapter 4

Photoluminescence studies of green emitting BaB_8O_{13}: Bi^{3+} phosphors

4.1 Introduction

Research activities in luminescent nanoparticles (nanophosphors) has generated interest in the last 2-3 decades due to their particle size dependent tunable emission and their potential applications in different types of light emitting devices [1] including displays, optical waveguides, lasers and light emitting diodes. In particular the focus has been on both light emitting semiconducting metal oxides/sulfides and insulating inorganic hosts doped with rare-earths and transition metal ions. In the case of light emitting materials or phosphors made from doping inorganic host lattice with rare-earths/transition metal ions, the host acts to capture primary excitation energy and transfer it to the dopant/activator ions that act as emission centres [2]. Examples of inorganic host lattices that are commonly used include borates, phosphates, aluminates, silicates, etc. [3]. In recent years, the interest in oxide materials of borate groups has increased due to their excellent properties such as a wide variety of structure types, transparency in the wide range of wavelength from ultraviolet (UV) extending to the visible, high damage threshold and excellent non-linearity [4]. They have also been extensively investigated as host lattices for luminescent materials or phosphors because of their large band gap, high chemical and thermal stability. Most borate hosts are transparent between 140 - 180 nm, so that VUV light can directly excite the incorporated dopant ions that serve as luminescent centres [5]. The structure of BaB_8O_{13} consists of two separate interlocking three-dimensional infinite networks as triborate and pentaborate groups, which form BO_3 triangle and BO_4 tetrahedral units [6, 7]. In

this study, BaB_8O_{13} was doped with bismuth (Bi^{3+}) resulting in a phosphors that gives a broadband emission in the green region of the visible spectrum with a maximum at 548 nm.

Luminescence properties of bismuth (Bi^{3+})-doped host lattices have attracted extensive attention and have been investigated for more than half a century. Undoubtedly, Bi^{3+} has revolutionized the lighting industry because of its versatility to act as an activator (energy acceptor) or a sensitizer (energy donor) [8]. Light emission from Bi^{3+} is a result of electron transitions from the 6s6p excited state to the $^6S_2$ ground state. Because the electron transitions from $^1S_0$ to $^3P_0$ and $^3P_2$ are completely spin forbidden, optical absorption is ascribed to the electron transitions from $^1S_0$ to $^3P_1$ or $^1P_1$ [9]. The $^3P_1$ excited state has lower energy and more stable than the $^1P_1$ excited state, therefore, the emission spectrum of Bi^{3+} ion at room temperature usually consists of a single broad band due to the $^3P_1 \rightarrow {}^1S_0$ transition [10]. The simplified energy level diagram of Bi^{3+} ion in the O_h symmetry showing the allowed and forbidden transitions is shown in **figure 4.1** below. The $^1S_0 \rightarrow {}^3P_1$, $^1S_0 \rightarrow {}^1P_1$ and $^3P_1 \rightarrow {}^1S_0$ shown by the solid lines show the allowed transitions while the $^1S_0 \rightarrow {}^3P_2$ and $^3P_2 \rightarrow {}^1S_0$ shown by dashed lines show the forbidden transitions [11].

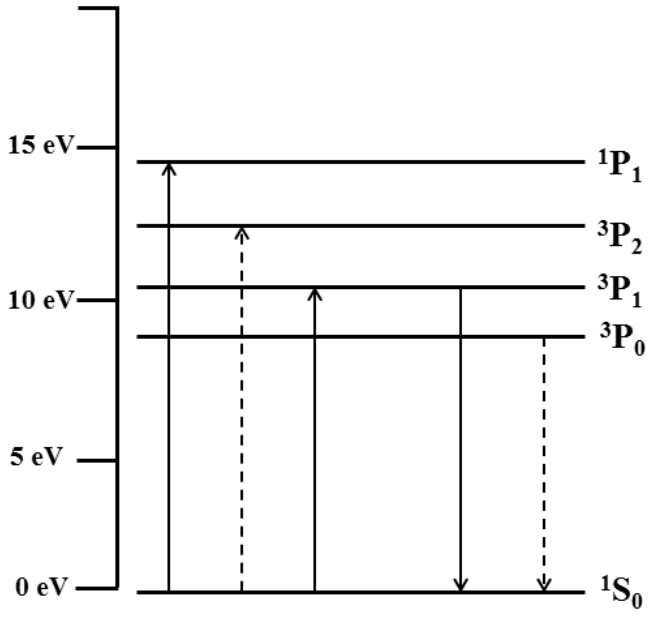

Figure 4.1: Energy level diagram of Bi^{3+} ion in the O_h symmetry [11].

Many researchers have reported luminescence behavior of Bi^{3+} ions doped in different host matrices. Its color varies from ultraviolet to blue/green/red because the outer $6s^2$ electronic configurations of Bi^{3+} depend strongly on their environmental conditions, such as covalence, coordination number and site symmetry [12]. For example, UV emitting Zn_2GeO_4: Bi^{3+} (376 nm), blue emitting $MgAl_2O_4$: Bi^{3+} (400 nm), green emitting $Ca_{10}(PO_4)_6F_2$: Bi^{3+} (538 nm) and many more have been reported in the literature [8, 13, 14]. In this work, BaB_8O_{13}: Bi^{3+} was synthesized by solution combustion method using urea as fuel. The choice of combustion method in this work is because it offers the possibility for controlling homogeneity, purity of phase, size distribution, surface area and microstructural uniformity of the materials [15]. The structure, photoluminescence properties and particle morphology of these phosphors are reported.

4.2 Experimental

4.2.1 Preparations

Powder samples of BaB_8O_{13}: $x$$Bi^{3+}$ ($0 \leq x \leq 0.13$) were synthesized by a solution combustion method. The following precursors all in analytical purity were used: Barium nitrate [$Ba(NO_3)_2$], boric acid [H_3BO_3], bismuth nitrate [BiN_3O_9] ,ammonium nitrate [NH_4NO_3] and urea [NH_2CONH_2]. In this experiment, NH_4NO_3 was used as an oxidizer while NH_2CONH_2 was used as a fuel. The stoichiometric amounts of reactants were mixed in a beaker with 10 mL of de-ionized water and stirred vigorously using a magnetic stirrer on a hot plate maintained at a temperature of 70 ºC for 30 min. The resulting solution was then transferred to a crucible and introduced into a muffle furnace preheated to 600 ºC. Within a few minutes, the solution boiled and ignited to produce a self-propagating flame. The entire combustion process was completed in less than 5 min but the crucible was left in the furnace for 10 min to ensure that decomposition is complete. After 10 min the crucible was removed from the furnace and allowed to cool to room temperature. The combustion ashes of the powder samples were ground gently into fine powders using pestle and mortar. The powders were post annealed at 800 °C for 5 hours in a muffle furnace. The procedure for the synthesis of the powder phosphors is shown schematically in **figure 4.2**.

4.2.2 Characterizations

The structure of the powder phosphors was analysed using a Bruker D8 Advanced X−ray diffractometer (XRD) equipped with a monochromatic *CuKα* radiation. Fourier transform infrared (FTIR) analysis was performed using a Perkin Elmer Spectrum 100 FTIR spectrometer. Thermogravimetric analysis (TGA) was carried out using Perkin Elmer STA 6000 Simultaneous Thermal Analyzer. Morphology and chemical composition were analyzed using Jeol JSM 7800F thermal field emission scanning electron microscope (FE-SEM) and the chemical composition analysis was carried out using an Oxford Instruments AzTEC energy dispersive spectrometer (EDS) attached to the FE-SEM. High-resolution transmission electron microscopy (HR-TEM) analysis were carried out with a JEOL-TEM 2100 instrument. Room temperature photoluminescence (PL emission and excitation) spectra were recorded by Hitachi F-7000 fluorescence spectrophotometer using a monochromatized xenon lamp as an excitation source. The diffuse reflectance measurements were carried out in the range of 200 – 800 nm using a Lambda 950 UV–Vis spectrophotometer.

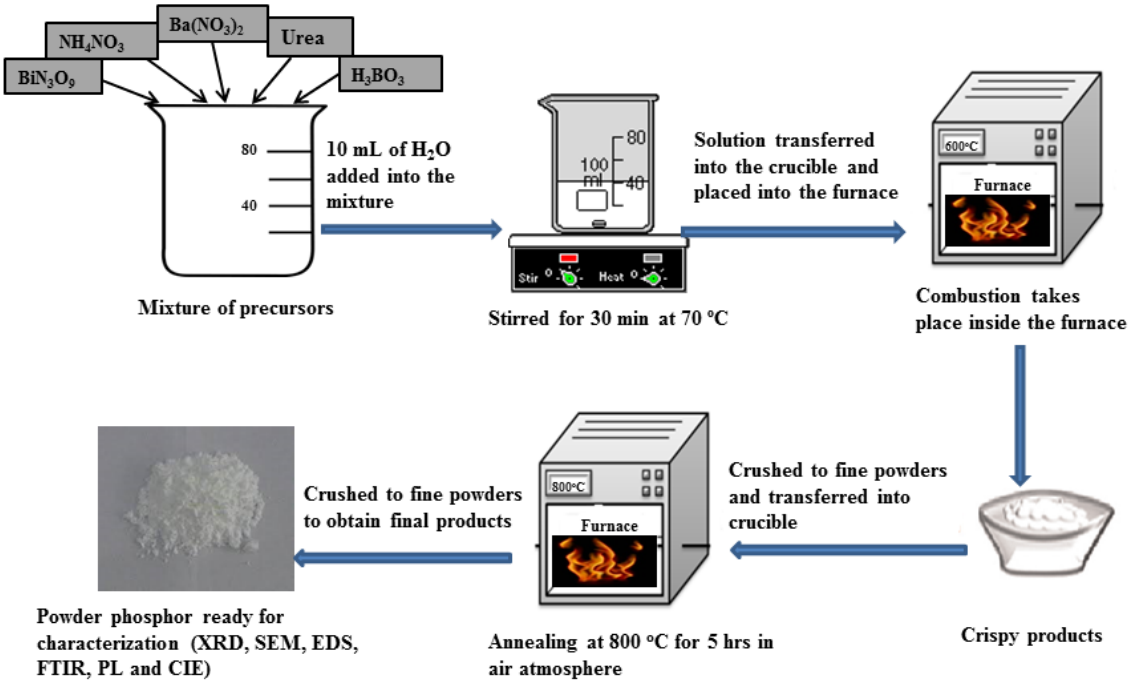

Figure 4.2: A schematic diagram illustrating the solution combustion synthesis procedure of BaB_8O_{13}: xBi^{3+} ($0 \leq x \leq 0.13$) powder phosphors.

4.3 Results and discussion

4.3.1 Structure and morphology

Figure 4.3 shows the X-ray diffraction (XRD) spectra of BaB_8O_{13}: xBi^{3+} ($0 \leq x \leq 0.13$). All intense peaks of the XRD patterns were indexed to orthorhombic structure of BaB_8O_{13} with cell parameters a = 8.550 Å, b = 17.350 Å and c = 13.211 Å, which are in good agreement with the standard referenced in the JCPDS file no: 20-0097 [4]. There are additional peaks marked with an asterisk (*) observed from the patterns and they are attributed to the unreacted $Ba(NO_3)_2$ during the combustion reaction. Haiyen et.al [16], reported that the presence of other phases or some of the precursors can be attributed to the fact that the combustion wave is not uniform and a portion of the precursors might not react completely. The other observed difference between the literature XRD spectrum and the prepared XRD spectra is that there is a peak shift to the lower angle and the peaks are broader. The XRD peak shift might be due tolattice strain, lattice defects or purely size effect [17]. The average crystallite sizes were estimated by using Scherer's equation [18, 19]:

$$D = \frac{0.9\lambda}{\beta \cos\theta} \tag{4.1}$$

where β represent full width at half maximum (FWHM) of the XRD lines in radians, λ is the wavelength of the X-rays (0.154 nm in the present case) and θ is the Braggs angle of the XRD peak. The average crystallite sizes for BaB_8O_{13} host and BaB_8O_{13}: xBi^{3+} (x = 0.11) phosphor powders were found to be 32 nm and 61 nm, respectively. The estimated crystallite sizes for all prepared BaB_8O_{13}: xBi^{3+} ($0 \leq x \leq 0.13$) powder phosphors were found to be in the range of 40 – 65 nm.

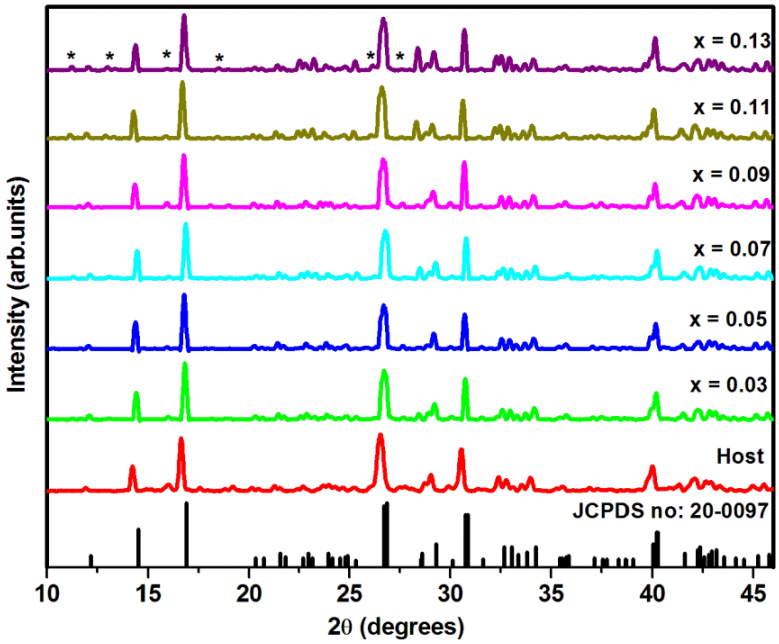

Figure 4.3: XRD spectra of BaB_8O_{13}: xBi^{3+} ($0 \leq x \leq 0.13$) powder phosphors.

The peak broadening of the X-ray diffraction peaks may be due to a combination of crystallite sizes and lattice strains. Strain and crystallite size effects in peak broadening are independent of each other and they can be differentiated by Williamson-Hall plot [20]. Williamson-Hall proposed a method for determining crystallite sizes and lattice strains by evaluating the peak width as a function of 2θ. The crystallite size of the powder phosphors were also calculated using analysis described by Williamson and Hall (W–H) method using the equation below [21, 22]:

$$\beta_{hkl} \cos\theta = \left(\frac{K\lambda}{D}\right) + 4\varepsilon \sin\theta \qquad (4.2)$$

The plot of $\beta_{hkl}\cos\theta$ versus $4\sin\theta$ from equation (4.2) gives a straight line with the slope equal to the strain (ε) and the intercept along the $\beta_{hkl}\cos\theta$ axis equal $K\lambda/D$ from where the crystallite size D can be calculated. The Williamson-Hall plots of BaB_8O_{13}: xBi^{3+} (x = 0 and 0.11) powder phosphors are shown in **figure 4.4**. The average crystallite sizes for BaB_8O_{13}: xBi^{3+} (x = 0 and 0.11) powder phosphors were found to be 39 nm and 82 nm, respectively. The larger crystallite sizes obtained using W-H plots (**figure 4.4 (a-b)**) are more accurate than those obtained using Eq. 1 because the Scherer's equation does not take into consideration the effect of lattice strain in the line broadening. The implication is that, the Scherrer's equation overestimates the effect of

crystallite size [22]. The estimated strain from W-H and the average crystallite size values are summarized in **table 4.1**.

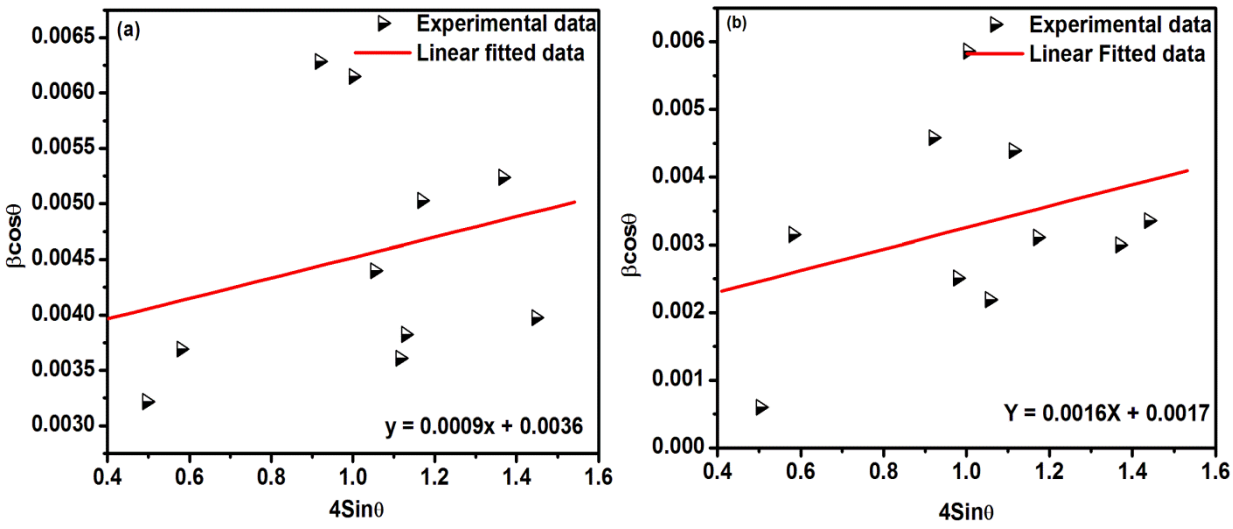

Figure 4.4: Williamson-Hall plot of BaB_8O_{13}: xBi^{3+} (x = 0 and 0.11) powder phosphor.

Table 4.1: Structural parameters of BaB_8O_{13}: xBi^{3+} (x = 0 and 0.11) powder phosphor.

Sample name	**Crystallite size D (nm)**		**Lattice constants (Å)**			**Microstrain (×10^{-4})**	**Cell volume (Å^3)**
BaB_8O_{13}: xBi^{3+}	**Scherer's**	**W-H**	**a**	**b**	**c**	**ε**	**v**
JCDPS card	-	-	8.55	17.35	13.21	-	1959.98
x = 0	32	39	8.60	17.56	13.56	9.0	2046.82
x = 0.11	61	82	8.57	17.47	13.50	16.0	2021.29

Shown in **figure 4.5** are the Fourier Transform Infra-red (FTIR) spectra of BaB_8O_{13} host and BaB_8O_{13}: xBi^{3+} (x = 0.11) powder phosphors. The spectra exhibit broad absorptions in the 650 - 1600 cm^{-1} range. The bands in the 1200 - 1600 cm^{-1} range correspond to the stretching of the B–O bonds of BO_3 units and the bands in the region of 800 - 1200 cm^{-1} correspond to the B–O bond stretching of tetrahedral BO_4 units. All the bands below 800 cm^{-1} correspond to the B–O–B bending vibrations of borate networks [23, 24]. It is clear that incorporation of Bi^{3+} ions in the BaB_8O_{13} host matrix did not have any effect in the main structure. This is in agreement with the XRD results, indicated that doping did not affect the crystal structure of the prepared powder phosphors.

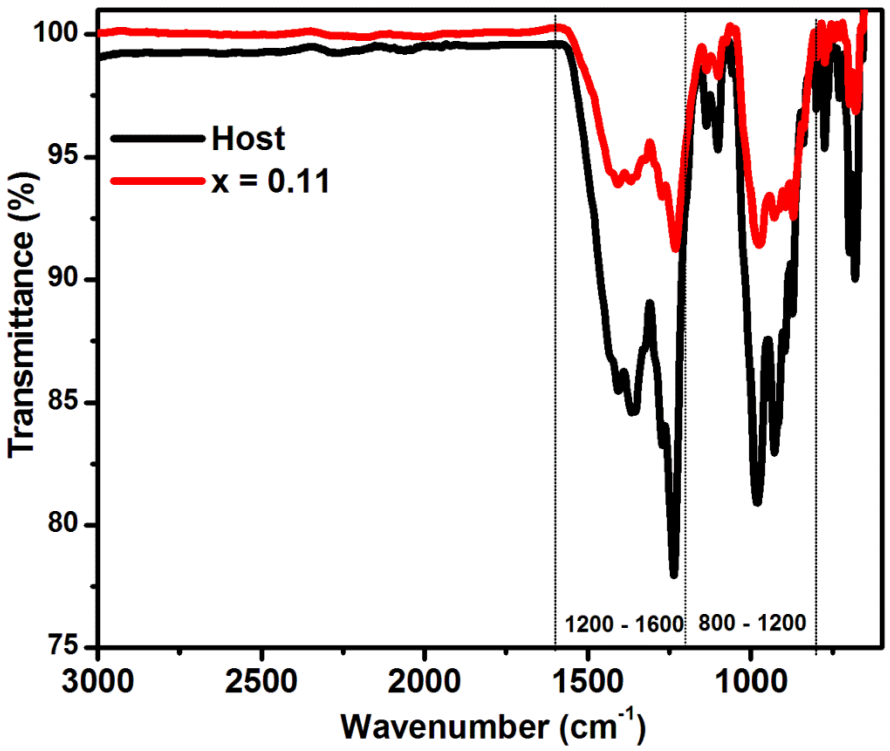

Figure 4.5: FTIR spectra of BaB_8O_{13}: xBi^{3+} (x = 0 and 0.11) powder phosphors.

The thermogravimetric analysis (TGA) curves of BaB_8O_{13} host and BaB_8O_{13}: xBi^{3+} (x = 0.11) powder phosphors are shown in **figure 4.6**. The weight loss before 600 °C was mainly contributed by the release of carbon dioxide (CO_2) and water (H_2O) from the decomposition of the starting materials [25]. It is observed from the spectra that BaB_8O_{13} host undergoes a rapid

weight loss, starting already at ~100 °C as compared to the doped powder phosphor. Li et.al [26], reported that the weight loss below 100 °C and between 100 and 200 °C are due to the removal of physically adsorbed and chemically adsorbed water, respectively .There was a weight loss of 0.7 % and 3.2 %, respectively, at this temperature from the powder phosphors of BaB_8O_{13}: xBi^{3+} (x = 0 and 0.11), respectively.

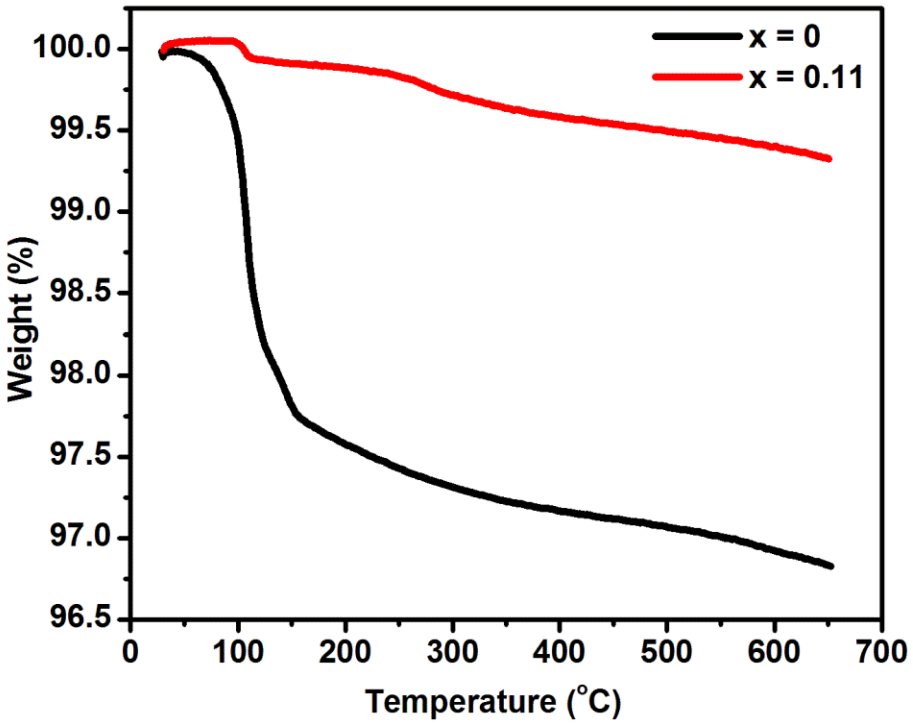

Figure 4.6: TGA spectra of BaB_8O_{13}: xBi^{3+} (x = 0 and 0.11) powder phosphors.

Scanning electron microscope (SEM) was used to investigate microstructures of the samples, such as surface morphology and other properties [27]. The surface morphology of prepared BaB_8O_{13}: xBi^{3+} (x = 0.11) powder phosphor is shown in **figure 4.7 (a)**. From the SEM image it is clear that the powder was made up of a network of irregular particles that are agglomerated together. The surface consists of voids that could have been formed as a result of evolving gaseous species during the combustion process. The endothermic reactions during the solution-combustion process are characterized by decomposition and removal of nitric oxides and vary significantly depending on the precursor ingredients and the ratio of metal nitrate to urea. Therefore pores and voids are attributed to these gases that evolved during combustion [28]. The HRTEM images of BaB_8O_{13}: xBi^{3+} (x = 0.11) are shown in **figure 4.7 (b and c)**. **Figure 4.7 (b)**

shows a cluster of uniformly distributed spherical nanoparticles. The lattice fringes shown in **Figure 4.7 (c)** have an estimated d-spacing of 2.52 Å corresponding to (105) plane. **Figure 4.7 (d)** shows the energy dispersive X-ray spectroscopy (EDS) spectrum of BaB_8O_{13}: $x$$Bi^{3+}$ (x = 0.11) powder phosphor. The EDS spectrum confirms the presence of barium (Ba), boron (B), oxygen (O) and bismuth (Bi) elements. The inset in **figure 4.7 (d)** gives the weight per cent of all the elements detected by the EDS. The concentration of O by weight exceeds that of all the other elements and the least concentration (also by weight) was recorded from Bi^{3+} dopant ions and this is probably due to their relatively low concentration. The surface composition and elemental distribution of BaB_8O_{13}: $x$$Bi^{3+}$ (x = 0.11) powder is shown in **figure 4.7 (a-d)**. The color mapping of the positive ions such as Ba, B and Bi are shown in **figure 4.7 (a, d and c),** respectively, while the negative ion such as O is shown in **figure 4.7 (d)**. The EDS spectrum and the corresponding EDS mapping confirms the formation of BaB_8O_{13}: Bi^{3+} powder phosphors and homogenous distribution of the elements present on the surface of the phosphor.

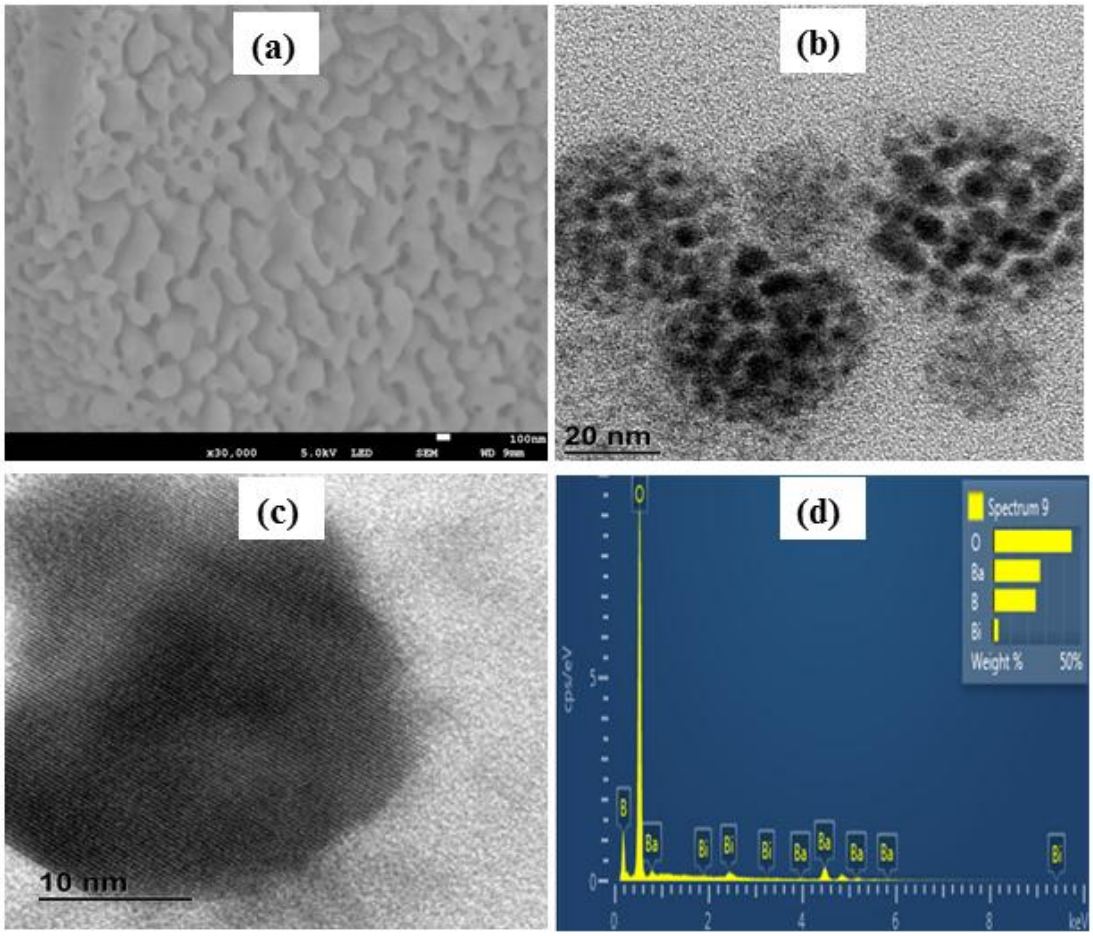

Figure 4.7: a) SEM image, **b-c**) TEM micrographs and **d**) EDS spectrum BaB_8O_{13}: xBi^{3+} (x = 0.11) powder phosphors.

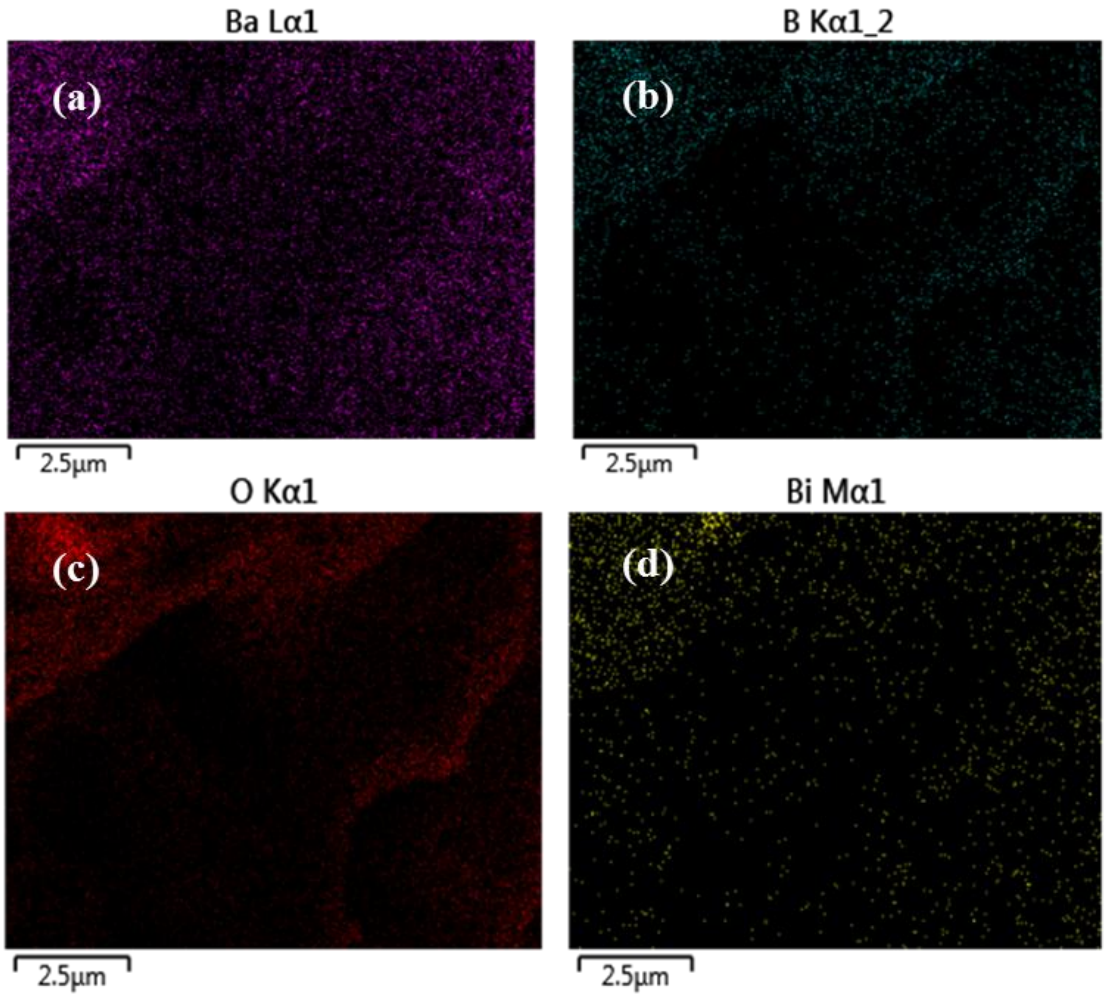

Figure 4.8: **a-d**) EDS elemental mapping of BaB_8O_{13}: xBi^{3+} (x = 0.11) powder phosphor.

4.3.2 Photoluminescence studies

Diffuse reflection spectroscopy was used to study the absorption characteristics of undoped and Bi^{3+}-doped BaB_8O_{13}. **Figure 4.9** shows the diffuse reflectance spectra (DRS) of BaB_8O_{13} host matrix and BaB_8O_{13}: xBi^{3+} (x = 0.11) powder phosphors. The spectrum of the host matrix (**figure 4.9 (a)**) displays three absorption bands in the range of 200 nm – 380 nm, with the absorption edges at ~215 nm, ~291 nm and ~347 nm. The 215 nm (5.77 eV) peak might be due to inter band absorption of the host while the 291 nm (4.26 eV) and 347 nm (3.57 eV) absorptions are assigned to intrinsic defects (e.g vacancies or incidental impurities) in the host [29]. After

incorporating Bi^{3+} into BaB_8O_{13} host matrix, there is an observed change in the diffuse reflectance spectrum due to the strong absorption of the Bi at wavelegth below the approximately 380 nm. The spectrum of BaB_8O_{13}: xBi^{3+} (x = 0.11) displays a broad absorption band in the range of 200 nm – 380 nm, with the absorption edge of ~271 nm (4.58 eV) which is attributed to $^1S_0 - {}^3P_1$ transition of Bi^{3+} ions [30]. The DR spectra for both BaB_8O_{13} host and BaB_8O_{13}: xBi^{3+} (x = 0.11) powder phosphors where used to estimate the band gap by using the Kubelka-Munk absorption coefficient (K/S) relation equation shown below [31, 32]:

$$\frac{K}{S} = \frac{(1-R)^2}{2R} \tag{4.3}$$

where K is the absorption coefficient, S the scattering coefficient and R represent the reflectivity. The band gap energy (absorption edge) of the host was estimated to be 3.43 eV while the band gap energy for BaB_8O_{13}: xBi^{3+} (x = 0.11) was estimated to be 5.01 eV (see **figure 4.10** (**a & b**)). It is observed that the E_g value is less in host powder phosphor when compared to Bi^{3+} doped powder phosphor. Umesh et al [15], reported that the variation in band gap values in host sample with doped samples can be related to the degree of structural order–disorder in the lattice which is able to change the intermediate energy level distribution within the band gap .It is further reported that the E_g values mainly depend on the preparation methods and different experimental conditions. In particular these key factors can favor or inhibit the formation of structural defects, which are able to influence the degree of structural order–disorder of the material and consequently the number of intermediate energy levels within the band gap [15].

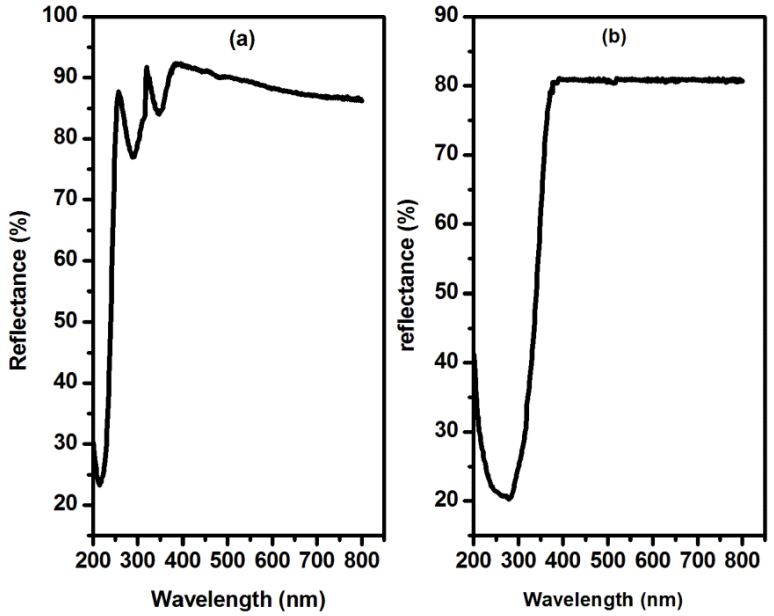

Figure 4.9: Diffuse reflectance spectra (DRS) of **a**) BaB_8O_{13} host and **b**) BaB_8O_{13}: xBi^{3+} (x = 0.11).

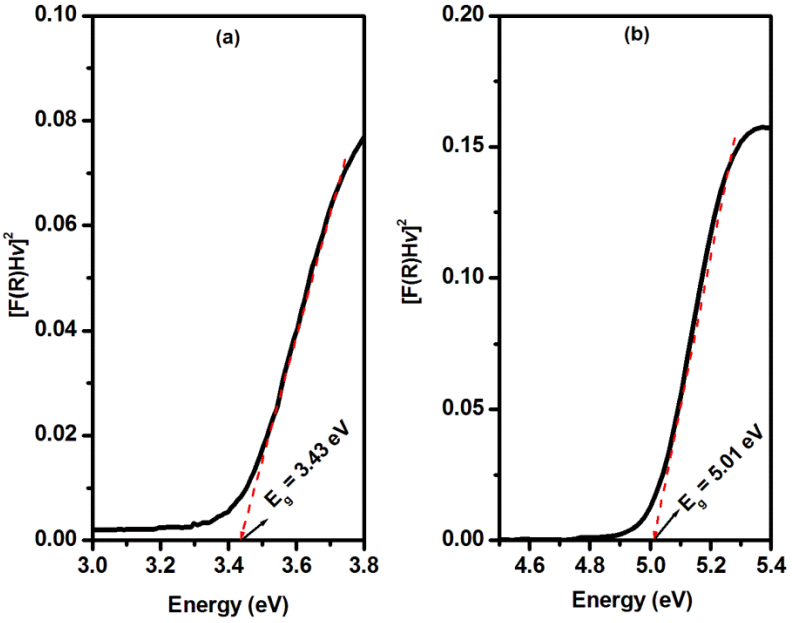

Figure 4.10: Kubelka-Munk absorption spectra of **a**) BaB_8O_{13} host and **b**) BaB_8O_{13}: xBi^{3+} (x = 0.11).

Bi^{3+} is a commonly used sensitizer in photoluminescence (PL) research and it can act as an activator as well [33]. First the luminescence behavior of BaB_8O_{13} host matrix without any dopant was measured. The excitation and emission spectrum of the BaB_8O_{13} host is shown in **figure 4.11 (a)**. The spectrum shows three excitation bands in the wavelength range of 200 – 400 nm with the maxima at 254 nm, 301nm and 370 nm. The spectrum was deconvoluted into three bands located at 253 nm, 289 nm and 371 nm. The peak at 253 nm is attributed to the host exciton creation and the peaks at 289 nm and 371 nm are attributed to intrinsic defects [29].The emission spectrum of the BaB_8O_{13} host matrix was observed at 427 nm with minor emission at 540 nm under the UV excitation of 254 nm as shown in **figure 4.11 (a)**. The spectrum was deconvoluted into three Gaussian peaks located at 413 nm, 447 nm and 521 nm. The blue emissions at 413 nm and 447 nm are possibly due to surface defects such as oxygen vacancies while the green emission at 521 nm might be associated with the intrinsic defect centers such as oxygen vacancies or oxygen interstitials [34]. In this study, the synthesis include organic materials that burn out in a very short time during the annealing process consuming a great amount of oxygen that could have probably led to creation of oxygen vacancies.

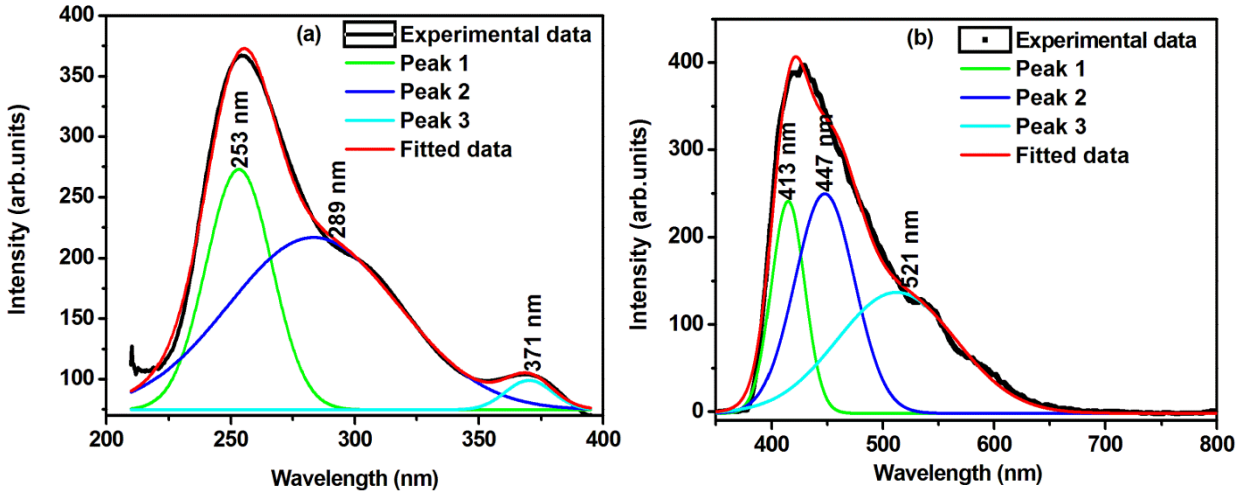

Figure 4.11: Deconvoluted **a)** excitation spectrum (λ_{emi} = 427 nm) and **b**) emission spectrum (λ_{exc} = 254 nm) of BaB_8O_{13} undoped phosphor.

Bi^{3+} possesses $6s^2$ lone pair electrons therefore the position of its excitation and emission bands depends largely on the nature of the host lattice [32]. **Figure 4.12 (a)** presents the photoluminescence excitation (PLE) of BaB_8O_{13}: xBi^{3+} (x = 0.11) powder phosphor. The spectrum consists of a broad excitation band with two peaks at 243 nm and 271 nm. The high energy excitation peak at 243 nm is due to the host lattice absorption while the low energy absorption band at 271 nm is due to the $^1S_0 - {}^3P_1$ transition of Bi^{3+}, which is allowed due to the mixing of the states in the spin orbit interaction [10]. Photoluminescence emission (PL) spectra of BaB_8O_{13}: xBi^{3+} ($0 < x \leq 0.13$) powder phosphors are shown in **figure 4.12(a)**. Upon the 271 nm excitation, a broad emission band with a maximum at 548 nm was observed. This broad band is attributed to the $^3P_1 - {}^1S_0$ transition of Bi^{3+} ions [35]. The PL emission intensity increased with Bi^{3+} concentration up to x = 0.11 mol, then decreased due to concentration quenching effect. This concentration quenching is due to the increase in the ion-ion interaction induced by the shorter distance between interacting activators as the concentration increases [36]. Blue host emission was also observed around 427 nm which is associated with defects in BaB_8O_{13} [34]. **Figure 4.12 (b)** shows the variation of the Bi^{3+} emission intensities at 548 nm with Bi^{3+} concentrations. The maximum PL emission intensity was attained when x = 0.11 mol.

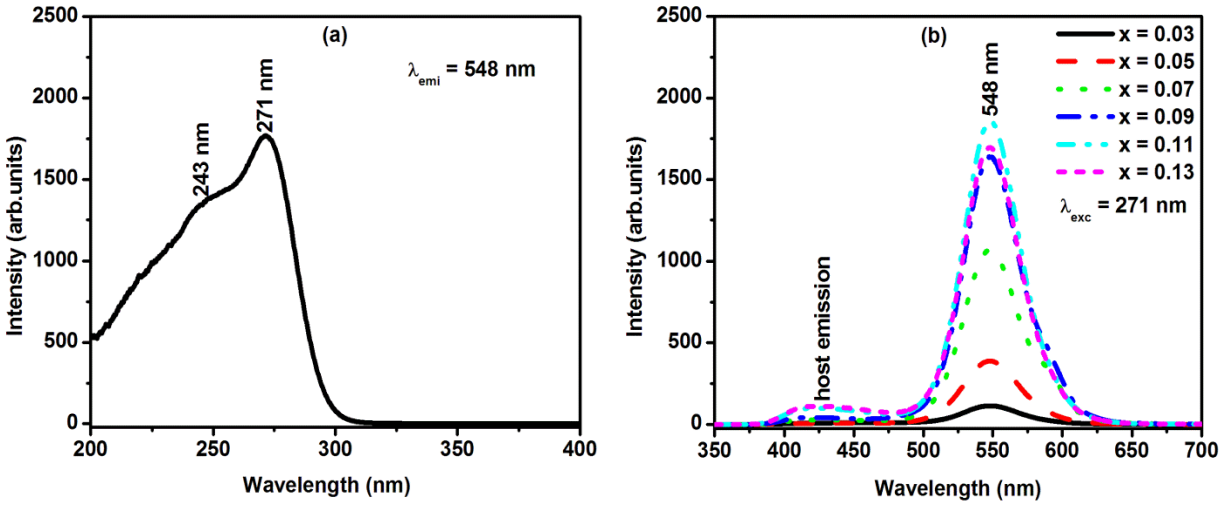

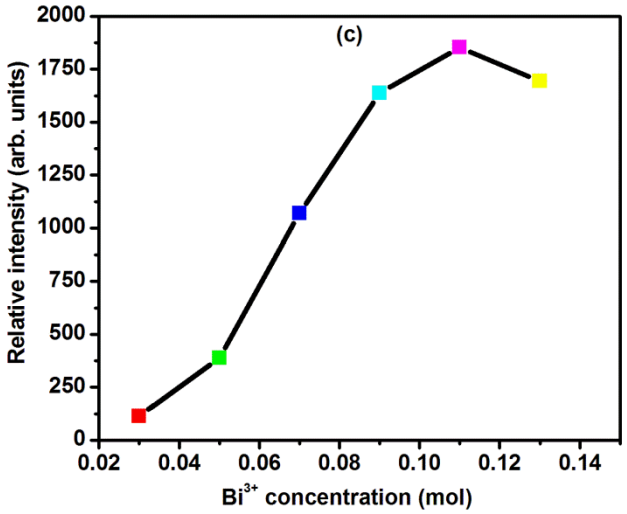

Figure 4.12: a) The PL excitation of BaB_8O_{13}: xBi^{3+} (x = 0.11) **b**) PL emission (λ_{exc} = 271 nm) of BaB_8O_{13}: xBi^{3+} ($0 < x \leq 0.13$) phosphors **c**) the variation of the luminescence intensity with the different concentrations of Bi^{3+}.

Analyzing the luminescence decay curves provides information on the luminescence processes. In order to evaluate the luminescence decay properties of barium octaborate based green emitting phosphor, the decay curves of BaB_8O_{13}: xBi^{3+} ($0 < x \leq 0.13$)) were recorded at room temperature. **Figure 4.13** shows the decay curves of BaB_8O_{13}: xBi^{3+} ($0 < x \leq 0.13$) powder phosphors under the excitation of 271 nm and emission of 548 nm. The decay curves were fitted by the following first order exponential equation [36]:

$$I = A_0 + I_0 \exp\left(\frac{-t}{\tau}\right) \qquad (4.4)$$

where I and I_0 are the luminescent intensities at time t and $t = 0$. A is the constant, t is the time and τ is the life-time. The life-time values of BaB_8O_{13}: xBi^{3+} ($0 < x \leq 0.13$) are presented in **table 4.2**. Consistent with the PL emission data, the decay time was maximum when the concentration of x = 0.11 mol, and then decreased indicating an efficient energy transfer between Bi^{3+} ions and causing concentration quenching [37]. A millisecond order of lifetime values of the powder phosphors reveals the suitability of these materials for use in field emission display and light-emitting diodes applications.

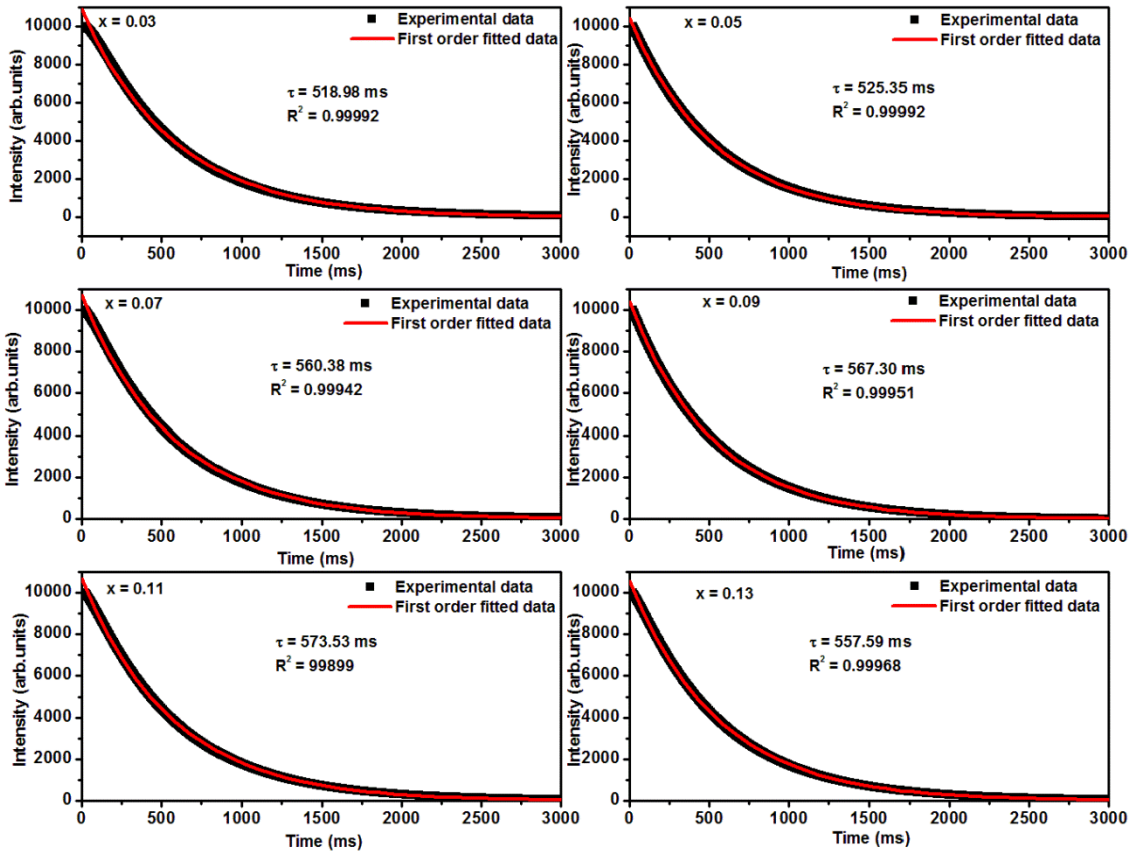

Figure 4.13: The first order fitted decay curves of BaB_8O_{13}: xBi^{3+} ($0 < x \leq 0.13$) powder phosphor.

Figure 4.14 shows the color coordinates for BaB_8O_{13}: xBi^{3+} (x = 0.11) computed by imaging software based on the standard formulations made available by CIE (Commission International de I' Enclairage, France) [38]. The CIE color coordinates for BaB_8O_{13}: xBi^{3+} (x = 0.11) powder phosphor was found to be x = 0.327, y = 0.600, which is green and might be suitable for use in application such as field emission display and light-emitting diodes. The color coordinates for BaB_8O_{13}: xBi^{3+} ($0 \leq x \leq 0.13$) are all listed in **table 4.2**.

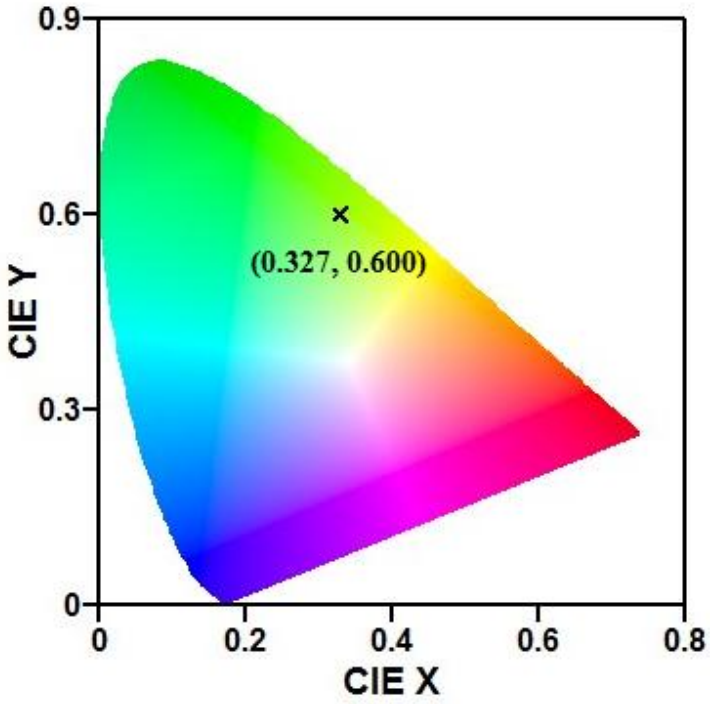

Figure 4.14: CIE chromaticity diagram of BaB_8O_{13}: xBi^{3+} (x = 0.11) phosphor powder.

Table 4.2: Comparison of CIE chromaticity coordinates of BaB_8O_{13}: xBi^{3+} phosphor powders excited at 271 nm.

Sample no:	Powder phosphor (BaB_8O_{13}: xBi^{3+})	Decay times τ (s)	CIE chromaticity coordinates	
			x	y
1	BaB_8O_{13} undoped	-	0.1935	0.2040
2	BaB_8O_{13}: *0.03*Bi^{3+}	0.5190	0.3440	0.6097
3	BaB_8O_{13}: *0.05*Bi^{3+}	0.5254	0.3309	0.6243
4	BaB_8O_{13}: *0.07*Bi^{3+}	0.5604	0.3473	0.6565
5	BaB_8O_{13}: *0.09*Bi^{3+}	0.5673	0.3143	0.5813
6	BaB_8O_{13}: *0.11*Bi^{3+}	0.5735	0.3267	0.6004
7	BaB_8O_{13}: *0.13*Bi^{3+}	0.5576	0.3238	0.5904

4.4 Conclusion

The BaB_8O_{13}: xBi^{3+} ($0 \leq x \leq 0.13$) phosphors were synthesized by simple, time saving and cost effective solution combustion method. From the XRD results, the crystal structure of the prepared powder phosphors was confirmed to be orthorhombic. Their crystallite sizes were calculated by both Scherrer and Williamson-Hall equations. The strain formed in the powders phosphors were also estimated from W-H plots. SEM images showed that the particles are agglomerated and have irregular shapes. The bandgap of the BaB_8O_{13} host matrix was found to be 3.43 eV and was increased after Bi^{3+} doping. Under UV 271 nm excitation, Bi^{3+} doped phosphors showed a broad emission at 548 nm which is attributed to the $^3P_1 - {}^1S_0$ –transition of Bi^{3+} ions. The CIE chromaticity coordinates indicated that the Bi^{3+} doped phosphors exhibit a green color. The results showed that BaB_8O_{13}: Bi^{3+} powder phosphor is a promising candidate for green emission for possible use in displays and light-emitting diodes.

References

[1] A. K. Bedyal, V. Kumar, V. Sharma, S. S. Pitale, E. Coetsee, M. M. Duvenhage, O.M. Ntwaeaborwa and H. C. Swart, *Journal of Material Sciences*, **48** (2013) 3327 - 3333.

[2] B. Wang, C. Chang and W. Yang, *International Journal of Minerals, Metallurgy and Materials*, **20** (2013) 678 - 683.

[3] L. He and Y. Wang, *Journal of Alloys and Compounds*, **454** (2008) 250 - 254.

[4] E, Erdogomus, E. Orkmaz and V.E. Kafadar, *Journal of Applied Spectroscopy*, **80** (2014) 952 - 956.

[5] J. T. Ingle, R. P. Sonekar, P. A. Nagpure and S. K. Omanwar, *Journal of Current Research*, **5** (2013) 529 - 531.

[6] R. P. Sonekar, S. K. Omanwar and S. V. Moharil, *Indian Journal of Pure and Applied Physics*, **47** (2009) 441 - 443.

[7] H. Ling, W. Yuhua and S. Weimin, *Journal of Rare Earths*, **27** (2009) 385 - 389.

[8] S. Zhang, Y. Hu, R. Chen. X. Wang and Z. Wang, *Optical Materials*, **36** (2014) 1830 - 1835.

[9] H. Ju, J. Liu, B. Wang, X. Tao, Y. Ma and S. Xu, *Ceramics International*, **39** (2013) 857 - 860.

[10] H. Ju, W. Deng, B. Wang, J. Liu, X. Tao and S. Xu, *Journal of Alloys and compounds*, **516** (2012) 153 - 156.

[11] C. Kim, C. Pyun, H. Choi ans S. Kim, *Bulletin of the Korean Chemical Society*, **20** (1999) 337 – 340.

[12] L. Wang, H. Guo, Y. Wei, H. M. Noh and J. H. Jeong, *Optical Materials*, **42** (2015) 233 - 236.

[13] W. A. I. Tabaza, H. C. Swart and R. E. Kroon, *Journal of Luminescence*, **148** (2014) 192 - 197.

[14] H. Zu, Z. Xia, H. Liu, R. Mi and Z. Hui, *Materials Research Bulletin*, **48** (2013) 3513 - 3517.

[15] B. Umesh, B. Eraiah, H. Nagabhushana, S. C. Sharma, D. V. Sunitha, B. M. Nagabhushana, C. Shivakumara, J. L. Rao, R. P. S. Chakradhar, *Spectrochimica Acta Part A*, **93** (2012) 228 - 234.

[16] D. Haiyen, L. Gengshen and S. Jaiyue, *Journal of Rare Earths*, **25** (2007) 19 - 22.

[17] H. M. Chenari, H. F. Moafi and O. Rezaee, *Material Research*, **19** (2016) 548 - 554.

[18] S. Thakur and A. K. Gathania, *Indian Journal of Physics*, **89** (2015) 973 - 979.

[19] G. Tiwari, N. Brahme, R. Sharma, D. P. Bisen, S. K. Sao and U. K. Kurrey, *Journal of Materials Science: Materials in Electronics*,, **27** (2016) 6399 - 6407.

[20] S. Som, S. K. Sharma and T. Shripathi, *Journal of Fluorescence*, **23** (2013) 439 - 450.

[21] A. K. Zak, W. H. A. Mjid, M. E. Abrishami and R. Yousefi, *Solid State Sciences*, **13** (2011) 251 - 256.

[22] I. Ahemen, A. N. Amah, B.E. AttahDaniel, A.Y. Fasasi, *Nanoscience and Nanotechnology*, **4** (2014) 7 - 15.

[23] O. Annalakshmi, M. T. Jose, U. Madhusoodanan, J. Sridevi, B. Venkatraman, G. Amarendra and A. B. Mandal, *Radiation Effects and Defects in Solids*, **169** (2014) 636 - 645.

[24] R. Li, L. Bao and X. Li, *Royal Society of Chemistry*, **13** (2011) 5858 - 5862.

[25] W. Liu, C. Huang, C. Wu, Y. Chiu, Y. Yeh and T. Chen, *Journal of Material Chemistry*, **21** (2011) 6869 - 6874.

[26] Y. Li, N. Sun, L. Li, N. Zhao, F. Xiao, W. Wei, Y. Sun and W. Huang, *Materials*, **6** (2016) 981 - 999.

[27] R. Huang, S. Li, S. Xue, Z. Jiang and S. Wu, *International Conference on Future Environment and Energy*, **28** (2012) 85 - 89.

[28] A. H. Wako, F. B. Dejene and H.C. Swart, *Journal of Rare Earths*, **32** (2014) 806 - 811.

[29] P. P. Mokoena, I. M. Nagpure, V. Kumar, R. E. Kroon, E. J. Olivier, J. H, Neethling, H. C. Swart and O. M. Ntwaeaborwa, *Journal of Physics and Chemistry of Solids*, **75** (2014) 998 - 1003.

[30] Z. Yang, J. Liao, T. Wang, H. Wu, J. Qiu, Z. Song, and D. Zhou, *Materials Express*, **4** (2014) 172 - 176.

[31] H. Yu, D. Deng, Y. Hua, C. Li and S. Xu, *Royal Society of Chemistry*, **6** (2016) 82824 - 82831.

[32] P. Gupta, A. K. Bedyal, V. Kumar, Y. Khajuria, V. Sharma, O. M. Ntwaeaborwa and H. C. Swart, *Materials Research Express*, **2** (2015) 076202.

[33] Q. Li, R. Cong, X. Zhou, W. Gao and T. Yang, *Journal of Materials Chemistry C*, **3** (2015) 6836 - 6843.

[34] V. H. Romero, E. De la Rosa, P. Salas, J. J. Velazquez-Salazar, *Journal of Solid State Chemistry*, **196** (2012) 243 - 248.

[35] B. N. Mahalley, S. J. Dhoble, R. B. Pode and G. Alexander, *Applied Physics A*, **70** (2000) 39 - 45.

[36] R. K. Tamrakar, D. P. Bisen and K. Upadhyay, *Journal of Radiation Research and Applied Sciences*, **8** (2015) 11 - 16.

[37] Z. Wang, J. Zhong, H. Liang and J. Wang, *Optical Materials Express*, **3** (2013) 418 – 425

[38] Y. Liu, B. Lei and C. Shi, *Chemistry of Materials*, **17** (2005) 2108 - 2113.

Chapter 5

Study on photoluminescence and energy transfer in Eu^{3+}-Sm^{3+} co-doped BaB_8O_{13} phosphors

5.1 Introduction

Recently, great interest in phosphors has resulted in rapid developments in display and illumination technologies. For general lighting, photoluminescent (PL) materials include oxides, silicates, aluminates, alumino silicates, nitrides, borates, etc. [1]. Among these hosts, borates are good candidates as host lattices due to their low synthetic temperature, ease of preparation and high luminescent brightness [2], among other things. Inorganic borate host compounds have long been a focus of research due to different crystal structures transparency to a wide range of wavelengths (extending from UV to the visible region of the electromagnetic wave spectrum), and high thermal and chemical stability, which makes them attractive for numerous practical applications [3]. In addition, barium octaborate (BaB_8O_{13}) is an excellent host material for luminescent ions. Its structure consists of two separate interlocking three-dimensional infinite networks as triborate and pentaborate groups, which form BO_3 triangle and BO_4 tetrahedral units [4].

Many rare earth ions are excellent centres of luminescence in many inorganic hosts including borates due to their special 4*f* intra-shell transitions [5]. Rare-earth ions such as europium (Eu^{3+}), erbium (Er^{3+}), terbium (Tm^{3+}) and samarium (Sm^{3+}) are well known luminescent activators in various host lattices due to their abundant energy levels in a wide range of wavelengths [6]. In particular, Eu^{3+} is widely used as the luminescent activator in a considerable number of inorganic

hosts serving as a source of red light for trichromatic fluorescence materials [7]. It has been recognized as an excellent activator in many red light emitting phosphors (light emitting materials) with its emission emanating from the $^5D_0 \rightarrow {}^7F_{J\ (J = 0, 1, 2, 3, 4)}$ transitions [8]. Eu^{3+} doped into different hosts often shows high fluorescence efficiency and its hypersensitive transition of $^5D_0 \rightarrow {}^7F_2$ is in the red part of the spectrum [6]. Sm^{3+} ion is also a well-known activator for many different inorganic lattices producing visible emission associated with its $^4G_{5/2} \rightarrow {}^6H_J$ (J = 5/2, 7/2, 9/2, 11/2) transitions [9]. The Sm^{3+} ($4f^5$) ion presents efficient emission in visible and near-infrared since its $^4G_{5/2}$ level shows different radiative emission channels [10]. The Sm^{3+} ions exhibit strong line absorption that belongs to $^6H_{5/2} \rightarrow {}^4K_{11/2}$ transition at about ~405 nm in many host lattices [11].

Co-doping can modify crystal structure, particle morphology, and the fluorescent properties of phosphor materials. Some co-dopants with small content are propitious to a high luminescent efficiency, which has been reported by many researchers [12]. In order to enhance the red emission intensity of Eu^{3+}, transition metal ions or rare earth ions, such as Sm^{3+}, are co-doped usually as sensitizers [13]. It has been reported that the energy mismatch between the $^4G_{5/2}$ level of Sm^{3+} and the $^5D_0$ level of Eu^{3+} is small, thus it is possible for the phonon-assisted energy transfer from Sm^{3+} to Eu^{3+} to take place [14]. Thus Eu^{3+}-Sm^{3+} co-doped phosphors have become a hot research topic in recent years in order to obtain the efficiently near-UV excited phosphors for white LEDs [15].

In the current study, Eu^{3+}/ Sm^{3+} single-doped and co-doped BaB_8O_{13} (BBO) phosphor samples were synthesized by a straightforward, cost-effective and time-saving solution combustion method. Photoluminescence (PL) properties and energy transfer mechanism were investigated. The results indicate that co-doping Sm^{3+} can effectively enhance the emission intensity of BaB_8O_{13}: Eu^{3+} and broaden the absorption band in the near-UV region.

5.2 Experimental

5.2.1 Preparations

Solution combustion method was employed to synthesize powder samples of BaB_8O_{13}: $x$$Eu^{3+}$ ($0.005 \leq x \leq 0.05$) singly doped, BaB_8O_{13}: $y$$Sm^{3+}$ ($0.005 \leq y \leq 0.04$) singly doped and BaB_8O_{13}: $0.05$$Eu^{3+}$; ySm ($0.005 \leq y \leq 0.07$) co-doped. All chemicals were used as received without further purification. The following precursors barium nitrate [$Ba(NO_3)_2$], boric acid [H_3BO_3], europium nitrate [$Eu(NO_3)_3.xH_2O$], samarium nitrate [$Sm(NO_3)_3.6H_2O$], ammonium nitrate [NH_4NO_3] and urea [NH_2CONH_2]. In this experiment, NH_4NO_3 was used as an oxidizer and NH_2CONH_2 was used as a fuel. In preparations of BaB_8O_{13}: $0.005$$Eu^{3+}$ and BaB_8O_{13}: $0.005$$Sm^{3+}$ powder phosphors, 0.9950 g of $Ba(NO_3)_2$, 1.8930 g of H_3BO_3, 0.3830 g of NH_2CONH_2 and 0.5107 g of NH_4NO_3 were used, together with 0.0065 g of $Eu(NO_3)_3.xH_2O$ and 0.0085 g of $Sm(NO_3)_3.6H_2O$. For the preparations of powder phosphors with different concentrations (x *and* y) increases, the masses of $Eu(NO_3)_3.xH_2O$ and $Sm(NO_3)_3.6H_2O$ used increases as the mass of $Ba(NO_3)_2$ decreases. For preparing BaB_8O_{13}: $0.05$$Eu^{3+}$; 0.005Sm powder phosphors, The same quantity of H_3BO_3, NH_2CONH_2 and NH_4NO_3 as above were used together with 0.0647 g of $Eu(NO_3)_3.xH_2O$. The masses of $Ba(NO_3)_2$ and $Sm(NO_3)_3.6H_2O$ were varying from 0.9450 to 0.8800 g and from 0.0081 to 0.1126 g, respectively. The schematic diagram in **figure 5.1** shows how the powder phosphors were prepared via solution combustion method.

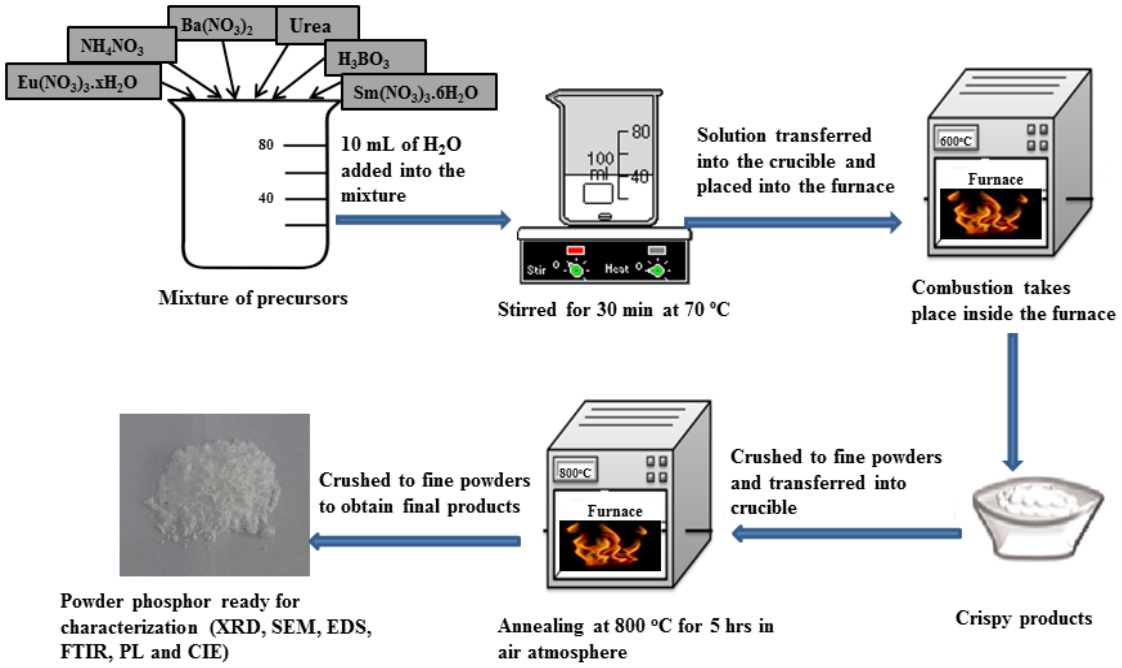

Figure 5.1: A schematic diagram illustrating the solution combustion synthesis procedure of BaB_8O_{13}: xEu^{3+} ($0.005 \leq x \leq 0.05$), BaB_8O_{13}: ySm^{3+} ($0.005 \leq y \leq 0.04$) and BaB_8O_{13}: 0.05Eu^{3+}; ySm ($0.005 \leq y \leq 0.07$) powder phosphors.

5.2.2 Characterizations

The structure of the powders was analyzed using a Bruker D8 Advanced X−ray diffractometer (XRD) equipped with monochromatic *CuKα* radiation. Fourier transform infrared (FTIR) analysis was performed using a Perkin Elmer Spectrum 100 FTIR spectrometer. Morphology and chemical composition were analyzed using Jeol JSM 7800F thermal field emission scanning electron microscope (FE-SEM) and the chemical composition analysis was carried out using an Oxford Instruments AzTEC energy dispersive spectrometer (EDS) attached to the FE-SEM. Room temperature photoluminescence (PL emission and PL excitation) spectra were recorded by Hitachi F-7000 fluorescence spectrophotometer using a monochromatized xenon lamp as an excitation source.

5.3 Results and discussion

5.3.1 Structural and Morphology

The X-ray diffraction (XRD) patterns of the BaB_8O_{13} host, BaB_8O_{13}: *0.05*Eu^{3+}, BaB_8O_{13}: *0.005*Sm^{3+} and BaB_8O_{13}: *0.05*Eu^{3+}, *0.03*Sm^{3+} powder phosphors are shown in **figure 5.2**. The intense XRD diffraction peaks were indexed to the orthorhombic structure of BaB_8O_{13} according to the JCPDS file no: 20-0097 [16]. The observed additional peaks in the XRD patterns marked with asterisks (*) are attributed to unreacted precursors during the combustion reaction [17]. The main diffraction peaks of the XRD patterns show broader peaks and a slight shift to lower values of 2θ. The diffraction peak shift might be caused by the lattice strain or lattice defects present in the powder phosphor [18]. Scherrer's equation was used to estimate the average crystallite sizes of BaB_8O_{13}: *0.05*Eu^{3+}, BaB_8O_{13}: *0.005*Sm^{3+} and BaB_8O_{13}: *0.05*Eu^{3+}, *0.03*Sm^{3+} powder phosphors [19] using equation 5.1:

$$D = \frac{0.9\lambda}{\beta \cos\theta} \tag{5.1}$$

where β represent full width at half maximum (FWHM) of the XRD lines in radians, λ is the wavelength of the X-rays (0.154 nm) and θ is the Braggs angle of the XRD peak. The estimated crystallite size values are presented in **table 5.1**.

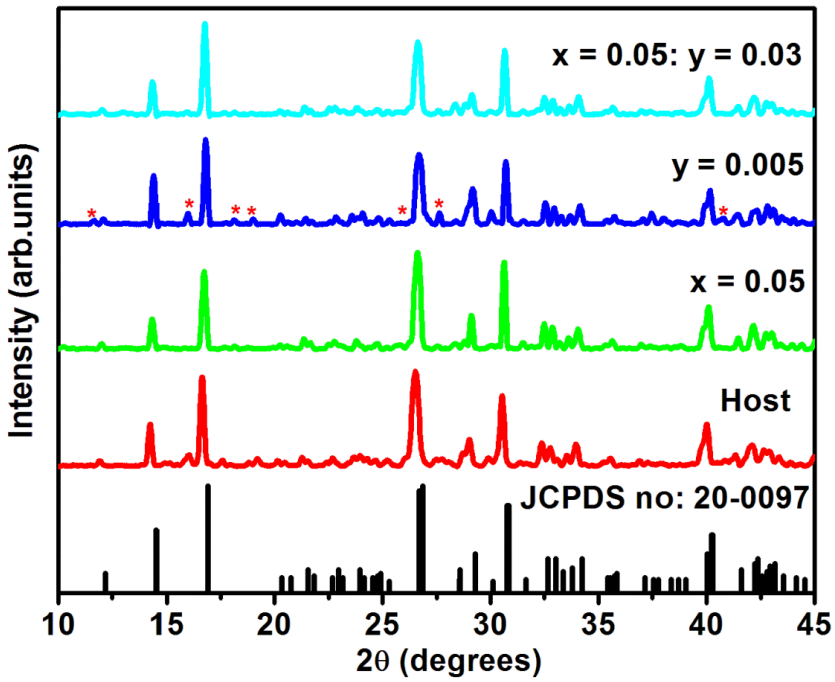

Figure 5.2: XRD patterns of BaB_8O_{13}: *0.05*Eu^{3+}, BaB_8O_{13}: *0.005*Sm^{3+} and BaB_8O_{13}: *0.05*Eu^{3+}, *0.03*Sm^{3+} powder phosphors, together with the JCDPS card file.

The crystallite size of the powder phosphors were also calculated using analysis described by Williamson and Hall (W–H) method using equation 5.2 [20]:

$$\beta_{hkl}\cos\theta = \left(\frac{K\lambda}{D}\right) + 4\varepsilon\sin\theta \qquad (5.2)$$

This equation stands for Uniform Deformation Model (UDM), where it is assumed that strain is uniform in all crystallographic directions [20]. From the above equation, D is the crystallite size in nanometers, λ is the wavelength of X-rays (0.154 nm), K is the shape factor, θ the peak position measured in degrees (º) and β is the full width at half maximum intensity (radians) [21]. The crystallite size from the Williamson-Hall equation was determined from the reciprocal of the intercept of its straight line plot and the microstrain (ε) present in the powder phosphor was calculated from the slope of the equation [22]. The Williamson-Hall plots shown in **figure 5.3** are of BaB_8O_{13}: *0.05*Eu^{3+}, BaB_8O_{13}: *0.005*Sm^{3+} and BaB_8O_{13}: *0.05*Eu^{3+}, *0.03*Sm^{3+} powder phosphors and their estimated strain and the average crystallite size values are presented in **table**

5.1. The crystallite size values calculated from W-H equation are larger than those calculated from Scherer's equation. Ahemen et.al [23], reported that the larger crystallite sizes obtained using W-H plots are more accurate because Scherer's equation does not take into consideration the effect of lattice strain in the line broadening.

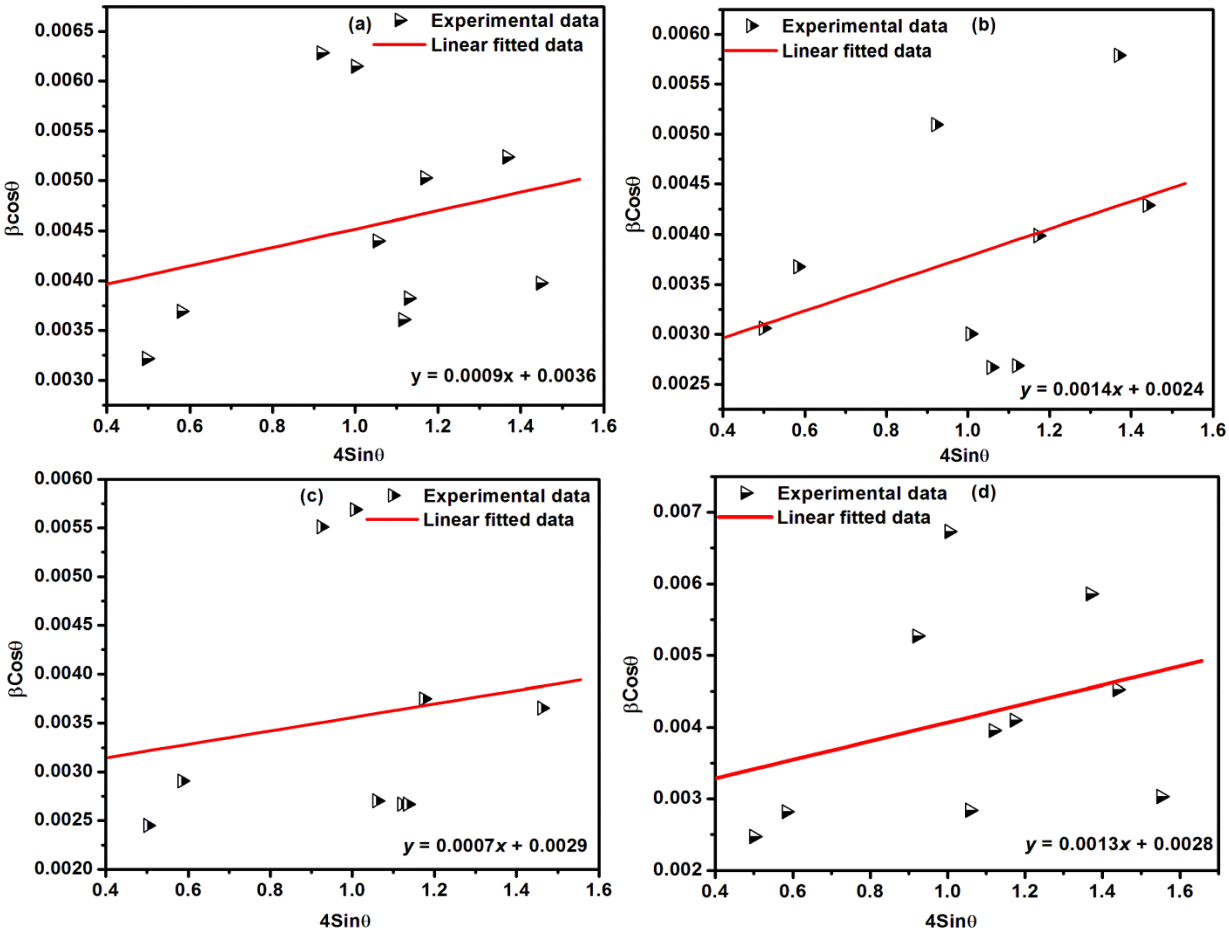

Figure 5.3: Williamson-Hall plot of a) Host, b) BaB_8O_{13}: *0.05*Eu^{3+}, c) BaB_8O_{13}: *0.005*Sm^{3+} and d) BaB_8O_{13}: *0.05*Eu^{3+}, *0.03*Sm^{3+} powder phosphors.

Table 5.1: Structural parameters of Host, BaB_8O_{13}: *0.05*Eu^{3+}, BaB_8O_{13}: *0.005*Sm^{3+} and BaB_8O_{13}: *0.05*Eu^{3+}, *0.03*Sm^{3+} powder phosphors together with the theoretical values.

	Crystallite size *D* (nm)		Lattice constants (Å)			Microstrain ($\times10^{-4}$)	Cell volume (Å^3)
Sample name	Scherer's	W-H	a	b	c	ε	v
JCDPS card	-	-	8.55	17.35	13.21	-	1959.98
Host	32	39	8.58	17.55	13.57	9.0	2043.36
BaB_8O_{13}: *0.05*Eu^{3+}	23-52	57	8.57	17.46	13.50	1.4	2020.03
BaB_8O_{13}: *0.005*Sm^{3+}	24-57	47	8.52	17.44	13.44	0.7	1997.03
BaB_8O_{13}: *0.05*Eu^{3+}, *0.03*Sm^{3+}	21-56	49	8.56	17.46	13.49	1.3	2027.73

Figure 5.4 shows the Fourier Transform Infra-red (FTIR) spectra of Host, BaB_8O_{13}: *0.05*Eu^{3+}, BaB_8O_{13}: *0.005*Sm^{3+} and BaB_8O_{13}: *0.05*Eu^{3+}, *0.03*Sm^{3+} powder phosphors. The spectra exhibit broad absorptions in the 650 - 1600 cm^{-1} range. All the bands in the 1200 - 1600 cm^{-1} range correspond to the stretching of the B–O bonds of BO_3 units while the bands in the region of 800 - 1200 cm^{-1} correspond to the B–O bond stretching of tetrahedral BO_4 units. All the bands below 800 cm^{-1} correspond to the B–O–B bending vibrations of borate networks [24]. Comparing the FTIR spectra of BaB_8O_{13} host, BaB_8O_{13}: *0.05*Eu^{3+}, BaB_8O_{13}: *0.005*Sm^{3+} and BaB_8O_{13}: *0.05*Eu^{3+}, *0.03*Sm^{3+} powder phosphors, it was observed that there is no change in the spectrum structure, and only slight difference in the peak intensities was observed. The transmission of Eu^{3+}/Sm^{3+} co-doped powder phosphors was observed to be higher than that of Eu^{3+} singly doped, followed by Sm^{3+} singly doped and the lowest was observed from the host matrix. In the case of doping different concentrations of rare ions into BaB_8O_{13} host matrix, there was an increase in transmittance. From the FTIR spectra, it can be concluded that incorporating Eu^{3+} and Sm^{3+} ions in the BaB_8O_{13} host matrix did not influence the main structure or form any new types of bonds.

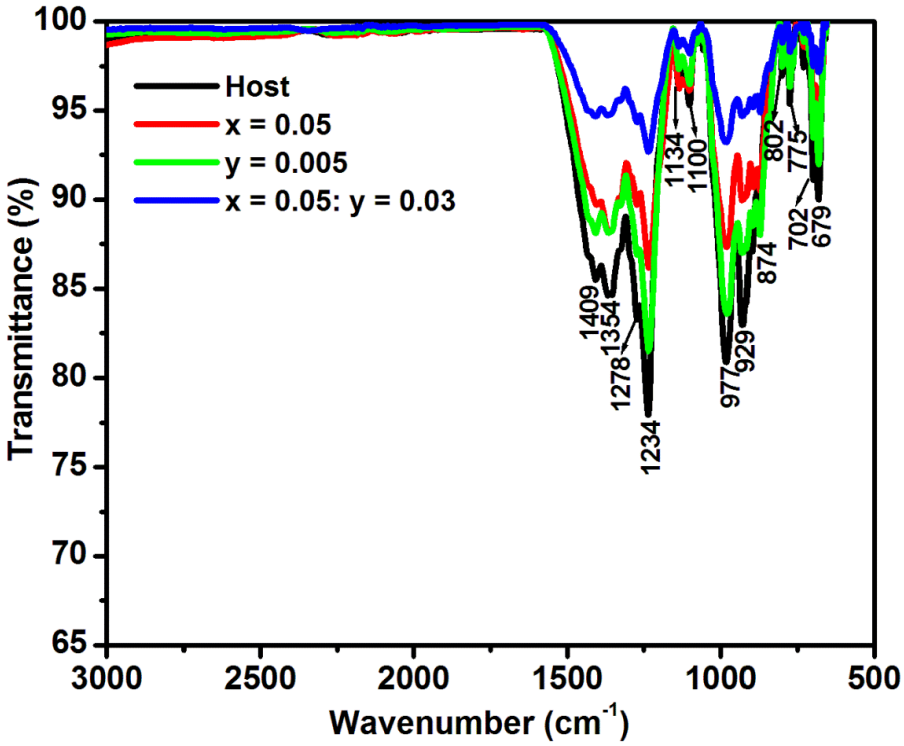

Figure 5.4: FTIR spectra of Host, BaB_8O_{13}: *0.05*Eu^{3+}, BaB_8O_{13}: *0.005*Sm^{3+} and BaB_8O_{13}: *0.05*Eu^{3+}, *0.03*Sm^{3+} powder phosphors.

Particle morphology of BaB_8O_{13}: *0.05*Eu^{3+}, *0.03*Sm^{3+} powder phosphors is shown in **figure 5.5 (a)**. The Scanning electron microscopy (SEM) image shows that the powder is made of a network of agglomerated irregular particles. The surface consists of voids due to the large gaseous matter that escaped due to high exothermicity during the combustion process [25]. Dispersive X-ray spectroscopy (EDS) spectrum of BaB_8O_{13}: *0.05*Eu^{3+}, *0.03*Sm^{3+} powder phosphor is shown in **figure 5.5 (b)**. The spectrum confirms the presence of barium (Ba), boron (B), oxygen (O), europium (Eu) and samarium (Sm) elements. The inset in **figure 5.5 (b)** shows that the concentration of O by weight exceeds that of all other elements and the least concentration (also by weight) was recorded from Eu and Sm dopant ions and this is probably due to their relatively low concentrations.

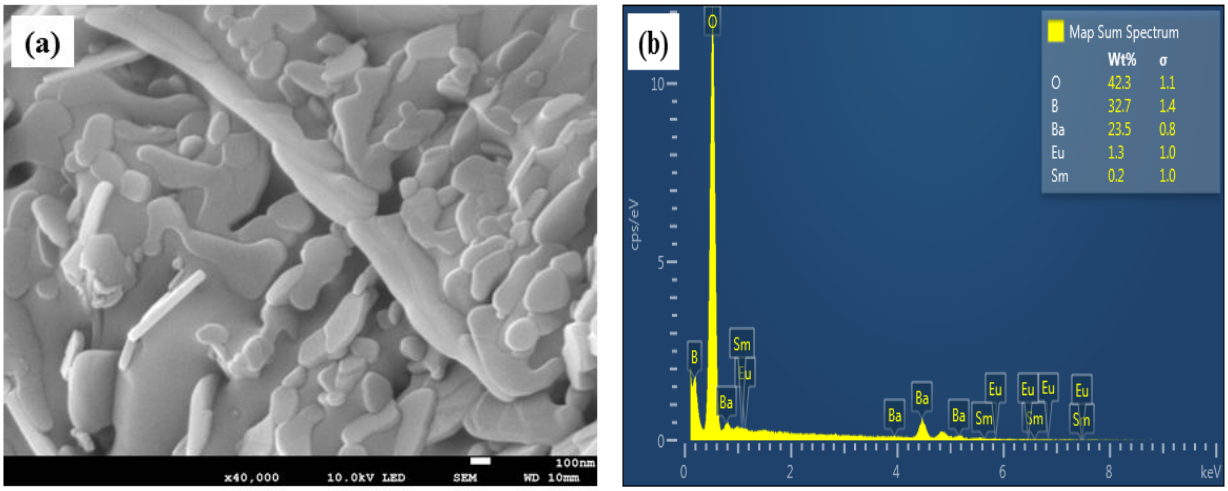

Figure 5.5: a) SEM and **b**) EDS spectrum of BaB_8O_{13}: $0.05Eu^{3+}$, $0.03Sm^{3+}$ powder phosphor.

5.3.2 Photoluminescence studies

Figure 5.6 shows the photoluminescence excitation (PLE) and emission spectra (PL) of BaB_8O_{13}: Eu^{3+} phosphor. In **figure 5.6 (a)**, the excitation spectrum consists of a broadband ranging from 200 to 300 nm with the maximum at 231 nm. The excitation peak at 231 nm is due to the charge transfer band (CTB) of $Eu^{3+} \rightarrow O^{2-}$ and less intense peaks at 317 nm, 360 nm, 379 nm and 394 nm are due to $^7F_0 \rightarrow {}^5H_3$, $^7F_0 \rightarrow {}^5D_4$, $^7F_0 \rightarrow {}^5L_7$ and $^7F_0 \rightarrow {}^5L_6$ transition lines of Eu^{3+} ion, respectively [25]. The emission spectrum monitored at 231 nm and 394 nm consist of a series of sharp bands at 589 nm ($^5D_0 \rightarrow {}^7F_1$), 614nm ($^5D_0 \rightarrow {}^7F_2$), 652 nm ($^5D_0 \rightarrow {}^7F_3$) and 698 nm ($^5D_0 \rightarrow {}^7F_4$) [26]. An et.al [27] reported that for the usual Eu^{3+}-doped phosphors the intensity of charge transfer band is much more intense than that of the f-f transitions in the excitation spectrum, thus the Eu^{3+} emission peak intensity at 614 nm excited at 231 nm is much higher than that excited at 394 nm. In order to have the optimal concentration of Eu^{3+}, a series of BaB_8O_{13}: xEu^{3+} (x = 0.005, 0.01, 0.02, 0.03, 0.04 and 0.05) phosphor powders were synthesized and their PL emission spectra are shown in **figure 5.6 (b)**. The spectra were recorded when monitoring excitation at 394 nm, which corresponds to the $^7F_0 \rightarrow {}^5L_6$ transition of Eu^{3+} ion [25]. The spectra show the same behavior with different doping concentration of Eu^{3+} and the highest PL intensity was observed from BaB_8O_{13}: $0.05Eu^{3+}$ powder phosphor. The inset in **figure 5.6 (b)** shows the excitation and emission spectra of BaB_8O_{13} host matrix. The excitation spectrum of BaB_8O_{13}

host matrix shows three excitation bands in the wavelength range of 200 – 400 nm with the maxima at 254 nm, 301nm and 370 nm. The peak at 254 nm is attributed to the host exciton creation and the peaks at 301 nm and 370 nm are attributed to intrinsic defects [28]. The emission of BaB_8O_{13} host matrix is observed at 427 nm with a small peak emission at 540 nm under the UV excitation of 254 nm. The emission at 427 nm might be due to surface defects such as oxygen vacancies while the green emission at 540 nm might be associated with the intrinsic defect centers such as oxygen vacancies or oxygen interstitials [29].

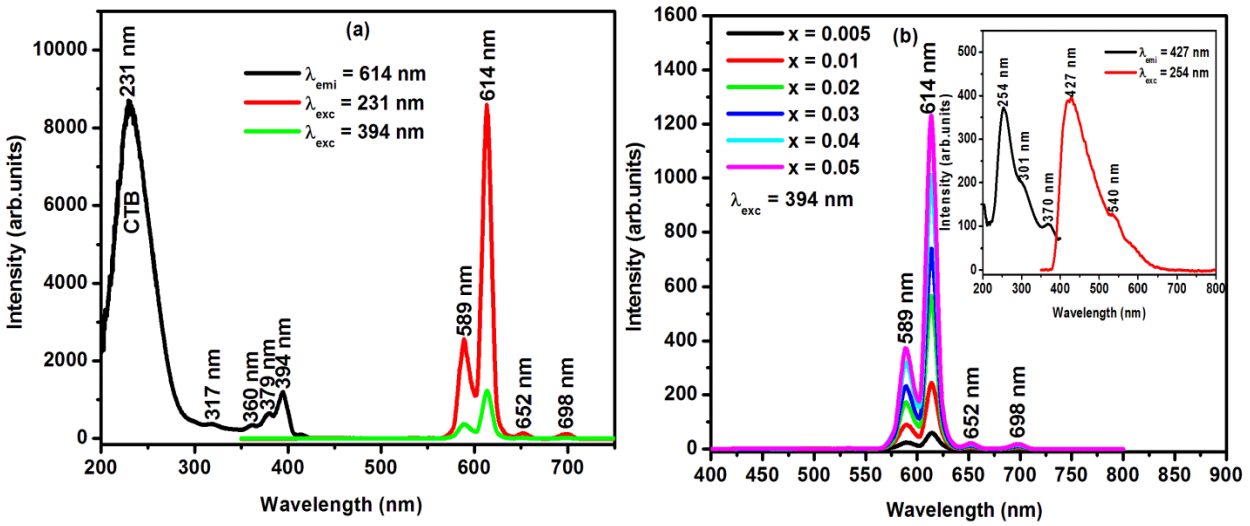

Figure 5.6: a) Excitation spectrum and Emission spectra of BaB_8O_{13}: *0.05*Eu^{3+}, **b)** Emission spectra of BaB_8O_{13}: *x*Eu^{3+} with different concentration of Eu^{3+} with excitation and emission spectra of BaB_8O_{13} as an inset.

Figure 5.7 shows the photoluminescence excitation (PLE) and emission spectra (PL) of BaB_8O_{13}: *0.005*Sm^{3+} phosphor powders. In **figure 5.7 (a)**, the excitation spectrum of BaB_8O_{13}: *0.005*Sm^{3+} was recorded in the wavelength range of 200–450 nm measured by monitoring emission at 596 nm. The spectrum consists of a broadband ranging from 200 to 300 nm due to the charge transfer band (CTB) of $Sm^{3+} \rightarrow O^{2-}$ and less intense 4f–4f transitions of Sm^{3+} at 339 nm, 368 nm and 402 nm [30]. It is observed that the intensity of excitation peak at 237 nm (CTB) is much stronger than that of the 4f–4f transitions, indicating a very efficient energy transfer from hosts to Sm^{3+} ions [31]. **Figure 5.7 (b)** shows the PL emission spectra of BaB_8O_{13}: *0.005*Sm^{3+} powder phosphor excited at 237 nm and 402 nm. The spectra shows three emission peaks in the visible region near 560 nm, 596 nm, and 641 nm, which are assigned to the intra-4f-

shell transitions from the excited level $^4G_{5/2}$ to ground levels $^6H_{5/2}$, $^6H_{7/2}$, $^6H_{9/2}$, of Sm^{3+} respectively [32]. For two different excitation wavelengths, the highest PL intensity was observed when exciting at 237 nm. The PL emission spectra of all the powder phosphors of BaB_8O_{13}: $x$$Sm^{3+}$ (x = 0.005, 0.01, 0.02, 0.03 and 0.04) are shown in **figure 5.7 (b)**. The highest PL intensity was observed from BaB_8O_{13}: *0.005*Sm^{3+} which is the lowest used concentration of Sm^{3+} and the intensity decreases with an increase in Sm^{3+} concentration due to concentration quenching.

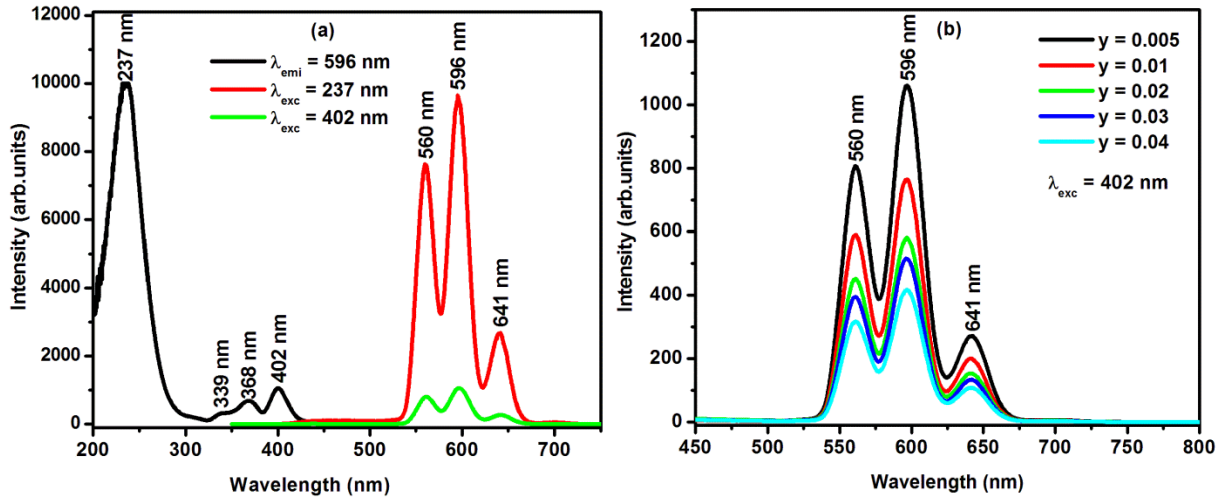

Figure 5.7: Excitation spectrum and Emission spectra of **a)** BaB_8O_{13}: *0.005*Sm^{3+}, **b)** Emission spectra of BaB_8O_{13}: $y$$Sm^{3+}$ with different concentration of Sm^{3+}.

In order to study the energy transfer between Sm^{3+} and Eu^{3+} co-doped BaB_8O_{13} powder phosphors, the concentration of Eu^{3+} was fixed at 5 mol% and that of Sm^{3+} was varied from 0 to 7 mol%. **Figure 5.8** shows the comparison between the excitation spectra of BaB_8O_{13}: 0.05Eu^{3+} and BaB_8O_{13}: *0.05*Eu^{3+}; *0.005*Sm^{3+} powder phosphors measured when monitoring Eu^{3+} emission at 614 nm. The characteristic peaks of Eu^{3+} show a slight shift to the right in the co-doped sample. The excitation spectral shape of Eu^{3+}/ Sm^{3+} co-doped phosphor powder is also widened and enhanced compared to that of Eu^{3+} singly doped powder phosphor. This change should be attributed to $^6H_{5/2} \rightarrow {}^4F_{7/2}$ transition of Sm^{3+} overlapping the $^7F_0 \rightarrow {}^5L_6$ transition of Eu^{3+}. The calculated FWHM values for the Eu^{3+} doped powder phosphor for 394 nm peak was observed to broaden from 13.52 to 16.72 nm accompanied by increase in peak intensity when Sm^{3+} was

introduced[33]. This suggest that the Sm^{3+} ions acted to harvest primary excitation energy and transfer it to Eu^{3+} ions non-radiatively, i.e Sm^{3+} ions served as efficient sensitizer to enhance the light emission of Eu^{3+} doped BaB_8O_{13} phosphor for a given amount of Sm^{3+} concentration. Similar observation was made by Li et.al [34].

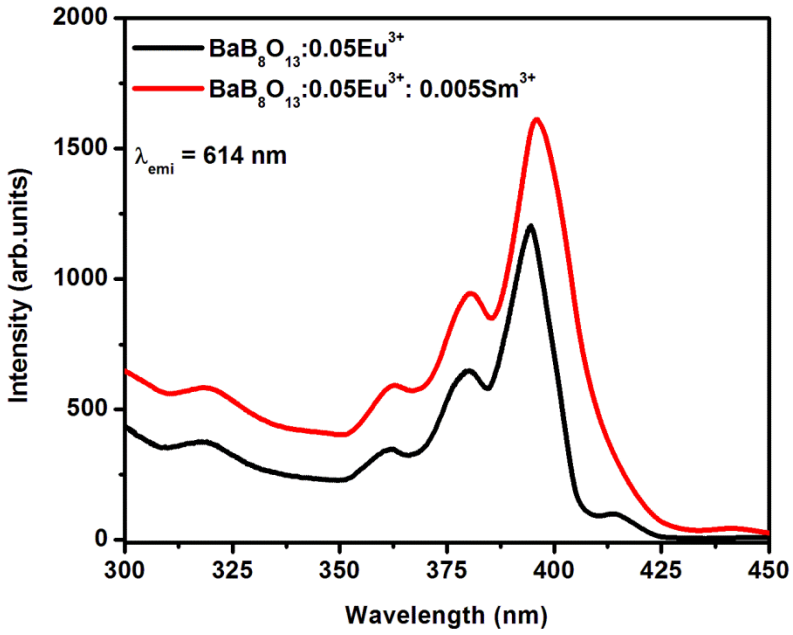

Figure 5.8: Excitation spectra of BaB_8O_{13}: *0.05*Eu^{3+} and BaB_8O_{13}: *0.05*Eu^{3+}; *0.005*Sm^{3+} powder phosphors.

The emission spectra of BaB_8O_{13}: *0.05*Eu^{3+}; *y*Sm^{3+} (*x* = 0.005, 0.01, 0.02, 0.03, 0.04, 0.05 and 0.07) under 402 nm excitation are shown in **figure 5.9** (**a**). The emission spectrum of BaB_8O_{13}: *0.05*Eu^{3+} single doped excited at 402 nm wavelength of Sm^{3+} is also shown in **figure 5.9** (**a**). The emission spectrum consists of sharp lines that originate from the intra-4f transition of Eu^{3+} ion and the strongest peak located at 614 nm is assigned to $^5D_0 \rightarrow {}^7F_2$ transition of Eu^{3+} [26]. By introducing Sm^{3+} in BaB_8O_{13}: *0.05*Eu^{3+} powder phosphor, it was observed that the emission spectra changes with the incorporation of different concentrations of Sm^{3+}. In BaB_8O_{13}: *0.05*Eu^{3+}; *y*Sm^{3+} (*y* = 0.005 and 0.01), the emission spectra show mainly the characteristic emission peaks of Eu^{3+} together with the Sm^{3+} emission peak at 562 nm (see **figure 5.9** (**b**)). The emission intensity at 614 nm of BaB_8O_{13}: *0.05*Eu^{3+}; *y*Sm^{3+} increased for *y* = 0.005, but as the

concentration of Sm^{3+} increases further, the intensity decreased due to concentration quenching effects (see also **figure 5.9** (**c**)). The observed increase in intensity of 614 nm emission peak of Eu^{3+} serves as a proof that there exists an energy transfer from $Sm^{3+} \rightarrow Eu^{3+}$ [8]. The intensity of BaB_8O_{13}: *0.05*Eu^{3+}; *0.005*Sm^{3+} phosphor powder is 1.6 times more intense compared to that of BaB_8O_{13}: *0.05*Eu^{3+}. For BaB_8O_{13}: *0.05*Eu^{3+}; *y*Sm^{3+} (*y* = 0.02, 0.03, 0.04, 0.05 and 0.07) powder phosphors, the emission spectrum contain the characteristics peaks of both Eu^{3+} and Sm^{3+} (see **figure 5.9** (**c**)). In this case, the spectra shows mainly Sm^{3+} with the emission peaks at 562 nm, 596 nm and 642 nm and the one of Eu^{3+} is observed only at 614 nm [32]. The emission peak intensity of Sm^{3+} increased with increase in Sm^{3+} concentration, reaching the maximum at *y* = 0.03 mol% and then decreased. Since the characteristic emissions of Eu^{3+} are also noticeable under 402 nm excitation into the $^4K_{11/2}$ level of Sm^{3+} in Eu^{3+} and Sm^{3+} co-doped powder phosphors , this indicates that the energy transfer from Sm^{3+} to Eu^{3+} took place [35].

From the PL emission spectra of the co-doped phosphor powders, we observed that at higher Sm^{3+} doping (*y > 0.005*), the red emission intensity of Eu^{3+}/Sm^{3+} co-doped BaB_8O_{13} tends to decrease due to the concentration quenching caused by Sm^{3+} - Sm^{3+} cross-relaxation. **Figure 5.9** (**d**) shows the relative intensity as a function of Sm^{3+} concentration for 562 nm and 614 nm emissions. The luminescence quenching in the Sm^{3+} doped BaB_8O_{13} was found to be higher than 0.5 mol % (*y > 0.005*) (**see figure 5.7** (**b**)). In the Eu^{3+}/Sm^{3+} co-doped BaB_8O_{13}**,** therefore there will be competition between Sm^{3+} - Sm^{3+} cross relaxation and Sm^{3+}- Eu^{3+} sensitization with the increase in Sm^{3+} doping concentration. The Sm^{3+} - Sm^{3+} cross relaxation will increase at a higher concentration of Sm^{3+} and suppress the Sm^{3+} - Eu^{3+} sensitization [36]. This led to luminescence quenching at higher Sm^{3+} concentration in Eu^{3+}/Sm^{3+} co-doped BaB_8O_{13} powder phosphors.

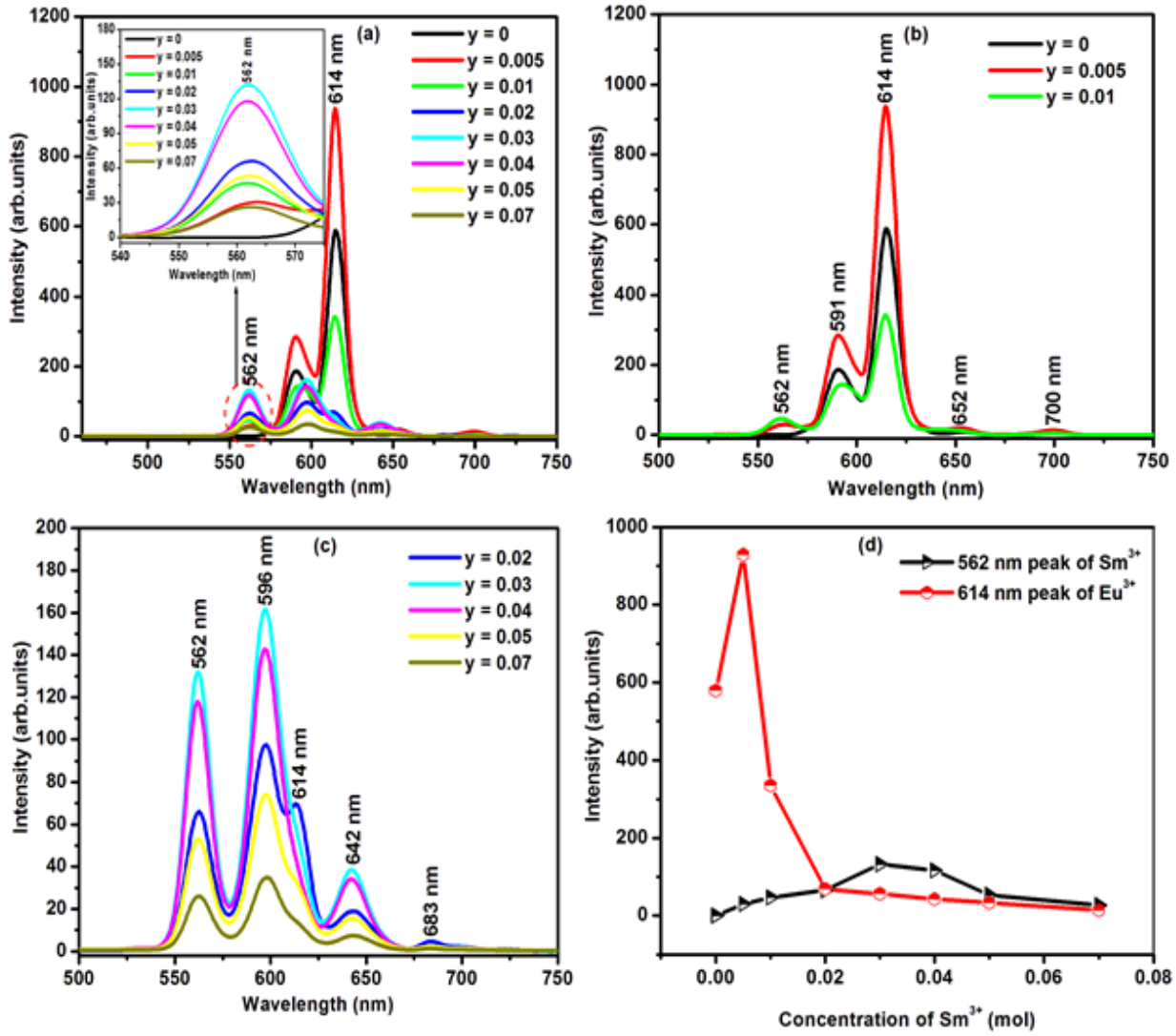

Figure 5.9: Emission spectra of BaB_8O_{13}: *0.05*Eu^{3+}; *y*Sm with **a**) *y* = 0, 0.005, 0.01, 0.02, 0.03, 0.04, 0.05 and 0.07 **b**) *y* = 0, 0.005 and 0.01 **c**) *y* = 0.02, 0.03, 0.04, 0.05 and 0.07 excited at 402 nm and **d**) Relative intensity as a function of Sm^{3+} concentration for 562 nm and 614 nm emissions.

Figure 5.10 present the schematic energy level diagram showing the efficient energy transfer process of Sm^{3+}→ Eu^{3+} in BaB_8O_{13}: *0.05*Eu^{3+}; *0.005*Sm^{3+} powder phosphor. Under near ulraviolet light excitation (402 nm), Sm^{3+} can be excited from their ground $^6H_{5/2}$ state to $^4K_{11/2}$ state, and then relaxes to the $^4G_{5/2}$ state by nonradiative (NR) relaxation. The energy of the $^4G_{5/2}$ level then relaxes to the $^6H_{5/2}$, $^6H_{7/2}$ and $^6H_{9/2}$ levels, respectively. At the same time, part of the

energy in $^4G_{5/2}$ level of Sm^{3+} is also transferred to the $^5D_0$ level of Eu^{3+} by the resonance between the two energy levels. The energy resonance transfer enhances the emission intensity of Eu^{3+} in BaB_8O_{13}: *0.05*Eu^{3+}; *0.005*Sm^{3+} powder phosphor (**figure 5.9** (**b**)). Therefore, the characteristic emission peaks at 589 nm, 614 nm, 652 nm and 698 nm are observed and enhanced due to the $^5D_0 \rightarrow {}^7F_K$ (K = 1, 2, 3, and 4) transitions of Eu^{3+} ion [37, 38].

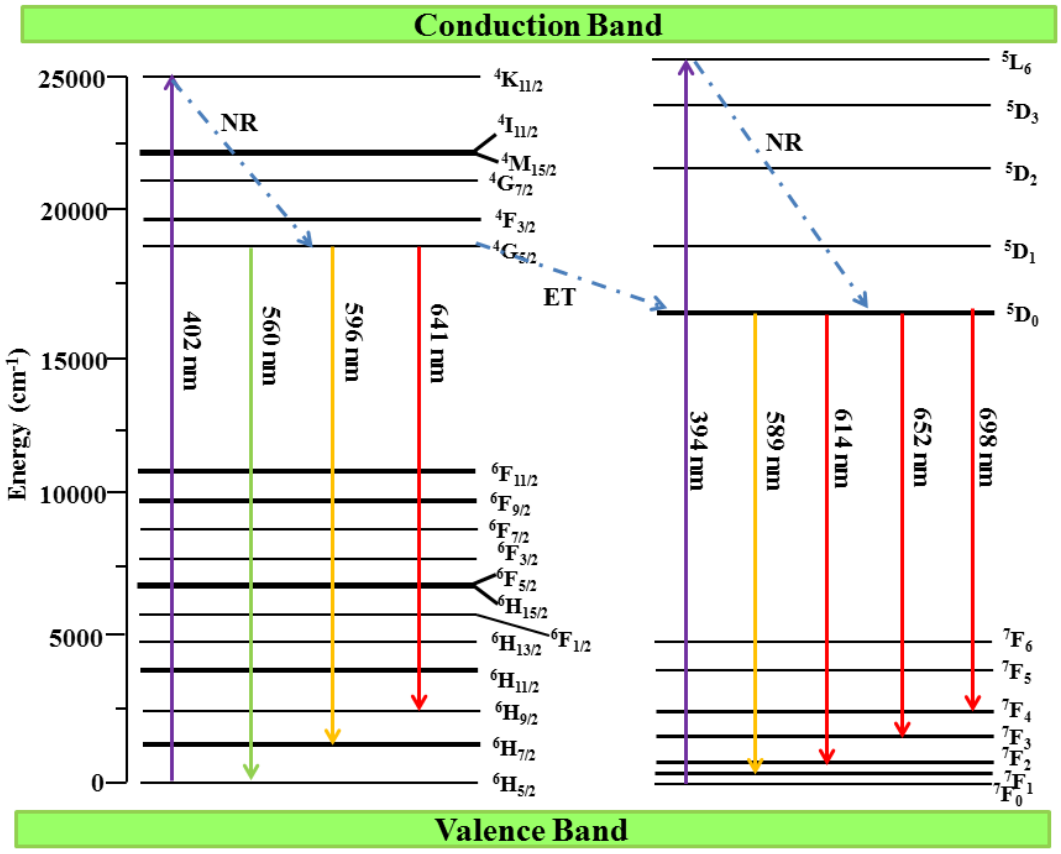

Figure 5.10: The schematic diagram of efficient energy transfer process from the Sm^{3+} to Eu^{3+} in BaB_8O_{13}: *0.05*Eu^{3+}; *0.005*Sm^{3+}.

Color coordinates are used for evaluating phosphors performance [39] and possible applications. **Figure 5.11** shows the color coordinates for the BaB_8O_{13}: *0.05*Eu^{3+}, BaB_8O_{13}: *0.005*Sm^{3+} and BaB_8O_{13}: *0.05*Eu^{3+}; *0.005*Sm^{3+} powder phosphors were calculated using the intensity-calibrated emission spectra data and the chromatic standard issued by the Commission International de I'Eclairage in 1931 (CIE 1931) [40]. The color coordinates of BaB_8O_{13}: *0.05*Eu^{3+} are (0.638,

0.361) which are located in the red region of the spectrum and are close to the standard red color coordinates (0.67, 0.33). For BaB_8O_{13}: *0.005*Sm^{3+}, the color coordinate are (0.529, 0.469) and are located in the orange-red region. For BaB_8O_{13}: *0.05*Eu^{3+}; *0.005*Sm^{3+} powder phosphor, the color coordinates (0.637, 0.362) are also located in the red region indicating that the phosphor has the potential to be used as red emitting phosphors.

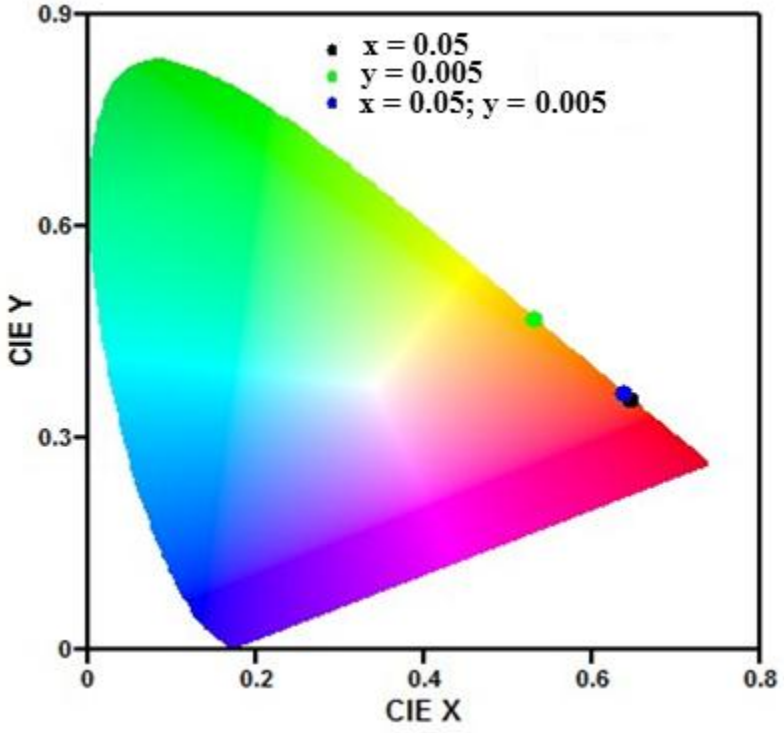

Figure 5.11: CIE chromaticity coordinates of BaB_8O_{13}: 0.*05*Eu^{3+}, BaB_8O_{13}: *0.005*Sm^{3+} and BaB_8O_{13}: *0.05*Eu^{3+}; *0.005*Sm^{3+} powder phosphors.

5.4 Conclusion

In conclusion, Eu^{3+}, Sm^{3+} single doped and Eu^{3+} - Sm^{3+} co-doped BaB_8O_{13} phosphor powders were successfully synthesized by solution combustion method. The PL emission of BaB_8O_{13}: Eu^{3+}; Sm^{3+} phosphor powders showed emissions from both Eu^{3+} and Sm^{3+} ions under 402 nm. The emission intensity of BaB_8O_{13}: *0.05*Eu^{3+}; *0.005*Sm^{3+} phosphor powder was enhanced 1.6 times compared to that of BaB_8O_{13}: *0.05*Eu^{3+} powder phosphor. The enhanced PL intensity confirmed energy transfer from Sm^{3+} to Eu^{3+} in BaB_8O_{13} host matrix which belongs to

multipolar interactions. BaB_8O_{13}: *0.05*Eu^{3+}; *0.005*Sm^{3+} powder phosphor with the CIE chromaticity coordinates of (0.637, 0.362) located in the red region indicated that the phosphor have the potential for application as a red emitting phosphor for n-UV-based LEDs.

References

[1] R. S. Palaspagar, A. B. Gawande, R. P. Sonekar and S. K. Omanwar, *International Journal of Chemical and Physical Sciences*, **3** (2014) 91 - 95.

[2] T. Kuo and T. Chen, *Journal of Luminescence*, **130** (2010) 483 - 487.

[3] N.S. Bajaj and S.K. Omanwar, Asian Journal of Chemistry, **24** (2012) 5945 - 5946.

[4] R. P. Sonekar, S. K. Omanwar and S. V. Moharil, *Indian Journal of Pure and Applied Physics*, **47** (2009) 441 - 443.

[5] B. H. Rudramadevi, S. Buddhudu and P. Bhatt, *Material Research Society Symposium Proceedings*, **1565** (2013) doi: 10.1557/opl.2013.883.

[6] J. Huang, Q. Li and D. Chen, *Materials Science and Engineering B*, **172** (2010) 108 - 113.

[7] J. Huang, L. Zhou, Q. Pang, F. Gong, J. Suna and W. Wang, *Luminescence*, **24** (2009) 363 - 366.

[8] T. Wang, Y. Hu, L. Chen and X. Wang, Journal of Materials Science: Materials in Electronics, **26** (2015) 5360 - 5367.

[9] L. Wang, H. Guo, Y. Wei, H. M. Noh and J. H. Jeong, *Optical Materials*, **42** (2015) 233 - 236.

[10] C. Gheorghe, A. Lupei, F.M. Voicu and C. Tiseanu, Journal of Alloys and Compounds, **588** (2014) 388 - 393.

[11] Y. Zhang, L. Xiong, X. Li, J. Guo and Z. Wang, Materials Science and Engineering B, **177** (2012) 341 - 344.

[12] G. Liu, Y. Zhang, J. Yin and W. F. Zhang, *Journal of Luminescence*, **128** (2008) 2008 - 2012.

[13] L. Li, Z. Leng, W. Zi and S. Gan, Journal of Electronic Materials, **43** (2014) 2588 - 2596.

[14] F. Zhang, W. Zhang, Z. Zhang, Y. Huang and Y. Tao, *Journal of Luminescence*, **152** (2014) 160 - 164.

[15] Z. Jianming, Z. Weiren, L. Licai and W. Jianqing, *Journal of Rare Earths*, **32** (2014) 5 - 11.

[16] E. Erdogomus, E. Orkmaz and V.E. Kafadar, *Journal of Applied Spectroscopy*, **80** (2014) 952 - 956.

[17] D. Haiyen, L. Gengshen and S. Jaiyue, *Journal of Rare earths*, **25** (2007) 19 - 22.

[18] H. M. Chenari, H. F. Moafi and O. Rezaee, *Material Research*, **19** (2016) 548 - 554.

[19] S. Thakur and A. K. Gathania, *Indian Journal of Physics*, **89** (2015) 973 - 979.

[20] M. S. Geetha, H. Nagabhushana and H. N. Shivananjaiah, *International Journal of Science and Research*, **5** (2016) 158 - 163.

[21] G. R. Dillip, B. Ramesh, C. Madhukar Reddy, K. Mallikarjuna, O. Ravi, S. J. Dhoble, S. W. Joo, B. Deva Prasad Raju, *Journal of Alloys and Compounds*, **615** (2014) 719 - 727.

[22] S. Som and S. K. Sharma, *Journal of Physics D: Applied Physics*, **45** (2012) 415102 (11pp) doi:10.1088/0022-3727/45/41/415102.

[23] I. Ahemen, A. N. Amah, B. E. AttahDaniel, A. Y. Fasasi, *Nanoscience and Nanotechnology*, **4** (2014) 7 - 15.

[24] R. Li, L. Bao and X. Li, *Royal Society of Chemistry*, **13** (2011) 5858 - 5862.

[25] G. R. Dillip, K. Mallikarjuna, S. J. Dhoble, B. Deva Prasad Raju , *Journal of Physics and Chemistry of Solids*, **75** (2014) 8 - 14.

[26] M. Yang, H. You, Y. Liang, J. Xu, F. Lu, L. Dai and Y. Liu, *Journal of Alloys and Compounds*, **582** (2014) 603 - 608.

[27] X. An, Y. XiMing, W. JuanJuan and W. Feng, *Science in China Series E: Technological Sciences*, **52** (2009) 1913 -1918.

[28] P. P. Mokoena, I. M. Nagpure, V. Kumar, R. E. Kroon, E. J. Olivier, J. H, Neethling, H. C. Swart and O. M. Ntwaeaborwa, *Journal of Physics and Chemistry of Solids*, **75** (2014) 998 -1003.

[29] V. H. Romero, E. De la Rosa, P. Salas, J. J. Velazquez-Salazar, *Journal of Solid State Chemistry*, **196** (2012) 243 - 248.

[30] J. Gou, D. Zhang, B. Yu, J. Wang and S. Liu, *Journal of Nanomaterials*, **2015** (2015) 1 - 5.

[31] M. Manhas, V. Kumar, O. M. Ntwaeaborwa and H. C. Swart, *Materials Research Express*, **2** (2015) 075008.

[32] Y. Li, Y. Changa, Y. Lin, Y. Chang, Y. Lin, *Journal of Alloys and Compounds*, **439** (2007) 367 - 375.

[33] F. Kang, Y. Hun, H. Wu, Z. Mu, G. Ju, C. Fu and N. Li, *Journal of Luminescence*, **132** (2012) 887 - 894.

[34] Q. Li, J. Huang and D. Chen, *Journal of Alloys and Compounds*, **509** (2011) 1007 - 1010.

[35] J. Ye and Z. Jinju, *Materials Letters*, **114** (2014) 4 - 6.

[36] Q. Wen, Z. Xiang, X. Gao, X. Yang, S. Xiao, *Materials Science and Engineering B*, **197** (2015) 82 - 86.

[37] Y. Ren, Y. Liu and R. Yang, *Superlattices and Microstructures*, **91** (2016) 138 - 147.

[38] G. Li, Y. Wei, W. Long and G. Xu, *Materials Research Bulletin*, **95** (2017) 86 - 94.

[39] L. Cai, L. Ying, J. Zheng, B. Fan, R. Chen and C. Chen, *Ceramics International*, **40** (2014) 6913 - 6918.

[40] F. Li, Y. Wang, S. Xin, F. Zhang and Jia Zhang, *Journal of Nanoscience and Nanotechnology*, **14** (2014) 3440 - 3445.

Chapter 6

Analysis of the structure, particle morphology and photoluminescent properties of green emitting $BaB_8O_{13}:Ce^{3+}$ phosphor

6.1 Introduction

Oxide materials such as borates are excellent hosts for luminescent dopant ions because of their excellent optical properties, such as high damage threshold and good non-linearity. They also have good chemical and thermal stability, and they can be synthesized cost-effectively at low temperature [1]. Barium octaborate BaB_8O_{13} is considered as an excellent host material for luminescent dopant ions. Its structure consists of two separated interlocking three dimensional infinite network as alternating triborate and pentaborate groups, which forms BO_3 triangles and BO_4 tetrahedral units [2]. Ce^{3+} ions have been widely used as activators in various fluoride and oxide materials. The preparation of rare earth doped phosphor materials for application in advanced illumination technologies has been the subject of intense research for many decades. This type of research has been encouraged by the need to increase the efficiency of white light emitting solid state devices which can serve as an alternative source of lighting [3].

In most Ce^{3+} doped phosphors, parity allowed 5d-4f emission ranging from ultra-violet to red color has been demonstrated and it is dependent on the host lattice and the site size, and the size symmetry and coordination number. In fact, the emission color of Ce^{3+} can range from the ultraviolet to visible region of the electromagnetic wave spectrum due to dependence of the 5d level of Ce^{3+} on the crystal field strength of the host lattice [4]. Different methods including wet chemistry and solid state have been used to prepare different types of phosphors. Among these

methods, the solution combustion has been widely used due to versality, easy of incorporation of dopant ions, cost effectiveness and relatively short reaction time. Depending on the type of precursors, as well as conditions used for the process, the solution combustion may occur as either volume or layer-by-layer propagating combustion modes. This process may not only yield nanosized materials but also uniform (homogeneous) doping of traces of rare-earth impurity ions in a single step [5]. In the current study, BaB_8O_{13}: Ce^{3+} powder phosphors were synthesized by the solution combustion method. The photoluminescent properties, structure and particle morphology of these phosphors are reported.

6.2 Experimental

6.2.1 Preparations

Powder samples of BaB_8O_{13}: xCe^{3+} (x = 0.03, 0.05, 0.07, 0.09 and 0.11) were synthesized by a solution combustion method. The following precursors all in analytical purity were used: barium nitrate [$Ba(NO_3)_2$], boric acid [H_3BO_3], cerium nitrate [$CeN_3O_9.6H_2O$] , ammonium nitrate [NH_4NO_3] and urea [NH_2CONH_2]. In this preparation, NH_4NO_3 was used as an oxidizer and NH_2CONH_2 was used as a fuel. The stoichiometric amounts of reactants were mixed in a beaker with 10 mL of de-ionized water and stirred vigorously using a magnetic stirrer on a hot plate maintained at a temperature of 70 ºC for 30 min. The resulting solution was then transferred to a crucible and was introduced into a muffle furnace preheated to 600 ºC. Within a few minutes, the solution boiled and ignited to produce a self-propagating flame. The entire combustion process was complete in less than 5 min but the crucible was left in the furnace for 10 min to ensure that decomposition was complete. After 10 min the crucible was removed from the furnace and allowed to cool to room temperature. The combustion ashes of the powder samples were ground gently into fine powders using pestle and mortar. The powders were post annealed at 800 °C for 5 hours in a muffle furnace. The flow diagram for the synthesis of the powder phosphors is shown in **figure 6.1**.

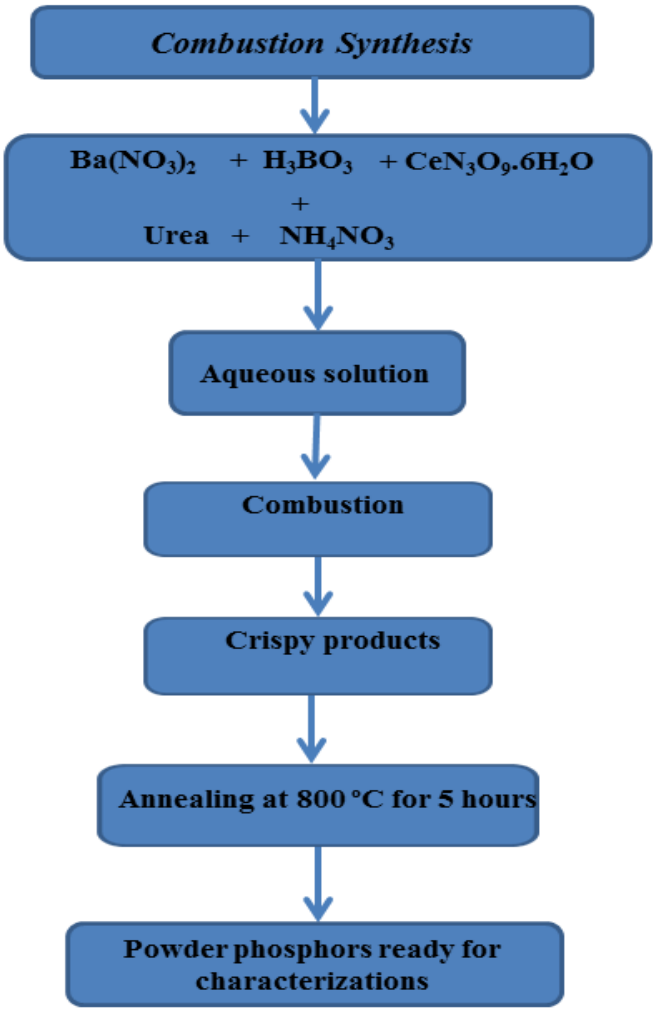

Figure 6.1: Flow diagram of solution combustion method for preparing BaB_8O_{13}: xCe^{3+} (x = 0.03, 0.05, 0.07, 0.09 and 0.11) powder phosphors**.**

6.2.2 Characterizations

The structure of the phosphor powders were analysed using a Bruker D8 Advanced X−ray diffractometer (XRD) equipped with monochromatic *CuKα* radiation. Morphology and chemical composition were analyzed using Jeol JSM 7800F thermal field emission scanning electron microscope (FE-SEM) and the chemical composition analysis was carried out using an Oxford Instruments AzTEC energy dispersive spectrometer (EDS) attached to the FE-SEM. The

stretching mode frequencies were determined using a Perkin Elmer Spectrum 100 FTIR spectrometer. Room temperature photoluminescence (PL emission and PL excitation) spectra were recorded by Hitachi F-7000 fluorescence spectrophotometer using a monochromatized xenon lamp as an excitation source.

6.3 Results and discussion

6.3.1 Structure and morphology

Figure 6.2 (**a**) shows the powder X-ray diffraction (XRD) patterns of BaB_8O_{13}: xCe^{3+} (x = 0.03, 0.05, 0.07, 0.09 and 0.11) powder phosphors. The XRD patterns of the powder phosphors were indexed to orthorhombic structure with cell parameters a = 8.550 Å, b = 17.350 Å and c = 13.211 Å according to JCPDS card no: 20-0097 [2]. The patterns shows some extra peaks marked with asterisks (*) which may be attributed to the unreacted precursors during the combustion reaction. The presence of other phases or some of the precursors attributed to the fact that the combustion wave is not uniform and portion of the precursors might not react completely during the combustion process [6]. The patterns also show a shift of peaks towards the lower angle as shown in **figure 6.2** (**b**). The observed XRD peak shifts might be caused by the lattice strain or lattice defects [7]. The average crystallite sizes of the phosphors were estimated by using Scherrer's equation [8].

$$D = \frac{k\lambda}{\beta \cos\theta} \tag{6.1}$$

where k = 0.9 is a constant, D is the crystallite size for the ($h\ k\ \ell$) plane, λ is the wavelength of the incident X-radiation (CuKα = 0.154 nm), β is the full width at half-maximum in radians, and θ is the diffraction angle for the ($h\ k\ \ell$) indices**.**The estimated average crystallite sizes of the calculated average crystallite size values of all prepared BaB_8O_{13} doped with different concentrations of Ce^{3+} are tabulated in **table 6.1**. The crystal structure of BaB_8O_{13} host matrix is shown in **figure 6.2** (**c**). It is observed from the crystal structure that BaB_8O_{13} consists of both tetrahedron (BO_4) and triangular (BO_3) groups. Looking at the ion bond between Ba, B and O ions, it is observed that B and Ba are connected via O ions. The average bond lengths between B-

O and Ba-O were calculated to be 1.415 Å and 2.713 Å, respectively. The average bond angles between O-B-O, B-O-B and Ba-O-B were calculated to be 111.34º, 128.47º and 115.57º, respectively.

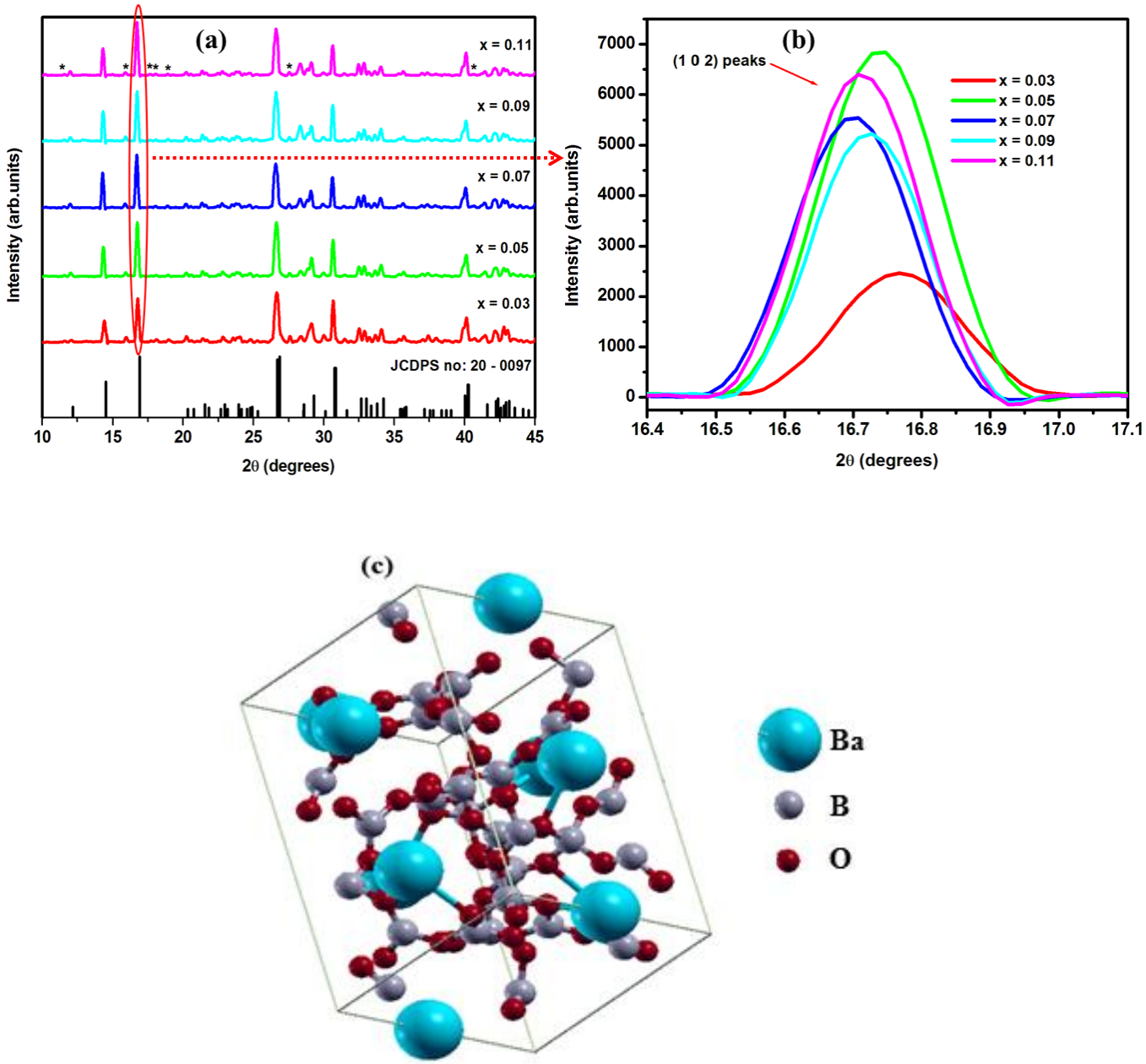

Figure 6.2: a) Room temperature XRD pattern of BaB_8O_{13}: xCe^{3+} powder phosphors **b**) magnified view of (102) plane for BaB_8O_{13}: xCe^{3+} powder phosphors and **c**) Crystal structure of

BaB_8O_{13} host (blue, grey and red balls represents barium, boron and oxygen atoms, respectively).

Strain and crystallite size effects in peak broadening are independent to each other and they can be distinguished by Hall-Williamson plot. The Hall-Williamson relation shown by equation 6.2 was used to calculate Strain and crystallite size effects of the powder phosphors [9]:

$$\beta_{hkl}\cos\theta = \left(\frac{K\lambda}{D}\right) + 4\varepsilon\sin\theta \tag{6.2}$$

The equation shown above expresses the FWHMs (β) as a linear combination of the contributions from the strain (ε) and crystallite size (D). The plot of $\beta_{hkl}Cos\theta$ versus $4Sin\theta$ for BaB_8O_{13}: $0.05Ce^{3+}$ powder phosphor is shown in **figure 6.3**. The reciprocal of intercept of the linear fitted line on the βcosθ/λ axis gives the average crystallite size (D) of the prepared phosphors [10]. The average crystallite of BaB_8O_{13}: $0.05Ce^{3+}$ powder phosphor was estimated to be 53 nm with the strain of 0.0015. The estimated strain and the average crystallite size values of all prepared BaB_8O_{13} doped different concentrations of Ce^{3+} from W-H are listed in **table 6.1**.

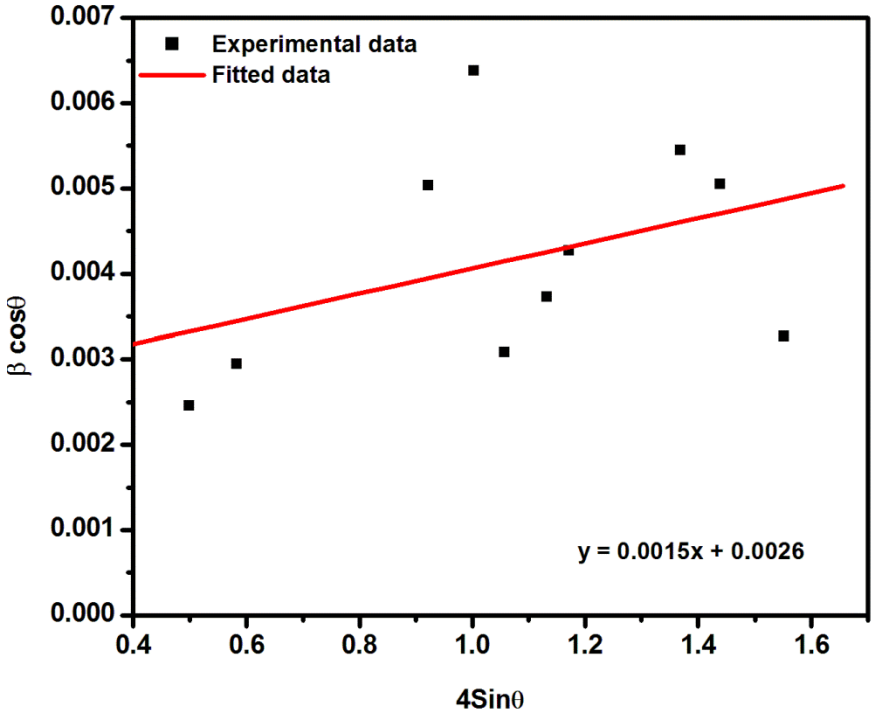

Figure 6.3: Williamson-Hall plot of BaB_8O_{13}: *0.05*Ce^{3+} powder phosphor.

Table 6.1: Average crystallite size values of BaB_8O_{13} doped with different concentrations of Ce^{3+} calculated from both W-H plot and Scherer's equation.

Sample ID	**Scherer's method**	**Williamson-Hall method**	**strain**
BaB_8O_{13}: *x*Ce^{3+}	**D (nm)**	**D (nm)**	**$\varepsilon \times 10^{-4}$**
x = 3	32	50	19
x = 5	36	53	15
x = 7	39	58	14
x = 9	43	76	25
x = 11	40	53	11

Figure 6.4 shows the Fourier Transform Infrared (FTIR) spectrum of BaB_8O_{13}: *0.05*Ce^{3+} powder phosphor. The FTIR spectrum was recorded in the spectral range of 650 - 3000 cm^{-1}.The spectrum exhibits some broad bands in the range 650 - 1600 cm^{-1}. The bands at 698, 730, 775, and 799 cm^{-1} are assigned to the out-of-plane bending mode of the group BO_3. The in-plane bending modes of the BO_3 group are shown by the bands at 871, 928, 980, 1101 and 1138 cm^{-1}. The bands peaking at 1235, 1270, 1319, 1363 and 1408 cm^{-1} are assigned to the asymmetric stretching vibration of the BO_3 group [1].

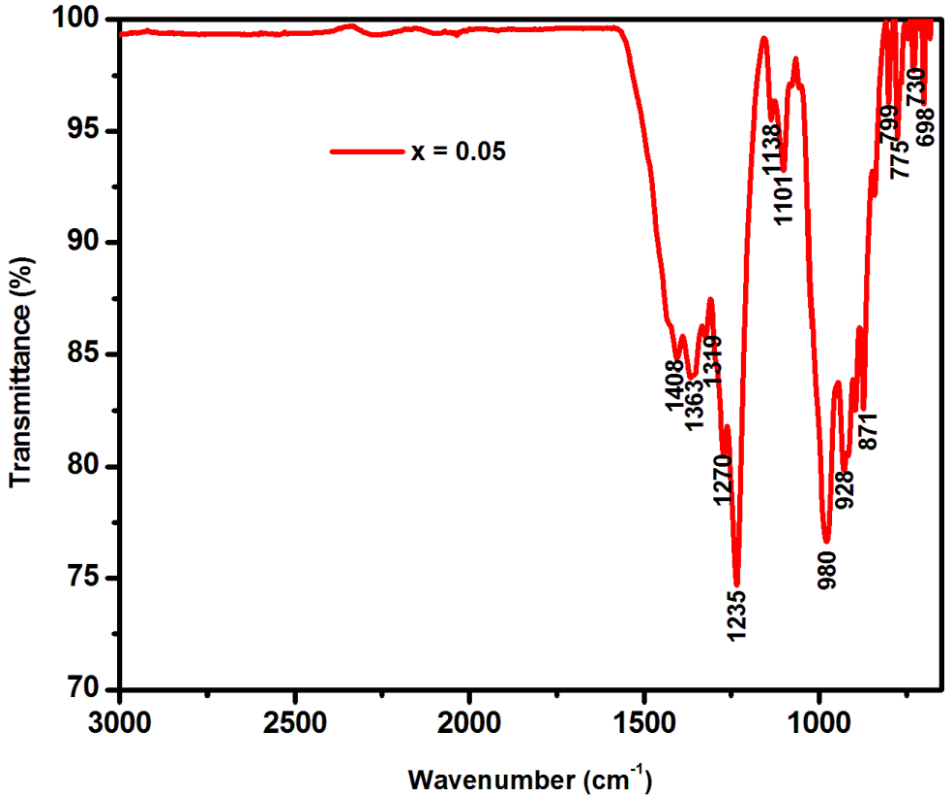

Figure 6.4: Room temperature FTIR spectrum of BaB_8O_{13}: *0.05*Ce^{3+} phosphor.

The scanning electron microscope (SEM) micrographs of BaB_8O_{13}: *0.05*Ce^{3+} powder phosphor taken at ×5000 and ×15000 magnifications are shown in **figure 6.5** (**a**). It is observed that the microstructures of the phosphor are agglomerated with irregular shapes. The surface of the SEM micrograph shows lots of voids and pores due to the large amount of gases such as NO_2 and CO_2

that evolve during combustion method [11]. **Figure 6.5** (**c**) shows the energy dispersive X-ray spectroscopy (EDS) spectrum of BaB_8O_{13}: *0.05*Ce^{3+} powder phosphor. The spectrum confirms the presence of barium (Ba), Boron (B), oxygen (O) and Cerium (Ce) elements. The concentration of Ba by weight exceeds those of all the other elements and the least concentration (also by weight) was recorded for Ce^{3+} used as a dopant. The surface composition and elemental distribution of BaB_8O_{13}: *0.05*Ce^{3+} powder is shown in **figure 6.6 (a-d**). The color mapping of the cations such as Ba, B and Ce are shown in **figure 6.6** (**a, b and d**), respectively, while the anion such as O is shown in **figure 6.6** (**c**). The EDS spectrum and the corresponding EDS mapping confirms the formation of BaB_8O_{13}: *0.05*Ce^{3+} powder phosphor and a homogenous distribution of the elements present on the surface of the phosphor**.**

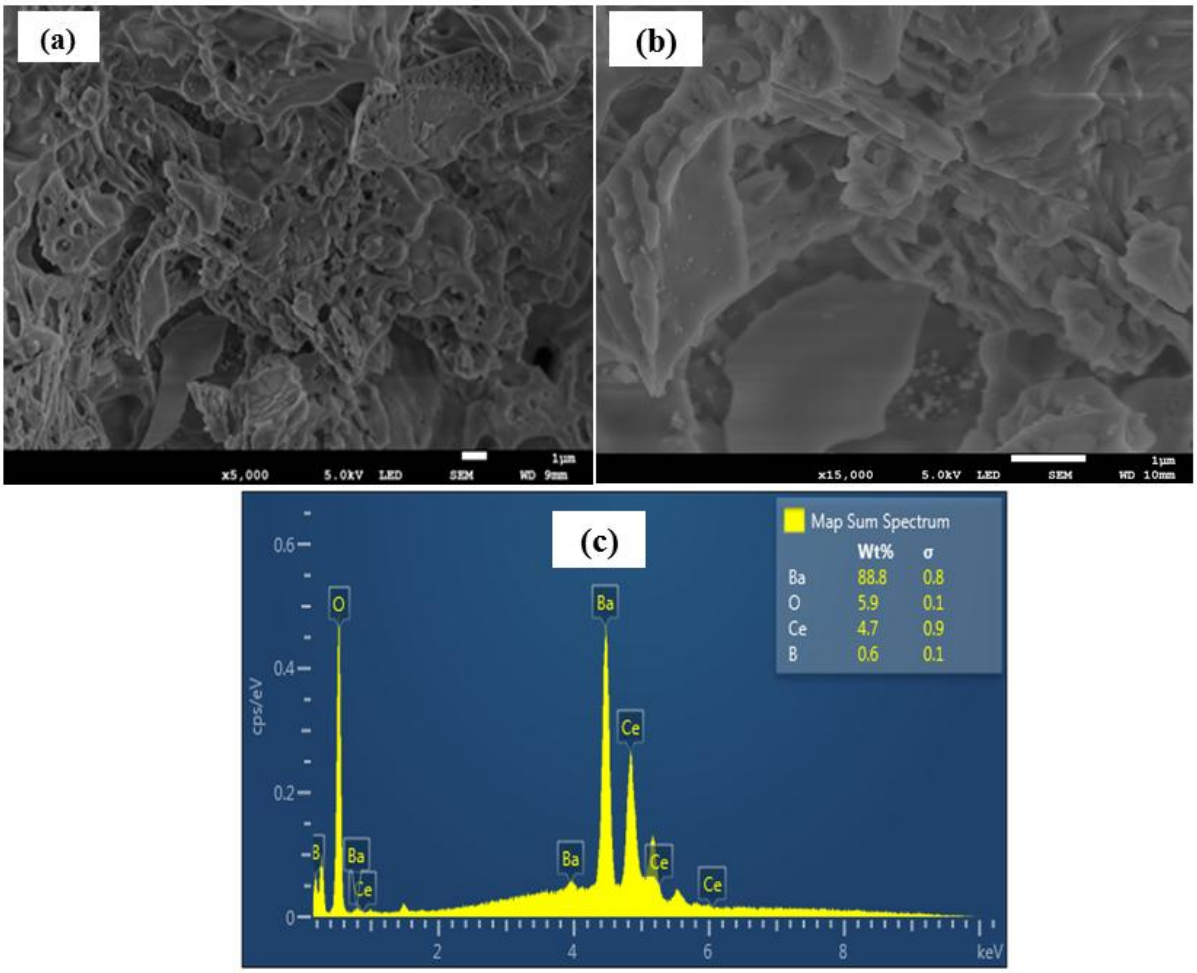

Figure 6.5: SEM micrographs and EDS spectrum of BaB_8O_{13}: *0.05*Ce^{3+} phosphor.

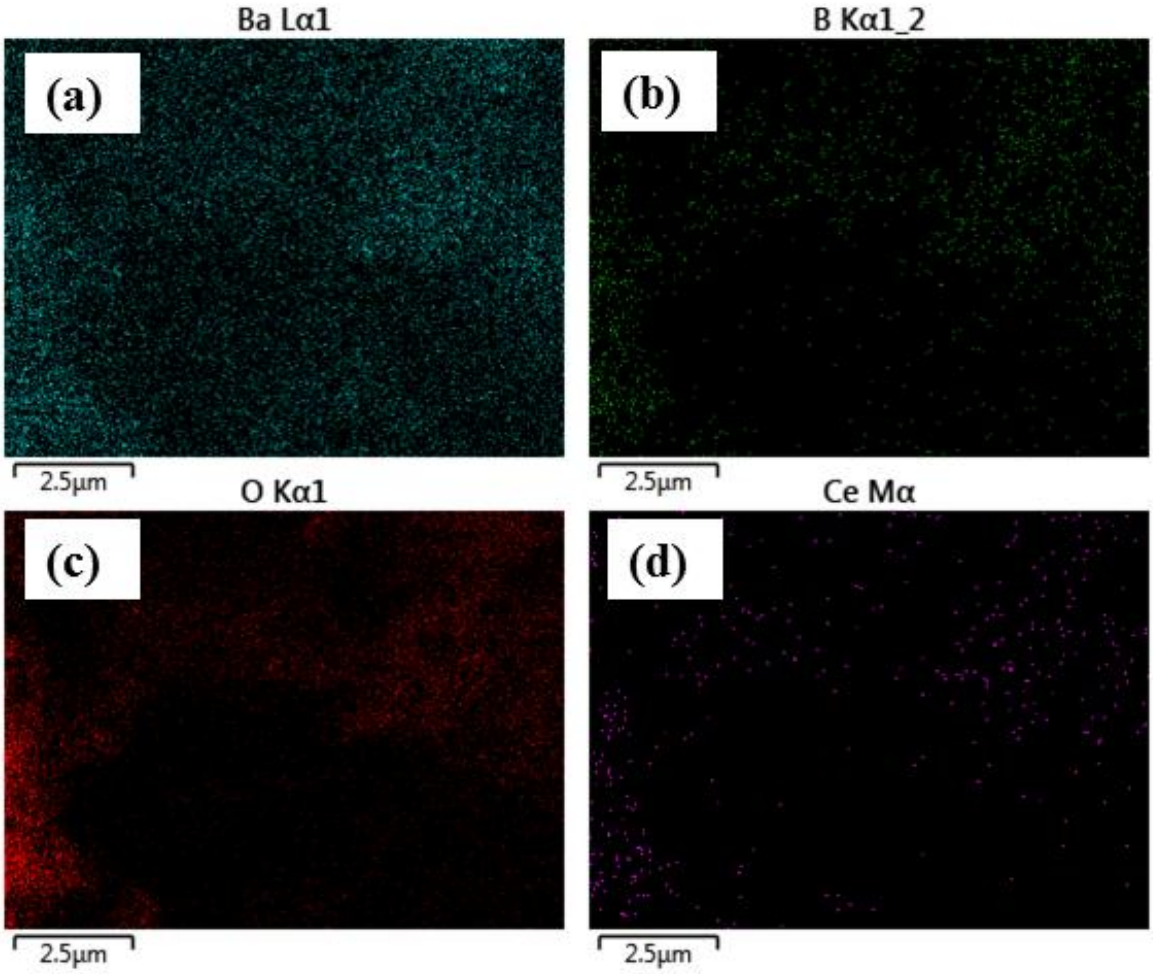

Figure 6.6: EDS elemental mapping of BaB_8O_{13}: *0.05*Ce^{3+} phosphor.

6.3.2 Photoluminescence studies

Figure 6.7 (a) shows the photoluminescence excitation (PLE) spectrum of BaB_8O_{13}: *0.05*Ce^{3+} powder phosphors. The PLE spectrum consists of a major peak centered at 270 nm and a minor peak at 212 nm due to the $4f^1 - 5d^1$ excitation transition of Ce^{3+} ions and the excitonic band, respectively [12]. The feature of the excitation spectrum remains the same when monitored using 515 nm emission peak indicating that the emission obtained is due to the same recombination center [13]. The photoluminescence emission (PL) spectrum of BaB_8O_{13}: *x*Ce^{3+} (*x* = 0.03, 0.05, 0.07, 0.09 and 0.11) powder phosphors are shown in **figure 6.7** (**b**). When exciting the powder

phosphors at 270 nm wavelength, a broad emission peak was observed at 515 nm, which is attributed to the inter-configuration $5d^1 – 4f^1$ allowed transition of Ce^{3+} [11, 14]. Generally, the emission of Ce^{3+} has a doublet character with an energy difference of about 2000 cm^{-1} due to the ground-state splitting ($^2F_{5/2}$ and $^2F_{7/2}$) [15]. To confirm this, the PL spectrum of BaB_8O_{13}: *0.05*Ce^{3+} (**figure 6.7** (**c**)) was deconvoluted into two Gaussian profiles with peaks centered at 508 nm (19685 cm^{-1}) and 551 nm (18149 cm^{-1}). The energy difference (Δk) between them is about 1536 cm^{-1}, which shows a small difference compared with the theoretical value of 2000 cm^{-1} [16]. This indicates that there is only one type of emission center in the BaB_8O_{13} host lattice [16]. The concentration of Ce^{3+} versus relative emission intensity plot of BaB_8O_{13} doped with different concentrations of Ce^{3+} under 270 nm excitation is shown as an inset in **figure 6.7** (**d**). The plot shows PL intensity increased with concentration from 0.03 and maximizes at 0.05 mol beyond which the PL intensity decreased. The decrease in the PL emission intensity beyond the critical concentration could be explained by concentration quenching effect. The probability of energy transfer is greatly dependent on the distance between the activator ions. As the Ce^{3+} doping amount increases the distance between Ce^{3+} ions shortens, which favors the non-radiative pathway by energy transfer among Ce^{3+} ions [17]. Non-radiative energy transfer process from one Ce^{3+} ion to another Ce^{3+} ion can be described by three different methods, namely exchange interaction, radiation reabsorption and multipolar interaction. The exchange interaction is a short-distance interaction and the typical critical distance (R_c) is about 5 Å [18]. The value of R_c for BaB_8O_{13}: $x$$Ce^{3+}$, can be calculated by the formula [19]:

$$R_c = 2\left[\frac{3V}{4\pi x_c N}\right]^{1/3} \qquad (6.3)$$

where V is the volume of the unit cell, N is the number of occupied sites in the unit cell, and x_c is the critical concentration. For the BaB_8O_{13}: $x$$Ce^{3+}$, N = 8 and V = 2017.54 $Å^3$. The critical concentration x_c is 0.05. Therefore, R_c is calculated as 21.28 Å, which is much larger than 5 Å. This value implies that electric multipolar interaction could be the main reason for concentration quenching.

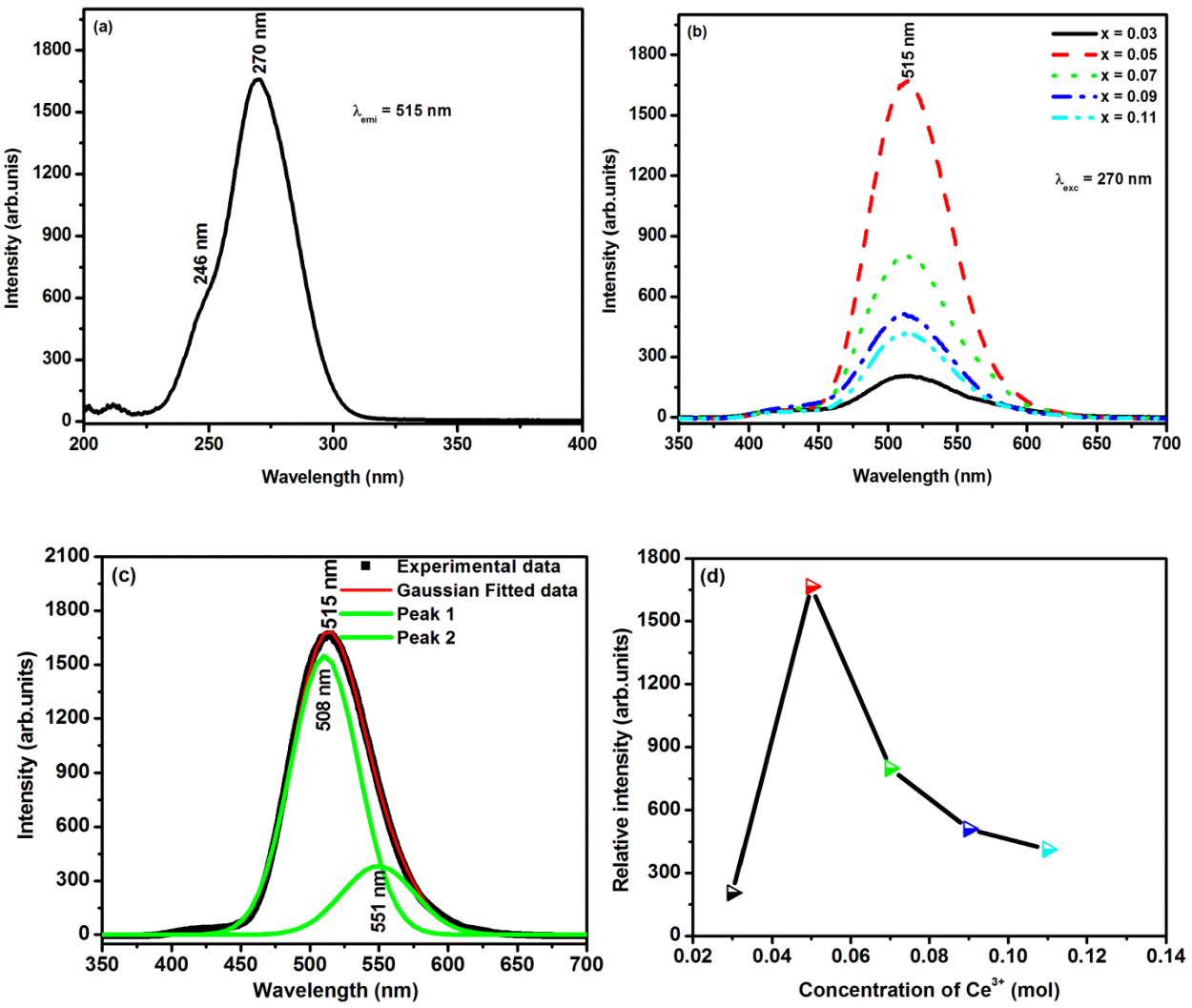

Figure 6.7: a) Excitation spectrum of BaB_8O_{13}: *0.05*Ce^{3+}, **b**) emission spectra of BaB_8O_{13}: *x*Ce^{3+} (*x* = 0.03, 0.05, 0.07, 0.09 and 0.11) powder phosphors, **c**) deconvoluted emission spectrum of BaB_8O_{13}: *0.05*Ce^{3+} powder phosphor and **d**) relative intensity versus concentration of Ce^{3+}.

The electric multipolar interaction type can be confirmed by the following equation [20]:

$$\frac{I}{x} = k\left[1+\beta(x)^{\theta/3}\right]^{-1} \qquad (6.4)$$

where *I/x* is the emission intensity (*I*) per activator concentration (*x*), *k* and β are constants for the same excitation condition, and θ is a function of multipole−multipole interaction. When θ is 6, 8, or 10, the form of the interaction corresponds to dipole−dipole, dipole−quadrupole, or

quadrupole−quadrupole interaction, respectively. When *x* exceeds the quenching concentration, equation 6.4 can be simplified as [20]:

$$\log \frac{I}{x} = c - \frac{\theta}{3} \log x \qquad (6.5)$$

The dependence of log (*I*/*x*) on log (*x*) is shown in **figure 6.8**, where −θ/3 equals the slope of the straight line. Thus, the value of θ is close to 8. The result demonstrates the nonradiative transition between Ce^{3+} ions occurs via dipole – quadrupole interaction for the concentration quenching of Ce^{3+} in BaB_8O_{13}: xCe^{3+}.

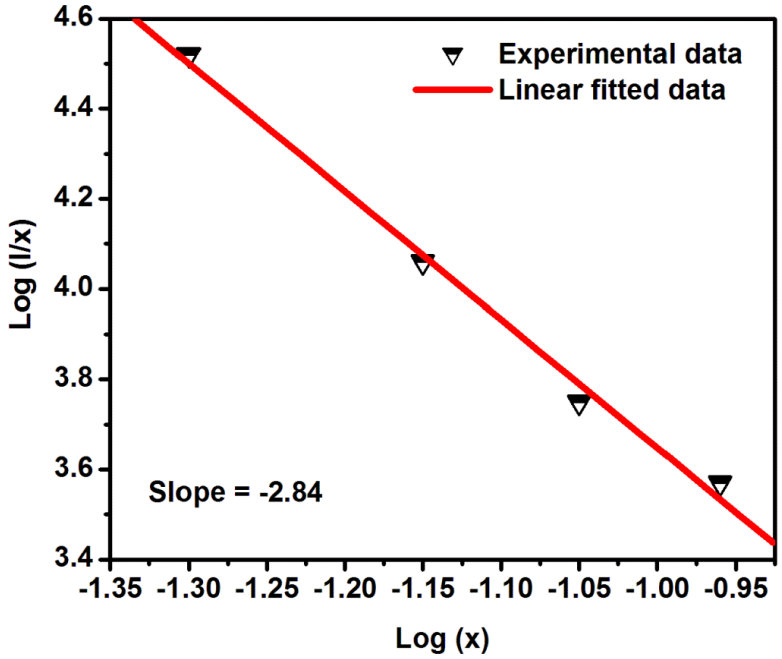

Figure 6.8: Log (I/x) versus log x of BaB_8O_{13}: xCe^{3+} powder phosphors.

Room temperature PL decay time studies were carried out on the prepared powder phosphors of BaB_8O_{13}: xCe^{3+} (x = 0.03, 0.05, 0.07, 0.09 and 0.11) with λ_{exc} = 270 nm and λ_{emi} = 515 nm. This is presented in **figure 6.9**. All the decay curves were fitted with single exponential function shown as equation 6.6 below [21]:

$$I = I_0 \exp\left(\frac{-t}{\tau}\right) \tag{6.6}$$

where I and I_0 are the luminescent intensities at time t and $t = 0$, respectively. t is the time and τ is the life-time value. The life-time values of the powder phosphors are listed in **table 6.2**. The lifetime values of BaB_8O_{13}: xCe^{3+} (x = 0.03, 0.05, 0.07, 0.09 and 0.11) were short. This short lifetime values are attributed to the spin and parity allowed transitions in the Ce^{3+} ion [22].

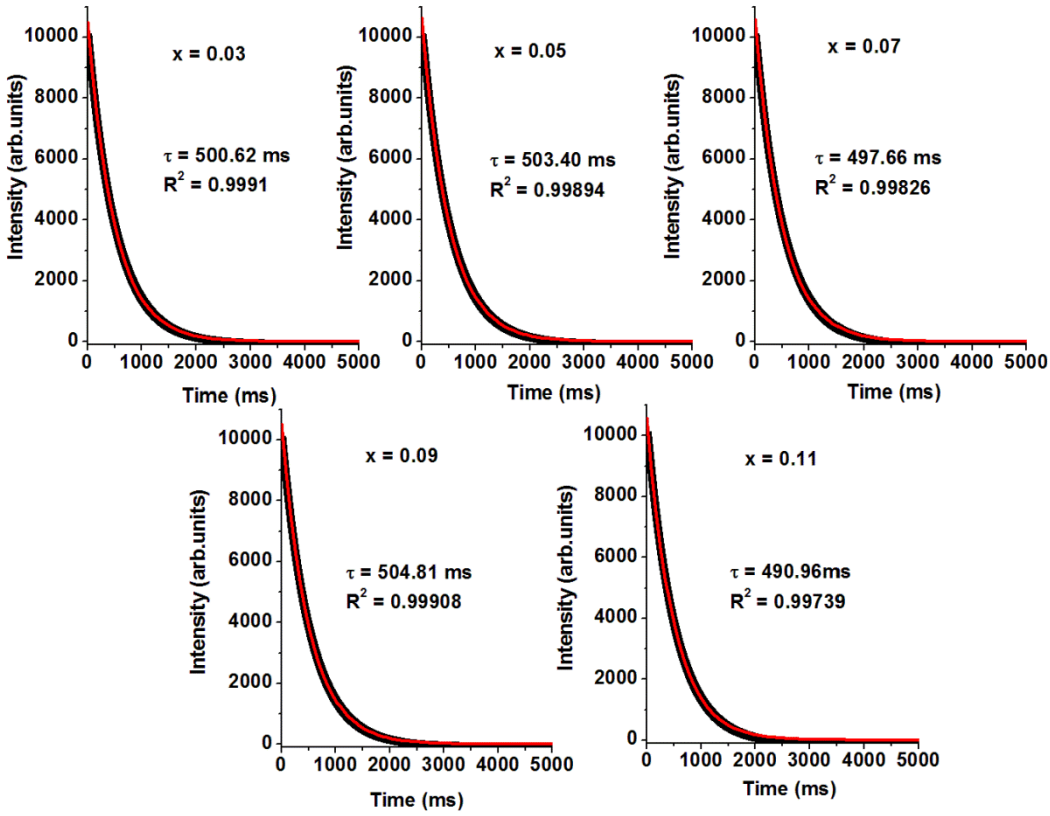

Figure 6.9: Decay curves of BaB_8O_{13}: xCe^{3+} (x = 0.03, 0.05, 0.07, 0.09 and 0.11) powder phosphors.

Figure 6.10 shows the Commission International de I'Eclairage (CIE) 1931 Chromaticity image for BaB_8O_{13}: xCe^{3+} (x = 0.03, 0.05, 0.07, 0.09 and 0.11) phosphor powders excited at 270 nm were calculated using the CIE calculator software [23]. From the CIE coordinates values in **table 6.2**, it is observed that the CIE coordinates are in the green region of the spectrum not far from the standard green phosphor with the coordinates (0.31, 0.60), which means that this phosphor can be used as a source of green light in many light emitting devices of different types.

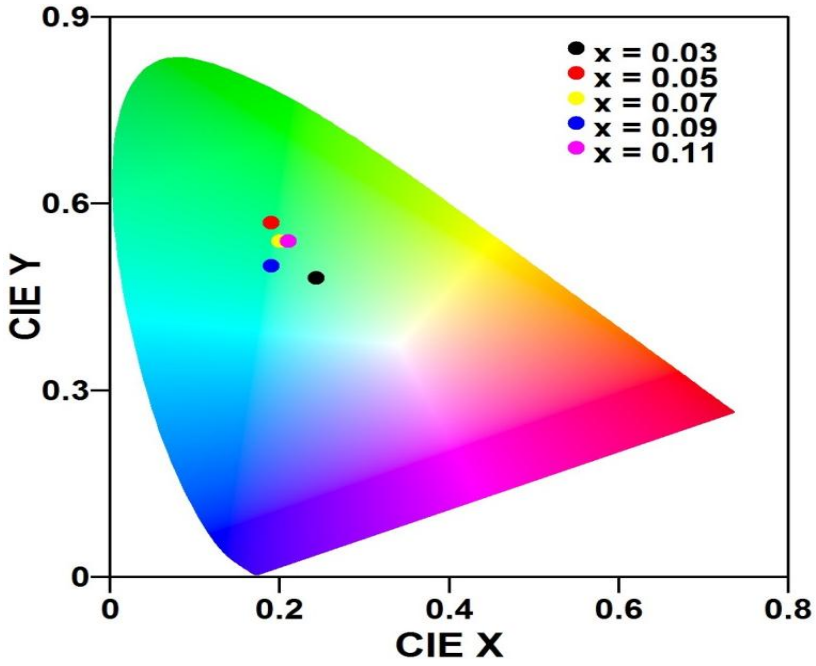

Figure 6.10: CIE chromaticity diagram BaB_8O_{13}: xCe^{3+} (x = 0.03, 0.05, 0.07, 0.09 and 0.11) powder phosphors.

Table 6.2: Lifetime values and CIE chromaticity coordinates of BaB_8O_{13} doped different concentrations of Ce^{3+} excited at 270 nm.

Sample ID	Decay times	CIE coordinates	
BaB_8O_{13}: *x*Ce^{3+}	**τ (s)**	**x**	**y**
x = 3	0.501	0.2429	0.4808
x = 5	0.503	0.1904	0.5721
x = 7	0.498	0.2007	0.5360
x = 9	0.505	0.1916	0.5031
x = 11	0.491	0.2094	0.5359

6.4 Conclusion

A detailed synthesis of a series of Ce^{3+} activated BaB_8O_{13} powder phosphors using combustion method was presented. The phosphors were evaluated for a possible application as a source of green light in light emitting devices. The XRD patterns of the phosphors were found to be consistent with the standard orthorhombic crystal structure of BaB_8O_{13}. The photoluminescence spectroscopy data showed a broad emission centered at 515 nm under the UV excitation of 270 nm. The PL emission intensity was dependent on the concentration of Ce^{3+} with the maximum concentration obtained from the 0.05 mol Ce^{3+} doping. The CIE chromaticity coordinates indicated that the Ce^{3+} doped phosphors exhibit a green color, with coordinates close to those of the standard green phosphor, suggesting that our material is a potential candidate to be used as a source of green light in different types of light emitting devices.

References

[1] J. Zhang, B. Han, Y. Zhang and Q. Lv, *Journal of Materials Science: Materials Electronics*, **27** (2016) 3906 - 3910.

[2] M. A Lephoto, K. G. Tshabalala, S. J. Motloung, I. Ahemen and O. M. Ntwaeaborwa, *Physica B*, (2017) doi.org/10.1016/j.physb.2017.06.063.

[3] E. Malchukova and B. Boizot, *Journal of Rare Earths*, **32** (2014) 217 - 220.

[4] S. Lee, C. Huang, T. Chan and T. Chen, *Applied Materials and Interface*, **6** (2014) 7260 - 7267.

[5] P. B. Devaraja, D. N. Avadhani, H. Nagabhusana, S. C. Prashantha, S. C. Sharma, B.M. Nagabhusana, H. P. Nagaswarupa and B. D. Prasad, *Journal of Radiation Research and Applied Sciences*, **8** (2015) 362 - 373.

[6] B. M. Mothudi, O. M. Ntwaeaborwa, Shreyas S. Pitale, H. C. Swart, *Journal of Alloys and Compounds*, **508** (2010) 262 - 265.

[7] H. M. Chenari, H. F. Moafi and O. Rezaee, *Materiasl Research*, **19** (2016) 548 - 554.

[8] R. K. Tamrakar and V. Dubey, *Journal of Taibah University of Sciences*, **10** (2016) 317 - 323.

[9] I. Ahemen, A. N. Amah, B. E. AttahDaniel, A.Y. Fasasi, *Nanoscience and Nanotechnology*, **4** (2014) 7 - 15.

[10] S. Som, S. K. Sharma and T Shripathi, *Journal of Fluorescence*, **23** (2013) 439 - 450.

[11] N. Dhananjaya, H. Nagabhushana, B. M. Nagabhushana, B. Rudraswamy, C. Shivhakumara and R. P. S Chakradhar, *Bulletin of Materials Science*, **35** (2012) 519 - 527.

[12] V. P. Pawade, N. S. Dhoble and S. J. Dhoble, *Materials Research Express*, **2** (2015) 095501 doi:10.1088/2053-1591/2/9/095501.

[13] G. S. Weon, P. Miso, K. Jinhyoung, W. J. Sang, C. Insu and S. Youngku, *Thin Solid Film*, **565** (2014) 293 - 299.

[14] S. K. Sharma, S. S. Pitale, M. M. Malik, R. N. Dubey and M. S. Qureshi, *Journal of Luminescence*, **129** (2009) 140 - 147.

[15] J. Zhong, W. Zhuang, X. Xing, R. Liu, Y. Li, Y. Liu and Y. Hu, *Journal of Physical Chemistry C*, **119** (2015) 5562 - 5569.

[16] J. Zhou, Z. Xia, M. Yang and K. Shen, *Journal of Materials Chemistry*, **22** (2012) 21935 - 21941.

[17] Y. Chen, K. W. Cheahand and M. Gong, *Journal of Luminescence*, **131** (2011) 1589 - 1593.

[18] J. Li, X. Li, H. Xing, Y. Zhang, A. Yang, Y. Pan and W. Liu, *Journal of Materials Science: Materials Electronics*, **28** (2017) 4738 - 4743.

[19] X. Zhang, J. Pan and F. Mo, *Journal of Electronic Materials*, **46** (2017) doi: 10.1007/s11664-017-5371-6.

[20] H. Yi, L. Wu, L. Wu, L. Zhao, Z. Xia, Y. Zhang, Y. Kong and J. Xu, *Inorganic Chemistry*, **55** (2016) 6487 - 6495.

[21] R.S. Yadav and S.B. Rai, *Journal of Alloys and Compounds*, **700** (2017) 228 - 237.

[22] A. M. Srivastava, A. A. Setlur, H. A. Comanzo, Y. Gao, M. E. Hannah, J. A. Hughes, U. Happek, *Optical Materials*, **30** (2008) 1499 - 1503.

[23] I. P. Sahu, D. P. Bisen, R. K. Tamrakar, *International Journal of Luminescence and applications*, **6** (2016) 25 - 34.

Chapter 7

Synthesis and photoluminescent properties of dysprosium doped BaB_8O_{13} phosphor

7.1 Introduction

In recent years, rare earth ion doped inorganic luminescent materials have been extensively studied in the fields of materials science, physics, chemistry and life sciences due to their various potential applications in light emitting devices (*e.g.*, cathode ray tubes, vacuum fluorescent displays, and field emission displays), lighting gadgets (*e.g.*, fluorescent tubes and white-light emitting diodes), solid-state lasers, biological labelling, X-ray, medical devices, ionization radiation and so on [1]. Among these applications, white light emitting diodes (w-LEDs) have been considered to be the next generation illumination sources in the field of solid-state lighting instead of traditional incandescent and currently implemented fluorescent lamps due to their numerous advantages such as small size, high energy efficiency, energy-saving, robustness, high brightness, fast switching, longer life time (>100000 h) and environmental friendliness [2, 3]. Nowadays, single-phase full-color phosphors are being developed as photoluminescence phosphors for white light-emitting diodes (w-LEDs). White light emission resulted from a single-phase phosphor is expected to obtain high luminous efficacy in comparison with that from two or three phosphors, because it does not show multi-phosphors re-absorption of emission colors. Therefore, single phase white-emitting phosphors are required for UV-pumped w-LEDs to improve the luminescence reproducibility and efficiency [4].

RE (rare earths)-doped inorganic materials are important for LED technology due to their ability to convert electromagnetic radiation (VUV and UV) into visible light. Because the 4f electrons of RE

ions are shielded by the outer 5s and 5p electrons, the intra-4f emission spectra of RE ions are characterized by narrow lines with high color purity. Recently, the development of RE^{3+} ions(such as Dy^{3+}, Sm^{3+}, and Tb^{3+}) activated novel inorganic phosphors have attracted more attention due to their potential applications in different optical display systems and lighting [5] .Trivalent dysprosium ion (Dy^{3+})-doped phosphors exhibit intense blue (484 nm) and yellow (575 nm) emissions and generate white-light emission; thus, Dy^{3+}-doped phosphors have been developed as single-phase full-color phosphors [6, 7, 8].

Recently, Dy^{3+}-doped phosphors have been investigated for many hosts such as phosphates [9], tungstate [10], vanadates [11], molybdates [12], silicates [13], aluminates [14] and borates [15]. Among these hosts, borates possess large electronic band gaps, attractive nonlinear optical (NLO) properties, chemical and environmental stability, and mechanical strength. Borates have strong absorption in vacuum ultra violet and this makes them strong phosphors, which give bright emission [16]. Different borate host materials doped Dy^{3+} such as $Ca_3B_2O_6$: Dy^{3+} [17], $GdAl_3(BO_3)_4$: Dy^{3+} [18], $NaSrBO_3$: Dy^{3+} [19], $LiSr_4(BO_3)_3$: Dy^{3+} [20] and $NaSr_4(BO_3)_3$: Dy^{3+} [21] were studied for use in LEDs.

It is known that the control of the particles size in a crystalline system can effect in remarkable modification of physical, chemical, and mechanical properties compared to those of bulk due to the effect of surface-to-volume ratio of particles. The modification of luminescence properties can be brought by imperfections using different preparation techniques, different capping agents and use of suitable sensitizer, etc. Different types and sizes of luminescent particles are now being synthesized via several physical and chemical methods such as the precipitation method, hydrothermal method, solid-state reaction method, laser synthesis, combustion synthesis, sol-gel method and microwave assisted chemical synthesis [22]. Combustion synthesis is cost effective, one step, and low temperature method for the synthesis of borates.

In this chapter, structure, particle morphology and luminescent properties of BaB_8O_{13}: $x$$Dy^{3+}$ with varying concentration of Dy^{3+} (x = 0.005, 0.01, 0.02, 0.03, 0.04 and 0.05) phosphors are presented. Solution combustion method was used to prepare the powder phosphors. Near white light emission when excited at 350 nm source was observed, and the CIE coordinates and correlated color temperature were also calculated to check the suitability of the prepared phosphors for LED applications.

7.2 Experimental

7.2.1 Preparations

Powder samples of BaB_8O_{13}: xDy^{3+} (x = 0.005, 0.01, 0.02, 0.04 and 0.05) were synthesized by a solution combustion method. The following precursors all in analytical purity were used: barium nitrate [$Ba(NO_3)_2$], boric acid [H_3BO_3], dysprosium nitrate hydrate [$Dy(NO_3)_3$. xH_2O], ammonium nitrate [NH_4NO_3] and urea [NH_2CONH_2]. In this experiment, NH_4NO_3 was used as an oxidizer while NH_2CONH_2 was used as a fuel. The stoichiometric amounts of reactants were mixed in a beaker with 10 mL of de-ionized water and stirred vigorously using a magnetic stirrer on a hot plate maintained at a temperature of 70 ^oC for 30 min. The resulting solution was then transferred to a crucible and introduced into a muffle furnace preheated to 600 ^oC. Within a few minutes, the solution boiled and ignited to produce a self-propagating flame. The entire combustion process was completed in less than 5 min but the crucible was left in the furnace for 10 min to ensure that decomposition is complete. After 10 min the crucible was removed from the furnace and allowed to cool to room temperature. The combustion ashes of the powder samples were ground gently into fine powders using pestle and mortar. The powders were post annealed at 800 $^{\circ}C$ for 5 hours in a muffle furnace.

7.2.2 Characterizations

The structure of the powder phosphors was analysed using a Bruker D8 Advanced X−ray diffractometer (XRD) equipped with a monochromatic *CuKα* radiation. Fourier transform infrared (FTIR) analysis was performed using a Perkin Elmer Spectrum 100 FTIR spectrometer. Morphology was analyzed using Jeol JSM 7800F thermal field emission scanning electron microscope (FE-SEM) and the chemical composition analysis was carried out using an Oxford Instruments AzTEC energy dispersive spectrometer (EDS) attached to the FE-SEM. Room temperature photoluminescence (PL emission and PL excitation) spectra were recorded using Varian Cary Eclipse fluorescence spectrophotometer using xenon lamp as an excitation source and 325 nm He-Cd laser.

7.3 Results and discussion

7.3.1 Structure and morphology

The X-ray diffraction (XRD) pattern of BaB_8O_{13}: xDy^{3+} (x = 0.005, 0.01, 0.02, 0.04 and 0.05) powder phosphors are shown in **figure 7.1**. It is obvious that most diffraction peaks can be indexed with the Joint Committee on Powder Diffraction Standards (JCPDS) card number 20-0027 indicating that it is almost single-phase structure. The intense XRD diffraction peaks were indexed to the standard orthorhombic structure of BaB_8O_{13} referenced in JCPDS card number 20-0027. The additional peaks marked with asterisks (*) are attributed to the unreacted precursors during the combustion reaction [23]. It is also observed from the XRD patterns that the diffraction peaks are broad and also show a slight shift to the lower 2θ angles. This change in the diffraction peaks may be due to the lattice strain or lattice defects [24]. The crystallite sizes of the BaB_8O_{13}: xDy^{3+} (x = 0.005, 0.01, 0.02, 0.04 and 0.05) powder phosphors were estimated by Debye Scherrer's equation: [25]:

$$D = \frac{k\lambda}{\beta \cos\theta} \tag{7.1}$$

where D is the crystallite size; k is the shape factor (k = 0.9); λ is wavelength of the X-ray radiation (0.154 nm for Cu-K radiation); θ is Bragg diffraction angle and β is the broadening of the diffraction peak measured at half of its maximum intensity (in radians). The estimated crystallite size values are presented in **table 7.1**. The lattice parameters a, b, c and volume of the prepared BaB_8O_{13}: xDy^{3+} (x = 0.005, 0.01, 0.02, 0.04 and 0.05) powder phosphors were calculated and compared to the theoretical values from the JCPDS card. The calculated experimental values were found to be higher than the theoretical values.

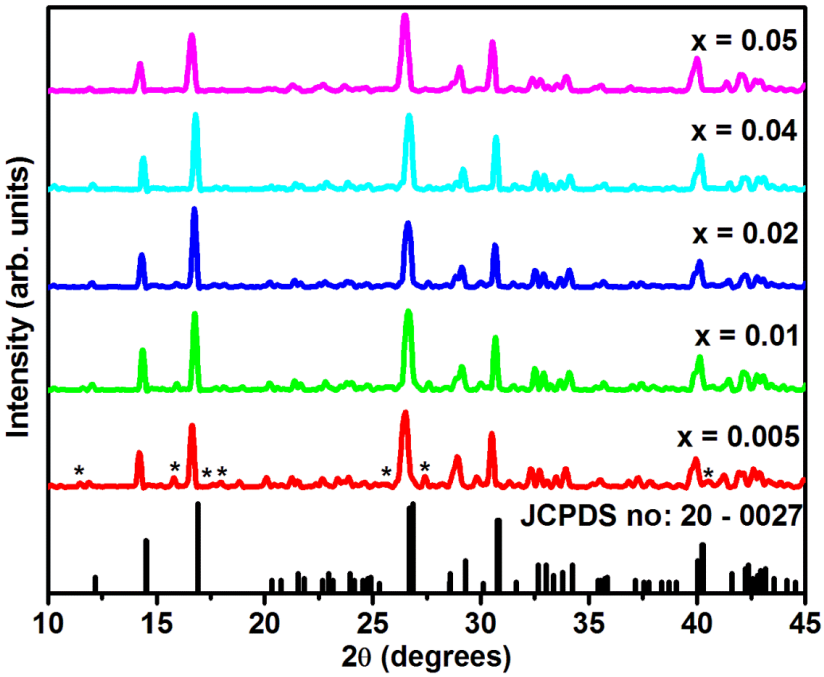

Figure 7.1: XRD pattern of BaB_8O_{13}: xDy^{3+} (x = 0.005, 0.01, 0.02, 0.04 and 0.05) powder phosphors.

Williamson-Hall method is a useful method to calculate the crystallite size and lattice strain which arises from crystal imperfections. In this method, the crystallite size and lattice strain are calculated from the XRD peak broadening [26]:

$$\beta_{hkl} = \beta_{inst} + \beta_{size} + \beta_{strain} \tag{7.2}$$

$$\beta = \beta_{size} + \beta_{strain} \tag{7.3}$$

where β_{hkl} is the FWHM from XRD peaks and βsize and βstrain are the crystallite size and strain broadening, respectively. In the Hall–Williamson method, it is assumed that the line broadening of a Bragg reflection originating from the small crystallite size follows the Scherrer (equation 7.1). Also, the strain-induced broadening is given by the Wilson formula as [26, 27]:

$$\beta = 4\varepsilon \tan\theta \tag{7.4}$$

where ε is the root mean square value of the microstrain. Therefore, (equation 7.3) becomes

$$\beta = \frac{k\lambda}{D\cos\theta} + 4\varepsilon\tan\theta \quad (7.5)$$

By rearranging the above equation, we get:

$$\beta\cos\theta = \frac{k\lambda}{D} + 4\varepsilon\sin\theta \quad (7.6)$$

Where β is the full width at half maximum of peak in radian, θ is the diffraction angle, λ is the wavelength of X-ray and *k* is the Scherrer constant equal to 0.9. Equation (7.6) represents the first correction to Debye – Scherrer's method, named uniform deformation model (UDM), where the strain is assumed to be uniform in all crystallographic directions, thus considering the isotropic nature of the crystal, where all the material properties are independent of the direction along which they are measured [28]. By plotting the value of βcosθ as a function of 4sinθ, the crystallite size and lattice strain can be estimated. The slope of the line gives the lattice strain ε, and the crystallite size D can be evaluated from the intercept. The crystalline properties of BaB_8O_{13}: xDy^{3+} (x = 0.005, 0.01, 0.02, 0.04 and 0.05) powder phosphors were obtained by using Williamson-Hall Method. The (βcosθ) was plotted as a function of (4sinθ) for the preferred orientation peaks of BaB_8O_{13}: xDy^{3+} (x = 0.005, 0.01, 0.02, 0.04 and 0.05) powder phosphors and the plots are shown in **figure 7.2**. The estimated strain and crystallite size values are also presented in **table 7.1**. The larger crystallite sizes obtained using W-H plots are more accurate because Scherrer's equation does not take into consideration the effect of lattice strain in the line broadening [23].

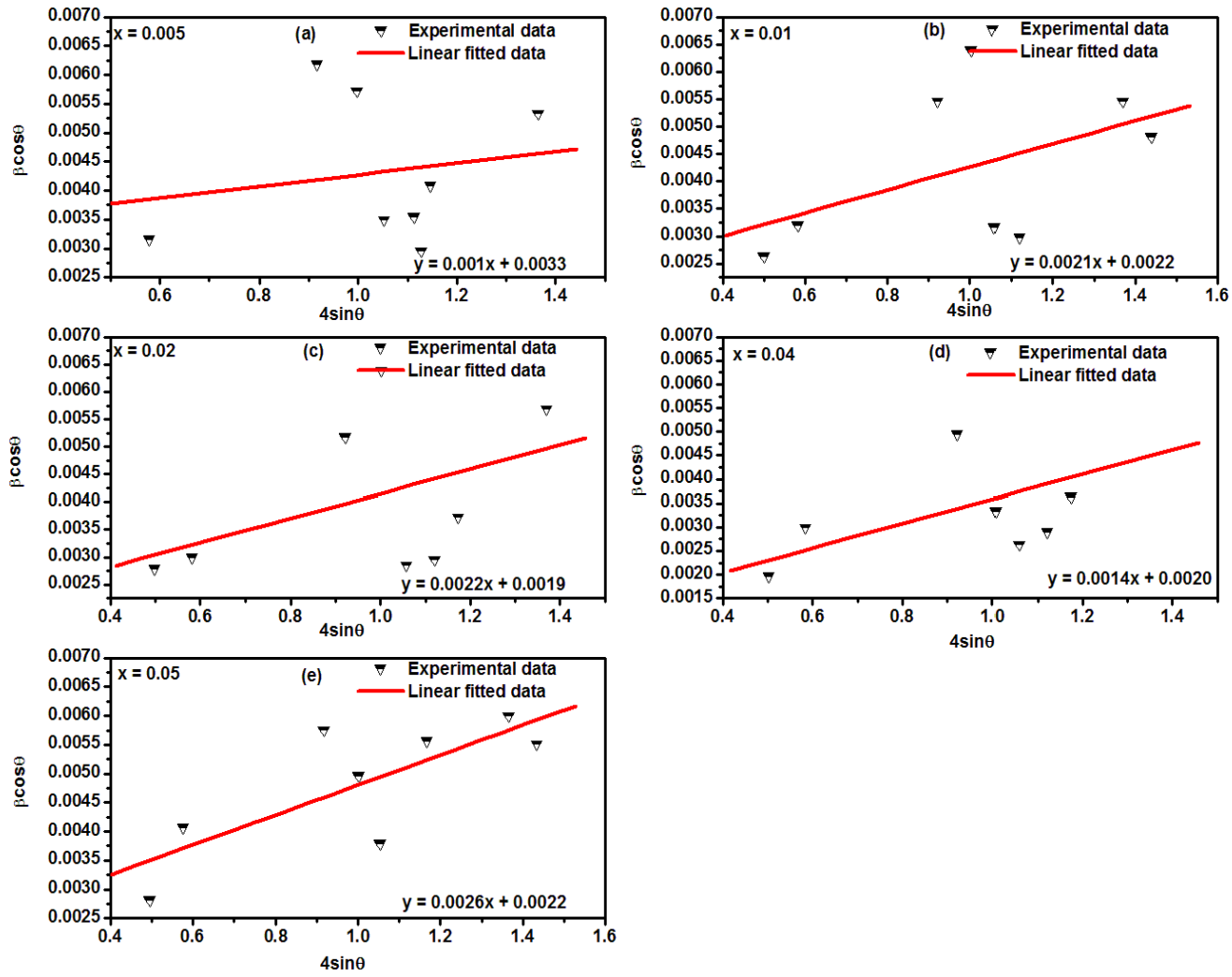

Figure 7.2: Williamson-Hall plots of BaB_8O_{13}: xDy^{3+} (x = 0.005, 0.01, 0.02, 0.04 and 0.05) powder phosphors.

Table 7.1: Structural parameters of BaB_8O_{13}: $x$$Dy^{3+}$ (x = 0.005, 0.01, 0.02, 0.04 and 0.05) powder phosphors together with the theoretical values.

Sample name	Crystallite size D (nm)		Lattice constants (Å)			Microstrain ($\times10^{-3}$)	Cell volume (Å^3)
BaB_8O_{13}: $x$$Dy^{3+}$	Scherer's	W-H	a	b	c	ε	v
JCDPS card	-	-	8.55	17.35	13.21	-	1959.98
x = 0.005	34	42	8.59	17.57	13.59	1.0	2050.38
x = 0.01	36	63	8.56	17.46	13.45	2.1	2010.20
x = 0.02	38	73	8.57	17.48	13.46	2.2	2017.59
x = 0.04	44	69	8.79	17.46	13.19	1.4	2023.85
x = 0.05	31	63	8.59	17.56	13.62	2.6	2054.46

Figure 7.3 shows the Fourier Transform Infra-red (FTIR) spectrum of BaB_8O_{13}: *0.005*Dy^{3+} powder phosphor. The spectrum exhibit broad absorptions in the 650 - 1600 cm^{-1} range. All the bands in the 1200 - 1600 cm^{-1} range correspond to the stretching of the B–O bonds of BO_3 units while the bands in the region of 800 - 1200 cm^{-1} correspond to the B–O bond stretching of tetrahedral BO_4 units. All the bands below 800 cm^{-1} correspond to the B–O–B bending vibrations of borate networks [29]. Comparing the FTIR spectra of BaB_8O_{13}: *0.005*Dy^{3+} and that of BaB_8O_{13}: $x$$Dy^{3+}$ (x = 0.01, 0.02, 0.03, 0.04 and 0.05) (not shown), it was observed that there is no change in the spectrum structure, and only slight difference in intensity was observed. It can be concluded that incorporating different concentration Dy^{3+} ions in the BaB_8O_{13} host matrix did not influence the main structure or form any type of bonds in the development of the powder phosphors, which is in agreement with the XRD spectra.

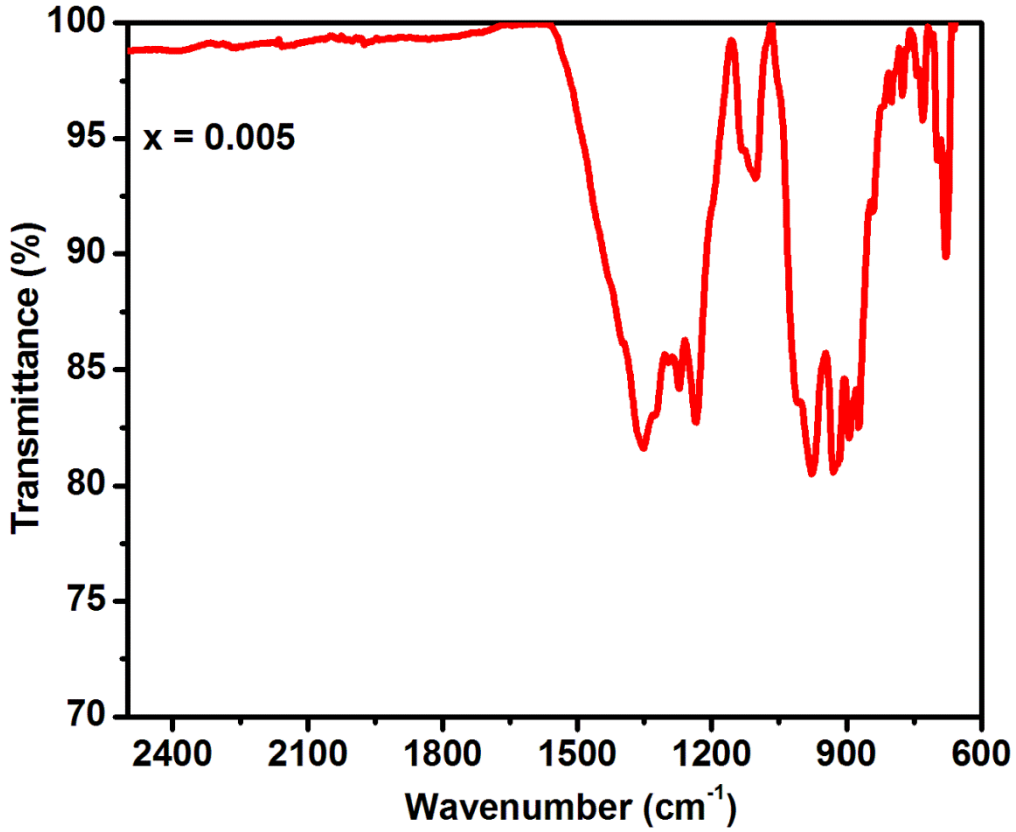

Figure 7.3: FTIR spectrum of BaB_8O_{13}: *0.005*Dy^{3+} powder phosphor.

Scanning electron microscopy (SEM) images of BaB_8O_{13}: *0.005*Dy^{3+} powder phosphors taken at different magnifications are shown in **figure 7.4** (**a-c**). The images show that the powder phosphor is made of a mixture of irregular and near spherical particles that are agglomerated together. The surface of the SEM micrograph shows lots of voids and pores due to the large amount of gases such as NO_2 and CO_2 that evolve during combustion method [30]. Dispersive X-ray spectroscopy (EDS) spectrum of BaB_8O_{13}: *0.005*Dy^{3+} powder phosphor is shown in **Figure 7.4** (**d**). The spectrum confirms the presence of barium (Ba), boron (B), oxygen (O) and dysprosium (Dy) elements. The inset in **figure 7.4** (**d**) shows that the concentration of Ba by weight exceeds that of all other elements and the least concentration (also by weight) was recorded from Dy dopant ions and this is probably due to their relatively low concentrations. The EDS elemental mapping of BaB_8O_{13}: *0.005*Dy^{3+} powder phosphor is shown in **figure 7.5**. From the elemental mapping results of (see **figure 7.5** (**a**)), it is clear that the elemental compositions of Ba, B, O and Dy^{3+} were uniformly distributed. The color mapping of the positive ions such as

Ba, B and Dy are shown in **figure 7.5** (**b, c and d**), respectively, while the negative ion such as O is shown in **figure 7.5** (**e**). The EDS spectrum and the corresponding EDS mapping confirms the formation of BaB_8O_{13}: Dy^{3+} powder phosphor and a homogenous distribution of the elements present on the surface of the phosphor.

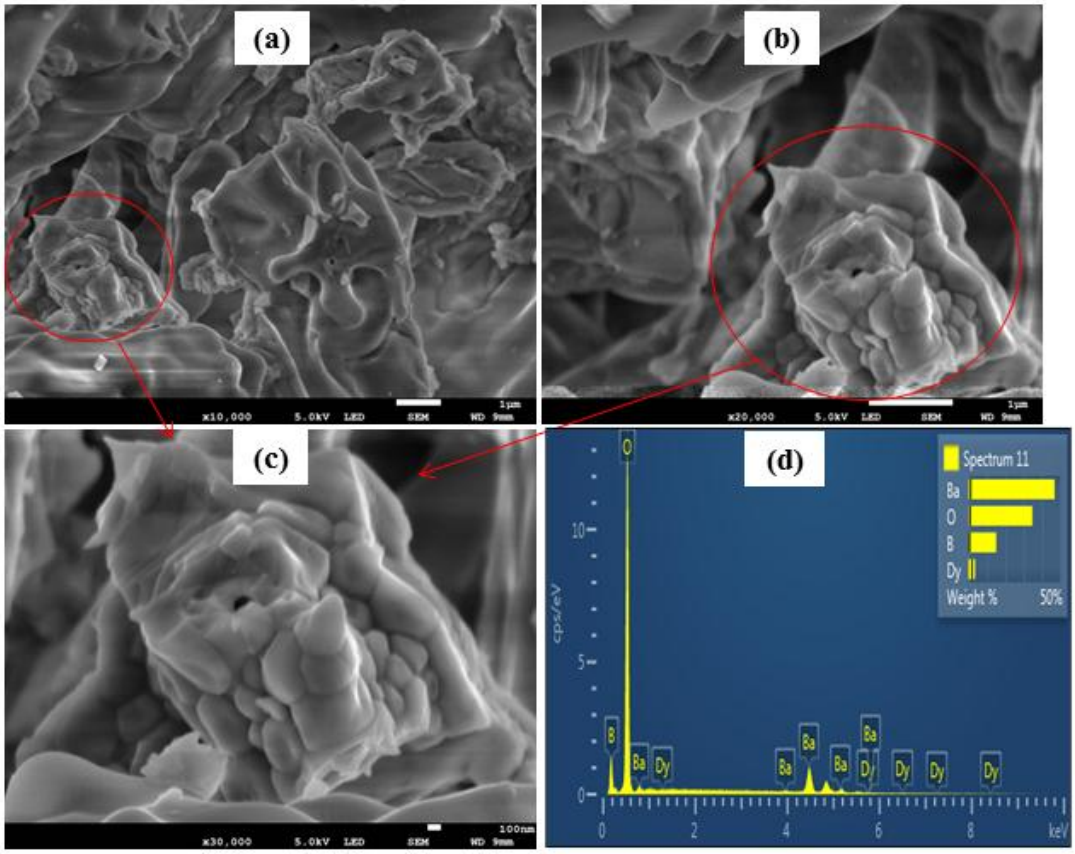

Figure 7.4: a-c) SEM images at different magnifications and **d**) EDS spectrum of BaB_8O_{13}: *0.005*Dy^{3+} powder phosphor.

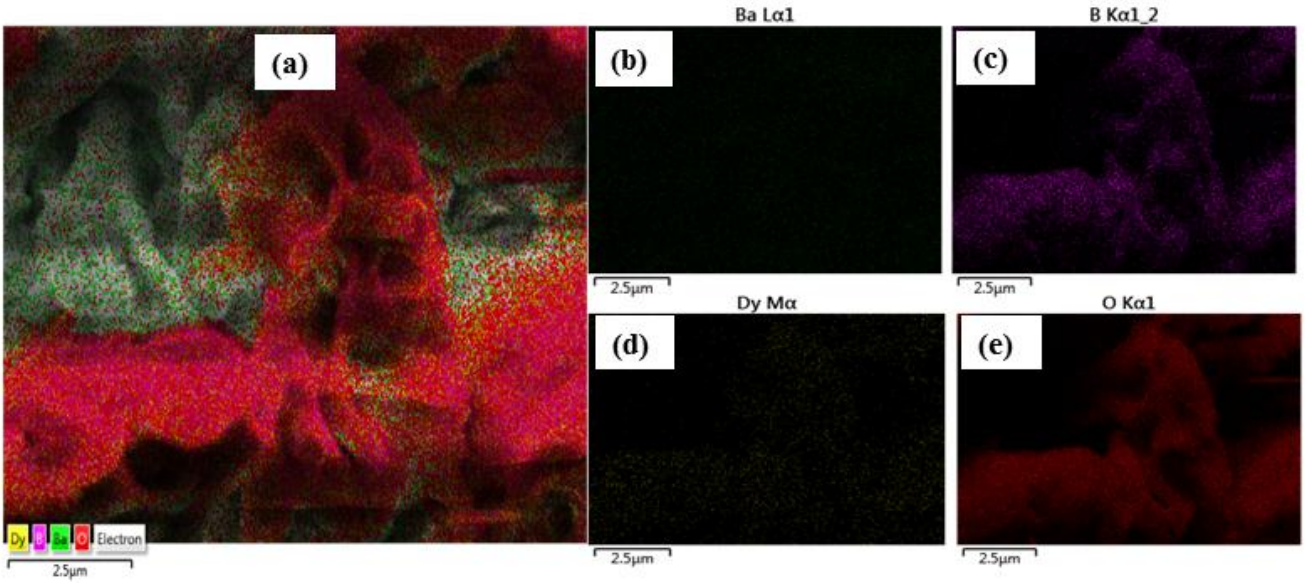

Figure 7.5: EDS elemental mapping of BaB_8O_{13}: *0.005*Dy^{3+} powder phosphor.

7.3.2 Photoluminescence studies

PL excitation and PL emission spectra of BaB_8O_{13}: *0.005*Dy^{3+} powder phosphors are shown in **figure 7.6** (**a**). The excitation spectrum consists of several peaks in the range of 250 – 500 nm obtained by monitoring the emission at 574 nm. The excitation peaks are located at 297, 325, 350, 386, 427, 453 and 473 nm and they are assigned to the transition from the ground $^6H_{15/2}$ state to the excited $^4D_{7/2}$, $^4M_{17/2}$, $^9P_{7/2}$, $^4I1_{3/2}$, $^4G1_{1/2}$, $^4I_{15/2}$ and $^4F_{9/2}$ states of Dy^{3+} respectively [31]. Thus, it is clear from the excitation spectrum that the BaB_8O_{13}: *0.005*Dy^{3+} powder phosphor can be effectively excited by ultraviolet (297, 325, 350 and 386 nm) and blue (427, 453 and 473 nm) light. The excitation peak at 350 nm corresponding to the $^6H_{15/2} \rightarrow {}^6P_{7/2}$ transition was found to be dominant among the other 4f-4f transition peaks in the excitation spectrum. The emission spectrum of BaB_8O_{13}: *0.005*Dy^{3+} powder phosphor under the excitation of 350 nm shows two intense emission peaks at 480 nm and 574 nm, and other less intense peaks at 661 nm and 752 nm. The blue emission at 480 nm and yellow emission at 574 nm are due to $^4F_{9/2} \rightarrow {}^6H_{15/2}$ and $^4F_{9/2} \rightarrow {}^6H_{13/2}$ transitions of Dy^{3+}, respectively [32, 33]. It is known that the yellow emission due to the hypersensitive $^4F_{9/2} \rightarrow {}^6H_{13/2}$ transition belongs to the electric dipole transition ($\Delta J = 2$) and its intensity depends on the crystal field around Dy^{3+}. However, blue

emission due to the $^4F_{9/2} \rightarrow {}^6H_{15/2}$ transition belongs to magnetic dipole transition which is hardly affected by chemical environment of Dy^{3+} ion. So the Dy^{3+} site can be of low symmetry with no inversion centers because the emission of 4 $^4F_{9/2} \rightarrow {}^6H_{13/2}$ transition is more intense than that of $^4F_{9/2} \rightarrow {}^6H_{15/2}$ transition [34, 35]. Moreover, the ionic radius of Dy^{3+} (r = 0.91 Å) is smaller than the ionic radius of Ba^{2+} (r = 1.35 Å) so it can easily occupy the Ba^{2+} site with low symmetry and hence, the intensity of $^4F_{9/2} \rightarrow {}^6H_{13/2}$ transition is more dominant in comparison to $^4F_{9/2} \rightarrow {}^6H_{15/2}$ transition [36]. In order to obtain the optimal Dy^{3+} doping concentration in BaB_8O_{13} host matrix, the PL emission spectra of BaB_8O_{13}: xDy^{3+} (x = 0.005, 0.01, 0.02, 0.03, 0.04 and 0.05) powder phosphors are plotted and shown in **figure 7.6** (**b**). The optimal doping concentration of Dy^{3+} in BaB_8O_{13}: xDy^{3+} is found to be x = 0.005, which is the lowest concentration used. As the concentration of Dy^{3+} increases, the PL intensity decreases due to concentration quenching [37]. **Figure 7.6** (**c**) shows the concentration quenching curve of BaB_8O_{13}: xDy^{3+} (x = 0.005, 0.01, 0.02, 0.03, 0.04 and 0.05) powder phosphors. As the concentration increases, the distance between Dy^{3+} ions becomes smaller, leading to a higher probability of energy transfer among Dy^{3+} ions. Concentration quenching is mainly caused by the non-radiative energy transfer among Dy^{3+} ions, which occurs as a result of an exchange interaction, radiation re-absorption, or a multipole – multipole interaction [38]. The type of the interaction mechanism can be understood by obtaining the critical distance (R_c) between the neighboring Dy^{3+} ions. According to Blasse theory, the critical distance (R_c) can be obtained by equation 7.7 [39, 40]:

$$R_c = 2\left[\frac{3V}{4\pi x_c N}\right]^{1/3} \qquad (7.7)$$

Where V is the volume of one unit cell, N is the number of cations in the unit cell and x_c is the critical concentration of the activator ion. According to the crystal structure of $LiBaBO_3$ V = 2050.38 Å^3, N = 8 and x_c = 0.005, respectively. The calculated value of critical distance (R_c) between Dy^{3+} - Dy^{3+} ions is 46 Å. If the value of Dy^{3+} - Dy^{3+} distance is greater than 5 Å, the exchange interaction become ineffective and only the multipole – multipole interaction is the major cause of concentration quenching of Dy^{3+} in the BaB_8O_{13}: xDy^{3+} phosphors [41]. The value of R_c for BaB_8O_{13}: xDy^{3+} powder phosphor was calculated to be 46 Å, which shows that

the multipole interaction plays an important role in the concentration quenching mechanism of Dy^{3+} in the powder phosphor.

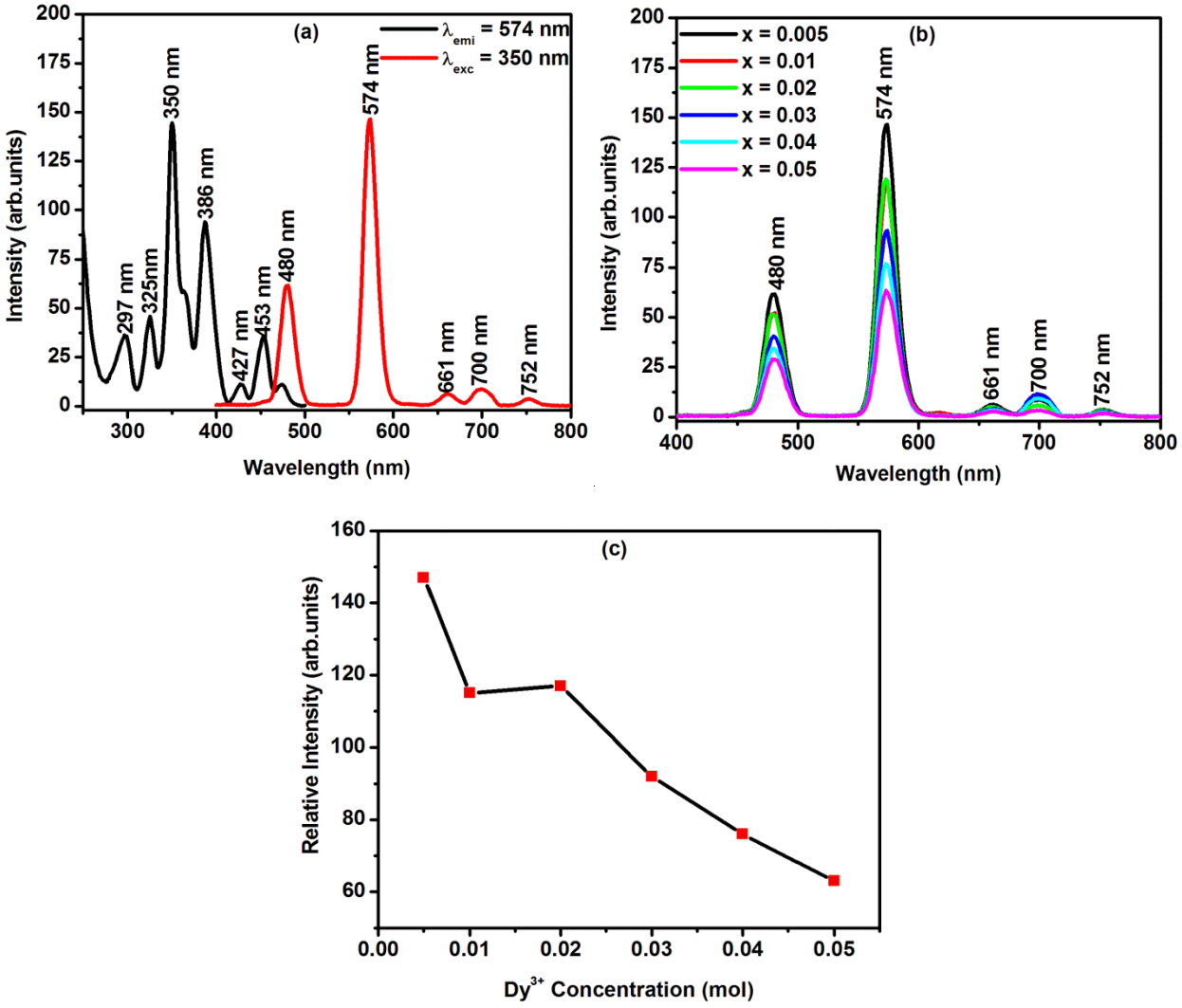

Figure 7.6: a) PL excitation and PL emission spectra of BaB_8O_{13}: *0.005*Dy^{3+} powder phosphor, **b**) PL emission spectra of BaB_8O_{13}: *x*Dy^{3+} (*x* = 0.005, 0.01, 0.02, 0.03, 0.04 and 0.05) powder phosphors and **c**) the variation of the luminescence intensity with the different concentrations of Dy^{3+}.

The strength of the multipolar interaction can be determined from the change in the emission intensity from the emitting level which has the multipolar interaction. When the concentration of

the dopant is sufficiently high, the luminescence intensity *I* and the dopant concentration *x* are related by the equation from the theory of Dexter [42]:

$$\frac{I}{x} = k\left[1+\beta(x)^{Q/3}\right]^{-1} \tag{7.8}$$

This equation can be approximated as,

$$\log\frac{I}{x} = c - \frac{Q}{3}\log x \tag{7.9}$$

Where, *k*, β and *c* are constants for the same excitation condition for the given host, *x* is the activator concentration which is greater than the critical concentration, Q is the series of multipole interaction for dipole–dipole (d–d), dipole–quadrupole (d–q) and quadrupole–quadrupole (q–q) interactions when the values of Q are 6, 8 and 10, respectively [43]. The value of Q can be obtained from the slope (-Q/3) of the linear line of the plot log (*I*/*x*) vs log(*x*). The relation between log (*I*/*x*) and log(*x*) in BaB_8O_{13}: xDy^{3+} powder phosphor is shown in **figure 7.7**. The presented curve is almost linear and the fitted line slope is -1.35. Then, the calculated value of Q is 4.05, which approaches 6, indicating that the electric dipole–dipole interaction is the main mechanism for concentration quenching of BaB_8O_{13}: xDy^{3+} powder phosphor.

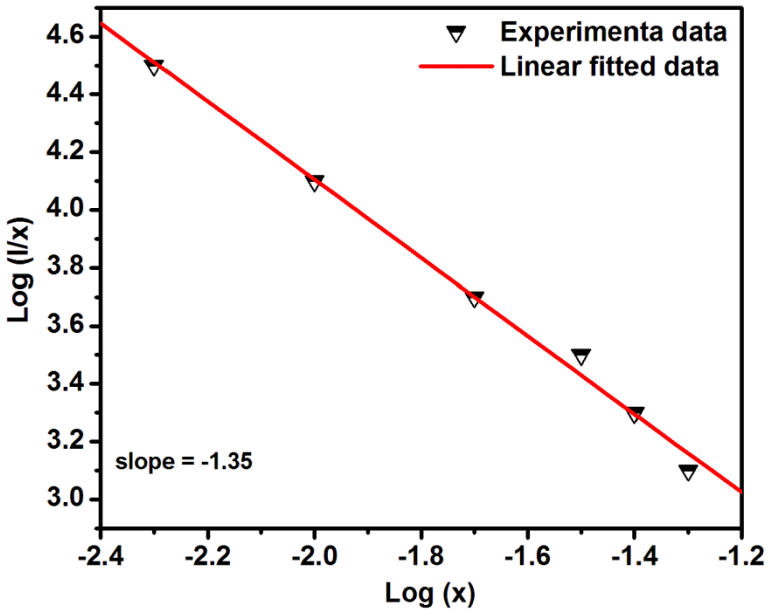

Figure 7.7: Log (*I/x*) versus log (*x*) of BaB_8O_{13}: *x*Dy^{3+} powder phosphors.

The PL emission spectrum of BaB_8O_{13}: *0.005*Dy^{3+} powder phosphor excited by 325 nm He-Cd laser is shown in **figure 7.8** (**a**). The spectrum is consists of a broad band in the range of 360 – 465 nm, which is attributed to the self-trapped emission (STE) of BaB_8O_{13} host. Intense emission peaks located at 478 nm and 572 nm together with the less intense peaks located at 660 and 751 nm were observed. The blue emission (478 nm) and the yellow emission (572 nm) are attributed to $^4F_{9/2} \rightarrow {}^6H_{15/2}$ and $^4F_{9/2} \rightarrow {}^6H_{13/2}$ transitions of Dy^{3+}, respectively [44]. The red emission (660 nm) and brownish red (751 nm) are attributed to $^4F_{9/2} \rightarrow {}^6H_{11/2}$ and $^4F_{9/2} \rightarrow {}^6H_{9/2}$ transitions of Dy^{3+}, respectively. It is also well known that the $^4F_{9/2} \rightarrow {}^6H_{15/2}$ (blue) transition hardly varies with the environment, while the $^4F_{9/2} \rightarrow {}^6H_{13/2}$ (yellow) is the hypersensitive transition, which is strongly influenced by the ligand environment. The relative intensities of these two emission bands depend strongly on the local symmetry of Dy^{3+} ions [45]. The variation of the luminescence intensity due to different concentrations of Dy^{3+} plot under 325 nm He-Cd laser is shown in **figure 7.8** (**b**). The highest PL intensity is observed for $x = 0.005$, which is the lowest concentration used.

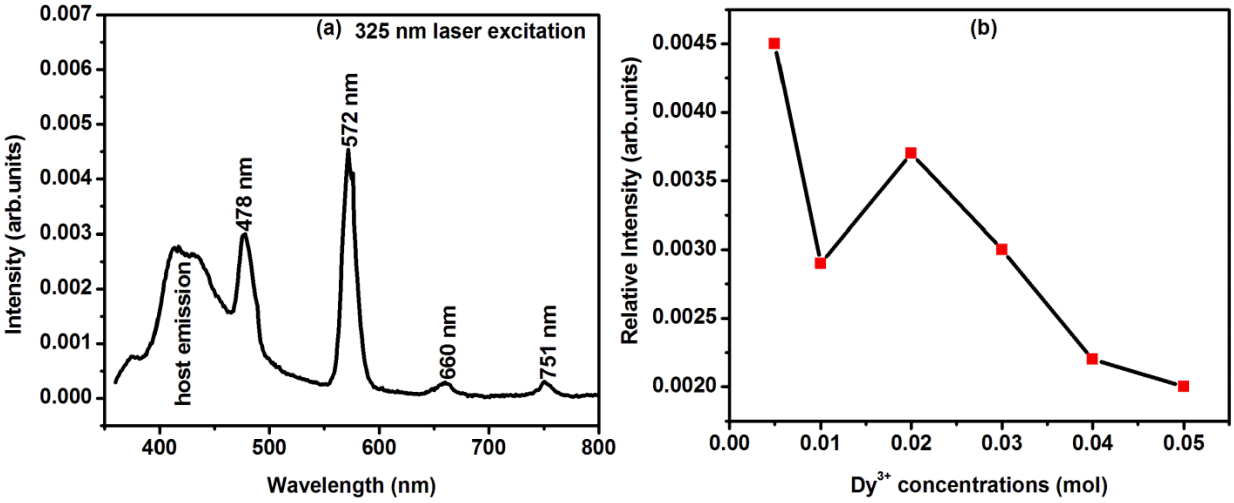

Figure 7.8: a) PL emission spectrum of BaB_8O_{13}: *0.005*Dy^{3+} powder phosphor excited by 325 nm He-Cd laser and **b**) the variation of the luminescence intensity with the different concentrations of Dy^{3+}.

Figure 7.9 represents the Commision Internationale de l'Eclairage (CIE) 1931 color space chromaticity diagram of BaB_8O_{13}: *0.005*Dy^{3+} powder phosphors excited at 350 nm and 325 nm He-Cd laser. The emission color coordinates of BaB_8O_{13}: *x*Dy^{3+} (*x* = 0.005, 0.01, 0.02, 0.03, 0.04 and 0.05) powder phosphors were calculated using the CIE calculator software [46]. The obtained color coordinates of BaB_8O_{13}: *x*Dy^{3+} (*x* = 0.005, 0.01, 0.02, 0.03, 0.04 and 0.05) powder phosphors excited at 350 nm lies in the yellowish white region of the spectrum and their calculated color coordinates are tabulated in **table 7.2**. The color coordinates of BaB_8O_{13}: *0.005*Dy^{3+} powder phosphor excited at 325 nm He-Cd laser lies in the white region of the spectrum with the coordinates (0.331, 0.365), which is close to that of the standard white coordinates (0.33, 0.33). Further, McCamy empirical formula was used to calculate the color correlated temperature (CCT) which is given by equation [47]:

$$CCT = -437n^3 + 3601n^2 - 6861n + 5514.31 \qquad (7.10)$$

where $n = (x - x_e)/(y - y_e)$ is the inverse slope line and (x_e = 0.332, y_e = 0.1858) is the epicenter. Generally, the preferred CCT values range from 3500 K to 6500 K but the range from 3000 K to

7800 K may also be accepted [48]. The calculated CCT values for BaB_8O_{13}: xDy^{3+} (x = 0.005, 0.01, 0.02, 0.03, 0.04 and 0.05) powder phosphors are tabulated in **table 7.2**. It has been found that it is difficult to generate cool white light with blue InGaN chip excited state - of - art YAG: Ce^{3+} yellow phosphor as it has correlated color temperature (CCT) of 7756 K with Commission International de I'Eclairage (CIE) chromaticity coordinates of (0.292, 0.325) [49]. CCT of BaB_8O_{13}: xDy^{3+} (x = 0.005, 0.01, 0.02, 0.03, 0.04 and 0.05) powder phosphors lies below 6000 K which indicates that the prepared powder phosphors can produce cool white light.

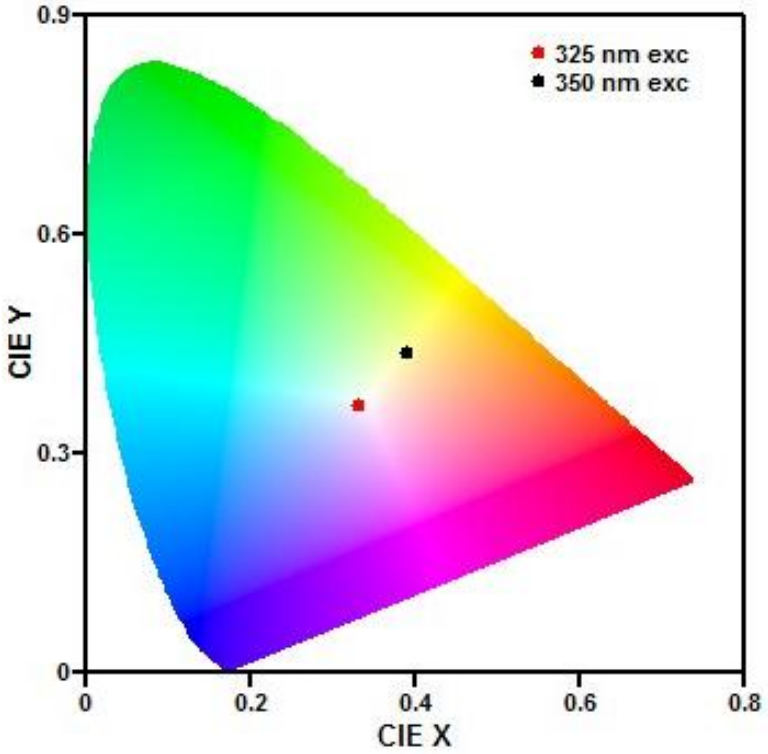

Figure 7.9: Commision Internationale de l'Eclairage (CIE) 1931 color space chromaticity diagram of BaB_8O_{13}: *0.005*Dy^{3+} powder phosphor excited by 350 nm and 325 nm He-Cd laser.

Table 7.2: CIE coordinates and color coordinates temperature of BaB_8O_{13}: xDy^{3+} (x = 0.005, 0.01, 0.02, 0.03, 0.04 and 0.05) powder phosphor.

Sample name	Excitation wavelength	Color coordinates		Color correlated temperature
BaB_8O_{13}: xDy^{3+}	λ_{exc} (nm)	x-coordinates	y-coordinates	CCT (K)
x = 0.005	350 nm	0.390	0.437	4059
x = 0.01	350 nm	0.390	0.433	4097
x = 0.02	350 nm	0.387	0.436	4175
x = 0.03	350 nm	0.391	0.436	4091
x = 0.04	350 nm	0.389	0.435	3853
x = 0.05	350 nm	0.391	0.432	4064
x = 0.005	325 nm He-Cd laser	0.331	0.365	5553

The decay curves recorded for BaB_8O_{13}: xDy^{3+} (x = 0.005, 0.01, 0.02, 0.03, 0.04 and 0.05) powder phosphor the under 350 nm excitations are shown in **figure 7.10**. The decay curves are well fitted by the following first order exponential equation [50]:

$$I = I_0 \exp\left(\frac{-t}{\tau}\right) \tag{7.11}$$

where, I_0 and I are the intensities at time zero and t seconds, respectively and τ is the lifetime. The experimental decay curves are single exponential and the decay times values observed are displayed on each spectrum as an inset. This single exponential behavior in decay measurements clearly indicate that for Dy^{3+} ions there exists only one site of symmetry in borate lattice [51]. The decrease in the decay times with increasing doping concentration provides a proof of energy transfer process between Dy^{3+} - Dy^{3+} ions [52]. A millisecond order of lifetime values of the

powder phosphors reveals the suitability of the prepared materials for the use in field emission display and light-emitting diodes applications.

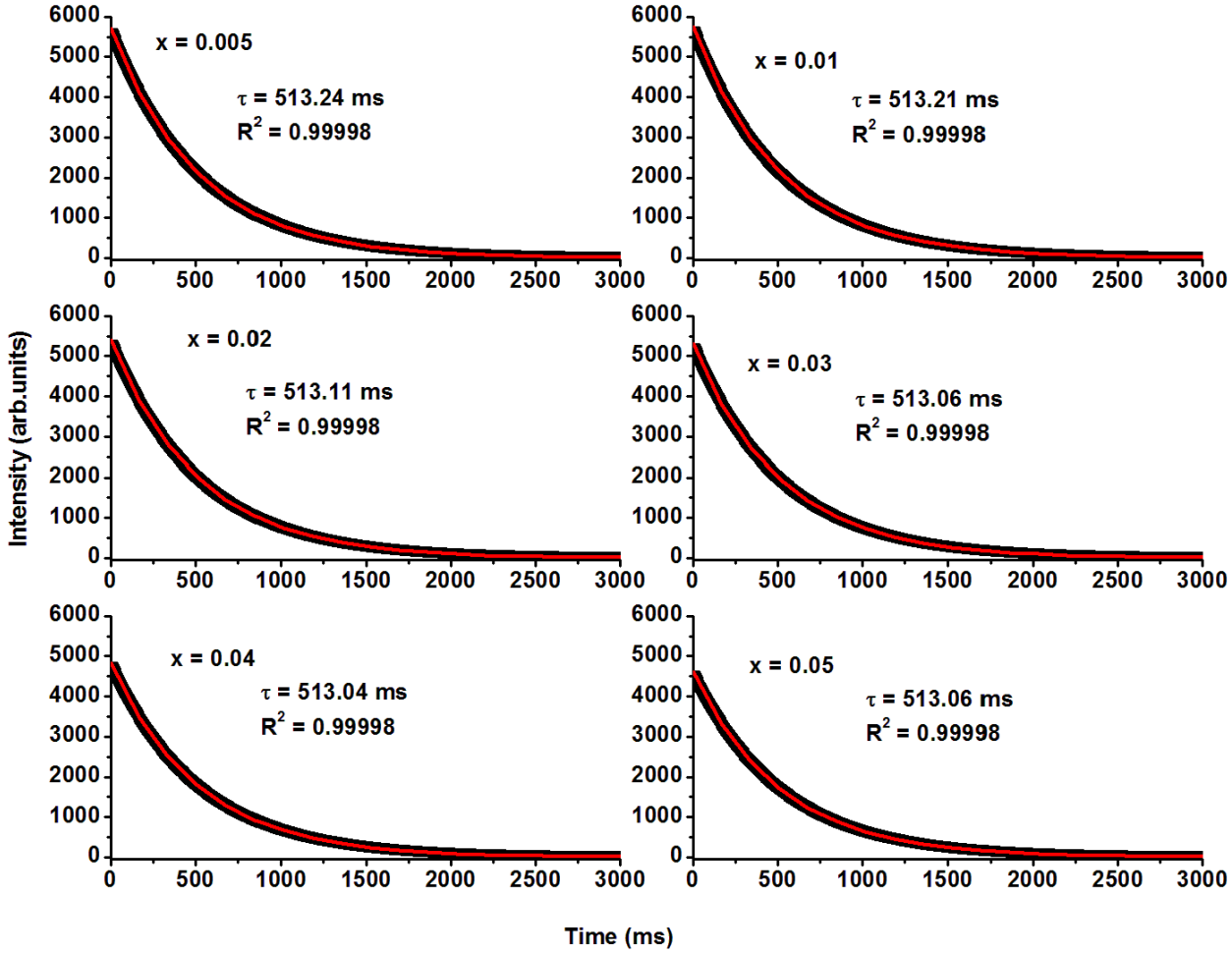

Figure 7.10: The first order fitted decay curves of BaB_8O_{13}: xDy^{3+} (x = 0.005, 0.01, 0.02, 0.03, 0.04 and 0.05) powder phosphors.

7.4 Conclusion

In summary, BaB_8O_{13}: xDy^{3+} phosphors were synthesized successfully by a solution combustion method. The study illustrated that the BaB_8O_{13}: xDy^{3+} could be excited by near ultraviolet (NUV) light 350 nm and the emission peaks are located at 480 nm (blue) and 574 nm (yellow). The

critical transfer distance of Dy^{3+} in BaB_8O_{13}: xDy^{3+} phosphor is about 46 Å and the dipole–dipole interaction is the major mechanism for the concentration quenching. The CIE chromaticity coordinates for BaB_8O_{13}: xDy^{3+} phosphors are located in the yellowish-white region. These results indicate that the BaB_8O_{13}: xDy^{3+} phosphor shows potential application in NUV white LEDs.

References

[1] A. K. Vishwakarma, K. Jha, M. Jayasimhadri, B. Sivaiah, B. Gahtoria,b and D. Haranath, *Dalton Transactions*, **44** (2015) 17166 - 17174.

[2] S. H. Lee, L. K. Bharat and J. S. Yu, *Journal of Alloys and Compounds*, **726** (2017) 698 - 706.

[3] Y. Zhang, W. Gong, J. Yu, Y. Lina and G. Ning, *Royal Society of Chemistry Advances*, **5** (2015) 96272 - 96280.

[4] Z. Zhang, X. Sun, L. Liu, Y. Peng, X. Shen , W. Zhang and D. Wang, *Ceramics International*, **39** (2013) 1723 - 1728.

[5] İ. Pekgözlü, H. Karabulut, A. Mergen and A. S. Basak, *Journal of Applied Spectroscopy*, **83** (2016) 504 - 511.

[6] Z. Zhang, L. Liu, Y. Wang, S. Song and D. Wang, *Journal of Materials Science: Material in Electronics*, **26** (2015) 4202 - 4206.

[7] B. Zhang, M. Shi, D. Zhang, Y. Guo, C. Chang and W. Song, *Journal of Materials Science: Material in Electronics*, **28** (2017) 11624 - 11630.

[8] L. Kong, X. Xiao, J. Yu, D. Mao and G. Lu, *Journal of Materials Science*, **52** (2017) 6310 -6321.

[9] G. Zhu and S. Xin, *Royal Society of Chemistry Advances*, **5** (2015) 106795 - 106799.

[10] G. Li, *Journal of Materials Science: Materials in Electronics*, **27** (2016) 11012 - 11016.

[11] P. Kumari and J. Manam, *Royal Society of Chemistry Advances*, **5** (2015) 107575 - 107584.

[12] D. Gao, Y. Li, X. Lai, Y. Wei, J. Bi, Y. Li, M. Liu, *Materials Chemistry and Physics*, **126** (2011) 391 - 397.

[13] G. Tiwari, N. Brahme, R. Sharma, D. P. Bisen, S. K. Saoa and S. J. Dhoble, *Royal Society of Chemistry Advances*, **6** (2016) 49317 - 49327.

[14] Z. Lei, X. Zhang, D. Wang, J. Chen, L. Cong, D. Meng and Y. Wang, *Journal of Materials Science: Materials in Electronics*, **27** (2016) 7089 - 7094.

[15] A. R. Beck, S. Das and J. Manam, *Journal of Materials Science: Materials in Electronics*, (2017) doi 10.1007/s10854-017-7645-4.

[16] Neharika, V. Kumar, J. Sharma, O. M. Ntwaeaborwa and H. C. Swart, *Advanced Materials Letters*, **6** (2015) 402 - 406.

[17] M. Manhas, V. Kumar, O. M. Ntwaeaborwa and H. C. Swart, *Ceramics International*, **42** (2016) 5743 - 5753.

[18] B. C. Jamalaiah and S. N. Rasool, *Materials Today: Proceedings*, **3** (2016) 4019 - 4022.

[19] A. K. Bedyal, V. Kumar, V. Sharma, F. Singh, S. P. Lochab, O. M. Ntwaeaborwa and H. C. Swart, *Journal of Material Sciences*, **49** (2014) 6404 - 6412.

[20] Z. Zhang, X. Sun, L. Liu , Y. Peng, X. Shen, W. Zhang and D. Wang, *Ceramics International*, **39** (2013) 1723 - 1728.

[21] Z. S. Khan, N. B. Ingale, S. K. Omanwar, *Optik*, **127** (2016) 6062 - 6065.

[22] M. Ferhi, S. Toumi, K. Horchani-Naifer and M. Ferid, *Journal of Alloys and Compounds*, **714** (2017) 144 - 153.

[23] M. A. Lephoto, K. G. Tshabalala, S. J Motloung, I. Ahemen and O. M. Ntwaeaborwa, *Phyica-B*, (2017) doi.org/10.1016/j.physb.2017.06.063.

[24] H. M. Chenari, H. F. Moafi and O. Rezaee, *Materials Research*, **19** (2016) 548 - 554.

[25] A. Pandey, V. Kumar, S. Som, A. Yousif, R. E. Kroon, E. Coetsee and H. C. Swart, *Applied Surface Science*, **423** (2017) 1169 - 1175.

[26] D. E. Bakeer, A. I. Abou-Aly, N. H. Mohammed, R. Awad and M. Hasebbo, *Journal of Superconductivity and Novel Magnetism*, **30** (2017) 893 - 902.

[27] B. R Kumar and B. Hymavathi, *Journal of Asian Ceramic Societies*, **5** (2017) 94 - 103.

[28] S. Aydogu, M. B. Coban and G. Cabuk, *Applied Physics A*, **123** (2017) 409 doi:10.1007/s00339-017-1027-x.

[29] D. Kumar, S. M. Rao and S. P. Singh, *Journal of Non-Crystalline Solids*, **464** (2017) 51 - 55.

[30] N. Dhananjaya, H. Nagabhushana, B. M. Nagabhushana, B. Rudraswamy, C. Shivhakumara and R. Chakradhar, *Bulletin of Materials Science*, **35** (2012) 519 - 527.

[31] S. Dutta and S. K. Sharma, *Journal of Material Sciences*, **51** (2016) 6750 - 6760.

[32] Z. Zhang, C. Han, W. Shi, Y. Kang, Y. Wang, W. Zhang and D. Wang, *Journal of Materials Science: Materials in Electronics*, **26** (2015) 1923 - 1931.

[33] D. Wu and C. Deng, *Journal of Materials Science: Materials in Electronics*, (2017) doi:10.1007/s10854-017-7538-6.

[34] B. Han, J. Zhang, P. Li, and H. Shi, *Optics and Spectroscopy*, **118** (2015) 135 - 141.

[35] S. Kumar, R. Prakash and V. Kumar, *Functional Materials Letters*, **8** (2015) 1550061 doi: 10.1142/S1793604715500617.

[36] D. K. Singh and J. Manam, *Electronic Materials Letters*, **13** (2017) 292 - 301.

[37] Y. Chen, K. W. Cheah and M. Gong, *Journal of Luminescence*, **131** (2011) 1589 - 1593.

[38] P. Kumari and J. Manam, *Journal of Materials Science: Materials in Electronics*, (2016) doi:10.1007/s10854-016-4990-7.

[39] H. Liu, L. Liao, M. S. Molokeev, Q. Guo, Y. Zhang and L. Mei, *Royal Society of Chemistry Advances*, **6** (2016) 24577 - 24583.

[40] T. Nakajima and T. Tsuchiya, *ACS Applied Materials and Interfaces*, **7** (2015) 21398 - 21407.

[41] X. Zou, L. He, R. Li, Q. Zheng, Y. Liu, C. Xu and D. Lin, *Journal of Materials Science: Materials in Electronics*, **28** (2017) 2826 - 2832.

[42] Y. Zaifa, S. Yumei, X. Qiguang and S. Jiayue, *Journal of Rare Earths*, **33** (2015) 1251 - 1255.

[43] B. Han, B. Liu, J. Zhang and H. Shi, *Journal of Materials Science: Materials in Electronics*, (2016) doi:10.1007/s10854-016-5176-z.

[44] L. Li, Y. Liu, R. Li, Z. Leng and S. Gan, *Royal Society of Chemistry Advances*, **5** (2015) 7049 - 7057.

[45] Y. P. Manwar, R. S. Palaspagar, R. P. Sonekar and S. K. Omanwar, *International Journal of Luminescence and applications*, **3** (2016) 149 - 151.

[46] I. P. Sahu, D. P. Bisen, R. K. Tamrakar, *International Journal of Luminescence and applications*, **6** (2016) 25 - 34.

[47] J. Zheng, Q. Cheng, S. Wu, Y. Zhuang, Z. Guo , Y. Lu and C. Chen, *Materials Chemistry and Physics*, **165** (2015) 168 - 176.

[48] Y. Parganiha, J. Kaur, V. Dubey, R. Shrivastava and S. J. Dhoble, *Superlattices and Microstructures*, **88** (2015) 262 - 270.

[49] Neharika, V. Kumar, V. K. Singh, J. Sharma, O. M. Ntwaeaborwa and H. C. Swart, *Journal of Alloys and Compounds*, **688** (2016) 939 - 945.

[50] R. S. Yadav and S. B. Rai, *Journal of Alloys and Compounds*, **700** (2017) 228 - 237.

[51] D. Alexander, K. Thomas, S. Sisira, G. Vimal, K. P. Mani, P. R. Biju, N. V. Unnikrishnan, M. A. Ittyachen and C. Joseph, *Materials Letters*, **189** (2017) 160 - 163.

[52] M. Jayasimhadri, K. Jha, B. V. Ratnam, H. Woo, K. Jang, A. S. Rao and D. Haranath, *Journal of Alloys and Compounds*, **711** (2017) 395 - 399.

Chapter 8

Tunable emission from $LiBaBO_3:Eu^{3+}$; Bi^{3+} phosphor for solid state lighting

8.1 Introduction

In a world facing energy crisis and the environmental impact occasioned by high energy consumption from conventional lighting technologies, significant reduction in energy wastage through efficient lighting technologies is crucial for human development and health. Globally, lighting technology contributes significantly to the overall energy end use [1]. Recently, solid-state lighting based on white light-emitting diodes (w-LEDs) has become a prevailing trend for illumination technology due to their significant advantages such as high luminous efficiency, low energy consumption, long lifetime, and being environmentally friendly. Therefore there is great potential for them to be considered as the next generation of light sources [1 - 3]. At present, w-LEDs have been used widely as next-generation solid state lighting in many fields such as traffic signals, mobile phones, residential and industrial lighting [3].The recent developments in the field of solid state lighting (SSL) have generated great interest in the search for novel efficient inorganic luminescent materials or phosphors [4] that could be used as sources of white light in LED lighting. This study was therefore aimed at developing inorganic light emitting materials (phosphors) with tunable emissions that could be used in solid state lighting.

Rare earths and transition metal ions act as important activators or dopants in many inorganic phosphors for application in modern age lighting and displays due to tunability of their emission colour in a wide range of the visible spectrum [5]. Borates are emerging as good host matrices

for rare earths or alkali earth metal ions to prepare phosphors due to their high thermal and chemical stability, quantum efficiency and also the fact that they can be easily crystallized at relatively low temperatures [6 - 9]. Trivalent or divalent europium (Eu^{3+} or Eu^{2+}) is the most commonly used activator because both Eu^{3+} and Eu^{2+} can be easily incorporated and excited in a variety of host lattices to give visible emission [5]. The past few decades have seen a lot of work reported on the use of divalent and/or trivalent europium as a dopant in phosphor materials as they display very good emission in the blue and red regions of the visible light, respectively, and they are widely used to develop a variety of light emitting devices [10].In addition, Eu^{3+} emission in doped materials such as borates, aluminates, phosphates, etc. is characterized by sharp lines which are due to f → f transitions [11]. This unique nature of Eu^{3+} doped materials play an important role in the lighting industry. The non-degenerate $^5D_0 \rightarrow {}^7F_0$ emission line of Eu^{3+} ions reveals the presence of crystallographic inequivalent sites in a given host matrix. The occupation of Eu^{3+} ions in a host can be well verified by the numbers of $^5D_0 \rightarrow {}^7F_0$ transitions [12].

Over the last few years, a great deal of progress has been made in the synthesis and characterization of luminescent materials (phosphors). In order to tune the emission colour or enhance the emission intensity, ions like Mn^{2+}, Bi^{3+} are co-doped with rare earth ions such as Eu^{3+}, Tb^{3+} and Ce^{3+} [13]. Bi^{3+} as a co-activator can act as a primary excitation energy center and transfer its energy non-radiatively to enhance the emission intensity of the other dopant ion [14, 15], i.e. it can play the role of a sensitizer. In our study, the well-known radiative emission from Bi^{3+} was detected when Bi^{3+} was co-doped with Eu^{3+} in $LiBaBO_3$ host. Nevertheless, the red emission intensity of Eu^{3+} was enhanced considerably, confirming that Bi^{3+} transferred energy to Eu^{3+} with the rate faster than its radiative transitions. It is well-known that the Bi^{3+} emission covers a very broad spectral range, from the ultraviolet (UV) to blue, green, yellow or even red spectral range and the associated Stokes shifts also vary in large proportions [16, 17]. In general, these luminescence behaviors are easily influenced by the surrounding chemical environment or by invoking an off-center positioning of the Bi^{3+} ions. The ground state ($^1S_0$) of the isolated Bi^{3+} ion has a $6s^2$ configuration and electronic transitions to a $6s^16p^1$ configuration raise the excited states $^3P_{0,\ 1,\ 2}$ to and from which absorption and emission is achieved [17, 18]. In this study, $LiBaBO_3$ host doped Eu^{3+} and co-doped Eu^{3+}/Bi^{3+} phosphors were synthesized using solid state method for the possible application in solid state lighting. Their photoluminescent, structural and

optical properties were studied in detail, and the energy transfer mechanism from Bi^{3+} to Eu^{3+} was investigated. Our materials displayed tunable emission based on simultaneous broadband emission at 593 nm and narrowband emission associated with the f – d and f-f transitions of Eu^{2+} and Eu^{3+} respectively. This result suggests that some of the Eu^{3+} ions were reduced to Eu^{2+}. Bi^{3+} co-doping enhanced the narrowband emission of Eu^{3+} at 613 nm suggesting that there was non-radiative energy transfer from Bi^{3+} to Eu^{3+}. The narrowband emission at 613 nm was dependent on the concentration of Eu^{3+} and Bi^{3+}.

8.2 Experimental

8.2.1 Preparations

$LiBaBO_3$ host either single doped with Eu^{3+} or co-doped with Bi^{3+} were synthesized using solid state method resulting in a phosphor that gave tunable emission. High purity barium carbonate ($BaCO_3$), lithium carbonate (Li_2CO_3), boric acid (H_3BO_3 (99.5%)), bismuth oxide (Bi_2O_3 (99.99%)) and europium oxide (Eu_2O_3 (99.99%)) were used as starting materials or precursors. These materials were weighed according to their stoichiometric ratios, and mixed thoroughly using mortar and pestle for ±20 min. The homogeneous mixtures were then transferred to crucibles and were placed into a muffle furnace, which was pre-heated to 800 ºC ± 10 ºC, for ±5 hours in air. The crucibles containing the resulting solid state products were removed from the muffle furnace and were then cooled down to room temperature and ground gently forming fine powders. The final products were $LiBa_{1-x}BO_3$: $x$$Eu^{3+}$ (x = 0.005, 0.010, 0.015, 0.020, 0.025 and 0.030) and $LiBa_{0.975-y}BO_3$: *0.025*Eu^{3+}; $y$$Bi^{3+}$ (y = 0.005, 0.010, 0.020, 0.030 and 0.050) powder phosphors. The powder phosphors were then characterized using different techniques.

8.2.2 Characterizations

The structure of the phosphor powders were analysed using Siemens diffractometer D5000 with CuKα = 1.54 Å. Morphology and chemical composition were analysed using Jeol JSM 7800F thermal field emission scanning electron microscope (FE-SEM). The chemical composition analysis was carried out using an Oxford Instruments AzTEC energy dispersive spectrometer

(EDS) attached to the FE-SEM and room temperature photoluminescence (PL emission) spectra were recorded using a 325 nm He-Cd gas laser as an excitation source. The diffuse reflectance measurements were carried out in the range of 200 – 800 nm using a Lambda 950 UV–Vis spectrophotometer.

8.3 Results and discussion

8.3.1 Structure and morphology

Shown in **figure 8.1**(**a**) are the X-ray diffraction (XRD) spectra of $LiBa_{1-x}BO_3$: xEu^{3+} (x = 0.015 and 0.025) and $LiBa_{0.975-y}BO_3$: *0.025*Eu^{3+}; yBi^{3+} (y = 0.005, 0.01 and 0.050). The XRD measurements for all the samples show similar diffraction patterns. All the diffraction peaks and the calculated lattice parameters (a = 6.456 Å, b = 7.105 Å and c = 7.414 Å) are consistent with those of the pure monoclinic phase of $LiBaBO_3$ referenced in the standard JCPDS file number 81-1808. The incorporation of Eu^{3+} and Bi^{3+} ions into the host lattice did not affect the crystalline structure. The only observed difference in each pattern is the relative increase in the peak intensity suggesting slight improvement in crystallinity. The average crystallite size was estimated by using Scherer's equation [19, 20]:

$$D = \frac{0.9\lambda}{\beta \cos\theta} \tag{8.1}$$

where β represent full width at half maximum (FWHM) of the XRD lines in radians, λ is the wavelength of the X-rays (0.154 nm in the present case) and θ is the Braggs angle of the XRD peak. The crystallite sizes for $LiBa_{1-x}BO_3$: *0.025*Eu^{3+} and $LiBa_{1-x}BO_3$: *0.025*Eu^{3+}; yBi^{3+} (y = 0.005 and 0.05) were calculated using (100), (110), ($\bar{1}$02), (111), (121), ($\bar{2}$11) and ($\bar{2}$12) planes from the XRD spectra. The average crystallite size was estimated to be 39.83 nm for $LiBa_{1-x}BO_3$: *0.025*Eu^{3+}, while the crystallite sizes for $LiBa_{1-x}BO_3$: *0.025*Eu^{3+}; yBi^{3+} (y = 0.005 and 0.05) increased to 43.29 nm and 58.28 nm, respectively. The schematic of the monoclinic crystal structure of lithium barium orthoborate ($LiBaBO_3$) is shown in **figure 8.1**(**b**). The crystal structure of $LiBaBO_3$ can be found in two different space groups: a- $P2_1/n$ space group in standard setting [21] and b- $P2_1/c$ space group in a non-standard setting [22]. The unit cell of the

$LiBaBO_3$ consists of three O^{2-} ions, one Li^+ ion, Ba^{2+} and B^{5+}. In $LiBaBO_3$ compound, the monometric triangular-planar unit BO_3 joins alternately to the distorted square pyramids LiO_5 by edges forming a ring [23]. The interatomic bond lengths of Ba-O vary from 2.658(5) to 3.173(4) Å with an average value of 2.821 ± 0.186 Å [21]. Ba atom has eight-coordinates (BaO_8 octahedron) [23] or has nine-coordinates (BaO_9 polyhedron) [21].

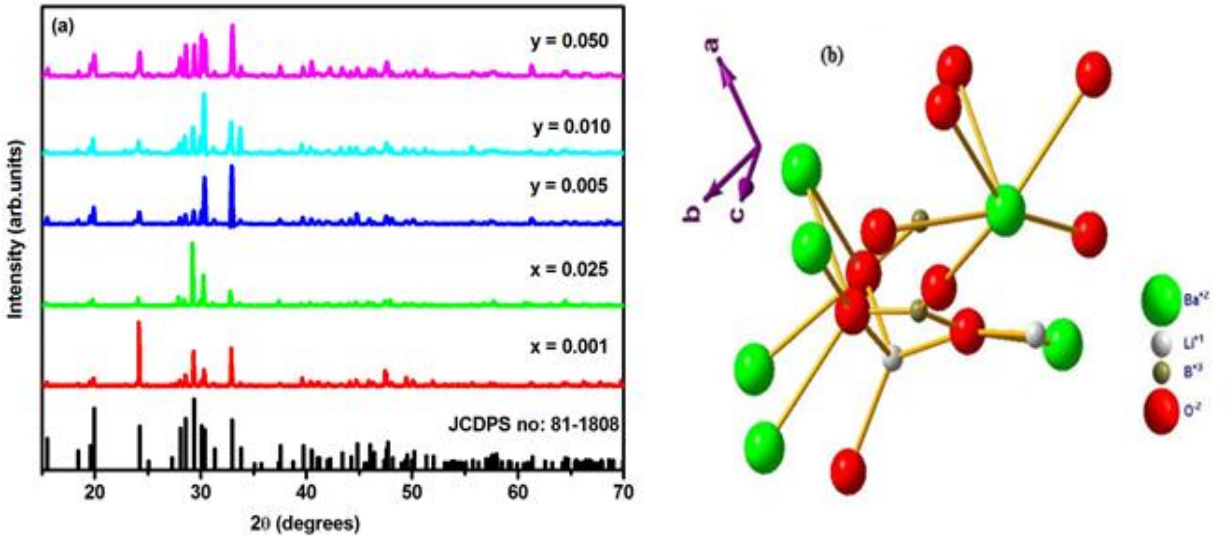

Figure 8.1: a) XRD patterns of $LiBa_{1-x}BO_3$: xEu^{3+} (x = 0.001 and 0.025) and $LiBa_{0.975-y}BO_3$: $0.025Eu^{3+}$; yBi^{3+} (y = 0.005, 0.01 and 0.050) and **b**) the crystal structure of $LiBaBO_3$ host matrix.

Figure 8.2 shows the Fourier transform Infrared (FTIR) spectra of $LiBaBO_3$ host, $LiBa_{1-x}BO_3$: xEu^{3+} (x = 0.025) and $LiBa_{0.975-y}BO_3$: $0.025Eu^{3+}$; yBi^{3+} (y = 0.01) in the 650 – 3000 cm^{-1} range. The inset shows the suppressed bands in the 650 – 1000 cm^{-1} range. It is clear that incorporation of Eu^{3+} and Bi^{3+} ions in the $LiBaBO_3$ host matrix has no effect in the shape of the spectra. This is in agreement with the XRD results that indicated that doping did not affect the structure. Annalakshmi et. al [24] studied the FTIR spectrum of MgB_4O_7: Gd phosphor and reported that the bands in the 1200 – 1600 cm^{-1} region correspond to the stretching modes of the B-O bonds of BO_3 units and the bands in the 800 –1200 cm^{-1} region corresponds to the stretching modes of B-

O bond of the tetrahedral BO_4 units. All the bands below 800 cm^{-1} corresponds to the B-O-B bending vibrations of the borate networks.

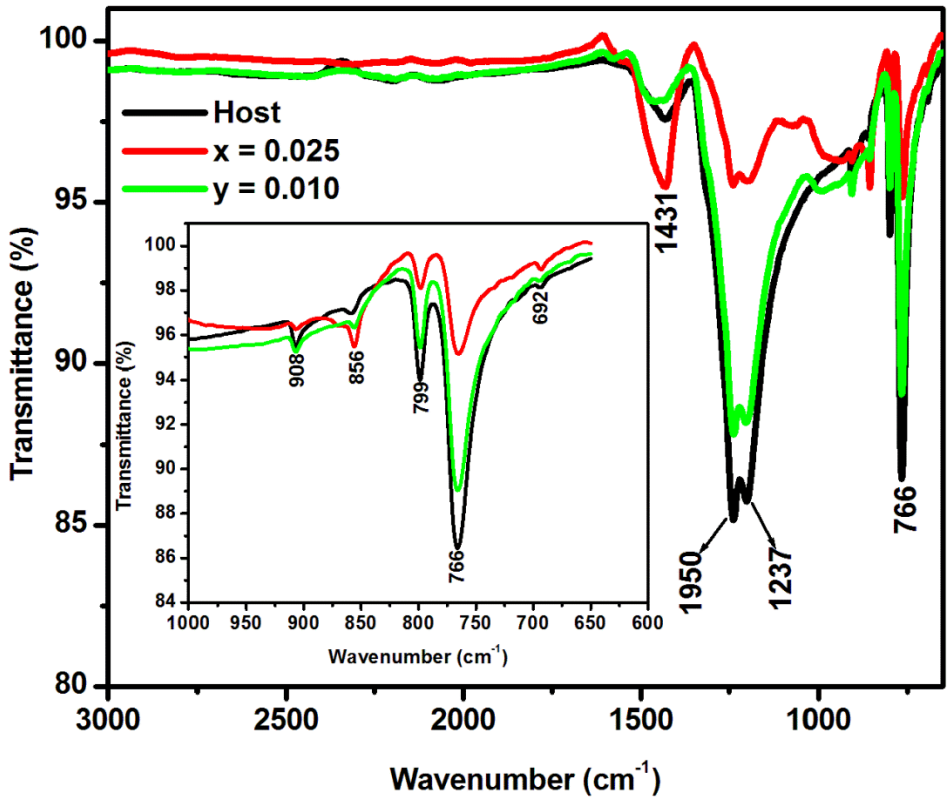

Figure 8.2: FTIR Spectra of $LiBaBO_3$ host, $LiBa_{1-x}BO_3$: xEu^{3+} (x = 0.025) and $LiBa_{0.975-y}BO_3$: $0.025Eu^{3+}$; yBi^{3+} (y = 0.01).

Figure 8.3 (**a-b**) shows the field emission scanning electron microscopy (FE-SEM) images of $LiBa_{1-x}BO_3$: $0.025Eu^{3+}$ and $LiBaBO_3$: $0.025Eu^{3+}$; $0.01Bi^{3+}$ respectively. The powders were made up of the fluffy needle-like particles which are clustered together in different orientations. The elemental compositions of the phosphors were determined using energy dispersive X-ray spectroscopy (EDS). The EDS spectra of $LiBa_{1-x}BO_3$: $0.025Eu^{3+}$ and $LiBaBO_3$: $0.025Eu^{3+}$; $0.01Bi^{3+}$ phosphor are shown in **figure 8.4** (**a-b**) respectively. The presence of barium (Ba), oxygen (O), boron (B), europium (Eu) and bismuth (Bi) in the EDS spectra confirms the formation of the desired compound. The presence of carbon in the EDS spectra can be from the

carbon tape used to mount the samples or environmental hydrocarbons. The absence of Li element in $LiBa_{1-x}BO_3$: xEu^{3+} and $LiBa_{0.975-y}BO_3$: $0.025Eu^{3+}$; yBi^{3+} is consistent with the results reported by Raja et.al [25] and Chun et al [26] from $LiSrPO_4$ and Li_2CaAl_4 $(PO_4)_4F_4$, respectively. This may be due to the EDS detector being less sensitive to Li [27]. The insets in **Figure 8.4** gives the weight per cent of all the elements detected by the EDS. The concentration of Ba by weight exceeds that of all the other elements and the least concentration (also by weight) was recorded for Eu^{3+} and Bi^{3+} co-dopants as shown in **figure 8.4** (**a-b**).

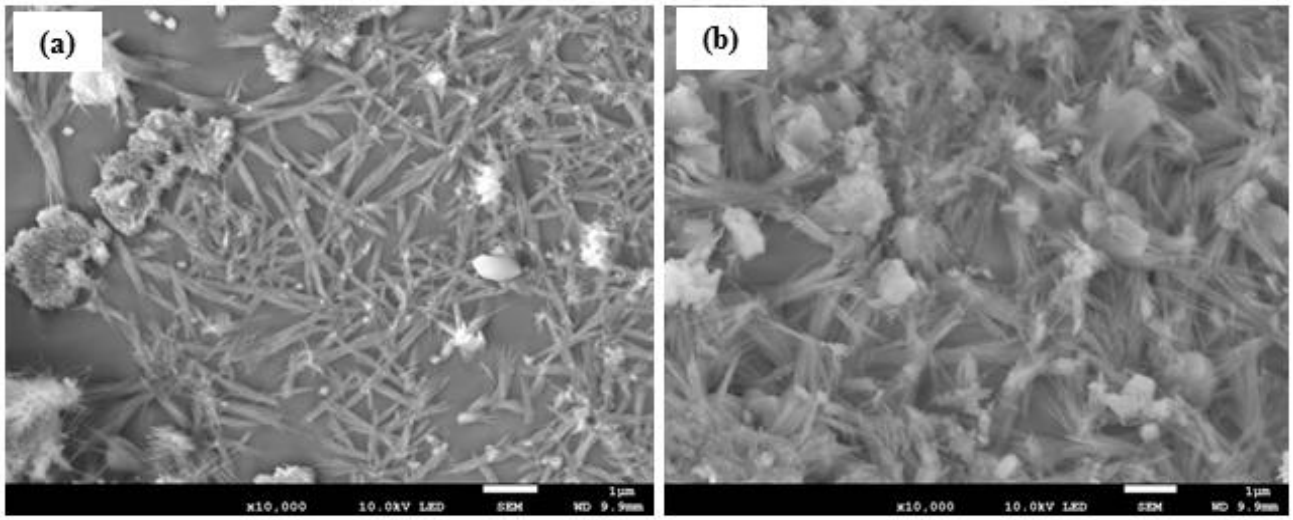

Figure 8.3: SEM images of **a**) $LiBaBO_3$: $0.025Eu^{3+}$ and **b**) $LiBaBO_3$: $0.025Eu^{3+}$; $0.01Bi^{3+}$.

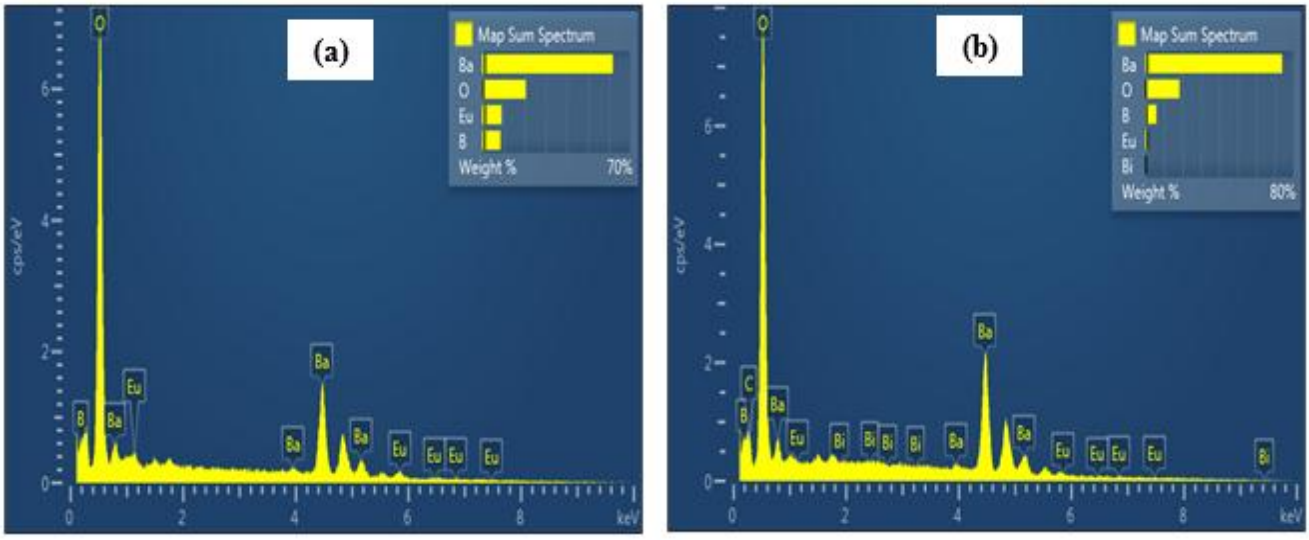

Figure 8.4: EDS images of **a**) $LiBa_{1-x}BO_3$: xEu^{3+} (x = 0.025) and **b**) $LiBa_{0.975-y}BO_3$: $0.025Eu^{3+}$; yBi^{3+} (y = 0.01).

8.3.2 Uv-Vis studies

The diffuse reflectance spectra (DRS) of $LiBa_{1-x}BO_3$: xEu^{3+} (x = 0, 0.005, 0.010, 0.015, 0.020, 0.025 and 0.030) phosphors are shown in **figure 8.5** (**a**). The spectra shows a strong absorption band at ~ 244 nm for the un-doped $LiBaBO_3$ sample, which is attributed to boron (B) to oxygen (O) charge transfer (CT) transition [4]. When the Eu^{3+} ions were incorporated in the $LiBaBO_3$ host matrix, the band at ~ 244 nm shifted towards the longer wavelength (red shift) region between 250 nm and 270 nm and the extent of shifting was dependent on the Eu^{3+} ions concentration. The same behaviour was reported by Dillip et al [4], after doping $NaSrB_5O_9$ with Eu^{3+} ions, and the behavior was attributed to energy transfer from borate groups to Eu^{3+} ions. In addition to the CT bands, the DRS also show several absorption bands in the wavelengths ranging between 350 nm and 540 nm, which originate from the 4f - 4f transition of Eu^{3+} ions [4]. These absorptions lines are assigned to $^7F_0 \rightarrow {}^5D_4$ (~364 nm), $^7F_0 \rightarrow {}^5L_1$ (~384 nm), $^7F_0 \rightarrow {}^5L_6$ (~394 nm), $^7F_0 \rightarrow {}^5D_3$ (~416 nm), $^7F_0 \rightarrow {}^5D_2$ (~465 nm) and $^7F_1 \rightarrow {}^5D_1$ (~533 nm) transitions of Eu^{3+} ions with the highest absorption peak located at 394 nm. Kubelka- Munk model was used to estimate the band-gap of these materials with different doping concentrations. The absorption spectra of $LiBa_{1-x}BO_3$: xEu^{3+} (x = 0, 0.005, 0.010, 0.015, 0.020, 0.025 and 0.030) are shown in

Figure 8.5(b). Equation (8.2) is the Kubelka-Munk absorption coefficient (*K/S*) relation used to determine the band-gap energies:

$$\frac{K}{S} = \frac{(1-R)^2}{2R} \tag{8.2}$$

where *K* is the absorption coefficient, *S* the scattering coefficient and *R* is the reflectivity [28]. The band-gap energy (absorption edge) of the host was estimated to be 3.33 eV (372 nm), which is higher than the band-gap of 2.90 eV (427 nm) reported by Xu et.al [29]. After doping $LiBaBO_3$ host with different concentrations of Eu^{3+} ions, the band-gap energy of the phosphors varied from 3.63 eV to 4.02 eV.

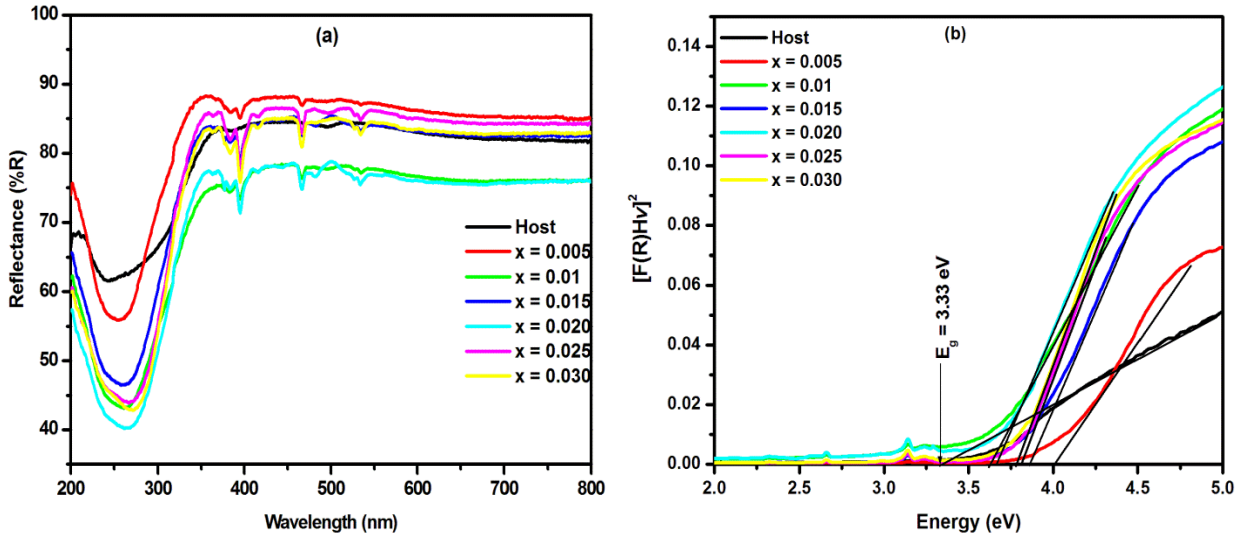

Figure 8.5: a) The diffuse reflectance spectra and **b)** Kubelka-Munk absorption spectra of $LiBa_{1-x}BO_3$: xEu^{3+} (x = 0, 0.005, 0.010, 0.015, 0.020, 0.025 and 0.030).

Figure 8.6 (**a**) shows the diffuse reflectance spectra of $LiBa_{0.975-y}BO_3$: *0.025*Eu^{3+}; yBi^{3+} (y = 0.001, 0.005, 0.010, 0.020, 0.030 and 0.050). From the DRS, it is observed that after co-doping with Bi^{3+}, the band at ~ 266 nm for $LiBa_{0.975}BO_3$: *0.025*Eu^{3+} phosphor shifted towards the longer wavelength and the spectrum became much broader. It can also be seen that the absorption bands at ~364 nm, ~384 nm, ~416 nm, and ~533 nm due to Eu^{3+} ions transitions were suppressed after the incorporation of Bi^{3+} ions and only the bands at ~394 nm and ~465 nm can be seen from the

spectra. The Kubelka-Munk calculation used to estimate the band-gap energy of the phosphors showed that as the concentration of Bi^{3+} ions increases the band-gap energy decreases **figure 8.6** (**b-c**). A decrease on the crystal size can influence the band-gap energy and, consequently, the optical properties of nanophosphors [30]. In the present case it is believed that the band-gap energy has decreased due to the increase in crystallite size.

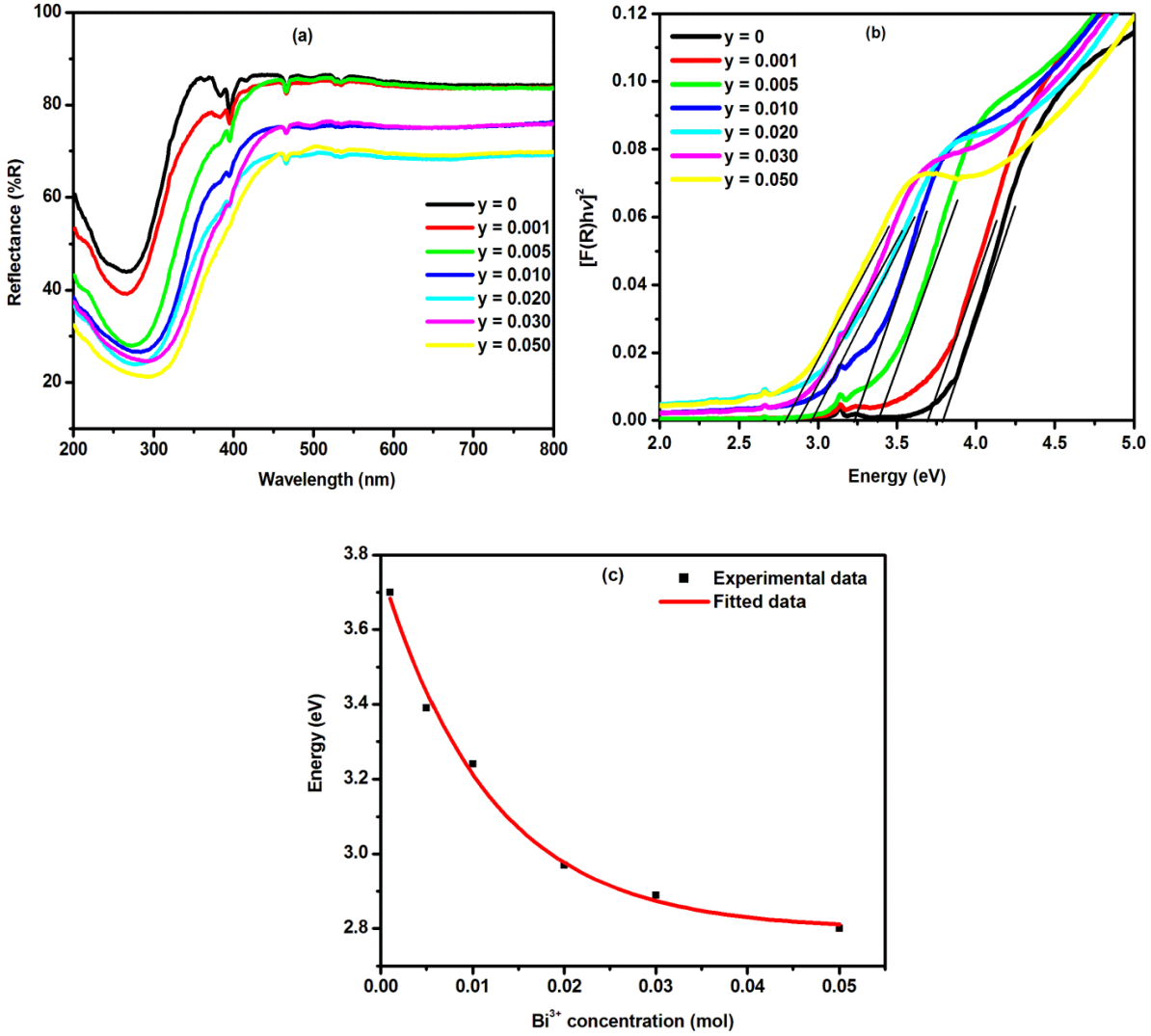

Figure 8.6: a) The diffuse reflectance spectra, **b**) Kubelka-Munk absorption spectra of $LiBa_{0.975-y}BO_3$: $0.025Eu^{3+}$; yBi^{3+} (y = 0.001, 0.005, 0.010, 0.020, 0.030 and 0.050) and **c**) Band-gap as a function of Bi^{3+} concentration.

8.3.3 Photoluminescence studies

Shown in **figure 8.7** (**a**) is the PL emission spectrum of the $LiBaBO_3$ host matrix. The un-doped (host) powder phosphor shows a broad blue emission band with two peaks at 413 nm, 436 nm and a shoulder at ~465 nm. The deconvoluted emission spectrum of the host is shown in **figure 8.7** (**b**). The fitted spectrum shows three peaks at 410 nm, 432 nm and 458 nm. The blue emission observed from the $LiBaBO_3$ host may be assigned to the recombination of self-trapped excitons (STE) that could be associated with band-gap excitations or molecular transitions within the BO_3^{3-} group [31, 32].

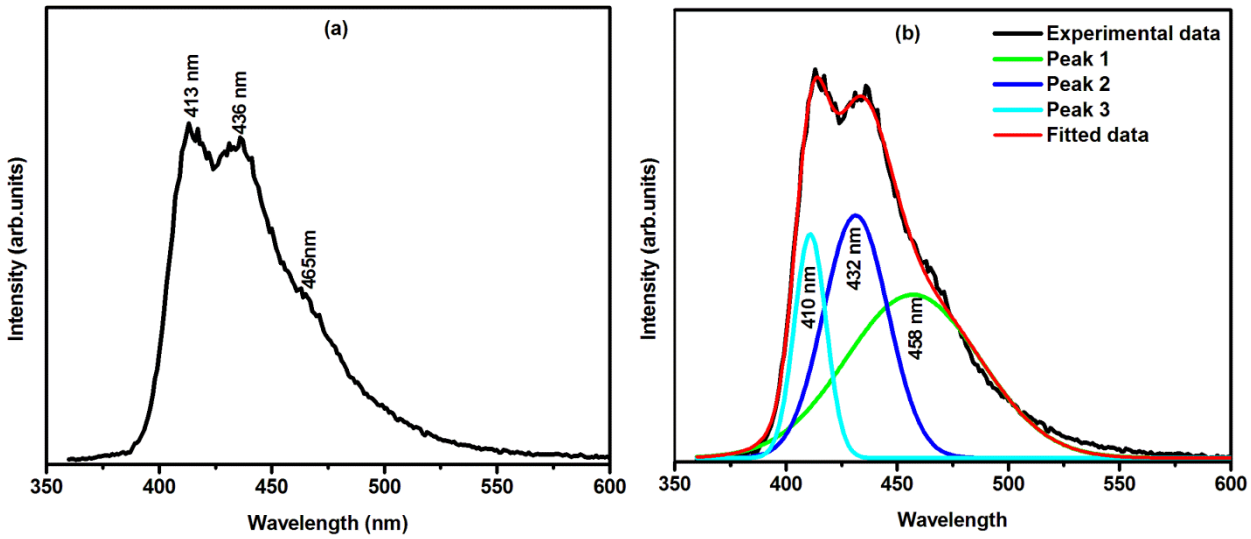

Figure 8.7: PL emission spectra of **a**) $LiBaBO_3$ host matrix and **b**) deconvoluted host matrix.

The photoluminescence spectra of $LiBa_{1-x}BO_3$: xEu^{3+} (x = 0, 0.005, 0.010, 0.015, 0.020, 0.025 and 0.030) phosphor powders are shown in **figure 8.8** (**a**). The spectra were recorded when the powders where excited using a 325 nm He-Cd laser. The spectra for the europium doped samples consist of several emission peaks from the host, Eu^{2+} and Eu^{3+}. The broad blue-greenish emission at 493 nm is attributed to the $4f^6 5d_1 \rightarrow 4f^7$ electronic dipole allowed transitions of Eu^{2+} ions [33], suggesting that some of the Eu^{3+} ions were reduced to Eu^{2+} ion. Xu et.al [2] also reported the coexistence of Eu^{2+} and Eu^{3+} emissions in $LiBaBO_3$ host. From the spectra it can also be seen that there are other emission lines which are attributed to $^5D_0 \rightarrow {}^7F_0$ (579 and 585 nm), $^5D_0 \rightarrow {}^7F_1$ (595 nm), $^5D_0 \rightarrow {}^7F_2$ (613 nm), $^5D_0 \rightarrow {}^7F_3$ (652 nm) and $^5D_0 \rightarrow {}^7F_4$ (685 nm and 704

nm) transitions of Eu^{3+} ions [34]. In particular, the most intense emission peak at 613 nm and is due to the forced electric dipole known to be forbidden by the Laporte selection rule. However, this transition is allowed due to the mixing of the 4f orbitals with the opposite parity at the low symmetry sites. The $^5D_0 \rightarrow {}^7F_1$ transition at 595 nm is magnetic dipole transition in nature and follows the selection rule $\Delta J = \pm 1$ [35]. Eu ions can coexist stably in a single host lattice as trivalent (Eu^{3+}) and divalent (Eu^{2+}) ions [36, 37]. As the ionic radii of dopant ion (Eu^{3+} or Eu^{2+}) and host lattice ion (Ba^{2+}) are similar, Eu^{3+} or Eu^{2+} can substitute Ba^{2+} [38]. Since Eu^{3+} ions occupy Ba^{2+} sites without inversion symmetry, that is the intensity of the electric dipole transition $^5D_0 \rightarrow {}^7F_2$ is stronger than that of the magnetic dipole transition $^5D_0 \rightarrow {}^7F_1$, the strong crystal-field effect of the host lattice on the Eu^{3+} ions causes the spectral lines to split into multiple components, hence the luminescence results confirmsthe coexistence of Eu^{2+} and Eu^{3+} ions in the powder phosphors [39]. The relative intensity of the main emission peak from Eu^{3+} at 613 nm as a function of doping concentration is shown in **figure 8.8** (**b**). From the results it is observed that with increase in concentration of Eu^{3+}, the PL intensity was gradually enhanced up to a maximum intensity when $x = 0.025$. Beyond $x = 0.025$, the intensity decreases probably due to concentration quenching effect.

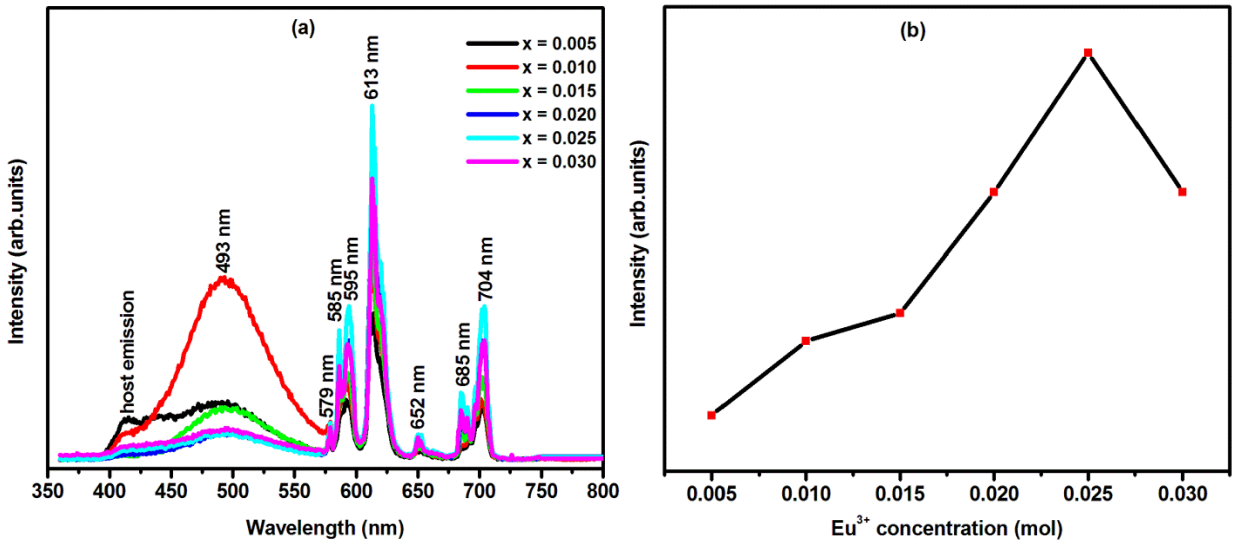

Figure 8.8: a) The PL emission spectra of $LiBa_{1-x}BO_3$: xEu^{3+} (x = 0, 0.005, 0.010, 0.015, 0.020, 0.025 and 0.030) excited by 325 nm laser **b)** Relative emission intensity as a function Eu^{3+} concentration for 613 nm peak.

Figure 8.9 (**a**) exhibits the PL emission spectra of $LiBa_{0.975-y}BO_3$: $0.025Eu^{3+}$; yBi^{3+} phosphors with different Bi^{3+} concentrations (y = 0.001, 0.005, 0.010, 0.020, 0.030 and 0.050) excited using 325 nm He-Cd laser at room temperature. Comparing these data with those without Bi^{3+} doping, the peak position and shape in the emission spectra remain unchanged except the luminescent intensity. It shows that the introduction of Bi^{3+} does not shift the electron transitions of Eu^{3+} ions [40]. The intensity of the PL emission peak at 613 nm is stronger than that without Bi^{3+} when the Bi^{3+} content is y = 0.010. The emission intensity of Eu^{3+} increases with Bi^{3+} concentration first, maximizes when y = 0.010 and then decreases with Bi^{3+} concentration. More evidence can be seen in **figure 8.9** (**b**), which shows the maximum PL emission intensity of the Eu^{3+} at 613 nm as a function of Bi^{3+} concentration for $LiBa_{0.975\ -y}BO_3$: $0.025Eu^{3+}$; yBi^{3+}. The above results show that the sensitization effect of Bi^{3+} on the activator Eu^{3+} depends on the concentration of Bi^{3+}.

Tang et.al, [40] explained that smaller Bi^{3+} concentration is not favourable for the improvement of luminescent intensity while higher Bi^{3+} concentration has a greater tendency to transfer more energy to Eu^{3+}. This kind of energy transfer from Bi^{3+} to Eu^{3+} improves the photoluminescence intensity, however excessive Bi^{3+} ions in the phosphor will lead to concentration quenching due to aggregates of Bi^{3+}. Aggregates can act as excitation trapping centers and cause the migration of excitation energy. The energy migration dissipates the absorbed energy, which results in non-radiative transition leading to quenching of luminescence intensity [40]. Wei et al, [41] reported that with high doping concentration, the distance between Bi^{3+} ions becomes short. The larger the concentration of Bi^{3+} ions is, the further the distance of energy transfer along the Bi^{3+} ions will be, resulting in the greater probability of transferring energy from Bi^{3+} ions to the quenching centers. So there will be less energy transfer from Bi^{3+} ions to Eu^{3+} ions, therefore the emission intensity of Eu^{3+} decreases. Ahemen et.al, [1] reported that different mechanisms could be responsible for energy transfer and the most common of these mechanisms are the exchange interaction and the multipolar processes. In order to know the mechanism involved in the energy transfer process between Bi^{3+} and Eu^{3+}, it is necessary to know the critical distance R_c. The critical distance R_c between the donor and activator ions is given by Blesse formula [1]:

$$R_c = 2\left(\frac{3V}{4\pi C_{Eu+Bi}N}\right)^{1/3} \tag{8.3}$$

where V = 300.24 Å^3 is the calculated volume of the unit cell for the prepared samples, $C_{Bi + Eu}$ is the total concentration of Bi^{3+} and Eu^{3+} ions and N is the number of ions per unit cell. The calculated critical distance is about 12.5 Å. This value is greater than 5 Å, indicating that the interaction mechanism is predominantly a multipolar process.

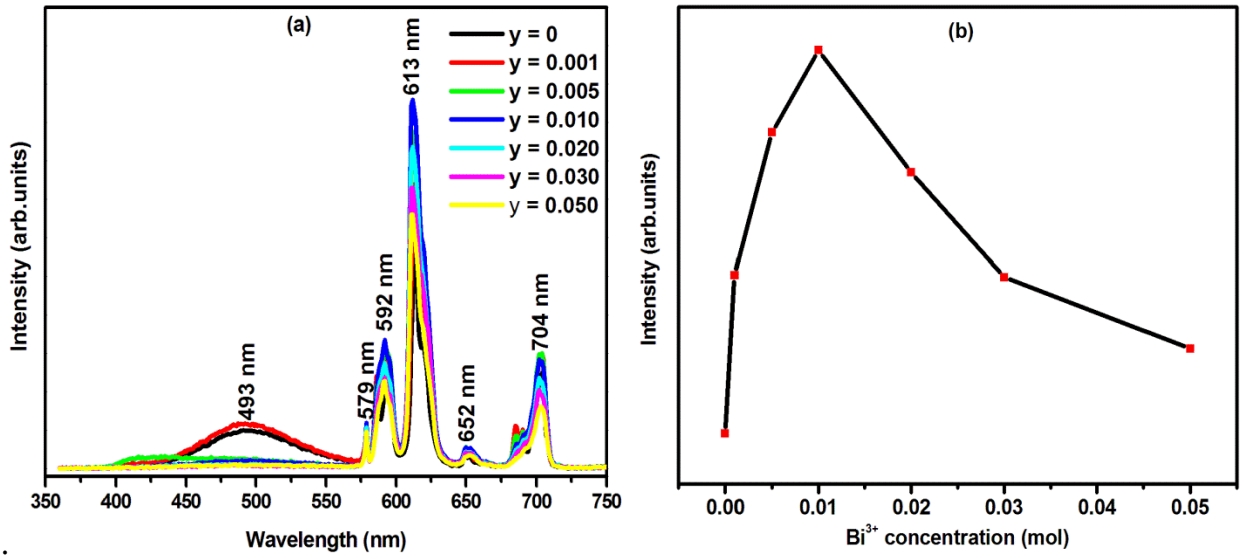

Figure 8.9: a) The PL emission spectra of $LiBa_{0.975-y}BO_3$: *0.025*Eu^{3+}; *y*Bi^{3+} (*y* = 0.001, 0.005, 0.010, 0.020, 0.030 and 0.050) excited by 325 nm He-Cd laser **b**) Relative emission intensity as a function Bi^{3+} concentration for 613 nm peak.

Shown in **figure 8.10** is the commission International de I'Eclarage (CIE) 1931 x-y color coordinates diagrams for (a) $LiBa_{1-x}BO_3$: *x*Eu^{3+} (*x* = 0, 0.005, 0.010, 0.015, 0.020, 0.025 and 0.030) and (b) $LiBa_{0.975-y}BO_3$: *0.025*Eu^{3+}; *y*Bi^{3+} (*y* = 0.001, 0.005, 0.010, 0.020, 0.030 and 0.050). The chromaticity coordinates for the phosphors using photoluminescence data and the interactive CIE software shows tuneable colours. White light emission was obtained from $LiBa_{1-x}BO_3$: *x*Eu^{3+} (*x* = 0.020 and *x* = 0.025) with the colour coordinates x = 0.368 and y = 0.378 and x = 0.376, y = 0.366, respectively. These colour coordinates falls within the white region and they are very close to standard white color (x = 0.333 and y = 0.333) in the CIE coordinate system. After co-doping with Bi^{3+}, the CIE coordinates show the color changing from whitish to orange with the increase in concentration of Bi^{3+}.

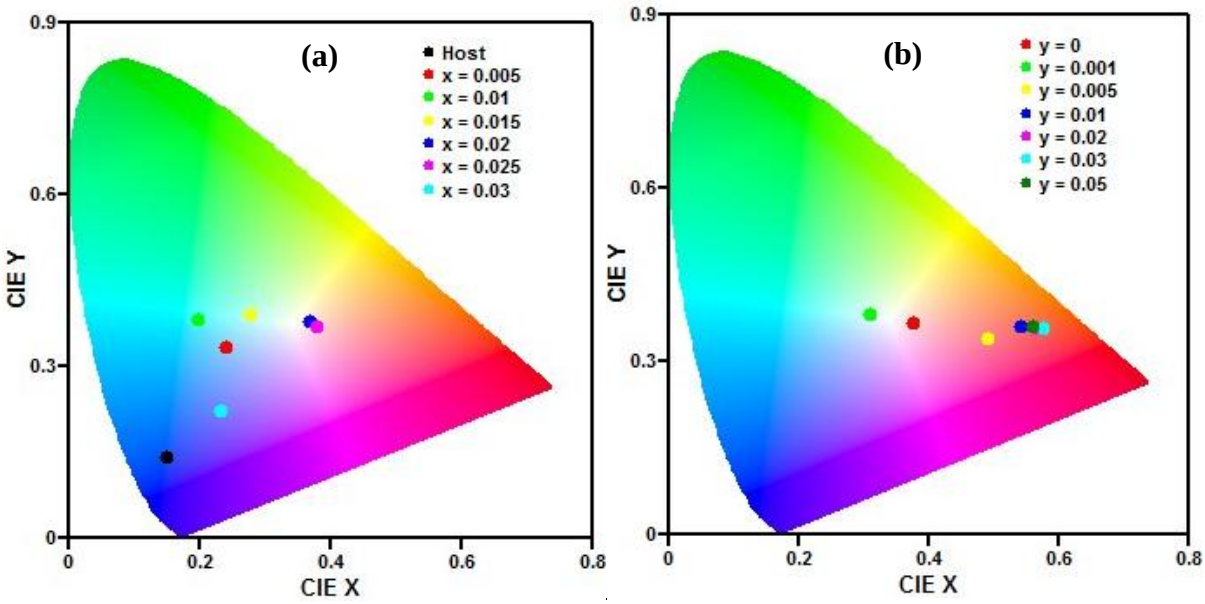

Figure 8.10: CIE coordinate diagram of **a**) $LiBa_{1-x}BO_3$: xEu^{3+} and **b**) $LiBa_{0.975-y}BO_3$: $0.025Eu^{3+}$; yBi^{3+}.

8.4 Conclusion

In summary, a series of $LiBa_{1-x}BO_3$: xEu^{3+} (x = 0, 0.005, 0.010, 0.015, 0.020, 0.025 and 0.030) and $LiBa_{0.975-y}BO_3$: $0.025Eu^{3+}$; yBi^{3+} (y = 0.001, 0.005, 0.010, 0.020, 0.030 and 0.050) phosphor powders were successfully synthesized by solid state method. The structure, morphology, chemical composition, UV-visible absorption and photoluminescent properties of the phosphors were examined. Blue emission was observed from $LiBaBO_3$ host matrix which is ascribed to self- activated emission. The red emission from Eu^{3+} is considerably enhanced after the Bi^{3+} co-doping. The tunable color properties of $LiBaBO_3$: Eu^{3+} indicated that the phosphors provide a potential to be a single component white light phosphor. White light emission was obtained from $LiBa_{1-x}BO_3$: xEu^{3+} (x = 0.020 and x = 0.025) phosphor powders with the color coordinates x = 0.368 and y = 0.378 and x = 0.376, y = 0.366, respectively.

References

[1] I. Ahemen and F. B. Dejene, Journal of Nanoparticle Research, **19** (2017) 6, doi:10.1007/s11051-016-3703-8.

[2] R. Mi, J. Chen, Y. Liu, M. Fang, L. Mei, Z. Huang, B. Wang and C. Zhao, *Royal Society of Chemistry Advances*, **6** (2016) 28887 - 28894.

[3] R. Cao, T. Fu, Y. Cao, H. Ao, S. Guo and G. Zheng, *Materials Letters*, **155** (2015) 68 - 70.

[4] S. Asiri Naidu, S. Boudin, U. V. Varadaraju and B. Raveau, *Journal of Electrochemical Society*, **159** (2012) J122 - J126.

[5] S. Xu, P. Li, Z. Wang, T. Li, Q. Bai, J. Sun and Z. Yang, *Journal of Materials Chemistry C*, **3** (2015) 9112 - 9121.

[6] G. R. Dillip, K. Mallikarjuna, S. J. Dhoble, B. Deva Prasad Raju, *Journal of Physics and Chemistry of Solids*, **75** (2014) 8 - 14.

[7] H.N. Luitel, R. Chand and T. Watari, *Advances in Condensed matter Physics*, **2015** (2015) 1 - 9.

[8] W. Liu, Y. Chiu, C. Tung, Y. Yeh, S. Jang, T. Chen, *Journal of The Electrochemical Society*, **155** (2008) J252 - J225.

[9] H. Van Tuyen, N. M. Son and V. X. Quang *International Journal of Engineering and Innovative Technology*, **3** (2014) 312 - 318.

[10] K. R. Sayana and K. V. R. Murthy, *International Journal of Engineering and Innovative*, **3** (2013) 356 - 360.

[11] K. A. Koparkar, N. S. Bajaj and S. K. Omanwar, *Journal of Materials Science Materials in Electronics*, **26** (2015) 2748 - 2753.

[12] F. Du, Y. Nakai, T. Tsuboi, Y. Huang and H. J. Seo, *Journal of Materials Chemistry*, **21** (2011) 4669 - 4678.

[13] B. C. Babu and S. Buddhudu, *Journal of Spectroscopy and Dyna*mics, **4** (2014) 1 - 8.

[14] C. Lei, J. Yang, Z. Guo-Bin, W. Can, Y. Guang-Tao, W. Chun and L. Guo-Hua, *Chinese Physical Letter*, **25** (2008) 1884 - 1887.

[15] D. Huang, Y. Zhou, W. Xu, Z. Yang, Z. Liu, M. Hong, Y. Lin and J. Yu, *Journal of Alloys and Compounds*, **554** (2013) 312 - 318.

[16] S. Zhang, Y. Hu, R. Chen, X. Wang and Z. Wang, *Optics Materials*, **36** (2014) 1830 - 1835.

[17] A. B. Gwande, R. P. Sonekar and S. K. Omanwar, *International Journal of Optics*, **2014** (2014) 1 - 6.

[18] L. Wang, H. Guo, Y. Wei, H. M. Noh and J. H. Jeong, *Optical Materials*, **42** (2015) 233 - 236.

[19] D. Singh, V. Tanwar, S. Bhangwan, V. Nishal, S. Sheoran, S. Kadyan, A. P. Samantilleke and P. S. Kadyan, *Indian Journal of Materials Science*, **2015** (2015) 1 - 8.

[20] R. K. Tamrakar, D. P. Bisen and K. Upadyay, *Journal of Radiation Research and Applied Sciences*, **8** (2015) 11 - 16.

[21] W. D. Cheng, H. Zhang, Q. S. Lin, F. K. Zheng, J. T. Chen, *Chemistry of Materials*, **13** (2001) 1841 - 1847.

[22] M. Schläger and R. Hoppe, *Journal of Inorganic and General Chemistry*, **619** (1993) 976 - 982.

[23] Z. Huang, H. Ji, M. Fang, M. S. Molokeev, S. Liu, Y. Liu, X. Wua, *Chemical Physics Letters*, **628** (2015) 21 - 24.

[24] O. Annalakshmi, M. T. Jose, U. Madhusoodanan, J. Sridevi, B. Venkatraman, G. Amarendra and A.B. Mandal, *Radiation Effects and Defects in Solids*, **169** (2014) 636 - 645.

[25] B. J. Raja, M. R. Yadov, V. P. Manjari, C. R. Krishma, R. V. S. S. N. Ravikumar, *Journal of Molecular structure*, **1076** (2014) 461 - 467.

[26] C. C, Lin, Z. R, Xiao, G. Guo, T. Chan and R. Liu, *American Chemical Society*, **132** (2010) 3020 - 3028.

[27] [27] T. V. Gavrilovic, D. J. Jonanovic, V. M. Lojpur and V. Dordevic, *Journal of Solid State Chemistry*, **217** (2014) 92 - 98.

[28] X. Chen, Z. Xia and Q. Liu, *Royal Society of Chemistry*, **43** (2014) 13370 - 13376.

[29] S. Xu, P. Li, Z. Wang, T. Li, Q. Bai, J. Sun and Z. Yan, *Royal Society of Chem*istry, **3** (2015) 9112 - 9121.

[30] H. C. Streit, J. Kramer, M. Suta and C. Wickleder, *Journal of Materials*, **6** (2013) 3079 - 3093.

[31] D. Wang, T. Chen and B. Cheng, *Inorganic Chemistry*, **51** (2012) 2961 - 2965.

[32] S. P. Feofilov, Y. Zhou, H. J. Seo, J. Y. Jeong, D. A. Keszler and R. S. Meltzer, *Physics Review B*, **74** (2006) 085101, doi: https://doi.org/10.1103/PhysRevB.74.085101.

[33] C. Huang, L. Luo and T. Cheng, *Journal of Electrochemical Society*, **158** (2011) J341 - J344.

[34] R. S. Palaspagar, A. B. Gawande, R. P. Sonekar. S. K. Omanwar, *Journal of Luminescence*, **154** (2014) 58 - 61.

[35] K. Vuković, M. Medić, M. Sekulić, M. D. Dramićanin, *Advances in Condensed Matter physics*, **2015** (2015) 1 - 7.

[36] M. Xie, D. Li, Z. Zhu, R. Pan and X. Fu, *Results in Physics*, **6** (2016) 70 - 73.

[37] V. Singh, Z. Zhu and V. Natarajan, *Physica Status Solidi*, **203** (2006) 2058 - 2064.

[38] B. Mari, K. C. Singh, N. Verma, M. Mollar and J. Jindal, *Transactions of the Indian Ceramic Society*, **74** (2015) 157 - 161.

[39] Z. Zhang, Y. Lomg, H. Zhang, B. Sun, W. Han and X. Sun, *Journal of Materials Chemistry C*, **2** (2014) 312 - 318.

[40] A. Tang, D. Zhang, L. Yang and X. Wang, *Photoelectronics and advanced materials-rapid communications*, **5** (2011) 1031 - 1034.

[41] X. T. Wei, Y. N. Chen, X. R. Cheng, M. Yin and W. Xu, *Applied Physics* B, **99** (2010) 763 - 768.

Chapter 9

Luminescent properties, structure and morphology analysis of $LiBaBO_3:Dy^{3+}$ phosphors prepared by solid state reaction method

9.1 Introduction

Considering the growing importance of energy saving and environmental friendliness, rare-earth ions (RE) and transition metal ions-doped phosphors have attracted extensive research and commercial interest. This is because they are efficient luminescent materials and irreplaceable components of light-emitting devices such as plasma display panels (PDPs), field emission display (FEDs), fluorescent lamps (FLs) and white light emitting Diodes (WLEDs) [1, 2]. Among them, WLEDs are considered to be next generation solid state lighting devices owing to their merits of high energy efficiencies, long operation lifetime, lower power consumption and eco-friendly constituents [2].

Among a large number of inorganic compounds, rare earth-doped phosphors have attracted much attention due to their advantages of a low synthesis temperature, high luminous efficiency, high colour purity and chemical stability [3]. As an efficient luminescent center, Dy^{3+} ion has been extensively studied to generate white light in various hosts owing to its two main emission components: the blue band (470–500 nm) due to the $^4F_{9/2}\rightarrow{}^6H_{15/2}$ transition and the yellow band (570–600 nm) due to the $^4F_{9/2}\rightarrow{}^6H_{13/2}$ transition. Consequently, white light can be obtained by balancing the ratio of blue to yellow emissions. Moreover, phosphors doped with Dy^{3+} ions based on their line-type f–f transitions, can emit narrow emissions in the visible range, resulting

in high efficiency and high lumen equivalence. As a result, there has been growing research interest in developing Dy^{3+} doped phosphors with high absorption in the near UV to blue range [4, 5]. The yellow emission of Dy^{3+} is rather hypersensitive to the local environment, whereas the blue emission of Dy^{3+} is not very sensitive to the local environment. Because of the high sensitivity to the local environment, Dy^{3+} can be used to probe the crystal structure of the host lattice. A white light emission with appropriate correlated color temperature (CCT) and chromaticity coordinates can be achieved through suitable adjustment of the yellow/blue (Y/B) intensity ratio of Dy^{3+}-doped phosphors. Because of this, Dy^{3+}-doped host lattices hold a promise to develop a single host phosphor for that can be used as used as sources of white light in light emitting devices [6, 7].

For general lighting, photoluminescence (PL) materials including oxides, silicates, aluminates, alumininoborates, aluminisilicates, nitrides, borates, etc., play very important roles for potential applications in UV light emitting diodes [8, 9]. Among them, inorganic borates have long been a focus of research not only because of their variety of structure type but also due to their wide electronic band gap, transparency to a wide range of wavelengths , high optical damage threshold and high optical quality [10, 11]. The ultraviolet-transparent range of borates materials is determined mainly by energy gap of the anionic groups if the cations are alkali or alkaline-earth metals [12]. Since the borate compounds show variety of application due to their physical and optical properties, the borates with isolated planar $[BO_3]^{3-}$ group in their structure are proven to be good birefringent materials [13]. Phosphors based on borates show excellent luminescence performance because of their abundant structures which can afford different crystal fields for the d or f metal cations to tune emission colour [14]. A variety of borate host materials doped with rare earths or other ions have been developed into phosphor materials for different applications [15, 16]. In the present work, Dy^{3+}-doped $LiBaBO_3$ doped phosphor samples were prepared by solid state method. Their photoluminescence properties, structure and morphology were investigated in detail.

9.2 Experimental

9.2.1 Preparations

$LiBaBO_3$: xDy^{3+} (x = 0.003, 0.005, 0.009, 0.01, 0.03 and 0.05 powder phosphors were prepared by a high temperature solid state method. $BaCO_3$, Li_2CO_3, H_3BO_3 and Dy_2O_3 (99.99%), all purchased at Sigma-Aldrich, were used as staring materials or precursors. These materials were weighed according to their stoichiometric ratios, and mixed thoroughly for ~20 min using a mortar and pestle. The homogeneous mixtures were transferred to crucibles and placed into a muffle furnace, which was preheated to 800 ± 10 °C, for ~5 hrs in air. The crucibles containing the resulting solid-state products were removed from the muffle furnace and cooled to room temperature. The contents were ground gently to give fine powders of $LiBaBO_3$: xDy^{3+} with different concentrations of Dy^{3+}. The prepared powder phosphors of $LiBaBO_3$: xDy^{3+} were then ready to be characterized using different techniques. The flow diagram for solid state synthesis of $LiBaBO_3$: xDy^{3+} powder phosphor is shown in **figure 9.1**.

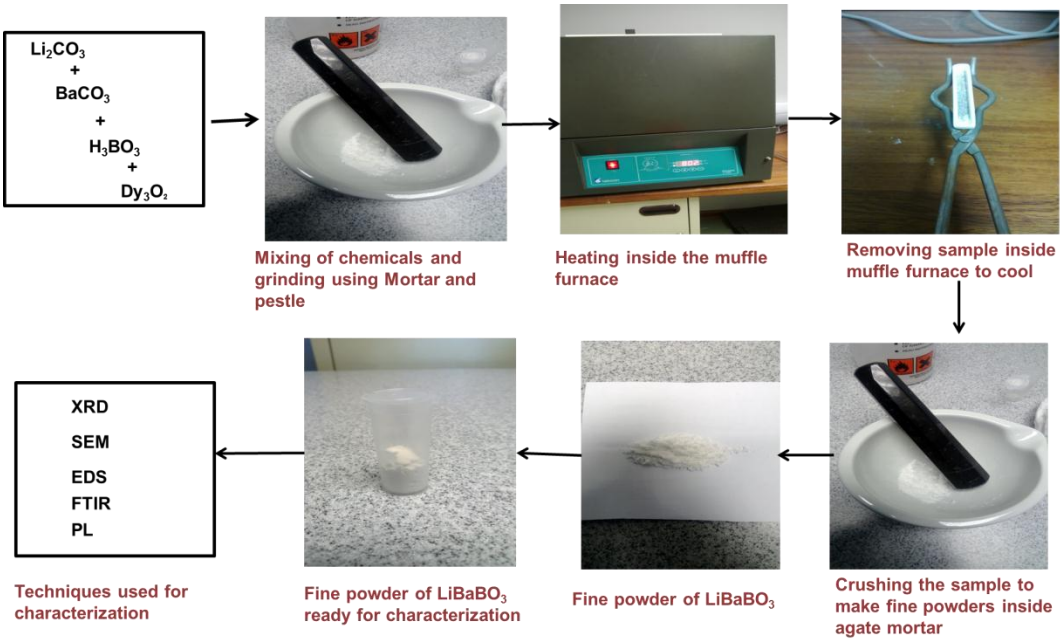

Figure 9.1: Flow diagram for solid state synthesis of $LiBaBO_3$: xDy^{3+} powder phosphors.

9.2.2 Characterizations

The crystalline structures of the phosphor powders were analysed using Bruker D8 Advanced powder X-ray diffractometer (XRD). The X-ray radiation used during the measurement was a CuKα source (λ= 1.5406 Å). Fourier transform infrared (FTIR) analysis was performed on the samples using a Perkin Elmer Spectrum 100 FTIR spectrometer. Morphology of the powder phosphors was analysed using Jeol JSM 7800F thermal field emission scanning electron microscope (FE-SEM). The chemical composition analysis was carried out using an Oxford Instruments AzTEC energy dispersive spectrometer (EDS), attached to the FE-SEM. High-resolution transmission electron microscopy (HR-TEM) analyses were carried with a JEOL-TEM 2100 instrument. Room temperature photoluminescence (excitation and emission) were recorded using Varian Cary Eclipse fluorescence spectrophotometer using xenon lamp as an excitation source.

9.3 Results and discussion

9.3.1 Structure and morphology

Figure 9.2 shows the X- ray diffraction (XRD) patterns of $LiBaBO_3$: $x$$Dy^{3+}$ powder phosphors with (x = 0, 0.003, 0.005, 0.01 and 0.03), together with the JCPDS card file of $LiBaBO_3$ for comparison. The XRD patterns agreed well with the Joint Committee on Powder Diffraction Standards card (JCPDS) card no: 81 – 1808 for $LiBaBO_3$ that has a monoclinic structure with P21/n space group with lattice parameters a = 0.6461 nm, b = 0.7107 nm and c = 0.7403 nm [17]. The XRD patterns showed that the host structure was not influenced by the Dy^{3+} dopant ions. The average crystallite size (D) and the lattice strain (ε) induced by defects and related crystal imperfections were calculated using the Williamson–Hall equation [18] given by:

$$\beta_{hkl}\cos\theta = 4\varepsilon\ \sin\theta + \frac{K\lambda}{D} \tag{9.1}$$

where λ is the X-ray wavelength in nanometer (nm), β_{hkl} is the full width of the diffraction peaks profile at half maximum height, θ is the Bragg angle and K is a constant related to the crystallite shape, usually taken as 0.9 or 0.89 for full width at half maximum (FWHM) of spherical crystals

with cubic unit cells. The crystallite sizes and lattice strains were estimated from the plot of βcosθ as a function of 4sinθ. From the linear fit to the data, the crystallite size was estimated from the intercept on βcosθ and the strain, ε, was estimated from the slope of the fitted line [18]. **Figure 9.3** shows the plot of βcosθ versus 4sinθ for $LiBaBO_3$: *0.01*Dy^{3+} powder phosphor. The average crystallites sizes and the lattice strains of $LiBaBO_3$: *x*Dy^{3+} (*x* = 0, 0.003, 0.005, 0.01 and 0.03) powder phosphors were estimated and their values are summarized in **table 9.1**. The peak widths were not corrected for the instrumental broadening therefore the actual crystallite sizes may be bigger than the values listed in **table 9.1** [18].

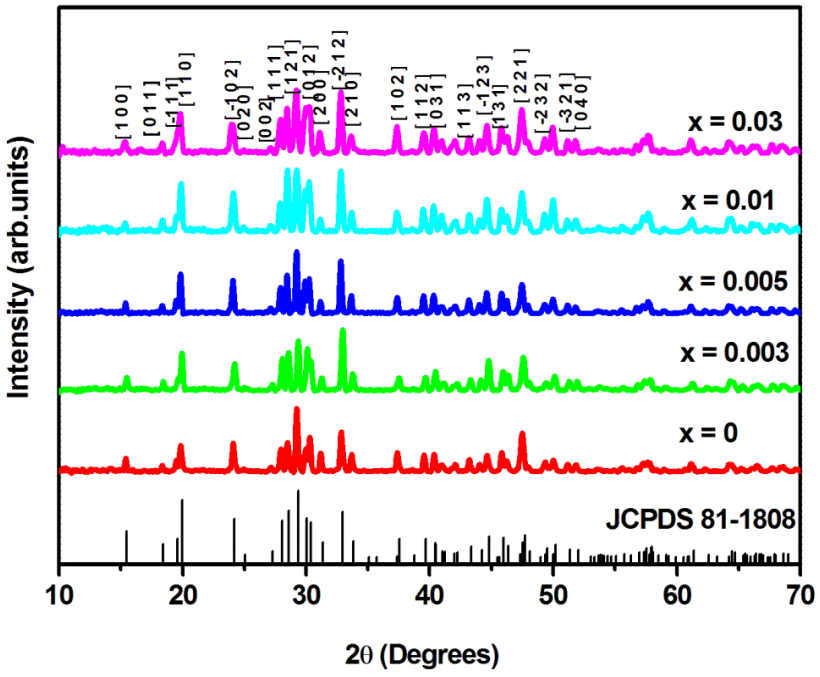

Figure 9.2: XRD patterns of the as-prepared $LiBaBO_3$: *x*Dy^{3+} (*x* = 0.003, 0.005, 0.01 and 0.03) powder phosphors compared with JCPDS card no: 81 -1808.

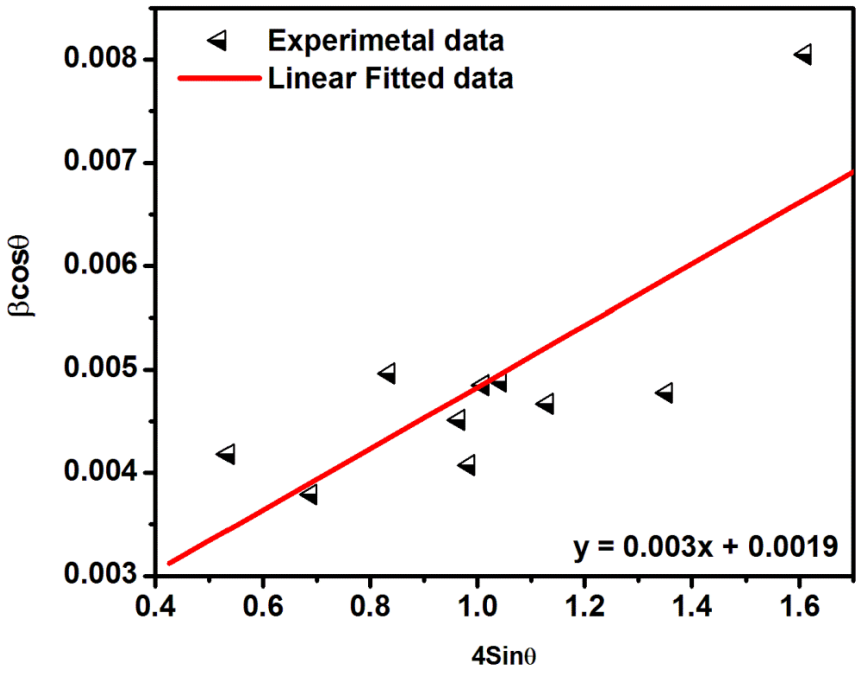

Figure 9.3: Plot of βcosθ versus 4sinθ for $LiBaBO_3$: *0.01*Dy^{3+} powder phosphor.

Table 9.1: Crystallite sizes and structural parameters of $LiBaBO_3$: *x*Dy^{3+} (*x* = 0, 0.003, 0.005, 0.01 and 0.03) powder phosphors.

Sample name	Crystallite size *D* (nm)	Lattice constants (Å)			Microstrain ($\times 10^{-4}$)	Cell volume (Å^3)
$LiBaBO_3$: *x*Dy^{3+}	Williamson-Hall	a	b	c	ε	v
x = 0	58	6.499	7.128	7.440	15.0	304.34
x = 0.003	41	6.462	7.094	7.412	9.0	300.03
x = 0.005	50	6.478	7.099	7.413	9.0	301.02
x = 0.01	73	6.529	7.134	7.438	30	305.92
x = 0.03	50	6.558	7.142	7.449	20	308.08

Figure 9.4 (**a**) shows the field emission scanning electron microscopy image of $LiBaBO_3$: xDy^{3+} (x = 0.01) powder phosphor. The SEM micrograph of $LiBaBO_3$: xDy^{3+} (x = 0.01) powder phosphor was taken at ×30000 magnifications and the micrograph shows that the powders were made up of fluffy needle-like particles which are clustered together in different orientations. **Figure 9.4** (**b**) shows the EDS spectrum of $LiBaBO_3$: xDy^{3+} (x = 0.01) powder phosphor. The spectrum confirms the presence of all major elements, namely Ba, O, B and Dy pointing to a succeful synthesis of the materials. However, Li element was not identified by SEM – EDS measurement. The reason may be due to the EDS detector being less sensitive to Li. [19].

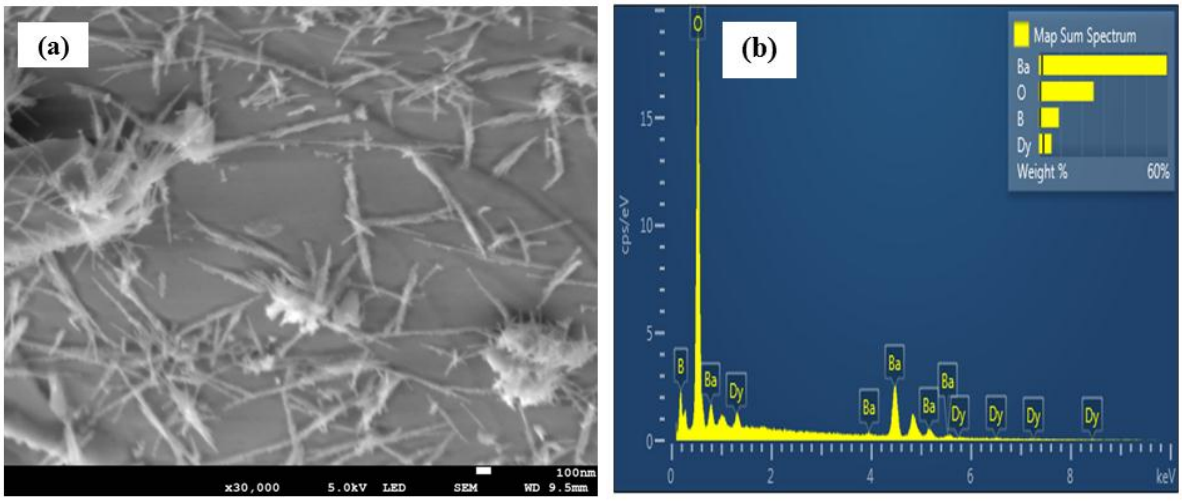

Figure 9.4: **a)** SEM micrograph and **b)** EDS spectrum of $LiBaBO_3$: xDy^{3+} (x = 0.01) powder phosphor.

High resolution transmission electron microscopy (HRTEM) images of $LiBaBO_3$: xDy^{3+} (x = 0.01) powder phosphor taken at different magnifications are shown in **Figure 9.5.** The HRTEM images in **figure 9.5** (**a, b and c**) for $LiBaBO_3$: $0.01Dy^{3+}$ show needle-like particles with different lengths overlapping each other. The lattice fringes shown in **figure 9.5** (**d**) have an estimated d-spacing of 0.181 nm corresponding to (230) plane of $LiBaBO_3$: xDy^{3+} (x = 0.01) monoclinic phase. The observed fine fringes are associated with the regular crystalline lattice.

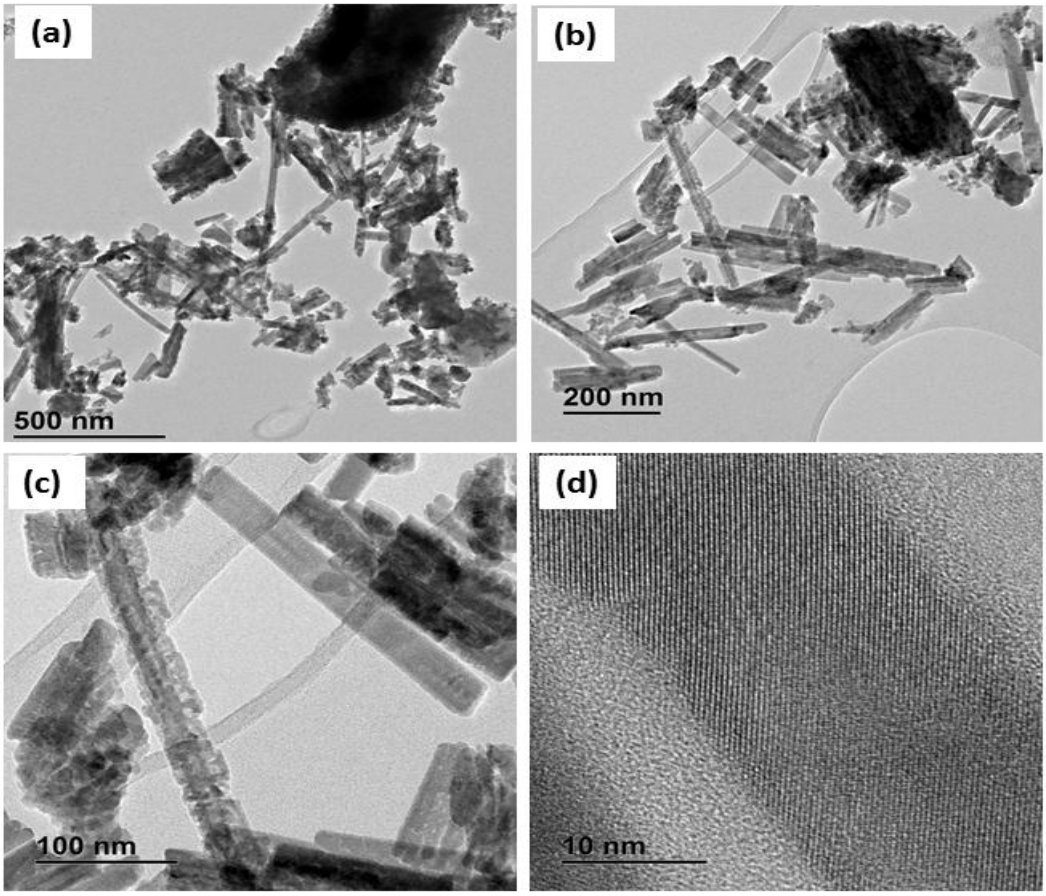

Figure 9.5: TEM images of $LiBaBO_3$: xDy^{3+} (x = 0.01) powder phosphor.

The room temperature FTIR spectra of both the host and the Dy^{3+} doped host are shown in **figure 9.6**. The absorption bands in the range of 600 – 800 cm^{-1} correspond to B-O-B bonding vibrations of borate networks, while those in the range of 800 – 1200 cm^{-1} correspond to the B-O bond stretching of tetrahedral BO_4 units and in thosein the 1200 – 1600 cm^{-1} range correspond to the B-O stretching bonds of the triangular BO_3 units **[**19, 20**]**. The inset in **figure 9.6** shows the same FTIR spectra of $LiBaBO_3$: xDy^{3+} (x = 0 and x = 0.01) from 650 to 1000 cm^{-1} to show bands in the specified range. The careful analysis of IR frequencies in the spectra Dy^{3+} doped phosphor powder shows that the exact positions of all the bands are coincident with the most prominent bands of the host. Therefore the incorporation of the dopant Dy^{3+} in $LiBaBO_3$ host did not affect the main structure and the results are in agreement with the XRD results.

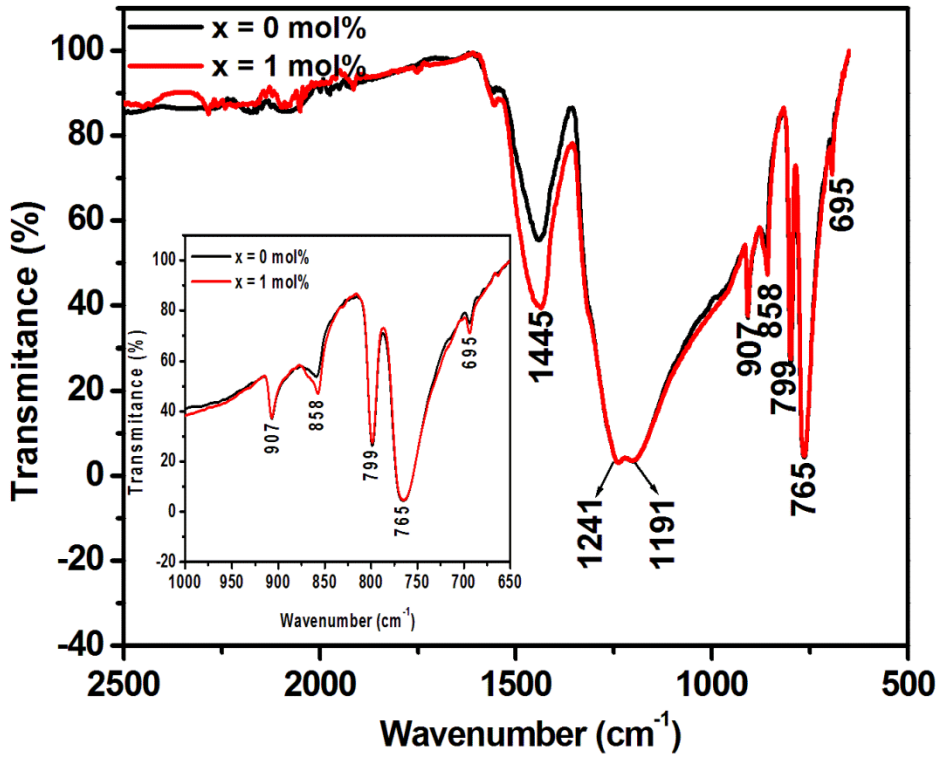

Figure 9.6: Fourier Transform Infrared spectroscopic (FTIR) spectra of $LiBaBO_3$: $x$$Dy^{3+}$ powder phosphors with x = 0 and x = 0.01.

ToF-SIMS analysis offers the possibility of imaging components based on the elemental or isotopic masses of their atomic and molecular ion fragments with high lateral resolution and sensitivity, yielding information including the identification of the peak composition and the distribution of the dopant and the homogeneity of the doping in the host lattice [21]. In this study, ToF-SIMS analysis was employed to study the composition of the elemental masses in $LiBaBO_3$: *0.01*Dy^{3+} powder phosphor. The compositional identification was achieved from the mass spectra (not shown) that were acquired at the surface of the phosphor, after sputtered clean, from Lithium (7 m/z), Barium (138 m/z), Boron (11 m/z), Dysprosium (163 m/z), Carbon (12 m/z) and Oxygen (16 m/z) peaks were used to obtain the maps. **Figure 9.7** shows the ToF-SIMS chemical images of LiBaBO3: *0.01*Dy^{3+} phosphor powder for positive ion mode for an area 100 µm × 100 µm. The images in **figure 9.7(a-d)** show the distribution of positive secondary ions such as Lithium (Li^+), Barium (Ba^+), Boron (B^+) and Dysprosium (Dy^+). The ToF-SIMS chemical images for negative ion mode for an area 100 µm × 100 µm is shown in **figure 9.8.** The

images in **figure 9.8** (**a-b**) shows the distribution of negative secondary ions such as Oxygen (O^-) and Carbon (C^-). The observed Carbon (C^-) signal is due to adventitious C from the environment [22]. The vertical scale bar in all the images represents the signal intensities of each ion. High intensity indicates region with high ionic concentration of the element in question and region of low intensity indicates low ionic concentration [18]. It this case, it can be seen from the images that there is a high distribution of O^- on the surface, followed by Li^+, C^-, Ba^+ and B^+. The dark pixels indicate a very low distribution of Dy^+ ions on the surface. **Figure 9.9** (**a and b**) shows the overlay distribution of Li^+, B^+ and Ba^+ and Li^+, Dy^+ and Ba^+, respectively. The overlayed Tof-SIMS images also confirmed that Li^+ is more distributed on the surface compared to other ions. Dy^+ ions as a dopand are not evenly distributed as seen in **figure 9.9** (**b**), which may be due to its small concentration.

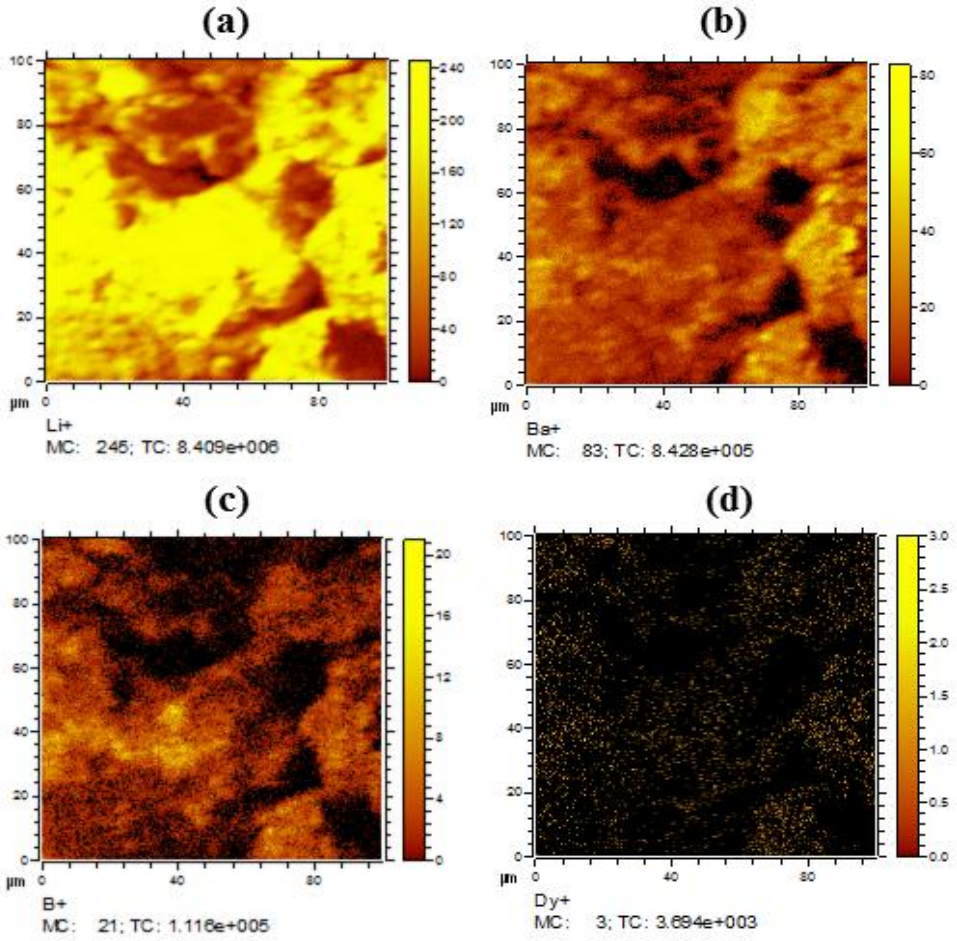

Figure 9.7: (Color online) (a) and (b) ToF-SIMS chemical images of LiBaBO3: *0.01*Dy^{3+} phosphor powder for positive ion mode for an area 100 µm×100 µm.

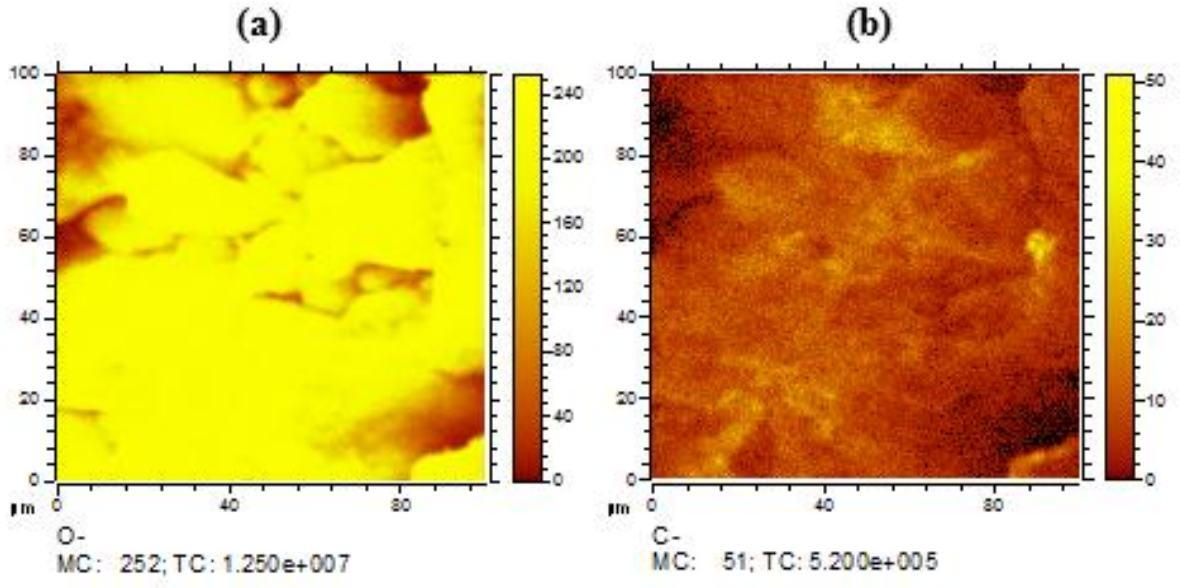

Figure 9.8: (Color online) (a) and (b) ToF-SIMS chemical images of $LiBaBO_3$: *0.01*Dy^{3+} phosphor powder for negative ion mode for an area 100 μm×100 μm.

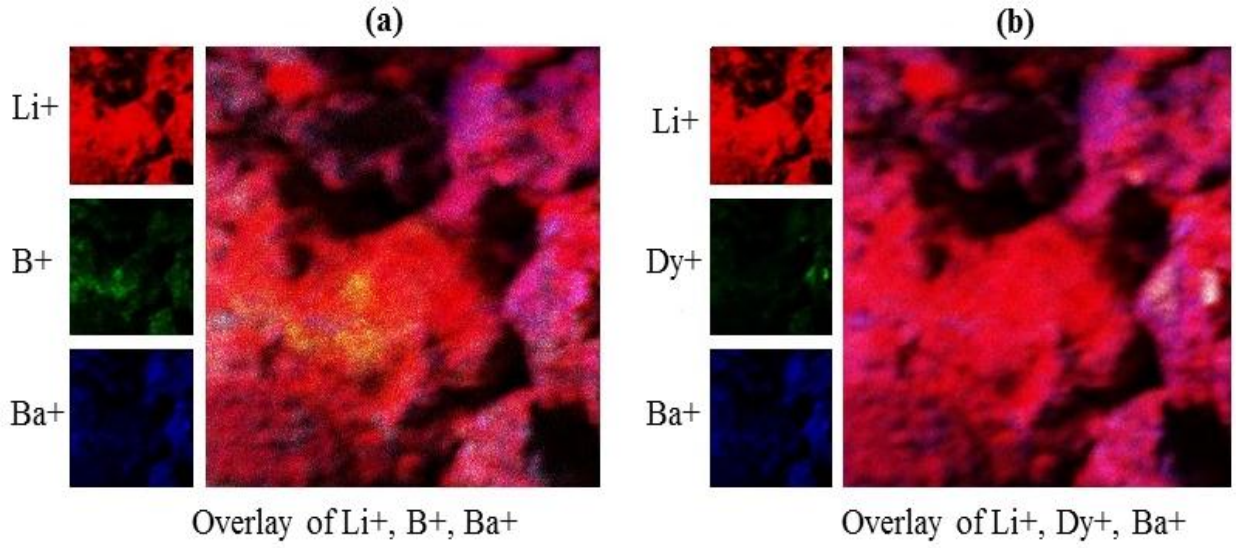

Figure 9.9: (Color online) Correlation analyses using an overlay images of a) Li^+, B^+ and Ba^+ and b) Li^+, Dy^+ and Ba^+, over an area of 100 μm×100 μm.

9.3.2 Photoluminescence studies

Figure 9.7 (**a**) represents the room temperature PL excitation spectra of $LiBaBO_3$: xDy^{3+} phosphors (x = 0.003, 0.005, 0.009, 0.01, 0.03 and 0.05). The excitation spectra recorded when monitoring 575 nm (yellow) emission has several bands at 298 nm, 325 nm, 354 nm and 389 nm attributed to the 4f - 4f transitions of Dy^{3+} **[**23**]**. The strongest excitation peak was observed at 354 nm and is assigned to the $^6H_{15/2} - {}^6F_{9/2}$ transition of Dy^{3+} [23]. The PL emission spectra of $LiBaBO_3$: xDy^{3+} (x = 0.003, 0.005, 0.009, 0.01, 0.03 and 0.05) powder phosphors excited at 354 nm are shown in **figure 9.7** (**b**). The spectra in addition to the well-known sharp lines peaked at 482 (blue) and 575nm (yellow), a minor line emission at 664 nm (red). These peaks are associated with the transitions of Dy^{3+} from the excited state $^4F_{9/2} - {}^6H_{15/2}$, $^4F_{9/2} - {}^6H_{13/2}$ and $^4F_{9/2} - {}^6H_{11/2}$, respectively [24]. It is well known that the blue emission at 482 nm ($^4F_{9/2} - {}^6H_{15/2}$) is associated magnetic dipole transition, which hardly varies with the crystal field strength around Dy^{3+}, while the stronger yellow emission at 575 nm ($^4F_{9/2} - {}^6H_{13/2}$) belongs to the hypersensitive force dielectric dipole transition, which is strongly influenced by the outside surrounding environment [25, 26].

According to the Judd–Ofelt theory, when Dy^{3+} is located at a low symmetry local site without inversion symmetry, a yellow emission according to the electric dipole transition $^4F_{9/2} - {}^6H_{13/2}$ will be dominant. Conversely, a magnetic dipole transition $^4F_{9/2} - {}^6H_{15/2}$ will be prominent, resulting in the blue emission being more intense than the yellow emission. In our case the yellow emission is dominant indicating that the Dy^{3+} was located at a low symmetry local site without inversion. The strong yellow emission is also instrumental in balancing the correlated color temperature of the phosphors and generates warm white light emission. Moreover, the hardly perceived transition $^4F_{9/2} - {}^6H_{11/2}$ emission at 664nm is ascribed to the disordered crystal field [27]. In **figure 9.7** (**b**), It can be seen that all the emission spectra have the peak at the same wavelength regardless of Dy^{3+} contents in $LiBaBO_3$: xDy^{3+} (x = 0.003, 0.005, 0.009, 0.01, 0.03 and 0.05) powder phosphors. With increase in Dy^{3+} ion concentration in $LiBaBO_3$ host material, the emission intensity increase with an increase in the Dy^{3+} concentration and reaches the maximum value at x = 0.01. After this, a decrease in emission intensity is observed with further increase in Dy^{3+} concentration. This decrease of PL emission intensity for Dy^{3+}concentration

above x = 0.01 may be due to concentration quenching phenomenon [28]. As the concentration increases, the distance between Dy^{3+} ions becomes smaller, leading to a higher probability of energy transfer among Dy^{3+} ions. The effect of Dy^{3+} concentration on the PL emission intensity of $LiBaBO_3$ phosphor is shown as an inset in **figure 9.7(c)**. The concentration quenching is mainly caused by the non-radiative energy transfer among Dy^{3+} ions, which occurs as a result of an exchange interaction, radiation re-absorption, or a multipole – multipole interaction [29]. This type of interaction mechanism can be understood by determing the critical distance (R_c) between the neighboring Dy^{3+} ions. According to Blasse theory, the critical distance (R_c) can be obtained by equation 9.2 [30, 31]:

$$R_C = 2\left[\frac{3V}{4\pi x_c N}\right]^{1/3} \qquad (9.2)$$

where V is the volume of one unit cell, N is the number of cations in the unit cell and x_c is the critical concentration of the activator ion. According to the crystal structure of $LiBaBO_3$ V = 305.92 $Å^3$, N = 4 and x_c = 0.01, respectively. The calculated value of the critical distance (R_c) between Dy^{3+} - Dy^{3+} ions was 24.4 Å. If the value of Dy^{3+} - Dy^{3+} distance is greater than 5 Å, the exchange interaction become ineffective and only the multipole – multipole interaction is the major cause of concentration quenching of Dy^{3+} in the phosphors [32]. Therefore our R_c value of 24.4 Å shows that the multipole interaction plays an important role in the concentration quenching mechanism of Dy^{3+} in the $LiBaBO_3$: Dy^{3+} powder phosphor.

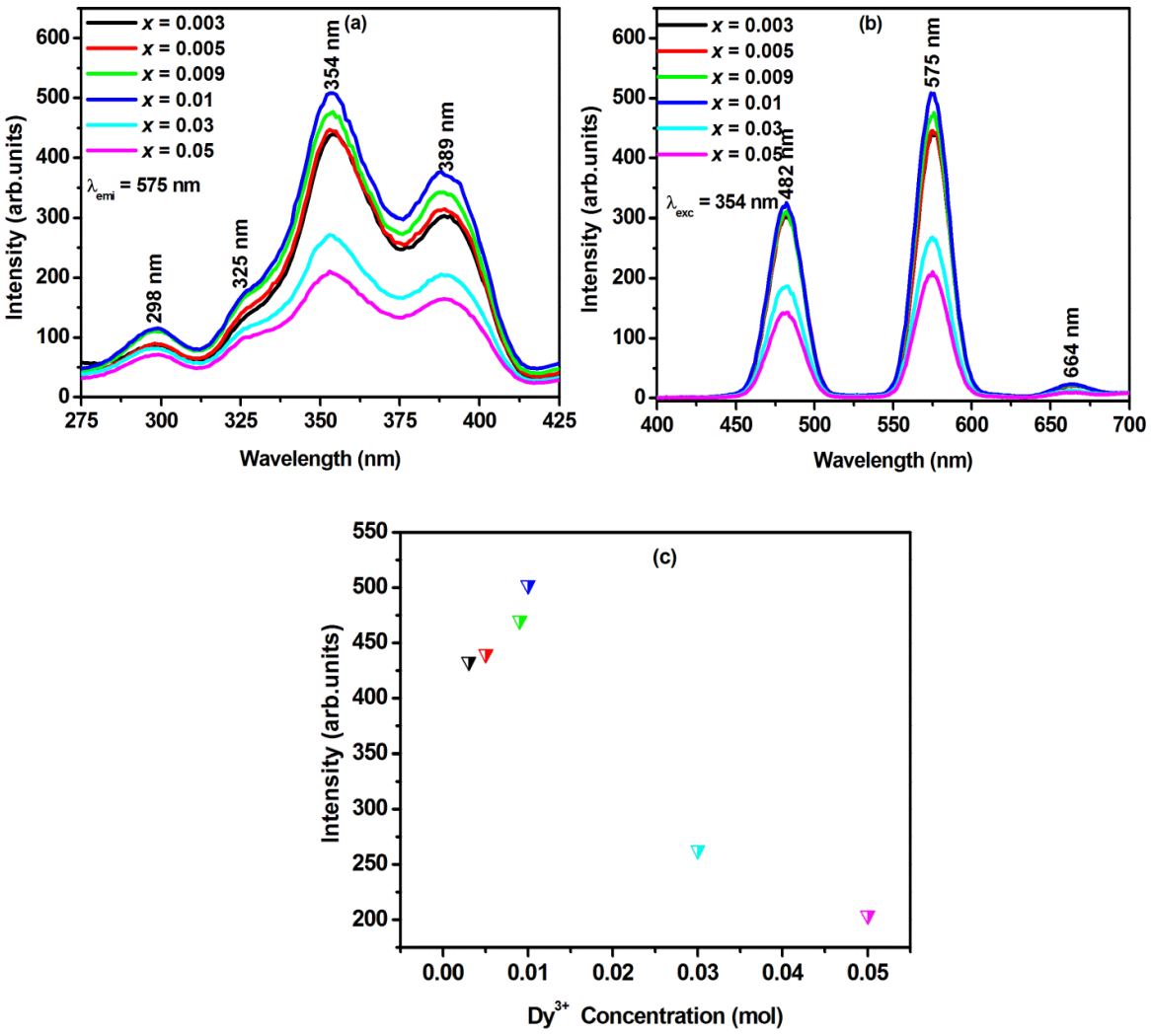

Figure 9.10: a) PL excitation spectra and **b)** PL emission spectra of the $LiBaBO_3$: xDy^{3+} (x = 0.003, 0.005, 0.009, 0.01, 0.03 and 0.05) powder phosphors and **c**) the variation of luminescence intensity with different concentrations of Dy^{3+}.

The strength of the multipolar interaction can be determined from the change in the emission intensity from the emitting level which has the multipolar interaction. When the concentration of the dopant is sufficiently high, the luminescence intensity I and the dopant concentration x can be related by the theory equation proposed by Dexter [33]:

$$\frac{I}{x} = k\left[1+\beta(x)^{Q/3}\right]^{-1} \qquad (9.3)$$

This equation can be approximated as,

$$\log \frac{I}{x} = c - \frac{Q}{3} \log x \qquad (9.4)$$

where, *k*, β and *c* are constants for the same excitation condition for the given host, *x* is the activator concentration which is greater than the critical concentration, *Q* is the series of multipole interaction for dipole–dipole (d–d), dipole–quadrupole (d–q) and quadrupole–quadrupole (q–q) interactions when the values of *Q* are 6, 8 and 10, respectively [34]. The value of *Q* can be obtained from the slope (-Q/3) of the plot of log (I/x) vs log(x). The relation between log (I/*x*) and log(*x*) in $LiBaBO_3$: xDy^{3+} powder phosphor is shown in **figure 9.8**. The plot is almost linear and the fitted line slope is -1.5734. Then, the value of *Q* was found to be 4.72 from equation (9.4), which is close to 6, indicating that the electric dipole–dipole interaction is the major mechanism for the concentration quenching of the $LiBaBO_3$: xDy^{3+} powder phosphor.

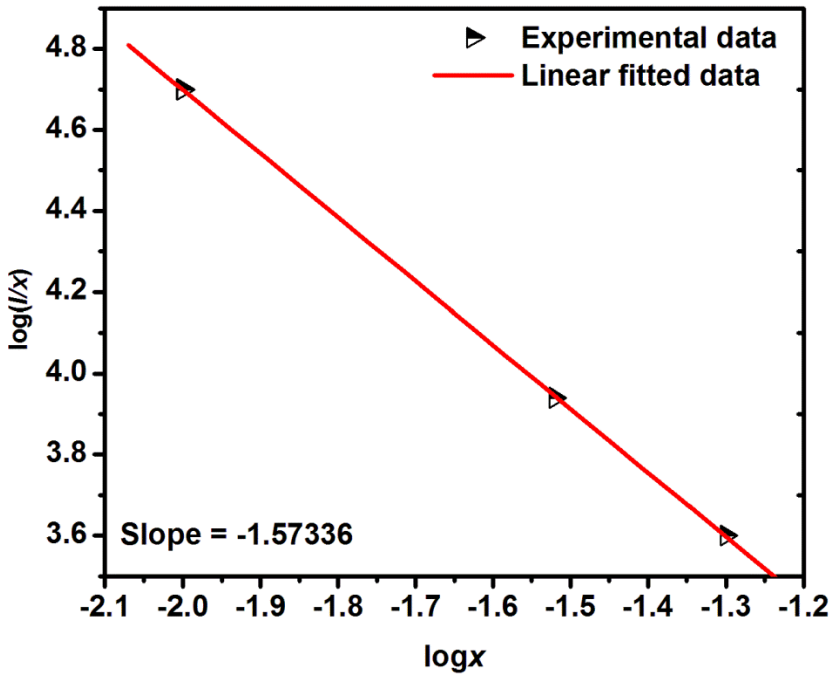

Figure 9.11: Graph of log (*I*/*x*) as a function of log (*x*) in $LiBaBO_3$: xDy^{3+} powder phosphor.

Figure 9.9 shows the proposed energy level diagram of Dy^{3+} ion in the $LiBaBO_3$ host lattice. When excited with UV-light, electrons are promoted from the valence band of the host to its conduction band and holes are generated in the valence band. Some of the excited electrons relax at the higher energy levels of Dy^{3+}. After undergoing non-radiative transitions to $^4F_{9/2}$ level, the excited electrons recombine to the various energy levels of Dy^{3+} and finally, the blue (482 nm), yellow (575 nm), and red (664 nm) emissions were observed [35, 36].

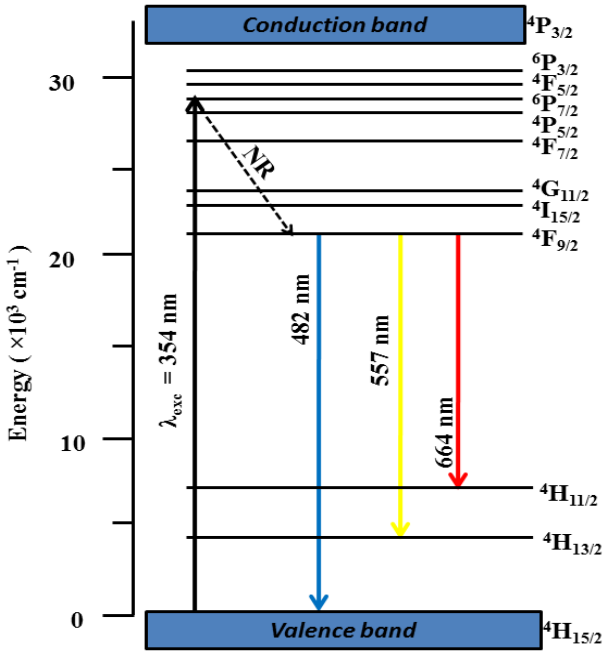

Figure 9.12: Energy level diagram of Dy^{3+} ion in the $LiBaBO_3$ host lattice [27, 35].

The Commission International de l'Eclariage (CIE) chromaticity is an important system for quantifying colours of phosphors [38]. **Figure 9.13** presents the CIE x-y coordinates diagram of $LiBaBO_3$: xDy^{3+} (x = 0.01) phosphor. The x-y coordinates of the phosphors are (x = 0.367 and y = 0.410) which gives a yellowish-white phosphor. From the CIE diagram it was found that the coordinates (0.367 and 0.410) lie within the white region, though they are far away from the ideal equal energy white light illumination (0.333, 0.333). All other phosphor powders of

$LiBaBO_3$: $x$$Dy^{3+}$ show the same yellowish-white color and their CIE coordinates and the CCT are given in **table 9.2.**

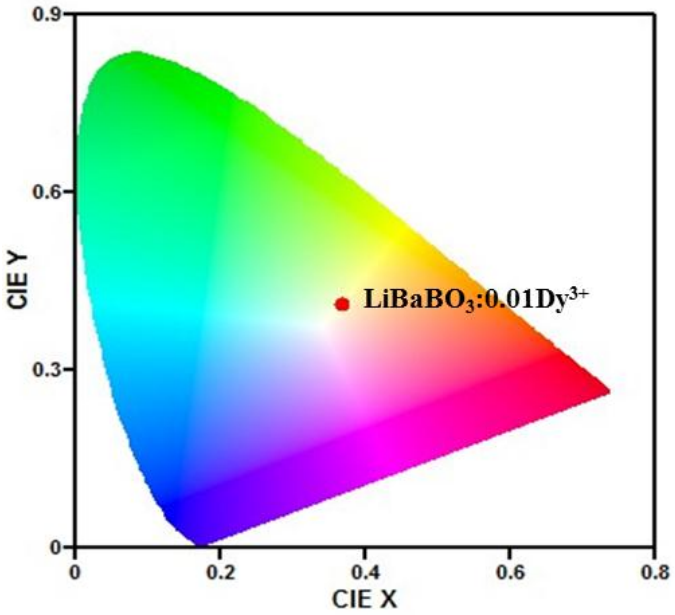

Figure 9.13: The CIE diagram showing coordinates of the as-prepared $LiBaBO_3$: $x$$Dy^{3+}$ phosphor with x = 0.01.

The correlated color temperature (CCT) is a specification of the color appearance of the light emitted by a light source, relating its color to the color of light with respect to a reference light source when heated up to a specific temperature, in degrees Kelvin (K). The CCT rating for a lamp or a source is a measure of the general ‘‘warmth’’ or ‘‘coolness’’of its appearance. However, opposite to the temperature scale, lamps with a CCT rating below 3200 K are usually considered ‘‘warm’’ sources, while those with a CCT above 4000 K are usually considered ‘‘cool’’ in appearance [39]. The colour quality of white light in terms of colour correlated temperature (CCT) is given by the McCamy empirical formula [40]

$$CCT = -437n^3 + 3601n^2 - 6861n + 5514.31 \quad (9.5)$$

where $n = (x - x_e)/(y - y_e)$ is the inverse slope line and ($x_e = 0.332$, $y_e = 0.186$) is the epicenter. Generally, the preferred CCT values range from 3500 K to 6500 K but the range from 3000 K to 7800 K may also be accepted [41]. The values of CCT calculated for each sample is summarized in **table 9.2**.

Table 9.2: CIE co-ordinates and CCT values of $LiBaBO_3$: xDy^{3+} powder phosphors.

	CIE chromaticity coordinates		
$LiBaBO_3$: xDy^{3+}	x	y	Correlated Color temperature CCT (K)
$x = 0.003$	0.3637	0.4035	4590
$x = 0.005$	0.3637	0.4042	4593
$x = 0.009$	0.3655	0.4079	4560
$x = 0.01$	0.3674	0.4104	4521
$x = 0.03$	0.3589	0.4038	4722
$x = 0.05$	0.3599	0.4053	4699

Shown in **figure 9.14** is the room temperature decay spectrum of the $LiBaBO_3$: xDy^{3+} phosphor with $x = 0.01$. The spectrum was fitted by the first order exponential decay, which can be fitted into approximate function as [42]:

$$I = I_0 \exp(-t / \tau) \quad (9.6)$$

where I_0 and I are the luminescence emission intensities at time 0 and t and τ is the luminescence decay lifetime. The luminescence decay lifetime of the prepared phosphor powder was determined to be 511 ms. A millisecond order of lifetime values of the powder phosphors reveals

the suitability of these materials for use in field emission display and light-emitting diodes applications [43].

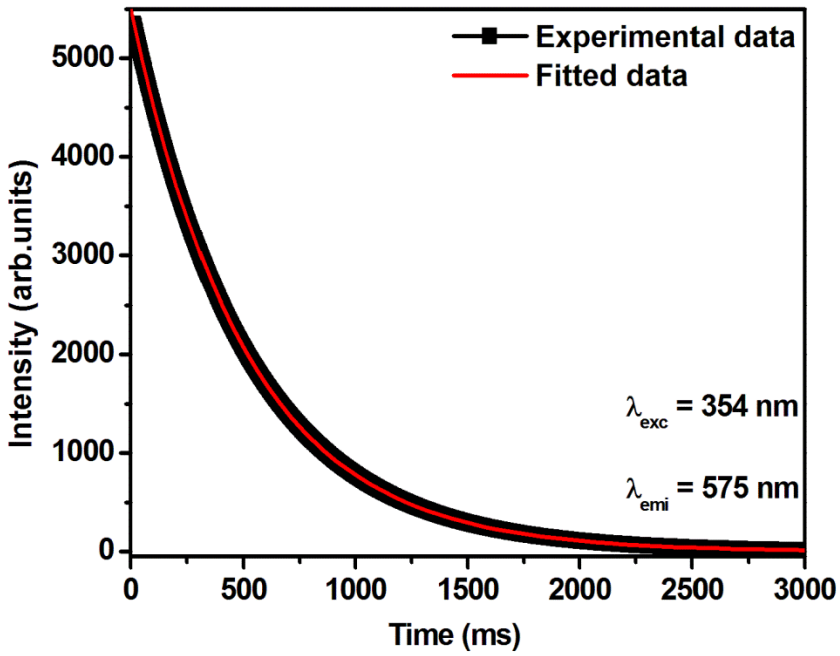

Figure 9.14: Room temperature decay spectrum of $LiBaBO_3$: $x$$Dy^{3+}$ phosphor with x = 0.01.

9.3.3 Thermoluminescence studies

Thermoluminescence is enhancement of the radiative emission of materials by the application of heat which are already being excited electronically. The crystal phosphors that respond to TL consist of certain traps which are the imperfections or defects in the crystal lattice. The electrons absorb excitation energy and get ejected from the luminescent center. The electrons then get captured in these traps. Trapped electrons absorb the additional thermal energy in order to be released from the traps and recombine with a center and undergo radiative transition [44]. The TL glow-curves of $LiBaBO_3$: *0.01*Dy^{3+} powder phosphor under different UV exposure times (5 – 30 min) with a constant heating rate of 2 ºC/sec are shown in **figure 9.15**. The glow curves show a broad TL glow peak from 10 ºC to 200 ºC centered at 104 ºC with a small shoulder at 56 ºC. It is observed that as the UV exposure time increases from 5 to 30 min, the intensities of the TL

peaks increases. The glow peaks shows no shift to either low or high temperatures as the UV exposure time increases.

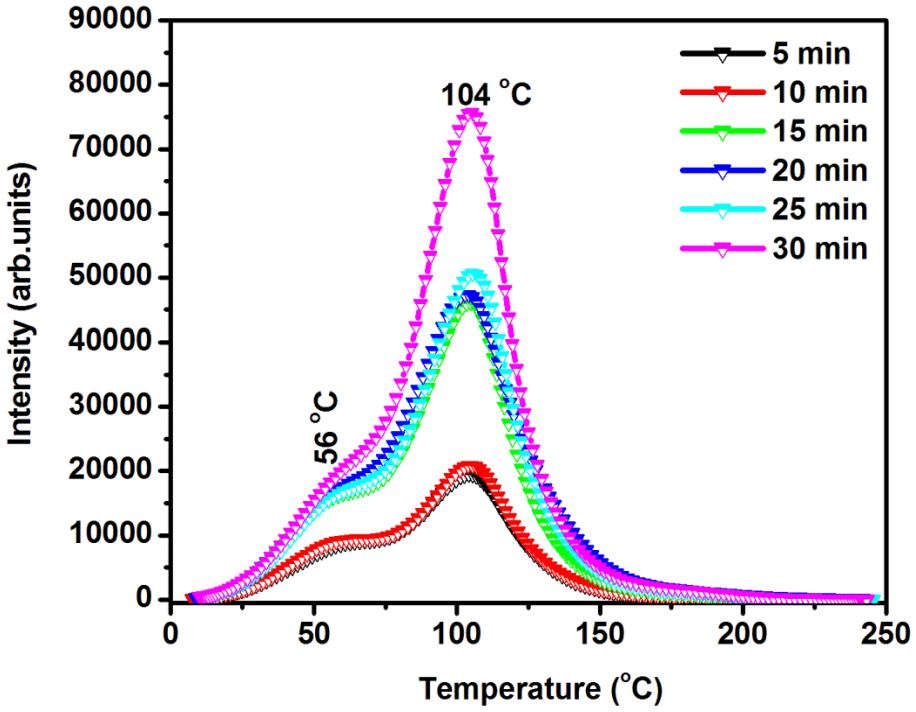

Figure 9.15: TL glow curve of $LiBaBO_3$: *0.01*Dy^{3+} for different UV exposure time.

The heating rate is a fundamental experimental variable in TL measurements. The TL glow curves of $LiBaBO_3$: *0.01*Dy^{3+} powder phosphor under different heating rates of 2 ºC/sec, 4 ºC/sec and 6 ºC/sec at constant UV exposure time of 5 min are shown in **figure 9.16.** It can be seen that with the increase in the heating rate from 2 ºC/sec - 6 ºC/sec the peak intensities of the TL glow curves decreases. Also a shift in the peak towards the higher temperature side is observed with the increase in the heating rate. This behaviour in the TL glow curve may be due to the well-known effect of thermal quenching of TL due to the increase in the heating rate.

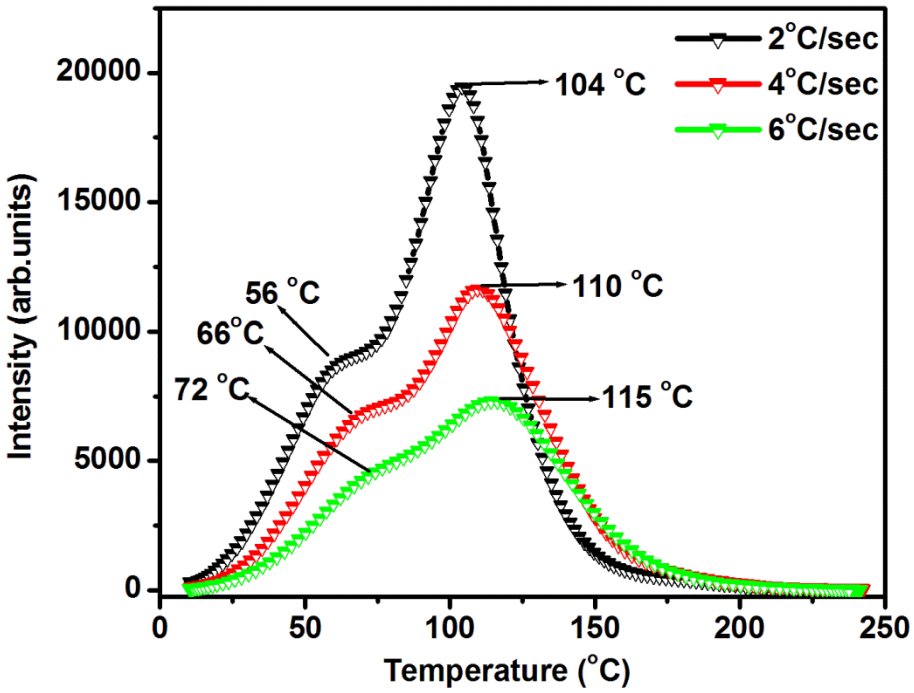

Figure 9.16: TL glow curve of $LiBaBO_3$: *0.01*Dy^{3+} for different heating rates.

The peak shape method, generally referred to as Chen's method [45], was used to determine the kinetic parameters such as the order of kinetics (*b*), activation energy (E_α) and frequency factor (*s*) of each of the deconvoluted glow peak of the TL materials. This method is mainly based on the temperatures *Tm*, T_1 and T_2, where *Tm* is the peak temperature while T_1 and T_2 are temperatures at half the intensity on the ascending and descending parts of the glow peak, respectively. Order of kinetics was evaluated from the symmetry factor (μ_g) of the glow peak given by equation (9.7). The values of μ_g for first- and second-order kinetics are 0.42 and 0.52, respectively. The deconvolution of the glow curves was done by using the TL Anal Program given by Chung et. al [46 - 48]:

$$\mu_g = \frac{T_2 - T_m}{T_2 - T_1} \tag{9.7}$$

The activation energy (E_α) can be calculated from the thermal peak temperature by using the following equation:

$$E_\alpha = c_\alpha\left(\frac{kT_m^2}{\alpha}\right) - b_\alpha(2kT_m) \tag{9.8}$$

with $\alpha = \tau, \delta, \omega$; $\tau = T_m - T_1$; $\delta = T_2 - T_1$; $\omega = T_2 - T_1$, $C_\tau = 1.51 + 3.0\,(\mu_g - 0.42)$;

$C_\delta = 0.976 + 7.3(\mu_g - 0.42)$; $C_\omega = 2.52 + 10.2(\mu_g - 0.42)$; $b_\tau = 1.58 + 4.2(\mu_g - 0.42)$;

$b_\delta = 0$; $b_\omega = 1$.

The frequency factor was calculated from the following equation:

$$\frac{\beta E}{kT_m^2} = s\exp\left\{\frac{-E}{kT_m}\right\}\left[1 + (Z-1)\Delta_m\right] \tag{9.9}$$

The GCD curves fitting of $LiBaBO_3$: *0.01*Dy^{3+} powder phosphor for different heating rates of **a**) 2 ºC/sec, **b**) 4 ºC/sec and **c**) 6 ºC/sec are shown in **figure 9.17**. For first, second and general order glow curves, equations (9.10) – (9.12) were proposed by Kitis et al [49], respectively**.**

For first order:

$$I(T) = I_m \exp\left[1 + \frac{E}{kT}\frac{T-T_m}{T_m} - \frac{T^2}{T_m^2}(1-\Delta)\exp\left\{\frac{E}{kT}\frac{T-T_m}{T_m}\right\} - \Delta_m\right], \tag{10}$$

For second order:

$$I(T) = 4I_m \exp\left\{\frac{E}{kT}\frac{T-T_m}{T_m}\right\}\left[\frac{T^2}{T_m^2}(1-\Delta)\exp\left\{\frac{E}{kT}\frac{T-T_m}{T_m}\right\} + 1 + \Delta_m\right]^{-2}, \tag{11}$$

and, *for general order:*

$$I(T) = I_m b^{b/b-1}\exp\left\{\frac{E}{kT}\frac{T-T_m}{T_m}\right\}\left[(b-1)(1-\Delta)\frac{T^2}{T_m^2}\exp\left\{\frac{E}{kT}\frac{T-T_m}{T_m}\right\} + Z_m\right]^{-b/b-1} \tag{12}$$

where, I(T) is the TL intensity at any temperature T(K), I_m is the maximum peak intensity, E is the activation energy in eV (calculated from Chen's formulae (equation (9.11)), k is the Boltzmann constant (8.6×10^{-5} eV K^{-1}), $\Delta = 2kT/E$; $\Delta_m = 2kTm/E$ and $Z_m = 1 + (b-1)\,\Delta m$. The trapping parameters of all the peaks at different heating rate (2 – 6 ºC/sec) calculated by using

the TL Anal program and Chen's formulism are summarized in **table 9.3**. The second-order kinetics was observed and the trap levels varied between 0.67 and 1.19 eV.

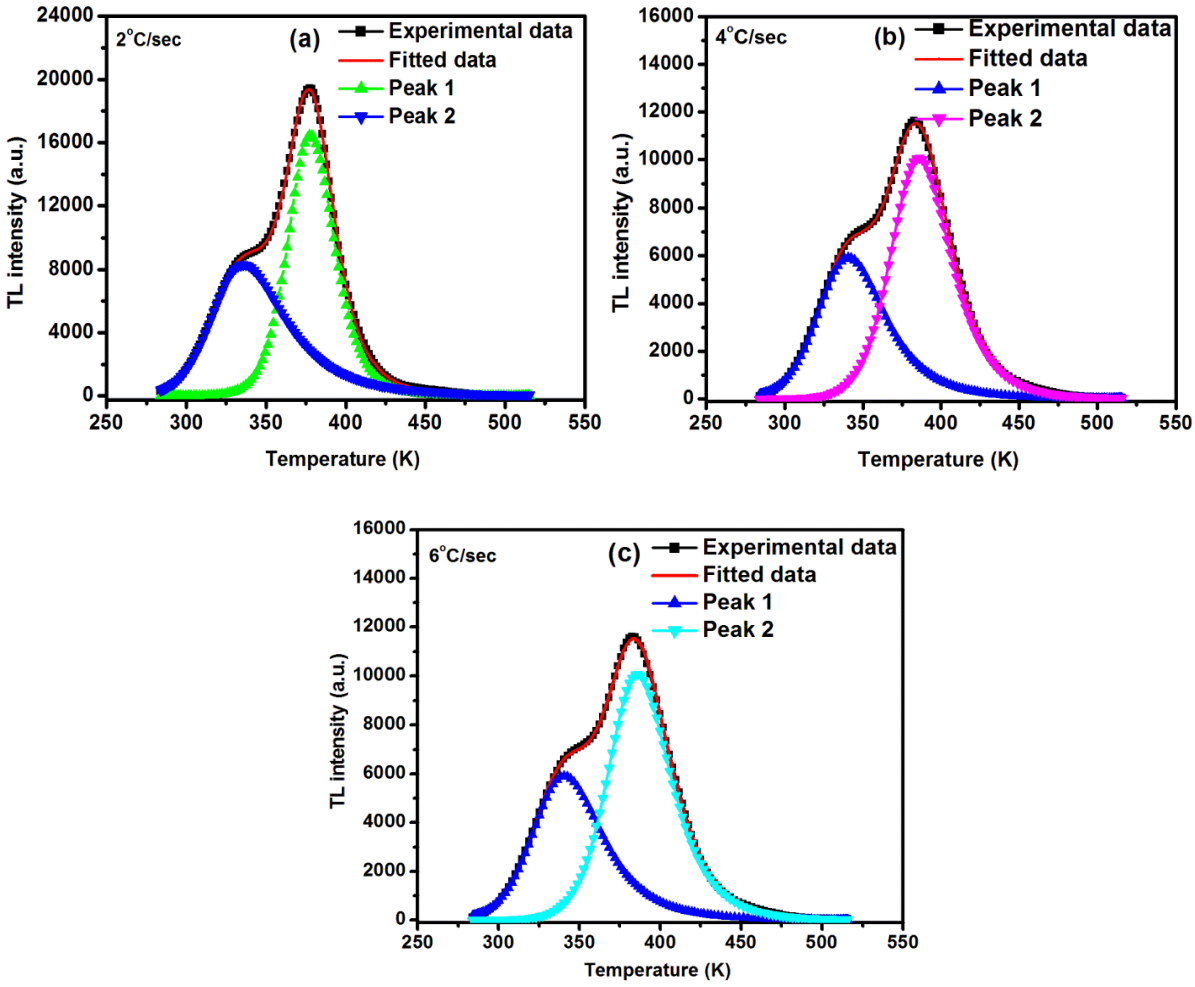

Figure 9.17: Deconvoluted curves of $LiBaBO_3$: *0.01*Dy^{3+} powder phosphors for different heating rates of **a**) 2 ºC/sec, **b**) 4 ºC/sec and **c**) 6 ºC/sec.

Table 9.3: Kinetic Parameters of the deconvoluted peaks of $LiBaBO_3$: *0.01*Dy^{3+} at different heating rates, calculated by TL Anal program and Chen's formulism.

Heating rate (ºC/sec)	Method used	T_1	T_2	T_M	Order of Kinetics (μ_g)	Activation energy (E in eV)	Frequency Factor (S in s^{-1})
2	1	312.70	366.07	335.98	0.56	0.67	1.40×10^{9}
	2	361.17	395.31	377.69	0.52	1.19	1.46×10^{15}
4	1	316.95	368.59	340.29	0.55	0.68	2.95×10^{9}
	2	364.50	410.12	385.05	0.55	1.01	4.83×10^{12}
6	1	317.36	368.45	340.31	0.55	0.69	7.23×10^{9}
	2	364.45	410.07	385.72	0.53	0.96	1.77×10^{12}

9.4 Conclusion

$LiBaBO_3$ phosphors doped with various concentrations of Dy^{3+} ions were prepared by the solid-state reaction method in air. The crystalline structure, excitation/ emission properties of the phosphors were characterized by XRD and photoluminescence spectrophotometry, respectively. The PL spectrum shows that $LiBaBO_3$: *x*Dy^{3+} powder phosphor exhibit a strong peak at 354 nm which is a suitable wavelength for w-LEDs. Upon 354 nm excitation, this phosphor shows peaks at 482 nm (blue), 575 nm (yellow) and 664 nm (red). The optimal doping concentration of Dy^{3+} in $LiBaBO_3$ host matrix was found to be $x = 0.01$. The value of R_c was calculated to be 24.4 Å and it was subsequently concluded that dipole- dipole (d-d) interaction is the main mechanism by which concentration quenching was triggered and this was confirmed by Dexter's theory. The CIE color coordinates for $LiBaBO_3$: *x*Dy^{3+} ($x = 0.01$) phosphor is calculated to be ($x = 0.367$; y = 0.410) which falls in the yellowish white region with the CCT value of 4521 K. All the results indicate that Dy^{3+} doped $LiBaBO_3$ powder phosphor could be used as an efficient luminescent material for solid state lighting as well as UV based w-LEDs. It is found that the intensity of TL

glow peak of $LiBaBO_3$: $x Dy^{3+}$ (x = 0.01) phosphor increases with increase in UV exposure time from (5 - 30) min. The effect of different heating rate shows the decrease in the TL intensity with a shift toward the higher temperature side. The activation energies calculated from both Anal program and Chen's formulism varied from 0.67 to 1.19 eV. The value of order of kinetics calculated from the shape parameter lies close to 0.52, which shows the presence of second order kinetic in the TL glows.

References

[1] R. Yu, S. Zhong, N. Xue, H. Li and H. Ma, *Royal Society of Chemistry*, **00** (2013) 1 - 3.

[2] J. Sun, Z. Lian, G. Shen and D. Shen, *Royal Society of Chemistry*, **3** (2013) 18395 - 18405.

[3] J. Zheng, Q. Cheng, J. Wu, X. Cui, R. Chen and W. Chen, *Material Research Bulleting*, **3** (2016) 38 - 47.

[4] G. Zhu, Y. Wang, Q. Wang, X. Ding, W. Geng and Y. Shi, *Journal of Luminescence*, **154** (2014) 246 - 250.

[5] Y. Ji, J. Cao, Z. Zhu, J. Li, Y. Wang, C. Tu, *Journal of Luminescence*, **132** (2012) 702 - 706.

[6] J. Zheng, Q. Cheng, J. Wua, X. Cui, R. Chen, W. Chen, C. Chen, *Materials Research Bulletin*, **73** (2016) 38 - 47.

[7] Z. Hu, T. Meng, W. Zhang, D.Ye , Y. Cui, L. Luo and Y. Wang, *Journal of Materials Sciences: Materials Electronics*, **25** (2014) 1933 - 1937.

[8] R. S Palaspagar, A.B. Gawade, R. P. Sonekar and S. K. Omanwar, *International Journal of Chemical and Physical Sciences*, **3** (2014) 2319 - 6602.

[9] W. Liu, Y. Chiu, C. Tung, Y. Yeh, S. Jang and T. Chen, *Journal of Electrochemical Society*, **155** (2008) 252 - 255.

[10] N. S. Bajaj and S.K. Omanwar, *Asian Journal of Chemistry*, **24** (2012) 5945 - 5946.

[11] P. A. Nagpure, N.S. Bajaj, R. P. Sonekar and S. K. Omamwar, *Indian Journal of Pure and Applied Physics*, **49** (2011) 799 - 802.

[12] L. Wu, X. L. Chen, H. Li, M. He, L. Dai, X. Z. Li and Y. P. Xu, *Journal of Solid State Chemistry*, **117** (2014) 1111 - 1116.

[13] N. S. Bajaj and S. K. Omanwar, *Optik- International Journal of Light and Electron Optics*, **125** (2014) 4077 - 4080.

[14] L. Wu, B. Wang, Y. Zhang, L. Li, H. R. Wang, H. Yi, Y. F. Kong and J. J. Xua, *Royal Society of Chemistry*, **43** (2014) 13845 - 13851.

[15] K. A. Koparkar, N. S. Bajaj, S. K. Omanwar, *Romanian Journal of Physics*, **60** (2015) 481 - 487.

[16] R. Velchuri, B. V. Kumar, V. R. Devi, G. Prasad, D. J. Prakash and M. Vithal, *Materials Research Bulletin*, **46** (2011) 1219 - 1226

[17] P. Li, L. Pang, Z. Wang, Z. Yang, Q. Guo and X. Li, *Journal of Alloys and Compounds*, **478** (2009) 813 - 815.

[18] S. N. Ogugua, S. K. K. Shaat, H. C. Swart, O. M. Ntwaeaborwa, *Journal of Physics and Chemistry of Solids*, **83** (2015) 109 - 116.

[19] M. A. Lephoto, K. G. Tshabalala, S. J. Motloung, S. K. K. Shaat, O. M. Ntwaeaborwa, *Luminescence*, **00** (2017) 1 - 8, *Doi.org/10.1002/bio.3295*.

[20] R. Li, L. Bao and X. Li, *Royal Society of Chemistry*, **13** (2011) 5858 - 5862.

[21] V. Kumar, A. K. Bedyal, S. S. Pitale, O. M. Ntwaeaborwa, H. C. Swart, *Journal of Alloys and Compounds* **554** (2013) 214 – 220.

[22] V. Kumar, V. Kumar, S. Som, M. M. Duvenhage, O. M. Ntwaeaborwa, H. C. Swart, *Applied Surface Science*, (2014) Doi.org/10.1016/j.apsusc.2014.04.192.

[23] J. Kuang, Y. Liu and J. Zhang, *Journal of Solid State Chemistry***, 179** (2006) 266 - 269.

[24] Y. Li and Y. Wang, *Journal of Information Display*, **12** (2011) 93 - 96.

[25] S. N. Ogugua, H. C. Swart, O. M. Ntwaeaborwa, *Physica B*, **480** (2016) 131 - 136.

[26] S. Kumar, R. Prakash and V. Kumar, *Functional Materials Letters*, **8** (2015) 1550061 (4 pages).

[27] I. P. Sahu, D. P. Bisen, N. Brahme and R. K. Tamraka, *Journal of Electronic Materials*, (2015) Doi: 10.1007/s11664-015-4284-5.

[28] B. V. Ratnam, M. Jayasimhadriz, K. Jangw, and H. S. Lee, S. Yi, J. Jeong, *Journal of the American Ceramic Society*, **93** (2010) 3857 - 3861.

[29] G. V. L. Reddy, L. R. Moorthy, B.C. Jamalaiah, T. Sasikala, *Ceramics International*, **39** (2013) 2675 - 2682.

[30] G. R. Dillip, B. Ramesh, C. M. Reddy , K. Mallikarjuna, O. Ravi , S. J. Dhoble, S. W. Joo, B. Deva Prasad Raju, *Journal of Alloys and Compounds*, **615** (2014) 719 - 727.

[31] P. Hu, W. Zhang, Z. Hu, Z. Feng, L. Ma, X. Zhang, X. Sheng and J. Luo, *Journal of Materials Science and Chemical Engineering*, **4** (2016) 37 - 44.

[32] M. Manhas, V. Kumar, O. M. Ntwaeaborwa, H.C. Swart, *Ceramics International*, **42** (2016) 5743 - 5753.

[33] G. B. Nair and S. J. Dhoble, *Royal Society of Chemistry*, **5** (2015) 49235 - 49247.

[34] Y. Zhou, W. Zhao, J. Chen and Z. Liao, *Royal Society of Chemistry*, **7** (2017) 17244 - 17253.

[35] S. N. Ogugua, S. K. K. Shaat, H.C. Swart and O. M. Ntwaeaborwa, *Journal of Luminesence*, **179** (2016) 154 -164

[36] P. Du, L. K. Bharat, X. Guan, and J. S. Yu, *Journal of Applied Physics*, **117** (2015) 083112-1 - 083112-6.

[37] S. Dutta, S. Som and S. K. Sharma, *Royal Society of Chemistry*, **42** (2013) 9654 - 9661.

[38] U. Fawad, H. J. Kim, S. N. Khan, and A. Khan, *Science of Advanced Materials*, **7** (2015) 2528 - 2535.

[39] R. Shrivastava, J. Kaur and M. Dash, *Superlattices and Microstructures*, **82** (2015) 262 - 268.

[40] S. Som, P. Mitra, V. Kumar, V. Kumar, J. J. Terblans, H. C. Swart and S. K. Sharma, *Royal Society of Chemistry*, **43** (2014) 9860 - 9871.

[41] G. Tiwari, N. Brahme, R. Sharma, D. P. Bisen, S. K. Sao and S. J. Dhoble, *Royal Society of Chemistry*, **6** (2016) 49317 - 49327.

[42] M. Parandamaiah, K. N. Kumar, S. Babu, S. V. Reddy and Y.C. Ratnakaram, *International Journal of Engineering Research and Applications*, **5** (2015) 126 - 131.

[43] S. Saha, S. Das, U. K. Ghorai, N. Mazumder, B. K. Guptac and K. K. Chattopadhyay, *Dalton Transactions*, 42 (2013) 12965–12974

[44] D. Singh, J. Kaur, N. S. Suryanarayana, R. Shrivastava, V. Dubey, *Journal of Material Sciences: Material Electronics*, **28** (2017) 2462 - 2470.

[45] R. Chen, Y. Krish, *Analysis of Thermally Stimulated Processes*, Pergamon Publishing Co. Pte. Ltd., New York, (1981).

[46] K .S. Chung, H. S. Choe, J. I. Lee, J. L. Kim, S. Y. Chang, *Radiation Protection Dosimetry*, **115** (2005) 343 - 349.

[47] A. K. Bedyal, V. Kumar, S. P. Lochab, F. Singh, O. M. Ntwaeaborwa, H. C. Swart, *International Journal of Modern Physics: Conference Series*, **22** (2013) 365 - 373.

[48] A. K. Bedyal, V. Kumar, V. K. Singh, S. P. Lochab, F. Singh, O. M. Ntwaeaborwa and H. C. Swart, *Radiation Effects & Defects in Solids*, **168** (2013) 1022 - 1029.

[49] G. Kitis, J. M. Gomez-Ros, J. W. N. Tuyn, *Journal of Physics D: Applied Physics*, **31** (1998) 2636 - 2641.

Chapter 10

Summary and Future work

10.1 Summary

Borates materials were successfully synthesized by solution combustion method and solid state method. All the prepared powder phosphors were characterized by various techniques to get the structure, morphology, stretching vibrations, chemical composition, thermal stability, photoluminescence, decay characterization and Thermoluminescence.

The powder phosphors of BaB_8O_{13}: xBi^{3+} were synthesized by solution combustion method. The XRD patterns confirmed the structure to be orthorhombic. Their crystallite sizes were calculated by both Scherrer and Williamson-Hall equations. SEM images showed that the particles were agglomerated together and without definite shapes. The bandgap of the BaB_8O_{13} host matrix was found to be 3.43 eV and was increased after Bi^{3+} doping. Under UV 271 nm excitation, Bi^{3+} doped phosphors showed a broad emission at 548 nm which is attributed to the $^1S_0 - {}^3P_1$ transition of Bi^{3+} ions. The CIE chromaticity coordinates indicated that the Bi^{3+} doped phosphors exhibit a green color. The results showed that BaB_8O_{13}: Bi^{3+} powder phosphor can be considered as promising candidates for green emitting phosphor for applications in the field emission display and white light-emitting diodes.

Eu^{3+}, Sm^{3+} single doped and Eu^{3+} - Sm^{3+} co-doped BaB_8O_{13} phosphor powders were prepared by solution combustion method. The PL emission of BaB_8O_{13}: Eu^{3+}; Sm^{3+} phosphor powders showed emissions from both Eu^{3+} and Sm^{3+} ions under 402 nm. The energy transfer from Sm^{3+} to Eu^{3+} in BaB_8O_{13} host matrix was observed and was attributed to multipolar interactions. BaB_8O_{13}: $0.05Eu^{3+}$; $0.005Sm^{3+}$ powder phosphor with the CIE chromaticity coordinates of

(0.637, 0.362) located in the red region indicated that the phosphor have the potential for application as a red emitting phosphor for n-UV-based LEDs.

The XRD patterns of the Ce^{3+} activated BaB_8O_{13} phosphors were found to be consistent with the standard orthorhombic crystal structure of BaB_8O_{13}. The photoluminescence spectroscopy data showed a broad emission centered at 515 nm under the UV excitation of 270 nm. The PL emission intensity was dependent on the concentration of Ce^{3+} with the maximum concentration obtained from the 0.05 mol Ce^{3+} doping. The CIE chromaticity coordinates indicated that the Ce^{3+} doped phosphors exhibited the green emission color, with coordinates close to those of the standard green phosphor, suggesting that our material is a potential candidate to be used as source of green light in different types of light emitting devices.

BaB_8O_{13}: $x$$Dy^{3+}$ phosphors were synthesized by a solution combustion method. The photoluminescence studies showed that BaB_8O_{13}: $x$$Dy^{3+}$ phosphor could be excited by near ultraviolet (NUV) light 350 nm and the emission peaks are located at 480 nm (blue) and 574 nm (yellow). The critical transfer distance of Dy^{3+} in BaB_8O_{13}: $x$$Dy^{3+}$ phosphor is about 46 Å and the dipole–dipole interaction is the major mechanism for the concentration quenching. The CIE chromaticity coordinates for BaB_8O_{13}: $x$$Dy^3$phosphors are located in the yellowish-white region. These results indicate that the BaB_8O_{13}: $x$$Dy^{3+}$ phosphor shows potential application in NUV white LED.

$LiBa_{1-x}BO_3$: $x$$Eu^{3+}$ and $LiBa_{0.975-y}BO_3$: *0.025*Eu^{3+}; $y$$Bi^{3+}$ powder phosphor were successfully synthesized by solid state method. Blue emission was observed from $LiBaBO_3$ host matrix which is ascribed to self- activated emission. The red emission from Eu^{3+} is considerably enhanced after the Bi^{3+} co-doping. The tunable color properties of $LiBaBO_3$: Eu^{3+} indicated that the phosphors provide a potential to be a single component white light phosphor. White light emission was obtained from $LiBa_{1-x}BO_3$: $x$$Eu^{3+}$ (x = 0.020 and x = 0.025) phosphor powders with the color coordinates x = 0.368 and y = 0.378 and x = 0.376, y = 0.366, respectively.

$LiBaBO_3$: $x$$Dy^{3+}$ ions were prepared by solid-state reaction method in air atmosphere. Tof-SIMS confirmed analysis the composition of the elemental masses and the distribution of different ions on the surface of $LiBaBO_3$: $x$$Dy^{3+}$ powder phosphor. Upon 354 nm excitation, $LiBaBO_3$: $x$$Dy^{3+}$ phosphor showed peaks at 482 nm (blue), 575 nm (yellow) and 664 nm (red). The optimal doping concentration of Dy^{3+} in $LiBaBO_3$ host matrix was found to be x = 0.01. The value of R_c

was found to be 24.4 Å and dipole - dipole (d-d) interaction was the main mechanism for concentration quenching as confirmed by Dexter's theory. The CIE color coordinates for $LiBaBO_3$: xDy^{3+} (x = 0.01) phosphor was calculated to be (x = 0.367; y = 0.410) which falls in the yellowish white region with the CCT value of 4521 K. All the results indicate that Dy^{3+} doped $LiBaBO_3$ powder phosphor could be used as an efficient luminescent material for solid state lighting as well as UV based w-LEDs. The intensity of TL glow peak of $LiBaBO_3$: xDy^{3+} (x = 0.01) phosphor increases with increase in UV exposure time from (5 - 30) min. The effect of different heating rate shows the decrease in the TL intensity with a shift toward the higher temperature side. The activation energies calculated from both Anal program and Chen's formulism varied from 0.67 to 1.19 eV. The value of order of kinetics calculated from the shape parameter lies close to 0.52, which shows the presence of second order kinetic in the TL glows.

10.2 Future work

In this study, all the prepared powder phosphors showed mainly red and green emissions. It would be good if more study is performed on borate phosphors to get a blue emitting powder phosphor. In order to generate white light in LEDs, it would be of great interest to prepare a triple doped phosphor which might give white light emission. In most cases phosphors are usually commercially found in powder form but in thin film forms for practical purposes. In thin film form, phosphors has more advantages than powders, as a results, in future, thin films will be prepared using these borate materials.

10.3 Publications

1. **M. A. Lephoto**, K. G. Tshabalala, S. J. Motloung, S. K. K. Shaat and O. M. Ntwaeaborwa, Tunable emission from $LiBaBO_3$: Eu^{3+}; Bi^{3+} phosphor for solid-state lighting, Luminescence, (2017), DOI: 10.1002/bio.3295
2. **M. A. Lephoto**, K. G. Tshabalala, S. J. Motloung, I. Ahemen and O. M. Ntwaeaborwa, Study on photoluminescence and energy transfer of Eu^{3+}/Sm^{3+} single-doped and co-doped BaB_8O_{13}, Physica B, (2017), Doi.org/10.1016/j.physb.2017.06.063

3. S. J Motloung, **M. A. Lephoto**, K. G. Tshabalala and O. M. Ntwaeaborwa, Combustion synthesis and characterization of $MV_{0.5}P_{0.5}O_4$: Sm^{3+}, Tm^{3+} (M = Gd, La, Y), (2017), Doi.org/10.1016/j.physb.2017.07.038
4. **M. A. Lephoto**, K. G. Tshabalala, S. J. Motloung and O. M. Ntwaeaborwa, Analysis of the structure, particle morphology and photoluminescent properties of green emitting BaB_8O_{13}: Ce^{3+} phosphor (SAIP 2017 Proceedings)
5. **M. A. Lephoto**, K. G. Tshabalala, S. J. Motloung, G. H. Mhlongo and O. M. Ntwaeaborwa, Photoluminescence studies of green emitting BaB_8O_{13}: Bi^{3+} phosphors prepared by solution combustion method, Journal of Luminescence (Issue: VSI: Lumin_ICL2017, *under review)*

10.4 Conferences

1. 53nd Annual Conference of the Microscopy Society of Southern Africa (MSSA), 30 November to 3 December 2015, St Georges Hotel Pretoria, South Africa

   Luminescent properties, structure and morphology analysis of $LiBaBO_3$: Dy^{3+} phosphors prepared by solid state.

   M. A. Lephoto, K. G. Tshabalala, S. S. K. Shaat and O. M. Ntwaeaborwa

2. 7th South African Conference on Photonic Materials, 27 - 31 March 2017, Amanzi Private Game Reserve, South Africa

   Study on photoluminescence and energy transfer of Eu^{3+}/Sm^{3+} single-doped and co-doped BaB_8O_{13} phosphors.

   M. A. Lephoto, K. G. Tshabalala, S. J. Motloung, I. Ahemen and O. M. Ntwaeaborwa

3. 7th South African Conference on Photonic Materials, 27 - 31 March 2017, Amanzi Private Game Reserve, South Africa

   Combustion synthesis and characterization of $MV_{0.5}P_{0.5}O_4$: Sm^{3+}, Tm^{3+} (M = Gd, La, Y)
   S. J Motloung, ***M. A. Lephoto***, K. G. Tshabalala and O. M. Ntwaeaborwa

4. 62nd South African Institute of Physics Conference (SAIP), 03 – 07 July 2017, Stellenbosch University, South Africa.

Luminescent, Structural and Morphological studies of a green-emitting BaB_8O_{13}: Ce^{3+} phosphors.

M. A. Lephoto, K. G. Tshabalala, S. J. Motloung, and O. M. Ntwaeaborwa

5. 18th International Conference on Luminescence (ICL2017), 27th August – 1st September 2017, João Pessoa/PB Brazil,

Photoluminescence studies of green emitting BaB_8O_{13}: Bi^{3+} phosphors prepared by solution combustion method.

M. A. Lephoto, K. G. Tshabalala, S. J. Motloung, G. H. Mhlongo and O. M. Ntwaeaborwa

6. European Advanced Energy Materials and Technology Congress (AEMC-2018), 25 – 28 March 2018, Stockholm, Sweden (*Abstract accepted*)

Synthesis and photoluminescent properties of dysprosium doped BaB_8O_{13} phosphor.

K. G. Tshabalala, ***M. A. Lephoto*** and O. M. Ntwaeaborwa